

DISSERTATION
SUBMITTED TO THE
COMBINED FACULTY OF
NATURAL SCIENCES AND MATHEMATICS
OF THE
RUPERTO-CAROLA-UNIVERSITY OF HEIDELBERG,
GERMANY
FOR THE DEGREE OF
DOCTOR OF NATURAL SCIENCES

PUT FORWARD BY

M. SC. FAVIOLA ZUHÉ MOLINA HERNÁNDEZ
BORN IN: MÉRIDA, VENEZUELA

ORAL EXAMINATION: 25 JULY 2013

STATISTICAL ANALYSIS OF SIMULATED
MOLECULAR CLOUDS

REFEREES:

PROF. DR. RALF. S. KLESSEN

PRIV.-DOZ. DR. HENRIK BEUTHER

Para mis padres que siempre me han apoyado en todo momento. También a mi hermano German Alberto, mi sobrino Diego, y muy especialmente a Héctor.

Abstract

Understanding molecular cloud formation is a major challenge in modern astrophysics. Although the improvements on computational power and novel astronomical instrumentation have allowed us to reach unprecedented accuracy, there are still many open questions. One key issue which helps us to understand the physics behind this problem is the correct comparison between numerical models and observations. Usually, the $^{12}\text{CO}(J=1-0)$ emission is considered to be a good tracer of the temperatures and structure of molecular clouds. However, it has been found that it may provide a biased picture of clouds, at best. In this thesis, we analyze a large set of numerical simulations with the aim of making direct comparison with observations. Using a 3D magneto-hydrodynamical simulation including time-dependent chemistry, we find that most of the CO is located at number densities greater than 100 cm^{-3} and kinetic temperatures (T_{K}) below 40 K, regardless of the mean number density (n_0), metallicity (Z) and UV radiation field strength (UV). Radiative transfer calculations are performed to analyze the $^{12}\text{CO}(J=1-0)$ rotational transition line intensity that comes out of the cloud. We then calculate the excitation temperature (T_{ex}) considering theoretical and observational approaches and find that the gas is mostly sub-thermally excited, indicating that T_{ex} represents a lower limit of T_{K} . T_{ex} is used for estimating the CO column density (N_{CO}). Considering the full position-position-velocity spectrum for inferring T_{ex} , instead of the usual way of using the maximum of the intensity along the line of sight, improves the estimates of N_{CO} by $\sim 30\%$. Besides, when a single Milky-Way like CO-to- H_2 conversion factor is assumed, the total inferred mass of H_2 is underestimated by a factor which typically increases from ~ 0.1 to 1, as the product $n_0 \times Z$ decreases, and/or UV becomes stronger. Moreover, we propose density variance–Mach number relations for supersonic, magnetized, turbulent gas, including an isothermal and non-isothermal equation of state. These analytical relations reproduce satisfactorily the measurements made on numerical simulations. We find that the magnetic field strength scales with density in a relationship of the kind $B \propto \rho^\alpha$ with $0 \leq \alpha < 1/2$.

Zusammenfassung

Die theoretische Beschreibung der Entstehung von Molekülwolken ist eine große Herausforderung der modernen Astrophysik. Obwohl mit verbesserter Computerleistung und neuartiger astronomischer Instrumentierung beispiellose Genauigkeit erreicht wird, bleiben dennoch viele Fragen offen. Der Vergleich von numerischen Modellen mit Beobachtungen fördert das Verständnis der physikalischen Prozesse dieses Problems. Gewöhnlich wird die $^{12}\text{CO}(J=1-0)$ Emission als guter Indikator der Temperaturen und der Struktur von Molekülwolken betrachtet. Jedoch wurde festgestellt, daß diese im besten Fall nur ein verzerrtes Bild der Wolken ergeben. In dieser Arbeit analysieren wir eine große Anzahl numerischer Simulationen mit dem Ziel direkte Vergleiche mit Beobachtungen zu ziehen. In 3D magnetohydrodynamischen Simulationen mit zeitabhängiger Chemie finden wir, daß sich der größte Teil des COs bei Teilchendichten über 100 cm^{-3} und kinetischen Temperaturen (T_K) unter 40 K befindet. Dieses Ergebnis ist unabhängig von der mittleren Teilchendichte (n_0), der Metallizität (Z) und der Stärke des UV Strahlungsfeldes (UV). Strahlungstransport-Rechnungen werden durchgeführt, um die aus der Molekülwolke entweichende Intensität der $^{12}\text{CO}(J=1-0)$ Rotationsübergangs-Linie zu analysieren. Anschließend berechnen wir mit theoretischen und beobachtungsbasierten Ansätzen die Anregungstemperatur (T_{ex}) und finden, daß das Gas meistens subthermisch angeregt ist, was anzeigt, daß T_{ex} eine untere Grenze von T_K darstellt. T_{ex} wird verwendet um die CO-Säulendichte (N_{CO}) abzuschätzen. Berücksichtigung des gesamten Position-Position-Geschwindigkeits-Spektrums bei der Ableitung von T_{ex} anstelle der üblichen Methode, in der das Maximum der Intensität entlang der Sichtlinie verwendet wird, verbessert die Abschätzung von N_{CO} um $\sim 30\%$. Bei Annahme des CO-zu- H_2 Konvertierungsfaktors der Milchstraße, wird die abgeleitete Maße des H_2 um einen Faktor unterschätzt, der typischerweise von ~ 0.1 bis 1 anwächst, wenn das Produkt $n_0 \times Z$ abnimmt und/oder die Stärke der UV Strahlung zunimmt. Andererseits leiten wir Dichteverianz-Machzahl Relationen für supersonisches, magnetisiertes, turbulentes Gas her, wobei wir eine isotherme sowie eine nicht-isotherme Zustandsgleichung berücksichtigen. Diese analytischen Relationen reproduzieren die Messungen aus den numerischen Simulationen. Wir zeigen, daß die Magnetfeldstärke und die Dichte einer Relation $B \propto \rho^\alpha$ folgen, wobei $0 \leq \alpha < 1/2$ gilt.

List of Publications

Refereed publications

- **Molina, F. Z.**, Glover, S. C. O., Federrath, C., & Klessen, R. S. The density variance – Mach number relation in supersonic turbulence: I. Isothermal, magnetised gas. 2012, MNRAS, 423, 2680
- **Molina, F. Z.**, Glover, S. C. O., Shetty, R., & Klessen, R. S. How well does CO($J=1-0$) emission trace the temperature in molecular clouds? 2013 - to be submitted soon.
- Lee, Min-Young; Stanimirović, Snežana; Wolfire, Mark G.; Shetty, Rahul; Glover, Simon C. O.; **Molina, Faviola Z.**; & Klessen, Ralf S. The CO-to-H₂ conversion factor across the Perseus Molecular Cloud 2013 - submitted to ApJ.

Conference proceeding

- **Molina, F.**, Glover, S., & Federrath, C. Analysis of CO and temperature distributions in simulated molecular clouds. 2011. The 5th Zermatt ISM-Symposium Conditions and Impact of Star Formation: New Results with Herschel and Beyond. EAS Publication Series, Volume 52, pp. 289-290

Contents

1	Introduction	1
1.1	Motivation of this thesis	9
1.2	Turbulence	11
1.2.1	Basic Equations of fluid dynamics	11
1.2.2	Solenoidal and compressive modes	13
1.2.3	The density probability distribution PDF	14
1.2.4	Intermittency	15
1.2.5	Effect of magnetic fields on interstellar turbulence	15
1.2.6	Turbulence & star formation	16
1.2.7	Power sources for interstellar turbulence	18
1.3	Chemistry	20
1.3.1	Effects of turbulence on interstellar chemistry	20
1.3.2	Gas-phase and grain-surface chemical reactions	21
1.3.3	H ₂ formation	24
1.3.4	Photodissociation of H ₂	25
1.3.5	H ₂ self-shielding	25
1.3.6	CO network	26
1.3.7	Photodissociation of CO	27
1.4	Radiative Transfer	29
1.4.1	The radiative transfer equation	29
1.4.2	The mean free path	31
1.4.3	The source function	32
1.4.4	Brightness temperature	32
1.4.5	The Einstein coefficients	35
1.4.6	Radiative transfer with Einstein coefficients	36
1.4.7	Excitation temperature	37
1.4.8	Extinction	37
2	Numerical method	41
2.1	Description of the simulation	41
2.2	Radiative transfer model	43

3	Tracing the temperatures of molecular clouds	47
3.1	Overview of the simulation	51
3.2	Number density and CO abundance distribution in 3D	52
3.2.1	Number density Probability Density Function	52
3.2.2	CO abundance	55
3.3	Tracing the temperature of the cloud	56
3.3.1	Kinetic temperature	56
3.3.2	Brightness temperature	59
3.3.3	Excitation temperature	62
3.4	CO column density	70
3.4.1	Total CO column density estimated from T_{ex}	80
3.5	Summary and conclusions	86
4	The H₂ mass	89
4.1	CO column density	91
4.2	CO ($J=1-0$) integrated intensity	95
4.3	The X factor	97
4.4	H ₂ column density estimate	99
4.5	Summary and Conclusions	100
5	Temperatures, CO and H₂ density distributions	109
5.1	CO and number density distributions	112
5.2	Tracing the temperature of molecular clouds	114
5.2.1	Kinetic temperature	114
5.2.2	CO ($J=1-0$) brightness temperature	116
5.2.3	Excitation temperature	117
5.3	CO column density	119
5.4	The X _{CO} -factor and H ₂ column density estimates	120
5.4.1	The $N_{\text{CO-to-}N_{\text{H}_2}}$ ratio	121
5.4.2	The $N_{\text{CO-to-}W_{\text{CO}}}$ ratio	122
5.4.3	The X-factor	124
5.5	H ₂ mass estimates	125
5.6	Summary and Conclusions	126
6	Density variance–Mach number relation	143
6.1	Analytical derivation	146
6.1.1	Density contrast in magnetohydrodynamics	146
6.1.2	The isothermal case	147
6.2	The isothermal σ_s – \mathcal{M} relation	151
6.2.1	Numerical test of the analytical model	153
6.2.2	Statistical Analysis	155

6.3	The non-isothermal case	161
6.3.1	Analytical derivation	161
6.3.2	The σ_s - \mathcal{M} relation	165
6.3.3	Numerical test	168
6.4	Summary and Conclusions	180
7	Conclusion and outlook	183
7.1	Analysis on the temperatures and CO distributions	183
7.2	Density variance–Mach number relation	184

Chapter 1

Introduction

Our perception of most of the astronomical objects changes dramatically depending on the instrument used for the observation. Starting from the basic, far from the light pollution in a clear night, looking to the sky with our naked eyes is always a fascinating experience. This picture improves significantly with the help of telescopes. It is not only matter of sensitivity, but having a panchromatic view of an astronomical source is the best way of studying it. For instance, Fig. 1.1 shows an ensemble of images of the Antennae galaxy¹ (other designations. Ringtail Galaxy, NGC 4038 / 4039, PGC 37967 / 37969, Arp 244, among others²) in different wavelengths, although the apparent colors in this figure are false. At the top, the images are from the center of the interacting galaxies, from left to right: X-rays ($10^{-2} \lesssim \lambda/[\text{nm}] \lesssim 10$, Rybicki and Lightman, 1979), Optical ($390 \lesssim \lambda/[\text{nm}] \lesssim 700$)³, Near Infrared ($800 \lesssim \lambda/[\text{nm}] \lesssim 2500$)⁴, Far Infrared ($25 \lesssim \lambda/[\mu\text{m}] \lesssim 350$)⁵, and Radiocontinuum ($\lambda = 20 \text{ cm} + \text{CO} (J=1-0)$ emission line at $\lambda = 2.6 \text{ mm}$ in white contours). Those images are beautifully complemented by the large scale images at the bottom, which correspond to (from left to right): Ultraviolet ($10 \lesssim \lambda/[\text{nm}] \lesssim 390$) (Rybicki and Lightman, 1979), Optical, and the neutral hydrogen (HI) transition at $\lambda = 21 \text{ cm}$. The many different features shown in each part of the electromagnetic spectrum are obvious from the separated images in Fig. 1.1. The features in one band may be “obscure” in another. From left to right at the top, the sequence of images show the hottest gas emission (X-rays) to the coldest (radiocontinuum+carbon monoxide). The physics dominating the radiation in each image may be treated differently,

¹<http://angelrls.blogalia.com/historias/55310>

²<http://simbad.u-strasbg.fr/simbad/>

³http://en.wikipedia.org/wiki/Visible_spectrum

⁴http://en.wikipedia.org/wiki/Near-infrared_spectroscopy

⁵https://en.wikipedia.org/wiki/Far_infrared

but it has to converge to a plausible explanation of the phenomenon.

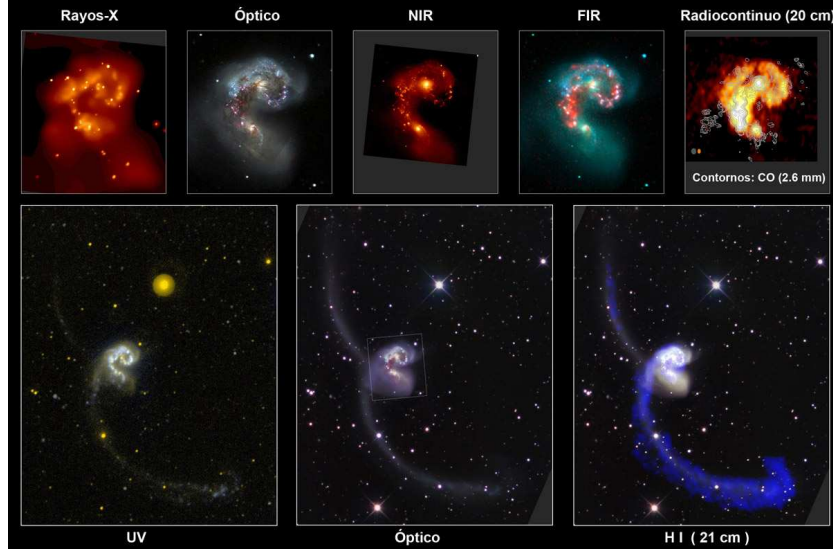


Figure 1.1: Composite images of the Antennae galaxy in different wavelengths (Arp 244) taken from <http://angelrls.blogalia.com/historias/55310> (false colors). At the top, from left to right, images in: X-rays, Optical, near-infrared, far-infrared, radio 20 cm (image) + CO ($J=1-0$) emission line at $\lambda = 2.6$ mm in white contours. At the bottom, from left to right, images in a wider field of view: UV, Optical, HI (21 cm).

The interstellar medium (ISM) is the gas and dust between the stars. It is the reservoir of material for the formation of the stars, covering a very wide range of densities and temperatures. It may be conveniently classified following the gas phases⁶ which can be observed in different wavelengths. The main characteristic of the phases of the ISM are shown in Table 1.1 (Tielens, 2005). It is noticeable that the coldest high density medium (molecular clouds) is located the closest to the Galactic mid-plane (H), and as the temperature of the gas increases, the gas locates at higher altitude above the Galactic mid-plane.

Star formation takes place in the mid-plane, with dense molecular clouds as the main site for this process (e.g. Reddish, 1975; Shu et al., 1987; Ward-Thompson et al., 2007). However, molecular clouds are intrinsically obscure in many wavelengths because of their high densities ($n \gtrsim 200 \text{ cm}^{-3}$) and

⁶The interstellar gas is composed by ions, atoms and molecules in the gas-phase. The interstellar dust are small solid particles with diameters typically less than $\sim 1 \mu\text{m}$, mixed with the interstellar gas (Draine, 2011).

Table 1.1: Main characteristics of the phases of the interstellar medium (Tielens, 2005)

Phase	n_0^a (cm $^{-3}$)	T^b (K)	H^c (pc)	Σ^d ($M_\odot\text{pc}^{-2}$)
Hot				
intercloud	0.003	10^6	3000	0.3
Warm				
neutral medium	0.5	8000	220^e	1.5
Warm				
ionized medium	0.1	8000	900^f	1.1
Cold				
neutral medium g	50	80	94	2.3
Molecular				
clouds	>200	10	75	1.0
HII regions	$1\text{-}10^5$	10^4	70^h	0.05

a Typical mean gas density for each phase. b Typical gas temperature for each phase. c Gaussian scale height above the Galactic mid-plane $\sim \exp[-(z/H)^2/2]$, unless otherwise indicated. d Surface density in the solar neighborhood. e Best represented by a Gaussian and an exponential. f Warm ionized medium represented by an exponential. g Diffuse clouds. h HII regions represented by an exponential.

low temperatures (typically of the order of few tens K). Part of the background starlight, for instance, cannot pass through this dense and cold gas. In addition, dust is well mixed with the gas and is an effective barrier to short wavelength radiation. It is caused because dust grains absorb short wavelengths (e.g. below optical wavelengths) and emit the excess of energy the infrared. Therefore, one has to choose another wavelengths which are suitable for their study. Given the low temperatures of molecular clouds, the most suitable and observed molecule in the ISM is carbon monoxide (CO) due to its excitation properties. For example, Fig. 1.2 shows a composite image of optical + mm wavelengths of the edge-on oriented Centaurus A galaxy. The image of the bright halo and obscure disk is taken in the optical part of the spectrum. It is evident that this galactic disk rich in dust and dense gas is totally opaque in the visible light. On the contrary, for the CO emission at $\lambda = 1.3$ mm (represented by the false colored cyan, violet, and dark blue features over-imposed to the optical image) part of the molecular gas structure is accessible. The violet-blue and cyan colored areas show the rotation of the disk of this galaxy. The violet-dark blue colored areas are moving towards us, while the cyan colored areas are moving away.

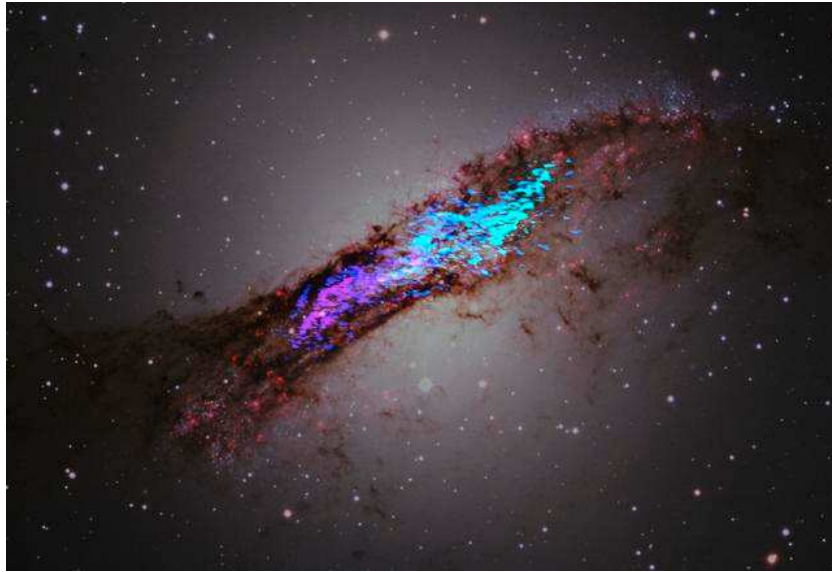


Figure 1.2: Composite image of the Centaurus A galaxy (false colors). The bright halo and the obscure disk is an optical image taken with the Wide Field Imager (WFI) of the MPG/ESO 2.2 mts. telescope located at the ESO's La Silla Observatory. The violet, blue, cyan features show the signal around CO($J=2-1$) - 1.3 mm from ALMA.

Since the first detection of CO in the ISM in mid-1970, it has been widely used to trace the molecular gas (e.g. [Wilson et al., 2009](#); [Bolatto et al., 2013](#)). Although, molecular hydrogen (H_2) is the principal component of molecular gas, it cannot be observed at the typical temperatures of molecular clouds. With two identical atoms, H_2 is a highly symmetric molecule with a small reduced mass $m_r = m_H/2$ and hence a small moment of inertia. Because its low mass and small moment of inertia, it has large separations between its rotational and vibrational levels ([Draine, 2011](#)). In addition, because of its symmetry, it has no a permanent dipole moment, and so its pure rotational transitions are electric quadrupole transitions. Together, these factor mean that H_2 emission becomes negligible once the gas temperature drops below $T \sim 200$ K ([Tielens, 2005](#); [Draine, 2011](#)). Other indirect methods are needed for tracing the molecular material of the ISM.

CO is the second most abundant molecule in the ISM. It is a diatomic molecule relatively easy to observe in millimeter wavelengths because it has a permanent dipole moment and a simple ladder of rotational levels. Its lowest transitions are very close to each other and within the same wavelength region ([Wilson et al., 2009](#)). The fundamental rotational level of ^{12}CO is excited at relatively low temperatures (≈ 5.5 K), compared to the typical temperatures of molecular clouds ($\sim 10\text{-}30$ K)⁷. CO ($J=1\text{-}0$) is therefore the most frequent observed line in molecular cloud studies ([Draine, 2011](#)). However, the amount of CO depends on the environmental conditions as is going to be shown in the course of this thesis manuscript.

Molecular clouds, taxonomy

The formation and structure of molecular clouds are mostly set by turbulence. In §1.2, we will expose about the role of turbulence in molecular clouds. In this thesis, we cover a wide range of physical parameters which are intended to simulate different environments. We are not intending to explain particular types of cloud, but rather compare statistically. To give an idea of different environments, table 1.2 (taken from [Mac Low and Klessen, 2004](#)) indicates the main physical properties of interstellar dense clouds.

Table 1.3 (taken from [Draine, 2011](#)) shows the cloud observable categories. The range in A_V in the table may change by few magnitudes from author to author, especially for Diffuse and Translucent molecular clouds. In the course of this text, we frequently refer to this classification.

⁷From now on, we will refer to ^{12}CO as CO for simplicity.

Table 1.2: Physical properties of interstellar dense clouds (Mac Low and Klessen, 2004)

	Giant molecular Cloud Complex	Molecular Cloud	Star- Forming Clump	Protostellar Core ^a
Size (pc)	10-60	2-20	0.1-2	$\lesssim 0.1$
Density [$n_{\text{H}_2}/\text{cm}^{-3}$]	100-500	10^2 - 10^4	10^3 - 10^5	$>10^5$
Mass (M_{\odot})	10^4 - 10^6	10^2 - 10^4	10 - 10^3	0.1-10
Linewidth (km s^{-1})	5-15	1-10	0.3-3	0.1-0.7
Temperature (K)	7-15	10-30	10-30	7-15
Examples	W51, W3, M17, Orion- Monoceros, Taurus-Auriga- Perseus complex	L1641,L1630, W33, W3A, B227, L1495 L1529		-

^aProtostellar cores in the “prestellar” phase, i.e., before the formation of the protostar in its interior.

Table 1.3: Cloud categories (Draine, 2011)

Category	A_V mag	Examples
Diffuse molecular cloud	$\lesssim 1$	ζ Oph cloud, $A_V = 0.84^a$
Translucent cloud	1 to 5	HD 24534 cloud, $A_V = 1.56^b$
Dark cloud	5 to 20	B68 ^c , B335 ^d
Infrared dark cloud (IRDC)	20 to $\gtrsim 100$	IRDC G0028.53-00.25 ^e

^avan Dishoeck and Black (1986). ^bRachford et al. (2002). ^cLai et al. (2003).
^dDoty et al. (2010). ^eRathborne et al. (2010).

Structure

8

The classification in Table. 1.3 is closely related to the interaction between matter and the incident radiation field. Fig. 1.3 (taken from [Draine \(2011\)](#)) shows a schematic view of a photodissociation region (PDR). It is defined as the interphase between the HII region⁹ (left) and the dense molecular cloud (right). Considering a frame at which the PDR is at rest, the UV radiation comes from strong stellar sources located at the left of the figure passing through the ionization front (where at least 50% of the hydrogen is ionized) entering into the PDR. As the molecular gas enters into the PDR, it is dissociated depending on the species. Molecules with weaker bonds are located towards higher density material (to the right of the figure). From this schematic view, one can infer that O₂ is poorly bond compared to CO, which in turn its bond is weaker than the one of H₂. The atomic gas resulting from the photodissociation process then flows towards the ionization front where it is ionized.

Part of the formation and dissociation processes of H₂ and CO are explained in §1.3.

⁸This subsection is based on the book of [Draine \(2011\)](#)

⁹A HII region is composed by ionized material surrounding new-born massive stars.

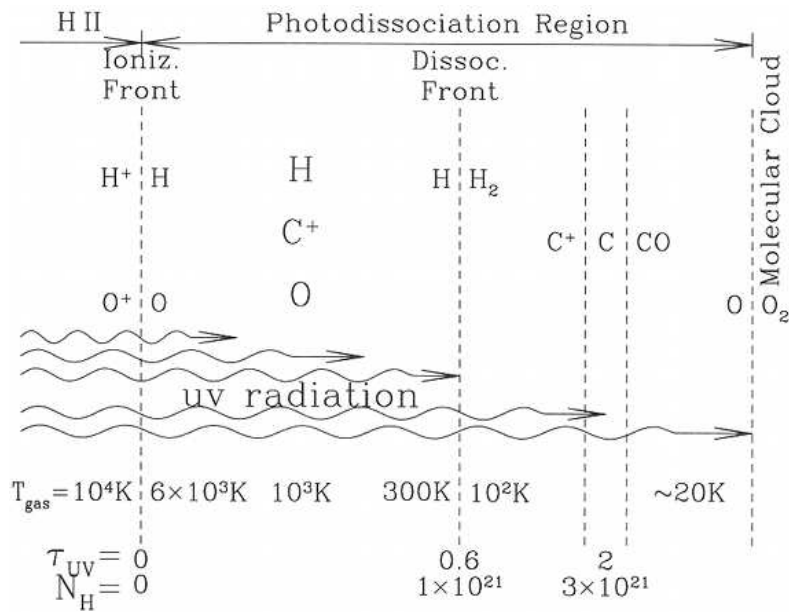


Figure 31.2 Structure of a PDR at the interface between an H II region and a dense molecular cloud.

Figure 1.3: Figure 31.2 from [Draine \(2011\)](#). Structure of a Photo-Dissociation Region at the interface between an H II region and a dense molecular cloud.

1.1 Motivation of this thesis

The understanding of astronomical phenomena mainly depends on the accurate interpretation of observational data. Theoretical models may help us to explain the physics behind the phenomena. However, the comparison between observations and theory is not always straightforward because of several reasons:

- Most of the information one has from astronomical objects comes from radiation. The relation between radiation and the underlying physics is not always well understood. The interpretation of many physical parameters, like masses and temperatures, are subject to approximations which sometimes provides a biased picture of the actual conditions.
- Models are limited. In one hand, computational power strongly constrains the physical processes that can be implemented in numerical models. This limitation force us to make many approximations that may compromise the physical interpretation of the outputs. On the other hand, good models have to be constrained by observational measurements, which frequently results on a bunch of parameters. In turn, the set of parameters have to be “tuned” in order to provide the result that better matches the observation.
- Projection effects. Observations are usually performed on a 2-dimensional basis. De-projections are very challenging, and particularly in sub-mm/mm/radio astronomy, the 3rd coordinate (given by the sight line) is frequently expressed in terms of velocities (e.g. [Goodman et al., 2009b](#)). Random velocity variations may create coherent features along the sight line in velocity space, which in real space may correspond to multiple, physically disconnected regions. Conversely, physically connected zones in real space, may be interpreted as different, separated features in velocity space ([Adler and Roberts, 1992](#); [Ballesteros-Paredes and Mac Low, 2002](#); [Glover et al., 2010](#); [Shetty et al., 2010](#)). On the other hand, simulations can be performed in 3D. However, translating 3-dimensional physical quantities into 2D counterparts may also introduce large uncertainties.

The comparison between simulations and observations of the ISM is particularly complicated. The objects in the ISM are extended and does not have a well defined and simple geometry. Many different complicated processes interplay within the ISM (details are given in the next subsections) making its structure vey dynamical (e.g. turbulence).

As molecular clouds are the site for star formation, here we present a rigorous analysis of a large set of numerical simulations which are intended to model the statistical properties of molecular clouds formation. This is done with the aim of understanding the physics of molecular clouds as well as doing direct comparisons with observations. We perform radiative transfer calculations in order to produce carbon monoxide (CO) synthetic “observations”. In the chapters 3, 4, and 5, we focus on the emission of the rotational transition $J=1-0$ (the most common observed line). The CO ($J=1-0$) spectra is then used for comparisons between physical quantities inferred from this emission and the “true” quantities¹⁰. Later, in chapter 6, we use analyze the density distribution and its relation with the Mach number.

¹⁰Since we are testing observational methods with our simulations, we define that the physical quantities directly calculated with the code as the “true” quantities.

1.2 Turbulence

11

Turbulence is observed in most of the flows in our everyday life. It is present in the water of a river, the smoke of a chimney, stirring a cup for coffee, or in the clouds. It is clear that the fluid looks irregular, unsteady, chaotic (Pope, 2011). The fluid velocity field varies irregularly and greatly with respect of the positions of the referential frame and time. A very important and useful feature of turbulence is that it is very efficient on transporting and mixing fluids elements (Pope, 2011). In the ISM for instance, the elements released by dying stars or supernova explosions are efficiently mixed by turbulence.

Molecular clouds are dynamical objects with relatively short lifetimes $\lesssim 10^7$ Myrs (e.g. Ballesteros-Paredes et al., 1999; Klessen, 2001; Glover et al., 2010, ESI, ESII). This indicates that the clouds disperse quickly because of supersonic turbulence may be the main mechanism which dominates the motion and the structure of them. At every scale, turbulence affects every physical process occurring in the ISM, like the density, temperatures, chemistry, etc. (ESI). On large scales, highly supersonic motions stir the gas by several possible mechanism like differential galactic rotation and Supernovae explosions (§1.2.7). It is dissipated on small scales by atomic viscosity (von Weizsäcker, 1951).

Turbulence is deterministic and unpredictable. It is a fluid nonlinear motion with too many degrees of freedom. *Hydrodynamic turbulence arises because the nonlinear advection operator $(\vec{v} \cdot \nabla)\vec{v}$, (in the Navier-Stokes Equation, 1.2) generates severe distortions of the velocity field by stretching, folding, and dilating fluid elements* (ESI). It is a very complicated process. However, we summarize some of the basic characteristics in this chapter.

1.2.1 Basic Equations of fluid dynamics

We often speak of number densities of particles of the different species which compose the clouds. The time scales and length of molecular motions ($\sim 10^{-10}$ s) are very small compared to the typical dynamical times used to characterize molecular clouds. Moreover, the spacing between molecular species (ions or atoms) and the mean free path is of the order of 10^{-6-7} cm (Pope, 2011). In contrast, grid based numerical simulations ranges for times and spatial resolutions which are several orders of magnitude higher than the

¹¹Most of the information in this section is based on the reviews of Elmegreen and Scalo (2004) (ESI) on Interstellar turbulence I, the book “Turbulent Flows” by Pope (2011), as well as in the lecture notes of R. S. Klessen on Theoretical Astrophysics.

molecular scales. In our particular case, spatial resolution is about 10^{17} cm and time steps run by $\Delta t \approx 10^{13}$ s. Due that molecular scales are negligible compared to the simulated scale, the collective dynamics of the particles can be treated as continuous media, where the fluid velocity v is the average velocity of the molecules at a given simulated volume \mathcal{V} (Pope, 2011).

The basic equations for fluid dynamics can be summarized as follow:

The mass transport-continuity equation

$$\frac{\partial \rho}{\partial t} + \vec{\nabla} \cdot (\rho \vec{v}) = 0, \quad (1.1)$$

where ρ is the density, \vec{v} the velocity, and t is the time. This equation indicates the conservation of mass.

The Navier-Stokes Equation

$$\frac{\partial \vec{v}}{\partial t} + (\vec{\nabla} \cdot \vec{v}) \vec{v} = -\vec{\nabla} \frac{P}{\rho} + \vec{F}, \quad (1.2)$$

where \vec{F} is a stochastic forcing term in turbulence is driven. We have neglected terms involving viscosity for simplicity¹². P is the pressure, which involves the thermal, magnetic and ram pressure

$$P = P_{th} + P_{mag} + P_{ram} = \rho \left(\frac{c_s^2}{\Gamma} + \frac{v_A^2}{2} + v^2 \right), \quad (1.3)$$

where Γ is the power of the equation of state, described by a polytrope:

$$P_{th} = K \rho^\Gamma, \quad (1.4)$$

the speed of sound is $c_s^2 = \partial P_{th} / \partial \rho = \Gamma P_{th} / \rho$, and the Alfvénic velocity $v_A^2 = \vec{B}^2 / 4\pi\rho$ (\vec{B} is the magnetic density). Eq. 1.2 indicates the transport momentum.

The transport equation of internal energy

$$\frac{\partial \epsilon}{\partial t} = T \frac{\partial s}{\partial t} - \frac{P}{\rho} \vec{\nabla} \cdot \vec{v} - \Lambda, \quad (1.5)$$

where the internal energy density $\epsilon = \rho \langle \vec{v}^2 \rangle / 2$, s is the entropy, and T is the temperature. Λ denotes the net rate at which the gas gain or loses internal energy due to radiative and chemical heating and cooling. The gravitational energy has to be also included in this equation. As we are not considering

¹²Usually, the viscosity is assumed to be constant for ISM turbulence (ESI). In our present work however, we assume that the fluid is inviscid.

the effects of self-gravity in this thesis, we leave the term regarding Gravity out of this equations. This equation indicates the conservation of energy.

For fluids in which magnetic and gravitational processes are considered, Eqs. 1.2 and 1.5 may include terms accounting for this processes.

For gravitation, the force is expressed as

$$\vec{f}_{grav} = -\vec{\nabla}\phi, \quad (1.6)$$

and the Poisson equation

$$\vec{\nabla}^2\phi = 4\pi G\rho, \quad (1.7)$$

where ϕ is the gravitational potential¹³.

For magnetism, the force is

$$\vec{f}_{mag} = -\vec{\nabla}\frac{\vec{B}^2}{8\pi} + \frac{1}{4\pi}(\vec{B} \cdot \vec{\nabla})\vec{B}, \quad (1.8)$$

and the Induction equation

$$\frac{\partial\vec{B}}{\partial t} = \vec{\nabla} \times (\vec{v} \times \vec{B}). \quad (1.9)$$

1.2.2 Solenoidal and compressive modes

Large scale motions are strongly influenced by the geometry of the flow (i.e., by the boundary conditions), and they control the transport and mixing. (Pope, 2011). They are governed by the forcing field \vec{F} in Eq. 1.2, which changes slowly in space and time. \vec{F} is derived from a stochastic Ornstein-Uhlenbeck process (Schmidt et al., 2009; Konstandin et al., 2012a). This process is generated by solving a differential equation¹⁴ which involves the projection tensor (in Fourier space)

$$\mathbf{P}_{ij}^\zeta(\vec{k}) = \zeta\mathbf{P}_{ij}^\perp(\vec{k}) + (1 - \zeta)\mathbf{P}_{ij}^\parallel(\vec{k}), \quad (1.10)$$

where $\mathbf{P}^\perp = \delta_{ij} - k_i k_j / k^2$ and $\mathbf{P}^\parallel = k_i k_j / k^2$ are the fully solenoidal and compressive projection operators respectively (Konstandin et al., 2012a). The wavenumber vector is given by $\vec{k} = 2\pi/\lambda\hat{k}$.

Setting $\zeta = 1$, the forcing field \vec{F} is purely solenoidal, i.e. $\vec{\nabla} \cdot \vec{F} = 0$. On the other hand, if $\zeta = 0$, \vec{F} is purely compressive, i.e. $\vec{\nabla} \times \vec{F} = 0$ (Federrath

¹³In this thesis gravitation is neglected.

¹⁴We do not go further on explaining the Ornstein-Uhlenbeck process because it is very complex. Including it here would add unnecessary complications to the point we want to explain.

et al., 2008b, 2010). We do not perform a Helmholtz decomposition¹⁵ of the force field, and thus the turbulent forcing consists of a natural mixture of solenoidal and compressive modes, i.e., $|\vec{F}_{sol}|/(|\vec{F}_{sol}| + |\vec{F}_{comp}|) \approx 2/3$. Notice that even purely solenoidal forcing also generates compressions (Konstandin et al., 2012a,b).

1.2.3 The density probability distribution PDF

Since the pioneer work of Vázquez-Semadeni (1994), many authors have agreed that the PDF of the logarithm of the dimensionless density ($s = \ln(\rho/\rho_0)$, where ρ_0 is the average density) is log-normal for purely hydrodynamical, supersonic isothermal, turbulent gas (e.g. Padoan et al., 1997; Passot and Vázquez-Semadeni, 1998; Nordlund and Padoan, 1999; Klessen, 2000; Ostriker et al., 2001; Li et al., 2003; Kritsuk et al., 2007; Federrath et al., 2008b; Lemaster and Stone, 2008; Schmidt et al., 2009; Glover et al., 2010; Federrath et al., 2010; Padoan and Nordlund, 2011; Collins et al., 2011; Price et al., 2011),

$$p_s ds = \frac{1}{\sqrt{2\pi\sigma_s^2}} \exp\left[-\frac{(s - s_0)^2}{2\sigma_s^2}\right] ds, \quad (1.11)$$

where the mean s_0 is related to the density variance by $s_0 = -\sigma_s^2/2$, due to the constraint of mass conservation. This shape is the result of the central limit theorem¹⁶ applied to a multiplicative random perturbations driven in a stationary system (Pope and Ching, 1993; Vázquez-Semadeni, 1994; Padoan et al., 1997; Federrath et al., 2010). In turbulent physical context, it applies to a hierarchical density field (ESI), which is characterized by the local density contrast

$$\frac{\rho}{\rho_0} = b\mathcal{M}, \quad (1.12)$$

where the rms sonic Mach number is given by $\mathcal{M} = v_{rms}/c_s$. b is a geometrical parameter of the order unity, which accounts for the turbulence driving modes of the forcing \vec{F} (Eq. 1.2). For a purely solenoidal forcing mode (divergence

¹⁵The Helmholtz decomposition theorem states that every smooth vector field, defined everywhere in space and vanishing at infinity together with its first derivatives can be decomposed into a rotational part and an irrotational part. (Joseph, 2006)

¹⁶The central limit theorem says that for a random variable U , the PDF of $\hat{U} = [\langle U \rangle_N - \langle U \rangle]N^{1/2}/\sigma_U$ (where N denotes the number of elements in the ensemble) tends to the normal distribution. But the only restriction it places on U that it has finite variance. (Pope, 2011)

free, $\vec{\nabla} \cdot \vec{F} = 0$), $b = 1/3$, while for a purely compressive forcing mode (curl-free, $\vec{\nabla} \times \vec{F} = 0$) $b = 1$.

When the gas is subject to a non-isothermal equation of state and/or to magnetic fields, the s -PDF does not deviate much from the log-normal shape (chapter 6, Glover and Mac Low, 2007a,b; Molina et al., 2012). However if gravitation is included, the s -PDF deviates from log-normal showing a power-law tail at high densities (Klessen, 2000; Federrath et al., 2008b; Kainulainen et al., 2009; Kainulainen and Tan, 2013).

1.2.4 Intermittency

Instant “observations” of shear flows suggest that there is a sharp and highly irregular interface towards the edge between turbulent and not turbulent regions. In these locations, the flow motion is sometimes turbulent and sometimes non-turbulent. The flow is there intermittent (Pope, 2011). This phenomena may affect the wings of the s -PDF. It is more evident at the low density end of the distribution.

Other evidence for intermittency is the 10^3 K collisionally excited gas required to explain CH⁺, HCO⁺, OH and excited H₂ rotational lines (ESI, Falgarone et al., 2005)

1.2.5 Effect of magnetic fields on interstellar turbulence

Magnetic fields are considered dynamically important in molecular clouds (Draine, 2011). Most of magneto-hydrodynamical simulations indicate that magnetic fields are relatively weak in molecular clouds, causing that the motions of the flow are mostly super-Alfvénic (Padoan and Nordlund, 1999), e.g. the rms velocity exceeds the Alfvénic rms velocity.

There is evidence that magnetic fields strengths increase by dynamo amplification during turbulent motions, if the flux is not conserved (Schleicher et al., 2010; Sur et al., 2010; Federrath et al., 2011; Schober et al., 2012b,b). Besides this point, the question of how magnetic fields interact with density is matter of debate. A relation of the kind $B \propto \rho^\alpha$, based on observations and simulations, has been proposed by several authors as well as several answers (Crutcher, 1999; Padoan and Nordlund, 1999; Hennebelle and Pérault, 2000; Kim et al., 2001; Crutcher et al., 2003; Banerjee et al., 2009). α may range between 0 and 1 (see chapter 6). In any case, magnetic fields seem to be incapable of quenching star formation, at least they are strong (ESI).

1.2.6 Turbulence & star formation

Together with gravity, turbulence plays a key role on regulating star formation. Even if turbulent movements are strong enough to suppress star formation at large scales, turbulence can trigger gravitational collapse at small scales (Mac Low and Klessen, 2004). Elmegreen (1993) suggest that dense cores of cloud cores could form in colliding turbulent gas streams and that gravitational instabilities in the shocked regions would lead to collapse and star formation (ESI). Mass accretion and core-core collisions are very likely, causing that more mass enter into the gravitational well (ESI).

Gravitational instabilities

Jeans criteria

The simplest case of gravitational instability is proposed for a non-rotating, unmagnetized, isothermal gas sphere in stationary steady state. From the equations of mass and momentum conservation and the Poisson Equation (Eqs. 1.1, 1.2, and 1.7, respectively), it can be determined the conditions for which the gas sphere will suffer gravitational collapse.

Following the book of Draine (2011), let us assume that the equilibrium steady state solution exists at a radius r , $\rho_0(\vec{r})$, $\vec{v}_0(\vec{r})$, $p_0(\vec{r})$, and $\phi_0(\vec{r})$ (with $r_c = 0$ at the center of the sphere), which satisfy Eqs. 1.1, 1.2, and 1.7. Now, considering a small perturbation (denoted by the index “1”) that can induce the gravitational collapse, Eqs. 1.1, 1.2, and 1.7 can be written in terms of the small perturbations $\rho = \rho_0 + \rho_1$, $\vec{v} = \vec{v}_0 + \vec{v}_1$, $p = p_0 + p_1$, and $\phi = \phi_0 + \phi_1$. From them, it is possible to define a equation like

$$\frac{\partial \vec{v}_1}{\partial t} + (\vec{v}_0 \cdot \vec{\nabla}) \vec{v}_1 + (\vec{v}_1 \cdot \vec{\nabla}) \vec{v}_0 = -c_s^2 \vec{\nabla} \left(\frac{\rho}{\rho_0} \right) \rho_1 - \vec{\nabla} \phi_1. \quad (1.13)$$

For an initially uniform stationary gas, $\nabla \rho_0 = 0$, $\nabla \phi_0 = 0$, and $\vec{v}_0 = 0$, Eq. 1.13 can be simplified. Then, taking the divergence of this equation (and considering Eqs. 1.1, 1.2, and 1.7 including the small perturbations), it is possible to obtain

$$\frac{\partial^2 \vec{v}_1}{\partial t^2} = c_s^2 \vec{\nabla}^2 \rho_1 + 4\pi G \rho_0 \rho_1. \quad (1.14)$$

If the perturbations are assumed to be plane-waves:

$$\rho_1 \propto e^{i(\vec{k} \cdot \vec{r} - \omega t)},$$

a dispersion relation is obtained

$$\omega^2 = k^2 c_s^2 - 4\pi G \rho_0 = (k^2 - k_J^2) c_s^2, \quad (1.15)$$

where k_J is the wavenumber of the “*Jeans instability*” defined as $k_J^2 \equiv 4\pi G \rho_0 / c_s^2$. ω is real for $k \geq k_J$. Therefore, the “*Jeans instability*” occurs for wavelengths

$$\lambda > \lambda_J \equiv \sqrt{\left(\frac{\pi c_s^2}{G \rho_0}\right)}. \quad (1.16)$$

For the “*Jeans instability*”, the “*Jeans mass*” is defined as

$$M_J \equiv \frac{4\pi}{3} \rho_0 \left(\frac{\lambda_J}{2}\right)^3 = \frac{1}{8} \left(\frac{\pi k T}{G \mu}\right)^{3/2} \frac{1}{\rho_0^{1/2}}. \quad (1.17)$$

Even though the assumption: $\nabla \phi_0 = 0$ is unphysical, considering Eq. 1.17 it is possible to predict reasonable stellar masses.

The Bonnor-Ebert mass

In addition to the “*Jeans criteria*”, there are other approaches to the gravitational instability for cloud collapse. The virial theorem including gravitation and magnetism, can be derived from Eq. 1.2 (see [Draine, 2011](#), in the Appendix J, he shows this derivation)¹⁷. For a region in equilibrium, with uniform pressure p_0 and magnetic field $\vec{B} = 0$ at the surface, the virial equation states

$$0 = 2E_{\text{KE}} + 3(\Pi - \Pi_0) + (E_{\text{mag}} - E_{\text{mag},0}) + E_{\text{grav}}, \quad (1.18)$$

where the kinetic energy is defined as

$$E_{\text{KE}} \equiv \int \rho \frac{v^2}{2} dV, \quad (1.19)$$

the thermal energy

$$\Pi \equiv \int p dV, \quad \Pi_0 = p_0 V, \quad (1.20)$$

the magnetic energy

$$E_{\text{mag}} \equiv \int \frac{B^2}{8\pi} dV, \quad E_{\text{mag},0} \equiv \oint d\vec{S} \cdot \left[\vec{r} \frac{B^2}{8\pi} - \frac{\vec{B}(\vec{r} \cdot \vec{B})}{4\pi} \right], \quad (1.21)$$

and finally, the gravitational energy

$$E_{\text{grav}} = -\frac{1}{2} \int dV_1 \int dV_2 \frac{\rho(\vec{r}_1) \rho(\vec{r}_2)}{|\vec{r}_1 - \vec{r}_2|}. \quad (1.22)$$

¹⁷We follow [Draine \(2011\)](#)s book in this subsection

V is the volume that encloses the region. \vec{r}_1 & \vec{r}_2 and V_1 & V_2 are the radius at two different points 1 & 2, and the volume enclosing the subregions at those points, respectively. \vec{S} is the surface vector.

Simplifying Eq. 1.18 into a non-rotating, unmagnetized, isothermal spherical core, with mass M and radius R , Eq. 1.18 results

$$0 = 3Mc_s^2 - 4\pi p_0 R^3 - \frac{3}{5}a \frac{GM^2}{R}, \quad (1.23)$$

where the gas is considered in equilibrium with $v = 0$, and

$$E_{\text{grav}} = -\frac{3}{5}a \frac{GM^2}{R}, \quad (1.24)$$

&

$$\Pi = Mc_s^2, \quad \text{with } c_s = \text{const.} \quad (1.25)$$

Going around with the terms in Eq. 1.23, it is possible to establish limits to the external pressure p_0 and find its maximum possible values. With this constrains, a criteria for the maximum mass that can be in equilibrium is set to

$$M_{\text{BE}}(p_0) = \frac{225}{32\sqrt{5}\pi} \frac{c_s^4}{(aG)^{3/2}} \frac{1}{\sqrt{p_0}}. \quad (1.26)$$

This is known as the Bonnor-Ebert mass. Cores with $M > M_{\text{BE}}$ are unstable to collapse.

1.2.7 Power sources for interstellar turbulence

The small scale motions are determined by the viscosity and the energy rate, which they receive from the large scales (Pope, 2011). It seems that turbulence is mostly driven at large scales, at which correlated velocity fluctuations observed (Brunt, 2003).

For molecular clouds, it seems that the dominant driver of turbulence is the development of HII regions around massive stars (Matzner, 2002). Although it is more accepted that supernovae and HII regions dominates the large scale turbulence (Brunt, 2003). In some numerical simulations, supernovae explosions are included (e.g. Avillez et al., 2000). For instance, Avillez et al. (2000) model the 3D vertical structure of the interstellar gas in a galaxy disk. They find an array of structures over 400 Myrs including a thin cold disk expelling vertical “worms” as well as a thick foamy disk of warm neutral gas. Moreover, this authors report the formation of smaller structures formed from the interaction of “worms” and sheets, and superbubbles connected by

tunnel-like structures, hot gas and “chimneys” which rise above of the plane (ESI).

1.3 Chemistry

Astro-chemistry describes the very important process through which the species constituent the ISM are formed. The most abundant and widespread molecule of molecular clouds is H_2 , other molecules are present only in smaller amounts. CO (the second most abundant molecule) has a ratio – compared to H_2 – of the order of 10^{-4} (Glover and Mac Low, 2007a). Even though this ratio is very low, CO is useful for molecular gas observations. We therefore focus this section mostly on the study of the CO formation network, as well as H_2 .

First, let's start this section by looking to the tight connection between turbulence and chemistry.

1.3.1 Effects of turbulence on interstellar chemistry

Turbulence may affect the chemistry of the ISM in the following ways (Scalo and Elmegreen, 2004):

- (a) Continuous transport of material between regions in different environments, like density, temperature, and/or incident UV radiation field strength.
- (b) Creation of localized heating which will trigger temperature-sensitive reactions.
- (c) Magnetically forcing ions to move faster than thermal movement, which can enhance the ion-neutral reactions sensitive to the temperature.
- (d) Turbulent heating. Creation of shock waves may affect the chemistry as well as vortices, ambipolar diffusion, and magnetic reconnection.

Particularly, (d) is very important. Temperature gradients enhance many different reaction which are sensitive to the temperature. In dense shielded clouds, the warm/diffuse regions drive reactions like



enhancing the H_2O abundance and preventing the formation of SO_2 , for instance (Scalo and Elmegreen, 2004). Moreover, other molecules like CO are also photodissociated in warm/diffuse gas. We will explain the CO chemistry later in this chapter.

1.3.2 Gas-phase and grain-surface chemical reactions

18

There is a variety of processes which lead to chemical reactions in the ISM. Typically, these reactions are classified in two major groups: the ones that can occur in the gas (like most of the CO chemistry), and those which occur in the surface surface of dust grains (like H₂ formation, although it can also happen in the gas-phase but with lower probability).

Gas-phase chemistry

These kind of reactions are in turn split into three categories of processes. The bond-formation reactions which link atoms into simple or complex species, like radiative association, collisional association and associative detachment reactions. Other processes break species into smaller ones, which are bond-destruction reactions and involve photodissociation, dissociative electron recombination, collisional dissociation, and cosmic rays reactions. The last group is conformed by the charge-transfer reactions: ion-molecule exchange, charge transfer, and neutral-neutral reactions. In table 1.4 (from Tielens (2005) + cosmic rays reactions), we summarize them for generic species denoted as A, B, C, D and M. Photons are specified by their energy $h\nu$ and cosmic rays as “cr”. The photons induced by the cosmic rays are included as cosmic rays reaction. Table 1.4 includes equilibrium reaction rates.

It is assumed that the degrees of freedom are in thermodynamical equilibrium, which in turn are described by a single temperature. The ISM is in general far from equilibrium. Therefore, more accurate reaction rates may take into account environmental conditions in which the reaction takes place (see Appendix B of Glover et al., 2010).

Grain-surfase reactions

Grains provide a surface on which accreted species meet and eventually react¹⁸. The energy released during the reaction is transferred to the surface helping to the ejection of the new species to the gas-phase. Fig. 1.4, taken from Tielens (2005), illustrates the grain-surface interaction process. First, the species are accreted to the surface which depends on the gas and dust temperature. The accretion also depends on the “stickiness” coefficient which is particular of the species involved, *the thermal velocity of the gas and the*

¹⁸most of this subsection is based on the book of Tielens (2005).

¹⁹Reactions can take place on dust or H₂O ices.

Table 1.4: Table 4.1 from [Tielens \(2005\)](#): Generic gas phase reactions and their rates

	reaction	rate	unit	note
Photodissociation	$AB + h\nu \rightarrow A + B$	10^{-9}	s^{-1}	(a)
Neutral-neutral	$A + B \rightarrow C + D$	4×10^{-11}	cm^3s^{-1}	(b)
Ion-molecule	$A^+ + B \rightarrow C^+ + D$	2×10^{-9}	cm^3s^{-1}	(c)
Charge-transfer	$A^+ + B \rightarrow A + B^+$	10^{-9}	cm^3s^{-1}	(c)
Radiative association	$A + B \rightarrow AB + h\nu$	-	-	(d)
Dissociative recombination	$A^+e \rightarrow C + D$	10^{-7}	cm^3s^{-1}	
Collisional association	$A + B + M \rightarrow AB + M$	10^{-32}	cm^6s^{-1}	(c)
Collisional dissociation	$AB + M \rightarrow A + B + M$	-	-	(e)
Associative detachment	$A^- + B \rightarrow AB + e$	10^{-9}	cm^3s^{-1}	(c)
Cosmic rays	$AB + cr(h\nu_{cr}) \rightarrow A + B$	2×10^{-10}	s^{-1}	(f)

(a) Rate in the unshielded radiation field.

(b) Rate in the exothermic direction and assuming no activation barrier (i.e., radical-radical reaction).

(c) Rate in the exothermic direction.

(d) Rate highly reaction specific.

(e) Line added by us, for clarification of the collisional reaction. This reaction and the preceding are very unlikely to take place in the ISM (3 bodies reaction), except for very dense gas ($\simeq 10^{11} \text{ cm}^{-3}$) typical of the gas near stellar photospheres or dense circumstellar disks.

(f) Rate only for the reaction $CO + h\nu_{cr} \rightarrow C + O$. ($h\nu_{cr}$) states for cosmic-ray induced UV emission.

excitation of the phonon spectrum of the grain, as well as the interaction energy of the gas phase species and the surface (Tielens, 2005).

The gas-phase species that approaches to the surface feel an attraction due to van der Waals forces²⁰. At short distances, the forces associated to the overlap of the wave functions of the approaching species and the surface lead to a strong binding (Tielens, 2005). The surface migration (diffusion in Fig. 1.4) scale is very important for the reaction network, which also depends on the species. In the case of hydrogen (and deuterium) at low temperatures, the migration occurs through quantum mechanical tunneling.

Once the species meet and mate (reaction in Fig. 1.4), the residence time on the surface depends on the vibrational frequency of the adsorbed species on the grain surface, the phonon energy of the surface and the dust temperature. This time is characteristic of each species, and it is essentially set by how long takes the species to acquire sufficient energy through thermal fluctuations to evaporate (ejection in Fig. 1.4).

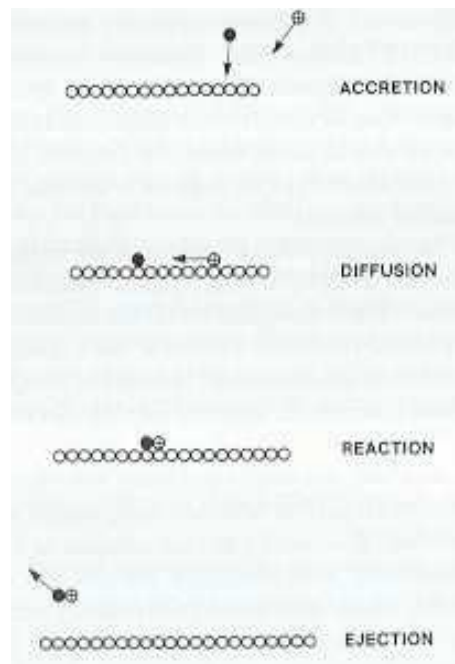


Figure 1.4: Figure 4.1 from Tielens (2005). A schematic of the formation of molecules on grain surfaces. Gas phase species accrete, diffuse, and react on an interstellar grain surface.

²⁰van der Waals force is the sum of the attractive or repulsive forces between molecules, or between part of those (wikipedia.com).

The extended residence time of the interacting species on the grain surface allows for reactions which are generally inhibited in the gas-phase due to strong activation barriers. This is one of the distinguishing characteristics of grain surface chemistry. The probability for reaction is given by the competition between migration and the penetration of the activation barrier. The particular case of H₂ formation is explained in the next subsection.

1.3.3 H₂ formation

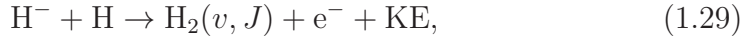
²¹

H₂ formation is dominated by dust grain surface reactions. A H atom arrives and stick to the grain surface. In this first contact, the binding energy may be weak enough to let the atom perform a random walk through some distance on the surface (diffusion). During this walk, it may arrive to a location where the binding becomes strong enough to “trap” the atom. The low temperature of the grain surface (~ 20 K) are unable of free the H atom for further exploration of the surface. Other H atoms arrive to the surface and perform their own random walks until they get trapped. In the course of the time, one of the newly arrived H atoms – which is undergoing its own random walk – meets a trapped H and react to form H₂. The energy released in this reaction (for H₂ in the ground state) is $\Delta E = 4.5$ eV, which is large enough to overcome the binding force with the surface. The H₂ molecule can be then released to the gas-phase.

The formation of H₂ may occur in the gas-phase as well. The dominant channel in this case starts by the formation of the ion H⁻ by radiative association



which is followed by the H₂ formation through associative detachment



where KE is the energy released from the reaction and H₂ is in its ground state. The abundance of H⁻ decreases towards high density/optically thick regions (through recombination $\text{H}^- + \text{H}^+ \rightarrow \text{H} + \text{H}$). In diffuse regions on the other hand, one would expect higher H⁻ abundances. However, its formation is slow and the destruction is rapid. Other channels are less likely to happen. For instance, two free H atoms in the ground state approach one another, however by symmetry there is no electric dipole moment. Hence, *there*

²¹This subsection is based on the book of [Draine \(2011\)](#).

is no electric dipole radiation that could remove energy from the system and leave the two atoms in a bound state (Draine, 2011). The possible radiation can be emitted from electric quadrupole transitions, but the rates are very low. The rate coefficient for the reaction: $\text{H} + \text{H} \rightarrow \text{H}_2 + h\nu$ is very small and it is usually ignored. A three bodies reaction like $\text{H} + \text{H} + \text{H} \rightarrow \text{H}_2 + \text{H} + \text{KE}$ is possible, but it is also ignored because its rate is too small for densities typical of molecular clouds.

1.3.4 Photodissociation of H_2

22

H_2 photodissociation is the main mechanism for H_2 destruction in the ISM. The reaction



occurs, but first the H_2 molecule has to be raised to an excited level. H_2 is initially in a level $X(v, J)$ of the ground electronic state $X^1\Sigma_g^+$ to a level $B(v, J)$ or $C(v, J)$ of the first and second excited states $B^1\Sigma_u^+$ and $C^1\Sigma_u$. 85% of the time, the excited H_2 may decay vibrationally to an excited bound level $X(v'', J'')$ of the ground state. However, it may happen that spontaneous decays from the excited level $B(v', J')$ will be to the vibrational continuum of the ground state and the H_2 molecule splits apart in $\sim 10^{-14}$ s.

Photodissociation has low probability to take place at the typical temperatures of molecular clouds ($T \approx 20\text{-}50$ K), because this process requires temperatures higher than 500 K.

1.3.5 H_2 self-shielding

23

Self-shielding corresponds to the phenomenon where the photoexcitation transitions becomes optically thick, i.e. $\tau > 1$ (see §1.4.8). In this sense, one molecule is “shielded” from the incident starlight by other molecules. *The H_2 molecule is the most important example of self-shielding* (Draine, 2011). H_2 absorbs UV photons $\lambda \gtrsim 1100\text{-}912\text{\AA}$ in the neutral zone (Fig. 1.3). At this point, H_2 can be dissociated. This corresponds to diffuse/translucent clouds. Deeper in the cloud (to the right of Fig. 1.3), where the location of the HI/H_2 transition is dominated by dust absorption (visual extinction $A_V \gtrsim 2$ mag, see §1.4.8), H_2 photodissociation is sufficiently reduced, and

²²This subsection is based on the book of Draine (2011).

²³This subsection is based on the books of Draine (2011) and Tielens (2005).

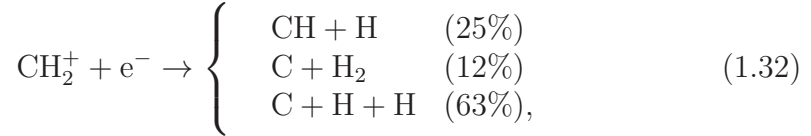
an appreciable H_2 column density can be built. Then, H_2 self-shielding takes over and the H_2 abundance relative to the total number of hydrogen nuclei increases towards the right of Fig. 1.3, until all hydrogen atoms are locked up into H_2 molecules (Tielens, 2005).

1.3.6 CO network

24

The CO abundance is a complex function of the environmental conditions of molecular clouds. It depends on the local density and temperature as well as the local UV radiation field (Glover and Clark, 2012a). In this subsection, we will present part of the CO chemical network.

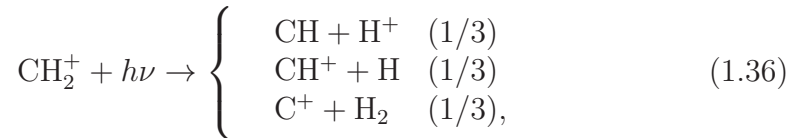
In diffuse molecular clouds, most of the carbon is ionized C^+ and a significant amount of H is locked up into H_2 molecules. In this case, CO is primarily formed by the sequence of reactions (taken from Draine, 2011):



where the percentage indicates the probability for this reaction to occur.

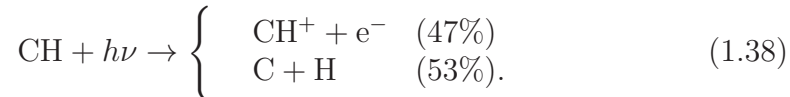


The first reaction (through radiative association) is slow but continuously produces CH_2^+ , which rapidly reacts with e^- to produce CH $\sim 25\%$ of the time. CH_2^+ can also be photodissociated or it may react with H_2 to produce:



²⁴Most of the subsection is base on the books of Draine (2011) and Tielens (2005).

In diffuse molecular clouds, the dissociative recombination of CH_2^+ (or the reaction with H_2) dominates over the photodestruction of CH_2^+ . In both cases, the radical is destroyed. The CH molecule produced by dissociative recombination (Eq. 1.32) can react with O to produce CO through the reaction indicated in Eq. 1.33. Although CH is very sensitive to photodissociation and photoionization



CO is frequently assumed to primarily form in the gas phase in diffuse molecular clouds. The formation of CO on grain surface is uncertain. Atoms of C and O may stick into dust grains and eventually react to form CO. The energy released in the formation may help the molecule to released itself into the gas-phase, or by photodesorption.

1.3.7 Photodissociation of CO

25

CO is strongly photodissociated in diffuse molecular clouds through the reaction represented in Eq. 1.34. CO self-shielding is very weak and the CO abundance increases where the gas shielding (dust and H_2 shielding) becomes important. This is equivalent to visual extinctions $\gtrsim 3$ mag. At this point in the cloud, photodissociation from UV photons are unimportant compared to cosmic-rays ionization. CO is dissociated by UV photons induced by cosmic rays



CO photodissociation rate from the chain in Eq. 1.39 depends on the abundance of H_2 relative the CO. In this thesis, this process seems to be unimportant at visual extinctions $\gtrsim 3$ mag. Moreover at high A_V , *cosmic-rays ionization of H_2 leads to the formation of H_3^+ which is the cornerstone of ion-molecule gas-phase chemistry. That is where reactions with H_2 will stop and dissociative electron recombination takes over, forming H_2O and OH in about 1 to 2 ratio. These O-bearing species are lost through reaction with hydrocarbon radicals, which burn them to (eventually) CO (Tielens, 2005).*

There are other reactions which leads to CO formation, like through HCO^+ or He^+ radicals. Explaining all the possible reactions of the network is very complicated. We prefer to finish this section summarizing that CO is

²⁵This subsection is based on the book of [Draine \(2011\)](#).

inefficient on preventing itself from photodissociation (weak self-shielding). The CO abundance increases towards regions where dust and H₂ shielding is strong enough to prevent the photodissociation of CO ([Glover et al., 2010](#)).

1.4 Radiative Transfer

26

Most of the information that can be obtained from astronomical sources is based on electromagnetic radiation. Therefore, the physical interpretation of the physics of these objects depends mainly on radiative transfer calculations. In some cases, the analytical derivation of the radiative transfer equations may be very complex, and so it is necessary to assess the results numerically. In observations neither the analytical or numerical solutions are not possible to be obtained, and it is therefore convenient to implement a bunch of approximations.

1.4.1 The radiative transfer equation

Lets assume that a source emits with a specific intensity I_ν at a given frequency ν which remains unchanged independently of the distance along a ray. This intensity changes only if it is absorbed or emitted by an “obstacle” interposed in the ray path between the source and the observer, as shown in Fig. 1.5. The incident I_ν at the right varies by dI_ν depending on the characteristics of the slab of material represented by the gray area with thickness s . This change is described by the equation of transfer.

I_ν may gain or lose intensity (by $dI_{\nu+}$ or $dI_{\nu-}$ respectively) in its interaction with the media. In this sense, the radiative transfer equation is built from two components

$$\frac{dI_\nu}{ds} = \frac{dI_{\nu-}}{ds} + \frac{dI_{\nu+}}{ds} = -\kappa_\nu I_\nu + \varepsilon_\nu, \quad (1.40)$$

where κ_ν is the absorption coefficient and ε_ν is the emissivity. Both parameters may depend on the microscopic properties of the media. However, Eq. 1.40 is related to a macroscopic theory for which κ_ν and ε_ν are represented as the average properties of the collective of particles.

ε_ν may also depend strongly on I_ν . However to deal with this kind of issues, there are several limiting cases for which the solution of Eq. 1.40 is simple.

1. Emission only: $\kappa = 0$

$$\frac{dI_\nu}{ds} = \varepsilon_\nu, \quad I_\nu(s) = I_\nu(s_0) + \int_{s_0}^s \varepsilon_\nu(s) ds. \quad (1.41)$$

²⁶The content of this section is based on the book of [Wilson et al. \(2009\)](#), [Rybicki and Lightman \(1979\)](#) and [Draine \(2011\)](#).

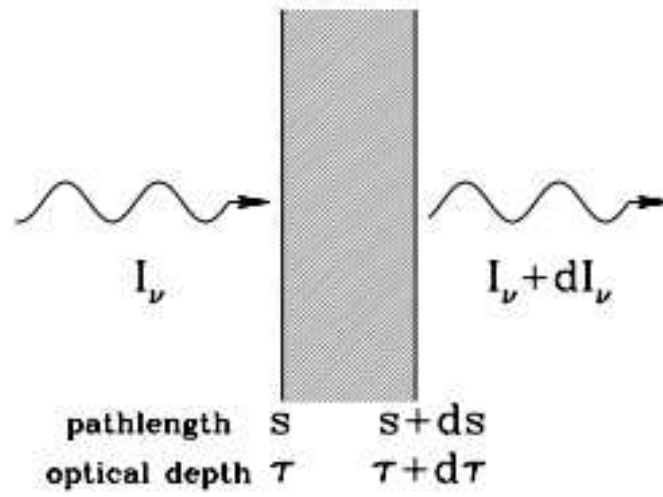


Figure 7.1 Radiative transfer geometry.

Figure 1.5: Figure 7.1 from [Draine \(2011\)](#). Radiative transfer geometry.

2. Absorption only: $\varepsilon = 0$

$$\frac{dI_\nu}{ds} = -\kappa_\nu I_\nu, \quad I_\nu(s) = I_\nu(s_0) \exp \left\{ - \int_{s_0}^s \kappa_\nu(s) ds \right\}. \quad (1.42)$$

3. Thermodynamic equilibrium (TE): In the case in which there is complete equilibrium of the radiation with the medium. There is no loss or gain of intensity. Both have a constant thermodynamic temperature T , and the brightness is described by the Planck function

$$B_\nu(T) = \frac{2h\nu^3}{c^2} \frac{1}{\exp h\nu/kT - 1} \quad (1.43)$$

$$\frac{dI_\nu}{ds} = 0, \quad I_\nu(s) = B_\nu(T) = \frac{\varepsilon_\nu}{\kappa_\nu}. \quad (1.44)$$

4. Local thermodynamic equilibrium (LTE): Thermodynamic equilibrium occurs in scales for which $ds \lesssim \ell_\nu$, where ℓ_ν is the mean free path.

$$\frac{\varepsilon_\nu}{\kappa_\nu} = B_\nu(T). \quad (1.45)$$

This relation is known as the Kirchhoff's law.

1.4.2 The mean free path

The mean free path ℓ_ν describes absorption of radiation (or photons) in an equivalent way. It is the average distance that a photon can travel through a medium without being absorbed. So then, the physical distance traveled by a photon in an homogeneous absorbing medium is

$$\ell_\nu = 1/\kappa_\nu, \quad (1.46)$$

κ_ν can be written as $\kappa_\nu = \rho\alpha_\nu$. α_ν represents the average absorbing characteristic of the particles (the mass absorption coefficient, sometimes called the opacity coefficient) which compose the medium, and the density ρ determines the amount of material. ℓ_ν is essentially, the probability of a photon traveling at least an optical depth $e^{-\tau_\nu}$. The optical depth is defined as

$$d\tau_\nu = \kappa_\nu ds, \quad \text{or} \quad \tau_\nu(s) = \int_{s_0}^s \kappa_\nu(s') ds'. \quad (1.47)$$

ℓ_ν and τ_ν are related by

$$\kappa_\nu \ell_\nu = \langle \tau_\nu \rangle \equiv \int_0^\infty \tau_\nu e^{-\tau} d\tau_\nu = 1. \quad (1.48)$$

1.4.3 The source function

The equation of transfer (Eq. 1.40) can be then written in terms of τ_ν

$$\frac{dI_\nu}{d\tau} = -I_\nu + S_\nu, \quad (1.49)$$

where S_ν is defined as the *source function*, which is the ratio of the emission to the absorption coefficient:

$$S_\nu \equiv \frac{\varepsilon_\nu}{\kappa_\nu}. \quad (1.50)$$

The formal solution of the radiative transfer equation in terms of I_ν and S_ν is

$$I_\nu(\tau_\nu) = I_\nu(0)e^{-\tau_\nu(s)} + \int_0^{\tau_\nu(s)} e^{-(\tau_\nu(s)-\tau'_\nu(s))} S_\nu(\tau'_\nu) d\tau'_\nu(s). \quad (1.51)$$

This equation is interpreted as the sum of two terms: the initial intensity is diminished by absorption (by a factor $e^{-\tau_\nu}$) plus the integrated source diminished by absorption.

1.4.4 Brightness temperature

In practice, Eq. 1.51 cannot be easily solved analytically. It can be approximately solved numerically through iterative methods. Therefore, it is frequent to assume several approximations for interpretation of astronomical data.

In the case that a source is in thermodynamical equilibrium, $S_\nu = B_\nu(T(\tau))$. Moreover, if the medium is assumed to be isothermal, i.e. $T(\tau) = T(s) = T$, Eq. 1.51 simplifies to

$$I_\nu(s) = I_\nu(0)e^{-\tau_\nu(s)} + B_\nu(T)(1 - e^{-\tau_\nu(s)}). \quad (1.52)$$

When $\tau \rightarrow \infty$, $I_\nu = B_\nu(T)$.

Now assuming that the intensity, I_ν can be characterized by a blackbody having the same brightness at that frequency ν . The temperature associated to this blackbody is the brightness temperature T_b , which is defined as

$$I_\nu = B_\nu(T_b), \quad (1.53)$$

Given the low frequencies in radio astronomy, the limit $h\nu \ll kT_b$ is applicable and the Rayleigh-Jeans approximation is commonly used. Therefore,

the intensity at a given ν can be written as

$$T_b = \frac{c^2}{2\nu^2 k} I_\nu. \quad (1.54)$$

Using Eq. 1.54, the radiative transfer equation can be expressed in terms of T_b

$$T_b(s) = T_b(0)e^{-\tau_\nu(s)} + T(1 - e^{-\tau_\nu(s)}). \quad (1.55)$$

From Eq. 1.55, two important assumptions are made:

1. For optically thin gas ($\tau \ll 1$), $T_b \approx \tau_\nu T$, and
2. if the gas is optically thick ($\tau \gg 1$), $T_b \approx T$.

However, in the ISM the gas is not expected to be in LTE. In a more realistic scenario, different processes may take place and make the emission of the source be very different from the black body radiation. In such case, T_b will depend on the frequency (Wilson et al., 2009). Therefore Eq. 1.54 is not necessarily the most accurate way of calculating T . Moreover, if the radiation is not thermalized, Eq. 1.53 does not describe the physical conditions of the source.

On the other hand, even though the source may be a black body, it is usually assumed that the Rayleigh-Jeans approximation is accurate for any frequency in the mm/sub-mm range of its spectrum. For instance, at $\nu_0 = 115.3$ GHz which is the frequency for the CO ($J=1-0$) transition, Eq. 1.54 is applied regardless the intrinsic T of the source. If $T = T_b \lesssim 1$ K, Eqs. 1.53 and 1.54 arise to very different results. To illustrate this point, Fig. 1.6 shows I_ν , calculated from Eq. 1.53 (solid lines) considering different brightness temperatures $T_b = 10^{-3}$ K (purple), 10^{-2} K (light-green), 0.147 K (red), 1 K (yellow), 5K (green), and 10 K (blue), as a function of ν . Colored dotted lines show I_ν as well but calculated from Eq. 1.54 for the same set of temperatures. The dashed line indicates $\nu_0 = 115.3$ GHz. For $T = T_b \gtrsim 1$ K, The intensities calculated from Eq. 1.53 or Eq. 1.54 are approximately equivalent (the Rayleigh-Jeans approximation holds). However, for $T = T_b \lesssim 1$ K, the intensities calculated from Eqs. 1.53 and Eqs. 1.54 are very different, and the discrepancies increases towards lower T_b . However, in astronomy we measure intensities which at given intensity, the brightness temperature inferred from Eq. 1.54 is always smaller than the brightness temperature calculated from Eq. 1.53.

In any case, Eq. 1.54 is the most used equation for calculating brightness temperatures, although the Rayleigh-Jeans approximation may not apply in

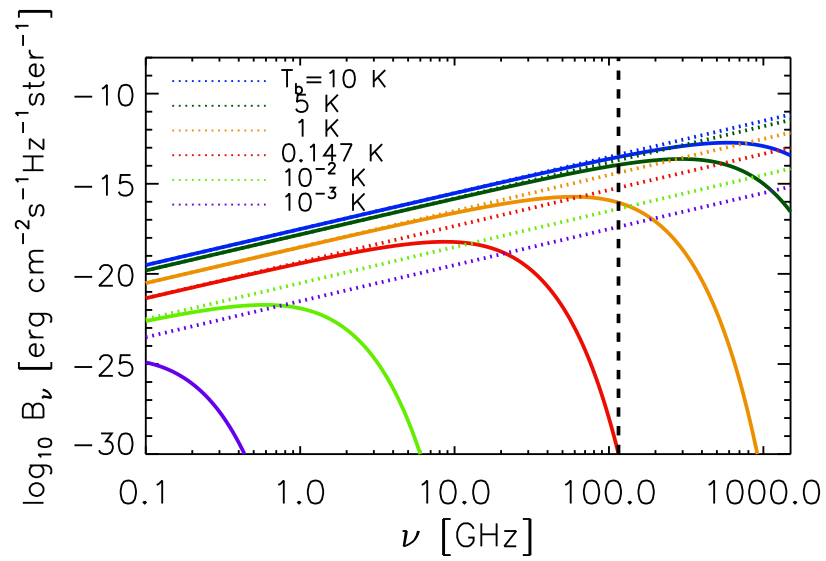


Figure 1.6: Black-body spectra $B_\nu(T_b)$ for different brightness temperatures $T_b = 10^{-3}$ K, 10^{-2} K, 0.147 K, 1 K, 5K, and 10 K, as a function of ν . The solid black lines show $I_\nu = B_\nu(T_b)$, Eq. 1.53 (higher fluxes correspond to higher temperatures). The colored dotted lines show the Rayleigh-Jeans approximation given by Eq. 1.54 for the same set of temperatures.

many cases. It is still a useful and practical quantity because I_ν and T_b are proportional. In observational works it is commonly called the “Antenna Temperature” (Wilson et al., 2009).

1.4.5 The Einstein coefficients

The Kirchhoff’s law, $\varepsilon_\nu = \kappa_\nu B_\nu$, relates the emission to absorption of a thermal emitter. This relation implies a relationship between emission and absorption at a microscopic level. Einstein was the first who discover this relationship. He made an analysis of the interaction of radiation with an atomic system. Considering the simple case of two discrete energy levels, the first of energy $E_i = E$ and statistical weight g_i , and the second of energy $E_j = E + h\nu_0$ with statistical weight g_j , the system makes a transition $i \rightarrow j$ and a photon with energy $h\nu_0$ is absorbed. For a transition $j \rightarrow i$, a photon with energy $h\nu_0$ is emitted. For this phenomenon, three processes are identified:

- **Spontaneous emission:** The system in a level j suddenly drops to level i emitting a photon. The transition probability per unit time for this emission is A_{ji} .
- **Absorption:** This process occurs in two possible scenarios:
 1. In the presence of photons of energy $h\nu_0$, the system makes a transition from level i to level j by absorbing a photon. The probability of this transition per unit time is $B_{ij}\bar{J}_{ij}$, where $\bar{J}_{ij} = 1/4\pi \int_0^\infty I_{ij}\phi_{ij} d\nu_{ij}$ (I_{ij} is the intensity of the transition at ν_{ij} and ϕ_{ij} is the line profile).
 2. The atom is immersed in a medium filled with particles that may collide with it. From a collision, the atom may absorb enough energy to make a transition $i \rightarrow j$. The probability per unit time of an absorption due to collisions is $C_{ij} = nK_{ij}$, where n is the number density of collisional partners and K_{ij} is the collision rate coefficient²⁷.
- **Stimulated emission:** Again, this process occurs in two possible scenarios:

²⁷The collision rate coefficient are derived from $K_{ij} = \int v\sigma_{ij}(v)f(v)dv$ [cm^3s^{-1}], where v is the velocity of the particles, $f(v)$ is the distribution of velocities, and $\sigma_{ij}(v)$ is the corresponding collision cross section.

1. In the presence of a radiation field, the system makes a transition from level $j \rightarrow i$ emitting a photon. The probability of this transition per unit time is $B_{ji}\bar{J}_{ij}$ (For convenience, we assume a symmetrical line profile for which $\bar{J}_{ij} = \bar{J}_{ji}$).
2. A collision may stimulate the atom to make a transition $j \rightarrow i$ emitting a photon. The probability per unit time of an absorption due to collisions is $C_{ji} = nK_{ji}$.

The coefficients A_x , B_x and C_x (with $x = ij$ or $x = ji$) are known as the Einstein coefficients.

Generalizing, in statistical equilibrium the number of transitions per unit time per unit volume out of level i = the number of transitions per unit time per unit volume into level j . If n_i and n_j are the number densities of atoms at level i and j respectively, the population of levels is governed by the equation of detailed balance:

$$\begin{aligned} \sum_{j>i}[n_j A_{ji} + (n_j B_{ji} - n_i B_{ij})\bar{J}_{ji}] - \sum_{j<i}[n_i A_{ij} + (n_i B_{ij} - n_j B_{ji})\bar{J}_{ij}] \\ + \sum_j[n_j C_{ji} - n_i C_{ij}] = 0. \end{aligned} \quad (1.56)$$

1.4.6 Radiative transfer with Einstein coefficients

Lets remember that the dependence of \bar{J} on I is given by

$$\bar{J}_\nu = \frac{1}{4\pi} \int_0^\infty I_\nu \phi_\nu d\nu. \quad (1.57)$$

The radiative transfer equation (Eq. 1.40) can be then couple to the Einstein coefficients, considering it as the contribution of the spontaneous and stimulated emission as well as the absorption. Eq. 1.40 is written as

$$\frac{dI_\nu}{ds} = -\frac{h\nu_0}{c}(n_i B_{ij} - n_j B_{ji})I_\nu \phi_\nu + \frac{h\nu_0}{4\pi}n_j A_{ji}\phi_\nu, \quad (1.58)$$

where

$$\kappa_\nu = \frac{h\nu_0}{c}(n_i B_{ij} - n_j B_{ji})\phi_\nu, \quad (1.59)$$

and

$$\varepsilon = \frac{h\nu_0}{4\pi}n_j A_{ji}\phi_\nu. \quad (1.60)$$

The source function (S_ν) can be written as

$$S_\nu = \frac{\varepsilon_\nu}{\kappa_\nu} = \frac{n_i A_{ij}}{n_j B_{ji} - n_i B_{ij}}. \quad (1.61)$$

As Eq. 1.61 has to be equivalent to $S_\nu = B_\nu(T)$, the Einstein A_x and B_x coefficients are related as follow

$$g_i B_{ij} = g_j B_{ji}, \quad (1.62)$$

and

$$A_{ji} = \frac{8\phi\nu_0^3}{c^3} B_{ji}. \quad (1.63)$$

The relation between the collisional coefficients C_{ij} and C_{ji} depends on the number density of particles and the velocity distribution of the gas. In the particular case of a thermal distribution of velocities, these coefficients relate as

$$\frac{n_i}{n_j} = \frac{C_{ji}}{C_{ij}}. \quad (1.64)$$

Their relation with the A_x and B_x is not simple. Although some approximations can be made and find the relation between them. As this coefficients do not explicitly appear in the source function Eq. 1.61, we do not refer here to those approximations.

1.4.7 Excitation temperature

The excitation temperature T_{ex} is defined by the relative number of atoms or molecules in the energy levels i and j accordingly to the Boltzmann distribution

$$\frac{n_i}{n_j} = \frac{g_i}{g_j} \exp\left(\frac{h\nu_0}{kT_{\text{ex}}}\right). \quad (1.65)$$

ν_0 is the peak frequency of the transition. For a system LTE, the number of transitions per unit time per unit volume out of state i is equal to the number of transitions per unit time per unit volume into state j , in which case $T_{\text{ex}} = T$.

1.4.8 Extinction

Astronomers are interested on tracing the structure of clouds. The most fundamental measure of the amount of material in molecular clouds is the number of particles along the line of sight (z). However, measuring directly

the total number density of the gas is an extremely challenging task. Even by approximating the cloud to be constituted by only the most abundant molecule H_2 , direct observations of H_2 cannot be performed under most circumstances.

It is necessary to use indirect methods, like measuring the extinction A_λ , which provides estimates of the total amount of dust along the line of sight. A_λ is measured in “magnitudes” and is defined by

$$\frac{A_\lambda}{\text{mag}} = 2.5 \log_{10} \left[\frac{F_\lambda^0}{F_\lambda} \right], \quad (1.66)$$

where F_λ is the observed flux from the source, and F_λ^0 is the flux of the source as it only suffers for attenuation due to the inverse square law of radiation. The extinction is proportional to the optical depth:

$$\frac{A_\lambda}{\text{mag}} = 2.5 \log_{10}[e^{\tau_\nu}] = 1.086\tau_\nu. \quad (1.67)$$

Reddening law

The observed extinction lines may change their shape from one line of sight to another. The slope of the extinction is characterized by comparing the extinction at the blue photometric band B (peak at $\lambda = 4405\text{\AA}$) and the “visual” photometric band V (peak at $\lambda = 5470\text{\AA}$)

$$R_V \equiv \frac{A_V}{A_B - A_V} \equiv \frac{A_V}{E(B - V)}. \quad (1.68)$$

$E(B - V) \equiv A_B - A_V$ is called as the “reddening”. As $E(B - V)$ increases, the emitter is considered “redder”. Conversely, as $E(B - V)$ decreases, the emitter is considered “bluer”.

The sources of extinction are different depending on the wavelength at which the astronomical object is observed. In the case of the Visual photometric band, the extinction is mostly caused by dust and dense gas. The reddening is caused by dust grains. The dust to gas distribution is not necessarily uniform along different sight lines (or even not uniform along one sight line). However, it is assumed to be constant for the Milky Way. There are observational works which provides measurements showing that it is the case (e.g. [Bohlin et al., 1978](#)). Although more recent studies search for variations of this ratio (e.g. [Sandstrom et al., 2012](#)).

Visual extinction

Many observational works assume a constant dust to gas ratio. For consistency and comparisons, we also hold this idea. Through the assumption of a reddening law and a constant dust to gas ratio ($R_V \approx 3.1$ for the Milky Way, [Bohlin et al., 1978](#); [Draine and Bertoldi, 1996](#)), it is possible to make a simple conversion between A_V and the total number density of particles along the line of sight (or total column density N):

$$A_V = \frac{N}{1.87 \times 10^{21} [\text{cm}^{-2}]} [\text{mag}].$$

Chapter 2

Numerical method

2.1 Description of the simulation

For our 3D simulation of ISM turbulence, we use a modified version of ZEUS-MP (Norman, 2000; Hayes et al., 2006), which includes a state-of-the-art atomic and molecular cooling function (described in Glover et al., 2010) and a simplified treatment of the non-equilibrium chemistry of the gas. Most of the simulations are performed following a chemical network of hydrogen (H), carbon (C), and oxygen (O). Each run traces the abundance of 32 species. 13 of them are assumed to be instantaneously in chemical equilibrium (H^- , H_2^+ , CH^+ , CH_2^+ , OH^+ , H_2O^+ , CO^+ , HOC^+ , O^- , C^- , and O_+^2). For the remaining 19 species (e^- , H^+ , H , H_2 , He , He^+ , C , C^+ , O , O^+ , OH , H_2O , CO , C_2 , O_2 , HCO^+ , CH , CH_2 , and CH_3^+) the full non-equilibrium evolution is followed (Glover et al., 2010).

Each simulation begins with an initially uniform gas distribution, with a mean hydrogen nuclei number density ranging from $n_0 = 30 \text{ cm}^{-3}$ to 1000 cm^{-3} . Initially, the gas has a uniform solar abundances of hydrogen and helium, and uniform metallicity¹ Z . Z ranges from $0.1 \times$ the solar metallicity (Z_\odot) to Z_\odot in our runs. All the elements scales from the solar abundances. We assume all carbon is initially in its ionized form C^+ and all oxygen is atomic O. The fractional abundances by number of carbon and oxygen relative to hydrogen are given by $x_{\text{C}^+} = x_{\text{C,tot}} = 1.41 \times 10^{-4}$ and $x_{\text{O}} = x_{\text{O,tot}} = 3.16 \times 10^{-4}$ (Sembach et al., 2000), where $x_{\text{C,tot}}$ and $x_{\text{O,tot}}$ refer to carbon and oxygen in all forms (ionized, neutral, or incorporated into molecules). We consider a background interstellar ultraviolet (UV) radiation field, with the spectral shape of the Draine (1978) field, and a strength

¹Metallicity is defined as the proportion of matter made up of elements other than hydrogen and helium

parametrized by G_0 , where $G_0=1.7$ in (Habing, 1968) units². The incident UV radiation field strength for each of the runs ranges from $UV=0 G_0$ to $1000 G_0$. To treat the effects of radiation, we use the six-ray approximation (Nelson and Langer, 1997; Glover and Mac Low, 2007a; Glover et al., 2010), which consists of averaging the photochemical rates over six lines of sight along the principal coordinate axes. We also assume a fixed cosmic ray ionization rate, $\zeta_H = 10^{-17} \text{ s}^{-1}$ (Goldsmith and Langer, 1978). We expect the results presented here to be largely insensitive to ζ_H .

The simulations domain is a cube with length $L = 20 \text{ pc}$, and a resolution of N_L^3 cells, where N_L is the number of zones along each side of the cube. We assume different values of N_L along this thesis. Our clouds model are complex, and so requires long computational time (see Glover and Clark, 2012a). For the simulations with the full chemical network, $N_L=128$ (used in chapter 5 and the second part of chapter 6). For the first part of chapter 6 in which we turn off the chemistry in order to treat isothermal simulations and use $N_L=256$. In chapters 3 and 4, we use a single “fiducial” cloud simulation with the aim of modeling a typical Milky Way molecular cloud, for which $N_L=512$.

We consider periodic boundary conditions for most of the parameters. However, we use non-periodic boundary conditions to treat radiation. The radiation enters the cube from the edges to the center. These two assumptions are not consistent, but we adopt this arrangement purely for the computational convenience that it offers (Glover et al., 2010). This structure of the grid + the boundary conditions do not allow us to model the morphology of particular clouds. It is however very useful for studying statistically the physical conditions of the clouds.

The initial velocity field is turbulent, with power concentrated on large scales, between wave numbers $k = 1$ and 2 and with an initial rms velocity of $v_0 = 5 \text{ km s}^{-1}$. Moreover, we drive the turbulence so as to maintain approximately the same rms velocity throughout the simulations, following the method described in Mac Low et al. (1998) and Mac Low (1999). We do not perform a Helmholtz decomposition of the force field, and thus the turbulent forcing consists of a natural mixture of solenoidal and compressive modes, i.e., $F_{\text{sol}}/(F_{\text{sol}} + F_{\text{comp}}) \approx 2/3$ (Federrath et al., 2010). We evolved all our runs until $t \approx 5.7 \text{ Myr}$, corresponding to roughly three turbulent crossing times, $t_{\text{cross}} = L/(2v_0) \approx 2 \text{ Myr}$. This period of time is long enough that we expect the turbulence to have reached a statistical steady state (Federrath et al., 2009; Federrath et al., 2010; Glover et al., 2010; Price and Federrath,

²This corresponds to an integrated flux $2.7 \times 10^{-3} \text{ erg cm}^{-2} \text{ s}^{-1}$, which is considered as standard UV radiation field strength for the solar neighborhood.

2010). We do not include the effects of self-gravity in this study.

Most of our runs begins with gas threaded by a uniform magnetic field with an initial field strength $B_i = 5.85 \mu\text{G}$ oriented parallel to the z -axis of the box. This particular selection was motivated by the 21 cm observations presented by Heiles and Troland (2005) who find a median magnetic field strength of about $6 \mu\text{G}$ for the cold neutral medium.

The initial temperature of the gas is $T_0 = 60 \text{ K}$. Moreover, it quickly adjusts itself to thermal equilibrium (Glover and Mac Low, 2011). The temperature of the dust is constant and fixed during the whole simulation at 10 K . We assume a standard gas-to-dust ratio, and take the dust to follow an extinction law characterized by the total-to-selective extinction ratio $R_V = 3.1$ – which is the typical accepted value for representing the Milky Way.

With the exception of H_2 , we include no grain surface chemistry in our model. In particular, we do not account for the effects of freeze-out of CO molecules onto dust grains in dense, cold regions of the cloud. The regions in which the process is effective will typically have very high optical depths in lines of CO (see e.g. Goldsmith, 2001) and so we do not expect this simplification to significantly alter our results.

In some chapters, we use modifications on some of the basic setup. In chapters 3 and 4, the simulation is run with a simpler chemical network for modeling the formation of CO introduced by Nelson and Langer (1999). In the first part of chapter 6, the chemical reactions are neglected in order to study the role of magnetic fields on the density distribution. When it is the case, we state the implemented changes on the initial conditions.

2.2 Radiative transfer model

We post-process the results of our simulations at $t \approx 5.7 \text{ Myrs}$ to produce a synthetic emission map of the $\text{CO}(J=1 \rightarrow 0)$ lines. We use the radiative transfer code RADMC-3D³ (Dullemond, 2012) to calculate the emergent CO line intensity. RADMC-3D is a code that performs dust and/or line radiative transfer on Cartesian or spherical grids (including adaptive mesh refinement). Since we are only interested in CO molecular line emission along each line of sight (LoS), we use the ray-tracing capability of RADMC-3D, including the Doppler catching method for dealing with models with large velocity gradients (Shetty et al., 2011a,b).

The level populations in each zone are calculated through the Sobolev (1957) approximation, also known as the large velocity gradient (LVG) method.

³<http://www.ita.uni-heidelberg.de/~dullemond/software/radmc-3d/>

This method takes the advantages of large spatial variations in velocity, as are present in molecular clouds, to define line escape probabilities (Shetty et al., 2011a). It provides a solution to the equation of detailed balance from local quantities (Eq. 1.56). A photon emitted in a 2 level transitions ($j \rightarrow i$) of a given species will have a Doppler-shifter frequency during its travel through the medium. This is due to the large velocity gradients present in clouds. When the frequency of the photon is sufficiently different from the one at its emission, it cannot interact with the medium at the new position or any other subsequent position. The escape probability of the photon is given by

$$\xi = \frac{1}{\tau} \int_0^\tau e^{-\tau'} d\tau' = \frac{1 - e^{-\tau}}{\tau}, \quad (2.1)$$

where τ is the optical depth §1.4.8 (e.g. Goldreich and Kwan, 1974; Goldsmith and Langer, 1978; Shetty et al., 2011a). The optical depth is calculated from Eq. 1.59 and can be written as

$$\tau = \frac{c^3}{8\pi\nu_{ij}^3} \frac{A_{ij}n_i}{1.065\langle |dv/dr| \rangle} \left(\frac{n_i g_i}{n_i g_j} - 1 \right), \quad (2.2)$$

where A_{ij} is the Einstein coefficient for spontaneous emission, n_i & n_j are the level populations, and g_i & g_j their statistical weights, respectively. The velocity gradients are given by dv/dr (van der Tak et al., 2007; Shetty et al., 2011a). This gradient multiplied by the distance traveled by the photon l , provides an approximate measurement of the microturbulent velocity-width (Goldsmith and Langer, 1978)

$$v_{\text{MTRB}} = \frac{dv}{dr} l. \quad (2.3)$$

We perform the calculations using a micro-turbulent velocity $v_{\text{MTRB}}=0.5$ km s^{-1} . Shetty et al. (2011b) demonstrate that the CO line profiles do not strongly depend on this choice for this turbulent model. Our model has the same rms velocity ($v_0 = 5$ km s^{-1}) as the fiducial model presented by Shetty et al. (2011b) and is also driven in the same fashion. We therefore expect that our choice for v_{MTRB} will not strongly affect the line intensity.

The local radiation field is then calculated from the Source function S_{ij} Eq. 1.61 and the photon escape probability ξ (Eq. 2.1)

$$\bar{J}_{ij} = S_{ij}(1 - \xi). \quad (2.4)$$

Given Eqs. 2.2, 2.1, 2.4 and the velocity gradient, the detailed balance equation (1.56) can be solve numerically (Shetty et al., 2011a). We use values for the radiative transition rates and collisional rate coefficients taken

from the LAMDA database ([Schöier et al., 2005](#)). The particular set of collisional rate coefficients that we use are those compiled by [Yang et al. \(2010\)](#). The detailed implementation of the LVG method into RADMC-3D is fully described in [Shetty et al. \(2011a\)](#)

Chapter 3

Tracing the temperatures of molecular clouds

1

The emission of CO and its isotopomers has been used to study not only the structure but also the temperature of molecular clouds. It is usually assumed that the lowest levels of CO are optically thick and close to local thermodynamical equilibrium (LTE), especially the CO ($J=1-0$) transition (e.g. Dickman, 1978; Martin et al., 1982; Pineda et al., 2008; Goldsmith et al., 2008; Wilson et al., 2009; Pineda et al., 2010). Given this premise, it is expected that the intensity of the CO ($J=1-0$) line (often expressed in terms of a brightness temperature) will indicate the kinetic temperature of the cloud. Hence, this line is often considered as a robust probe of the temperature of the diffuse molecular gas (Martin et al., 1982; Walmsley and Ungerechts, 1983). Unfortunately, this may not be the case. For one thing, CO is not necessarily thermalized (Liszt and Lucas, 1998; Goldsmith et al., 2008; Pineda et al., 2010), making any direct conversion from emission to temperature difficult (White, 1997). In addition, CO does not reliably trace the molecular structure of clouds. It has been found that the CO column density (N_{CO}) and the H_2 column density (N_{H_2}) are not linearly correlated (Langer et al., 1989; Goodman et al., 2009a; Pineda et al., 2010; Shetty et al., 2011a). The reason is that CO requires high column densities (corresponding to visual extinction $A_V \gtrsim 3$ mag) to prevent its photodissociation because it is weakly self-shielded, while the corresponding process for H_2 becomes effective at much lower column densities (equivalent to $A_V \gtrsim 0.1$ mag) (Glover and Mac Low, 2011). Moreover, simulations show that CO is mostly located

¹The content of this chapter is part of a publication by F. Z. Molina, S. C. O Glover, R. Shetty & R. S. Klessen, which is in preparation. We expect to submit this paper within a couple of weeks.

at densities $n \gtrsim 100 \text{ cm}^{-3}$, regardless of the metallicity of the cloud and the incident UV radiation field strength (Molina et al., 2011). Therefore, the temperature estimates from CO emission are frequently biased, because it is expected to only trace the well-shielded cold regions of molecular clouds.

The temperature distribution in molecular clouds is in general very complex. Small and large scale processes, like collisions, radiation, cooling and heating from dust and the formation and destruction of the constituent species, magnetic fields, turbulent and gravitational heating, among many others; are important on shaping this distribution (e.g. Goldsmith, 1988; Tielens, 2005). Therefore, it is not straightforward to assume that molecular clouds are in LTE. However, obtaining a reliable picture of the temperature from CO ($J=1-0$) observations alone is not possible. In this sense, many authors assume that, at first order, the CO ($J=1-0$) transition occurs in LTE and calculate the excitation from the brightness temperature (e.g. Dickman, 1978; Garden et al., 1991; Liszt and Lucas, 1998; Pineda et al., 2008; Goldsmith et al., 2008; Roman-Duval et al., 2010; Pineda et al., 2010).

It is common to use the excitation temperature T_{ex} of CO ($J=1-0$) emission alone for estimating N_{CO} when observations of the other transitions are not available. This is because in local molecular clouds, most of the CO molecules are in the ground state or the first two or three lowest excited rotational states (Liszt and Lucas, 1998). However, there are some issues which prevent us from inferring correctly the CO column density. On one hand, Shetty et al. (2011a) find that CO ($J=1-0$) emission does not provide direct information about the CO mass. They argue that this line is optically thick, and as a consequence, the distribution of the integrated CO ($J=1-0$) intensity does not directly follow the distribution of N_{CO} . Therefore, the CO column density inferred from T_{ex} may be different from the true N_{CO} , even if one does not consider any approximation for calculating T_{ex} , or the CO column density. On the other hand, considering an excitation temperature calculated under LTE conditions might also affect the estimates of N_{CO} .

In this chapter, we rigorously assess the common assumptions employed when estimating temperatures from CO ($J=1-0$) observations. Our aim is to understand and quantify the impact of the CO ($J=1-0$) excitation temperature as a tool for inferring CO column densities. We use a numerical simulation with mean number density, metallicity and UV radiation field strength typical of a Milky Way molecular cloud. The setup is described in §2.1. The chemical network used for this particular simulation is based on an approximation for modeling the formation of CO introduced by Nelson and Langer (1999), and is described in detail in Glover et al. (2010), see (Glover and Clark, 2012a). Together with a Monte Carlo radiative transfer code, the ^{12}CO ($J=1-0$) emission is calculated (see §2.2). We start this chapter with

an overview of the CO distribution in our cloud example. Then, we perform a detailed analysis of the temperatures, testing LTE assumptions with a comparison between the kinetic, brightness temperatures, as well as the excitation temperature T_{ex} . We then compare two different methods for calculating the excitation temperature: 1) a theoretical approach, in which we use the population levels of the transition into the Boltzmann Equation, and 2) an “*observational*” approach that considers the brightness temperature in the commonly-used Dickman (1978) formula. Finally, we use T_{ex} (calculated from the previous approaches) to estimate the CO column densities, and quantify the differences regarding the true N_{CO} .

In the course of the text, we will refer to a large number of different physical quantities. In an effort to reduce confusions, we produce a brief guide to these different quantities in Table 3.1.

Physical quantity	Acronym
number density of hydrogen nuclei	n
logarithm of the dimensionless density $\ln(n/n_0)$	s
CO abundance n_{CO}/n	x_{CO}
Optical depth	τ
critical number density	n_{cr}
Statistical weight	g_i
Intensity	I_ν
3D Brightness temperature	T_{b}
CO intensity integrated along the line of sight	W_{CO}
3D kinetic temperature	T_{K}
Column kinetic temperature – total mass weighted average [†]	$T_{\text{K}}^{\text{col}}$
Column kinetic temperature –	$T_{\text{K}}^{\text{co-col}}$
3D excitation temperature – calculated from Boltzmann Equation	T_{ex}

Column excitation temperature – CO mass weighted average [†]	$T_{\text{ex}}^{\text{col}}$
3D excitation temperature – calculated from Dickman (1978) Equation	$T_{\text{ex,obs}}$
Column excitation temperature – CO mass weighted average	$T_{\text{ex,obs}}^{\text{col}}$
Total column number density of hydrogen nuclei	N
Visual extinction	A_V
H ₂ column density	N_{H_2}
CO column density	N_{CO}
critical column density	N_{cr}
CO($J=0$) column density	$N_{\text{CO},J=0}$
Estimated CO($J=0$) column density* using T_{ex}	$N_{\text{CO},J=0}^{\text{th},3\text{D}}$
Estimated CO($J=0$) column density* using $T_{\text{ex,obs}}$	$N_{\text{CO},J=0}^{\text{obs},3\text{D}}$
Estimated CO($J=0$) column density* using $T_{\text{ex}}^{\text{col}}$	$N_{\text{CO},J=0}^{\text{th},2\text{D}}$
Estimated CO($J=0$) column density* using $T_{\text{ex,obs}}^{\text{col}}$	$N_{\text{CO},J=0}^{\text{obs},2\text{D}}$
Estimated CO column density [‡] using T_{ex}	$N_{\text{CO}}^{\text{th},3\text{D}}$
Estimated CO column density [‡] using $T_{\text{ex,obs}}$	$N_{\text{CO}}^{\text{obs},3\text{D}}$
Estimated CO column density [‡] using $T_{\text{ex}}^{\text{col}}$	$N_{\text{CO}}^{\text{th},2\text{D}}$
Estimated CO column density [‡] using $T_{\text{ex,obs}}^{\text{col}}$	$N_{\text{CO}}^{\text{obs},2\text{D}}$

[†]projection made by considering the mass-weighted average
along the line of sight

* calculated from Eq. [3.11](#)

[‡] calculated from Eq. [3.16](#)

3.1 Overview of the simulation

The particular chemical network implemented for this chapter and chapter 4 is based on an approximation for modeling the formation of CO introduced by Nelson and Langer (1999), and is described in detail in Glover et al. (2010), see (Glover and Clark, 2012a). This chemical network is much simpler than the one described in §2.1. Although it also includes a small number of reactions which involves magnesium Mg, iron Fe, calcium Ca, and sodium Na. Even though the chemistry is simplified, the temperature, number density, and CO, C, & C⁺ number density distributions are very similar to the ones of the full chemical network.

Fig. 3.1a shows the column density of molecular hydrogen, N_{H_2} , projected along the z -axis of the simulation volume at time $t = t_{\text{end}} \approx 5.7$ Myr. Fig. 3.1b illustrates a similar plot but for the column density of carbon monoxide, N_{CO} . Both images show similar morphology: the gas has a filamentary structure, and there are large spatial variations in the column densities. The gas appears to have a prominent over-dense region visible towards the top-right of the figure, and an under-dense region visible near the center-left of the image. Several authors have particularly shown that N_{CO} is not linearly correlated to N_{H_2} , particularly in regions with low visual extinction A_V where CO can be easily photodissociated (e.g. van Dishoeck and Black, 1988; Visser et al., 2009; Glover and Mac Low, 2011). In a detailed analysis at different densities, Shetty et al. (2011a) showed that the Probability Density Function (PDF) of N_{H_2} and the total column density N are well described by a log-normal function (Eq. 6.2), but that this is not the case for the PDFs of CO column density and integrated intensity. Therefore, we do not expect the ratio $N_{\text{CO}}/N_{\text{H}_2}$ to be uniform. Fig. 3.1c indicates that the cloud is not chemically homogeneous by showing the ratio of N_{CO} to N_{H_2} . Although the average ratio of CO to H₂ column densities is $\langle N_{\text{CO}}/N_{\text{H}_2} \rangle = 4.1 \times 10^{-5}$, the ratio of $N_{\text{CO}}/N_{\text{H}_2}$ shows significant spatial variation. In regions with a high density of H₂, the gas is well-shielded leading to higher CO abundances. In low density regions, however, the CO abundance is very low, because the gas is poorly shielded.

Fig. 3.1d illustrates the CO($J=1 \rightarrow 0$) velocity integrated intensity, again for the same LoS (equivalent to the z -axis of the simulation volume). In this image, the filamentary structure is again evident, particularly in the high density regions, although comparison of Figures 1b and 1d shows that there is not a one-to-one correlation between structures in the column density map and in the integrated intensity map. A similar result was previously noted by Shetty et al. (2011a). In diffuse regions, the integrated intensity is so low that little of the structure of the gas is visible. This fact is in agreement

with the analysis of CO distribution performed in [Molina et al. \(2011\)](#). In that work, we showed that the majority of CO is located in zones where the gas is well shielded, typically at number density $>100 \text{ cm}^{-3}$ regardless of the environmental conditions of our cloud models (such as mean density, metallicity and UV radiation field strength). Fig. 3.2 shows the cumulative total mass of the cloud (solid line) and the cumulative H_2 (dashed line) and CO (dotted line) masses as a function of the number density for the particular simulation in this study. Although 96% of the mass of the cloud is in regions with densities $\gtrsim 20 \text{ cm}^{-3}$, the majority (95%) of the CO mass is in zones with $n \gtrsim 400 \text{ cm}^{-3}$. The H_2 mass follows the total mass fraction very closely.

3.2 Number density and CO abundance distribution in 3D

For a given species i , the column density ratio N_i/N roughly corresponds its volume abundance $x_i = n_i/n$. In this section, we analyze the number density distribution and the volume CO abundance $x_{\text{CO}} = n_{\text{CO}}/n$ in detail. This will help us understand the range in which CO is distributed and the associated emission.

3.2.1 Number density Probability Density Function

It is widely accepted that the PDF of the logarithm of the density of an isothermal, unmagnetized, supersonic turbulent flow has a log-normal shape around the peak (e.g. [Vázquez-Semadeni, 1994](#); [Padoan et al., 1997](#); [Klessen, 2000](#); [Ostriker et al., 2001](#); [Li et al., 2003](#); [Federrath et al., 2008b](#); [Kainulainen et al., 2009](#); [Glover et al., 2010](#); [Federrath et al., 2010](#); [Padoan and Nordlund, 2011](#); [Molina et al., 2012](#); [Kainulainen and Tan, 2013](#)),

$$p_s ds = \frac{1}{\sqrt{2\pi\sigma_s^2}} \exp\left[-\frac{(s-s_0)^2}{2\sigma_s^2}\right] ds, \quad (3.1)$$

where $s = \ln(n/n_0)$ (n_0 is the mean density of the simulation), and σ_s is the density variance. The mean s_0 is related to the density variance by $s_0 = -\sigma_s^2/2$.

When the gas is subject to other processes like heat exchange, magnetic fields and/or gravitation, the density PDF may or may not deviate from a log-normal shape. In the present work, we include a non-isothermal equation of state and magnetic fields. The resulting PDF (Fig. 3.3) nevertheless still closely follows a log-normal distribution (solid line). The dashed line shows

3.2. NUMBER DENSITY AND CO ABUNDANCE DISTRIBUTION IN 3D53

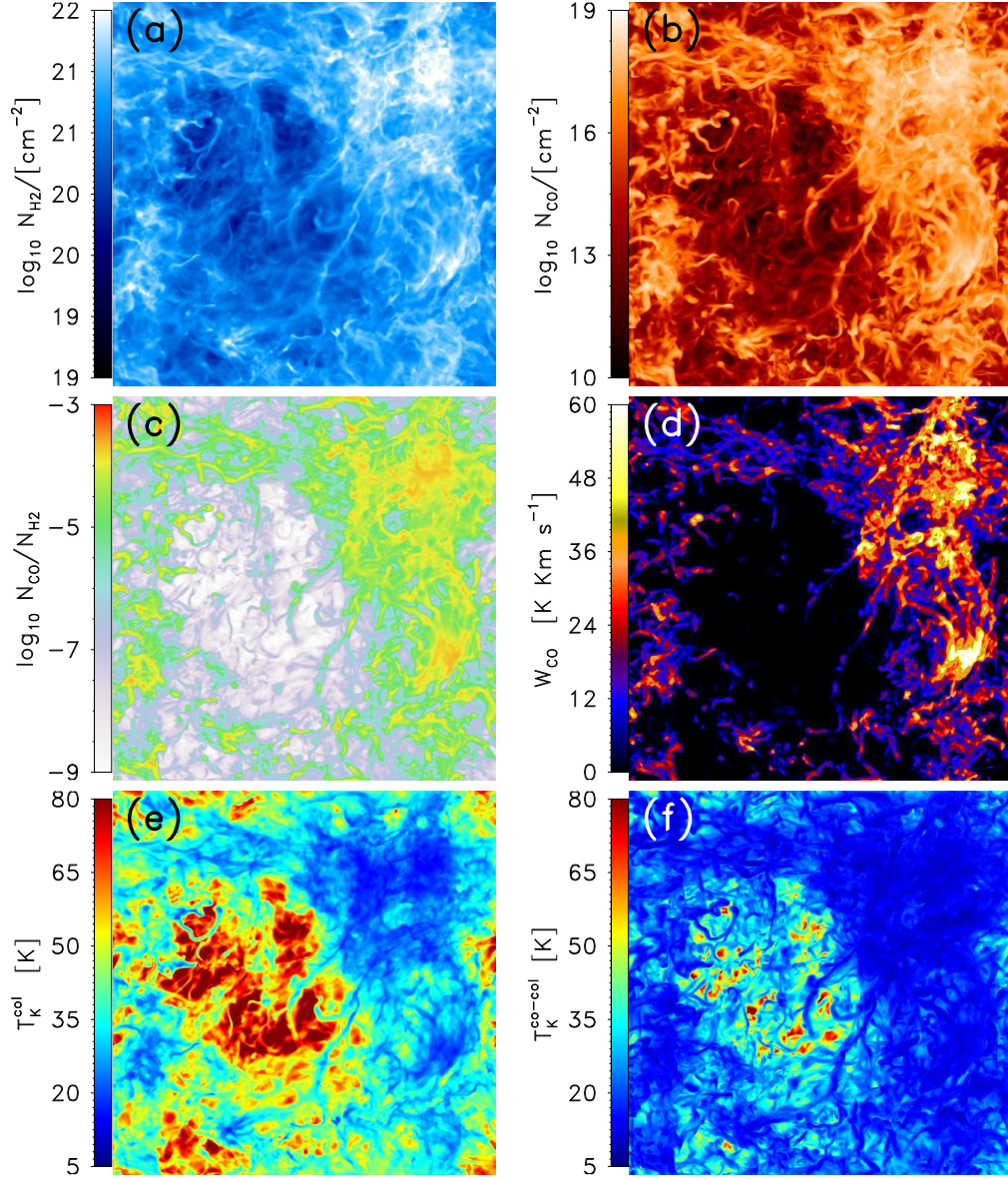


Figure 3.1: Images of: (a) the column density of molecular hydrogen, N_{H_2} , viewed along a LoS parallel to the z -axis of the simulation volume. (b) As (a), but for the CO column density, N_{CO} . (c) As (a), but for the ratio of N_{CO} to N_{H_2} . (d) Integrated CO ($J=1-0$) intensity W_{CO} along the same LoS. (e) and (f) Projected kinetic temperature along the z -axis of the simulation volume: in (e) we show a mass-weighted average along the LoS, while in (f) we show a CO mass-weighted average.

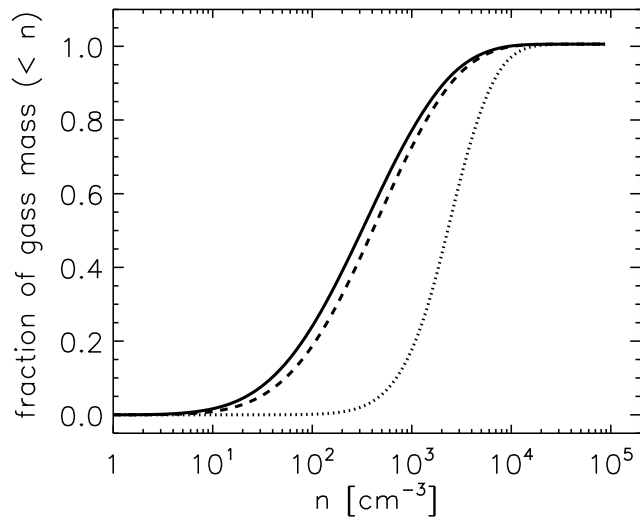


Figure 3.2: Cumulative total mass (solid line), H₂ mass (dashed line), and CO mass (dotted line) below a given number density n versus total number density. The masses are normalized by the total mass of the cloud and the total mass of H₂ and CO, respectively.

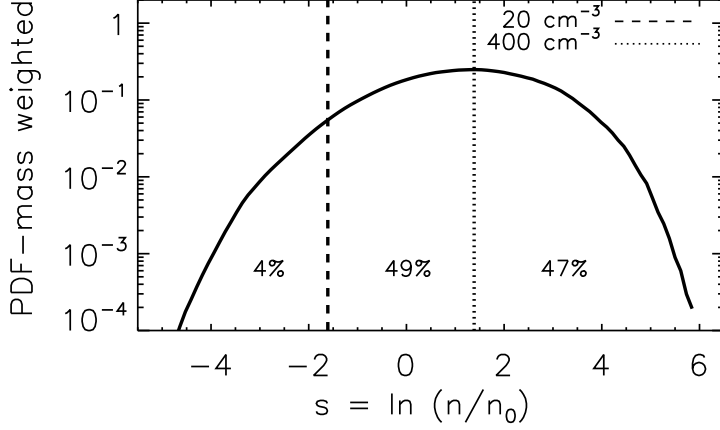


Figure 3.3: Mass-weighted PDF of the dimensionless logarithmic density s . The dashed line indicates $n = 20 \text{ cm}^{-3}$, and dotted line corresponds to $n = 400 \text{ cm}^{-3}$. The fraction of the cloud mass to the right of the dashed line (96%) is approximately equal to the fraction of the CO mass to the right of the dotted line.

$n = 20 \text{ cm}^{-3}$, and the dotted line denotes $n = 400 \text{ cm}^{-3}$, the density above which 95% of the CO mass exists, but which corresponds to only 47% of the total mass of the cloud (Fig. 3.2). As the remaining 5% of the CO fraction is distributed throughout 53% of the total mass, we expect the mean abundance of CO below $n = 400 \text{ cm}^{-3}$ to be very low.

3.2.2 CO abundance

Fig. 3.4 shows the mass-weighted 2D PDF of the CO abundance as a function of the number density. The white line indicates the average $\langle x_{\text{CO}} \rangle$ in every number density bin. As expected, the abundance of CO increases with increasing number density until it reaches the maximum value $x_{\text{CO}} = x_{\text{C,tot}} = 1.41 \times 10^{-4}$, where all the carbon is locked into CO molecules. Most of the mass of the cloud is above $n = 20 \text{ cm}^{-3}$ (black dashed line) with $\log_{10} x_{\text{CO}} \gtrsim -10$. At $n = 20 \text{ cm}^{-3}$, the dispersion of x_{CO} is the largest of the distribution, ranging from $\log_{10} x_{\text{CO}} \approx -11.8$ ($x_{\text{CO}} \approx 2 \times 10^{-12}$) to $\log_{10} x_{\text{CO}} \approx -4.2$ ($x_{\text{CO}} \approx 6 \times 10^{-5}$). The distribution becomes narrower towards higher number densities. At $n \geq 400 \text{ cm}^{-3}$, 47% of the mass is concentrated into regions where the abundance ranges from $\log_{10} x_{\text{CO}} \approx -9$ to the maximum at $\log_{10} x_{\text{CO}} = -3.85$. The average at $n = 400 \text{ cm}^{-3}$ is

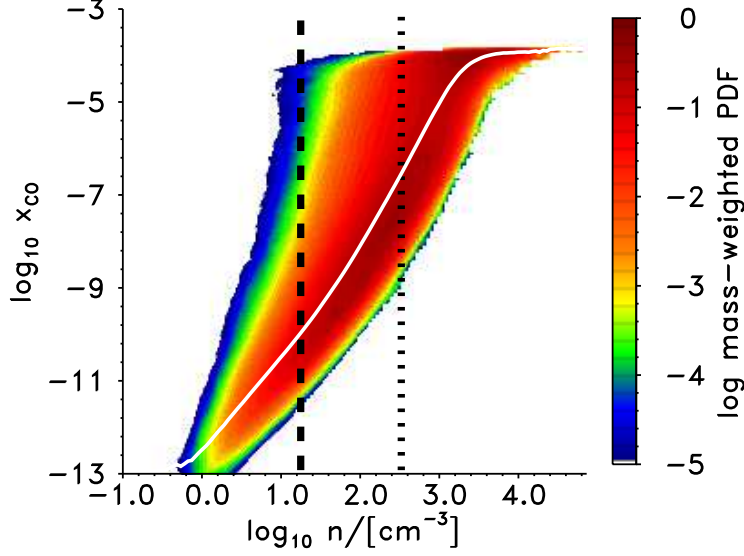


Figure 3.4: Mass-weighted 2D PDF of the CO abundance $x_{\text{CO}} = n_{\text{CO}}/n$ vs. volume density. The white line shows the average $\langle x_{\text{CO}} \rangle$ in every n bin. The black dashed line is located at $n = 20 \text{ cm}^{-3}$, showing that 96% of the total mass of the cloud is located at densities above this line. The black dotted line indicates $n = 400 \text{ cm}^{-3}$. 95% of the CO mass is located at densities above this line.

$\langle \log_{10} x_{\text{CO}} \rangle \approx -6.6$ ($\langle x_{\text{CO}} \rangle \approx 3 \times 10^{-7}$). It increases steeply with number density up to $\log_{10} n/\text{cm}^{-3} \approx 3.4$ ($n \approx 2500 \text{ cm}^{-3}$), the density at which the average of x_{CO} flattens and smoothly approaches the maximum value.

CO is often assumed to provide a reliable guide to the temperature of gas within molecular clouds (Martin et al., 1982; Walmsley and Ungerechts, 1983; Wielen et al., 2012). However, as we shall see in the next section, the assumption that CO provides accurate estimates of the temperature of the cloud is incomplete at best.

3.3 Tracing the temperature of the cloud

3.3.1 Kinetic temperature

The kinetic temperature of the gas in molecular clouds is often assumed to be between 10 and 20 K. However the range in temperatures is actually much broader (Fig. 5.1). In this simulation, 96% of the mass exhibits temperatures

ranging from roughly $\log_{10} T_{\text{K}}/\text{K} \approx 1$ ($T_{\text{K}} \approx 10$ K) to $\log_{10} T_{\text{K}}/\text{K} \approx 1.95$ ($T_{\text{K}} \approx 90$ K). The gas with temperatures below 10 K and above 100 K represents only 7% of the mass (although this fraction of the mass occupies around 28% of the total volume). Further, the kinetic temperature decreases with increasing density, scaling approximately as $T_{\text{K}} \propto n^{-1/4}$ at $n < 3 \times 10^3 \text{ cm}^{-3}$, but with significant scatter around this relationship (see also [Glover and Clark, 2012b](#)). Although the temperature of the gas at $n \gtrsim 400 \text{ cm}^{-3}$ (white dotted line) ranges from $\log_{10} T_{\text{K}}/\text{K} \approx 0.8$ ($T_{\text{K}} \approx 6.5$ K) to $\log_{10} T_{\text{K}}/\text{K} \approx 1.6$ ($T_{\text{K}} \approx 40$ K), $\sim 97\%$ of the CO mass lies between $T_{\text{K}} = 7$ and $T_{\text{K}} = 20$ K (interval within the solid white lines).

The temperature distribution in the cloud is not an observable quantity. This is because our observations typically are of projected quantities, and hence produce some degree of averaging along the LoS. Particularly in the case of temperatures, the mean is dominated by the densest zones. We therefore consider the mass-weighted average of the temperature over the cells along each LoS. We refer to this quantity as the ‘‘column temperature’’². We prefer to use CO mass in order to calculate the column temperatures, because it gives a better view of the temperature of the gas where most of the CO is located.

Fig. 3.1e illustrates the column kinetic temperature $T_{\text{K}}^{\text{col}}$; and Fig. 3.1f shows a similar map, but weighting the average by CO mass, $T_{\text{K}}^{\text{co-col}}$. One of the most notable characteristics is the low temperature region visible towards the top-right of the figure, in the same location as the apparent over-dense regions in Figures 3.1a and 3.1b. Another notable aspect is the hot region located near the center-left of the figure, matching the low density region in Figs. 3.1a and 3.1b. This behavior is not surprising, because we expect low temperature at higher densities. In the case of $T_{\text{K}}^{\text{co-col}}$ (Figure 3.1f), the trend is similar. Although the map in Fig. 3.1f in general exhibits lower temperatures than Fig. 3.1e, the feature visible towards the center-left of Fig. 3.1e with $T_{\text{K}}^{\text{col}} > 65$ K is still notable in Fig. 3.1f. The low temperature feature towards the top-right is still present, but the material that surrounds it shows a similar $T_{\text{K}}^{\text{co-col}}$, rendering it less pronounced.

Figs. 3.6a and 3.6b show the mass-weighted 2D PDFs of both estimates of $T_{\text{K}}^{\text{col}}$ and $T_{\text{K}}^{\text{co-col}}$ (corresponding to the maps in Figs. 3.1e and 3.1f) respectively, as a function of the column density. The equivalent A_V is indicated at the top of the figure for reference. Given that the regions with the highest density dominate the mass along the LoS, the cold, high density regions dominate the mass-weighted average of the temperature, so the projected

²‘‘Column temperatures’’ are an accurate measure for optically thin emission, as described by [Shetty et al. \(2009\)](#).

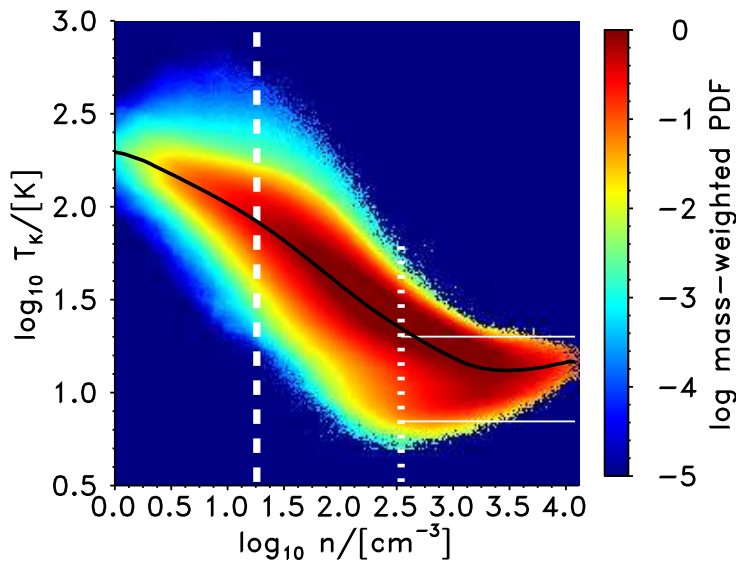


Figure 3.5: Mass-weighted 2D PDF of the kinetic temperature T_K vs. number density. The black line shows the average $\langle T_K \rangle$ in every n bin. The white dashed and dotted lines shown here indicate the same densities as the black dashed and dotted lines in Fig. 3.4. Approximately 97% of the CO mass has T_K ranging from 7 K to 20 K. This interval is indicated by the solid white lines.

temperatures (T_K^{col} and $T_K^{\text{co-col}}$) are always lower than the actual 3D temperature distribution T_K (Fig. 5.1). For a better visualization, the black line indicates the average of the column temperatures in every N bin. In Figure 3.6a, 76% of the cloud mass has a value of T_K^{col} ranging from ~ 20 K to 50 K, although the whole range of temperatures extends from 15 K to 115 K. In Figure 3.6b, $T_K^{\text{co-col}}$ is distributed along a lower and narrower range than T_K^{col} . 93% of the CO mass has $T_K^{\text{co-col}}$ ranging from 10 K to only 30 K (matching the standard values accepted for molecular clouds). This is a direct consequence of the fact that CO mostly traces cold, dense gas (Molina et al., 2011).

3.3.2 Brightness temperature

For a cloud in thermodynamical equilibrium, its specific intensity I_ν can be accurately characterized by a Planck blackbody spectrum with the same brightness. The temperature associated with this blackbody is the brightness temperature T_b , defined as

$$I_\nu = B_\nu(T_b), \quad (3.2)$$

where B_ν is the Planck function. Given the low frequencies in radio astronomy, the limit $h\nu \ll kT_b$ is often applicable and the Rayleigh-Jeans approximation is commonly used. In this limit, the intensity at a given ν can be written as

$$T_b = \frac{c^2}{2\nu^2 k} I_\nu. \quad (3.3)$$

In reality, the condition $h\nu \ll kT_b$ is only fulfilled for the CO ($J=1-0$) line when $T_b \gg 6$ K. This brightness temperature can be translated to intensity (using either Eq. 3.2 or Eq. 3.3), allowing us to write this criteria as $I_\nu \gg 10^{-14} \text{ erg s}^{-1} \text{ cm}^{-2} \text{ Hz}^{-1} \text{ ster}^{-1} = I_{\nu,0}$. In our cloud model, the maximum intensity is only $9 \times I_{\nu,0}$. At this value, our estimate of the brightness temperature is $T_b = 22.3$ K when we use the Rayleigh-Jeans approximation or 25 K if we use the Planck function (Eq. 3.2). Using the Rayleigh-Jeans approximation for $I_\nu \lesssim I_{\nu,0}$ always underestimates the brightness temperature and this discrepancy grows with decreasing intensity.

The radiation from our cloud model is mostly not thermalized. Therefore, the physical properties of the gas in our simulation cannot be interpreted as a blackbody. Consequently, we then cannot discern with physical arguments if Eq. 3.2 is better than the approximation in Eq. 3.3. However, because most observational reports in the literature often make use of the Rayleigh-Jeans approximation (F. Bigiel, private communication), we will likewise do so throughout the rest of this study.

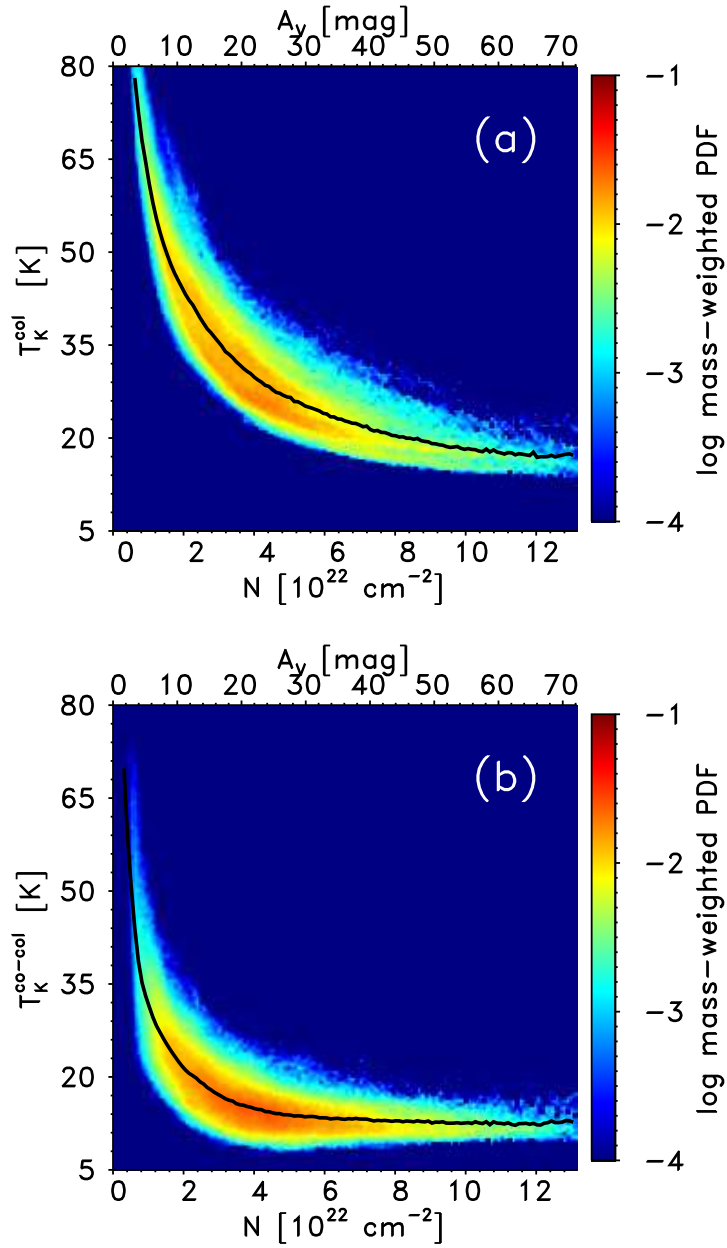


Figure 3.6: (a) Mass-weighted 2D PDF of T_K^{col} , the column kinetic temperature of the gas (i.e. the mass-weighted average along the LoS) versus the column density. The black line shows the average $\langle T_K^{\text{col}} \rangle$ in every N bin. (b) Same as (a), but considering the CO mass-weighted average along the LoS, $T_K^{\text{co-col}}$. The black line shows the average $\langle T_K^{\text{co-col}} \rangle$ in every N bin. In both figures, the visual extinction A_V is indicated at the top for reference.

If the gas is optically thick ($\tau \gg 1$), $T_b \approx T_K$. This relation is based on the assumption of LTE, and that the temperature of the gas is constant. We test if a relation like $T_b \approx T_K$ holds for our cloud model (for $\tau \gg 1$). Fig. 3.7 shows the mass-weighted 2D PDF of the brightness temperature as a function of T_K . In order to visualize how the brightness temperature varies with the kinetic temperature, we need to transform T_K from the position-position-position (PPP) space into position-position-velocity (PPV) space, in which T_b is arranged. The method we use to do this is explained in the Appendix. The data is selected for $T_b \geq 0.1\text{K}$, because above this the emission tends to be optically thick. This limit is also in agreement with the sensitivity limit of recent observational analyses, such as the COMPLETE survey in the Perseus cloud (Ridge et al., 2006). In this figure, the majority of the emission comes from regions with $T_b > 1\text{ K}$, and is associated with optically thick gas. Fig. 3.8 (solid line) shows the CO ($J=1-0$) emission-weighted PDF of the optical depth, which indicates that 81% of the emission comes from regions with $\tau \geq 1$. On the kinetic temperature side, 65% of the emission comes from zones with $\log_{10} T_K/\text{K} < 1.54$ ($T_K < 35\text{ K}$, indicated by the yellow dotted line). About 36% of the emission is emitted from zones with kinetic temperatures $1.54 \leq \log_{10} T_K/\text{K} \leq 1.78$ ($35\text{ K} \leq T_K \leq 60\text{ K}$), and only $\sim 13\%$ from regions which have $\log_{10} T_K/\text{K} > 1.78$ ($T_K > 60\text{ K}$). The CO ($J=1-0$) emission from “warm” gas (50 – 100 K) has been observationally detected for more than one decade (e.g. Liszt and Lucas, 1998; Goldsmith et al., 2008; Liszt et al., 2010; Pety et al., 2011).

In general, in Fig. 3.7 the gas shows no clear relationship between T_b and T_K suggesting that for the majority of the gas $T_b \neq T_K$. In a more detailed analysis, we find that the fraction of cells with $T_K \approx T_b \pm \sigma_{T_b}$ (with $\sigma_{T_b} = 0.25\text{ K}$) is only 5×10^{-5} of the total number of zones³. We can therefore conclude that 99.995% of the radiation is not thermalized. The PDF of the brightness temperature also shows a wide dispersion around the peak. For better visualization, the average brightness temperature; $\langle T_b \rangle$, in every kinetic temperature bin is shown by the solid yellow line. Between $1 < \log_{10} T_K/\text{K} < 2$ ($10\text{ K} < T_K < 100\text{ K}$), the $\langle T_b \rangle$ decreases as the kinetic temperature increases, clearly contradicting $T_b = T_K$. This is not surprising because in Fig. 5.1, T_K decreases with increasing density. We then would expect intuitively that the abundance of CO (and therefore the emission) will grow as the kinetic temperature decreases. At $\log_{10} T_K/\text{K} \gtrsim 1.7$, there is only 5% of the CO mass but almost 50% of the total gas mass. Because

³We chose 0.25 K as this is comparable to the typical noise level in the COMPLETE survey (Pineda et al., 2008). However, if we consider $\sigma_{T_b} = 0.05\text{ K}$, the fraction of cells satisfying the condition is still $\sim 10^{-5}$.

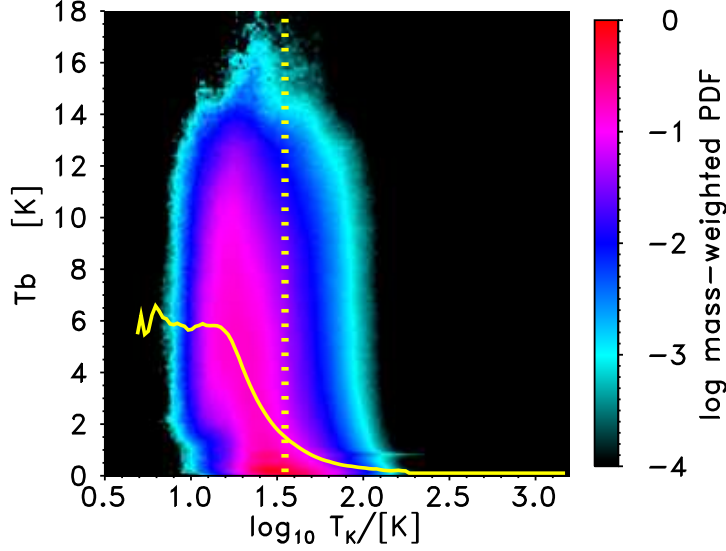


Figure 3.7: Mass-weighted 2D PDF of the brightness temperature T_b vs. T_K . The yellow solid line shows the average brightness temperature $\langle T_b \rangle$ in every T_K bin. The yellow dotted line shows $T_K = 35$ K, 95% of the CO mass is found in regions with kinetic temperatures lower than this value of T_K .

the mean CO abundance is so small, the CO emission is very weak and $\langle T_b \rangle$ approaches zero. On the other hand, at $\log_{10} T_K / \text{K} < 1.2$ ($T_K < 16$ K), the average is almost constant with T_K with a value $\langle T_b \rangle \approx 6$ K. At this regime the emission is mostly optically thick with T_b from 2 K up to ~ 12 K independent of the variations of the optical depth.

3.3.3 Excitation temperature

The excitation temperature T_{ex} is calculated from the relative number of atoms or molecules in two energy levels. T_{ex} is defined from the Boltzmann equation

$$\frac{n_l}{n_u} = \frac{g_l}{g_u} \exp\left(\frac{h\nu_0}{kT_{\text{ex}}}\right), \quad (3.4)$$

where n_l is the number density of molecules in the lower energy level l and n_u is the number density of molecules in an excited level u , with statistical weights g_l and g_u respectively. ν_0 is the frequency of the transition. For a system in LTE, the number of transitions per unit time per unit volume out

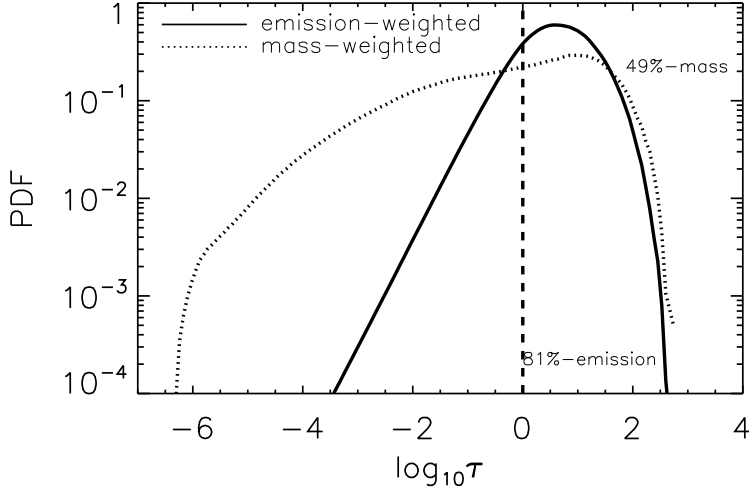


Figure 3.8: PDF of the optical depth in the CO ($J=1-0$) line. The solid line shows the emission-weighted PDF. The dotted line shows the mass-weighted PDF. The dashed line indicates $\tau = 1$. 81% of the emission comes from regions with $\tau \geq 1$, which represent 49% of the mass.

of state l is equal to the number of transitions per unit time per unit volume into state u , in which case $T_{\text{ex}} = T_{\text{K}}$.

Fig. 3.9a shows the mass-weighted 2D PDF of T_{ex} as a function of the number density. We use the level populations obtained from RADMC-3D for each cell in the simulation in order to calculate the excitation temperature for the $J=1-0$ transition⁴; for this transition $\nu_0 = 115.3$ GHz. 67% of the mass of the cloud has $T_{\text{ex}} \leq 5$ K, while 23% is in regions with $5 \text{ K} \leq T_{\text{ex}} \leq 12$, and 10% has $T_{\text{ex}} > 12$ K. T_{ex} increases with increasing density. This behavior is simple to understand. At low densities, radiative de-excitations of the $J > 0$ levels of CO dominates over collisional de-excitations, and most of the CO molecules sit in the $J = 0$ ground state, meaning that T_{ex} is small. As the density increases, however, collisional effects become increasingly important, leading to an increase in n_u/n_l and hence an increase in T_{ex} . The average T_{ex} approaches its maximum value (≈ 12 K) at $n \gtrsim 2 \times 10^3 \text{ cm}^{-3}$, where the mass fraction of H_2 approaches its own maximum. Approximately half of the CO mass is located above this number density. Comparing Figures 3.9a and 5.1, it is evident that T_{ex} has the opposite behavior to T_{K} . In Fig. 3.9a, the cyan line indicates $\langle T_{\text{ex}} \rangle$ and the white line shows $\langle T_{\text{K}} \rangle$ in every n bin. The

⁴We will hereafter refer to the excitation temperature calculated from Boltzmann Equation as T_{ex} .

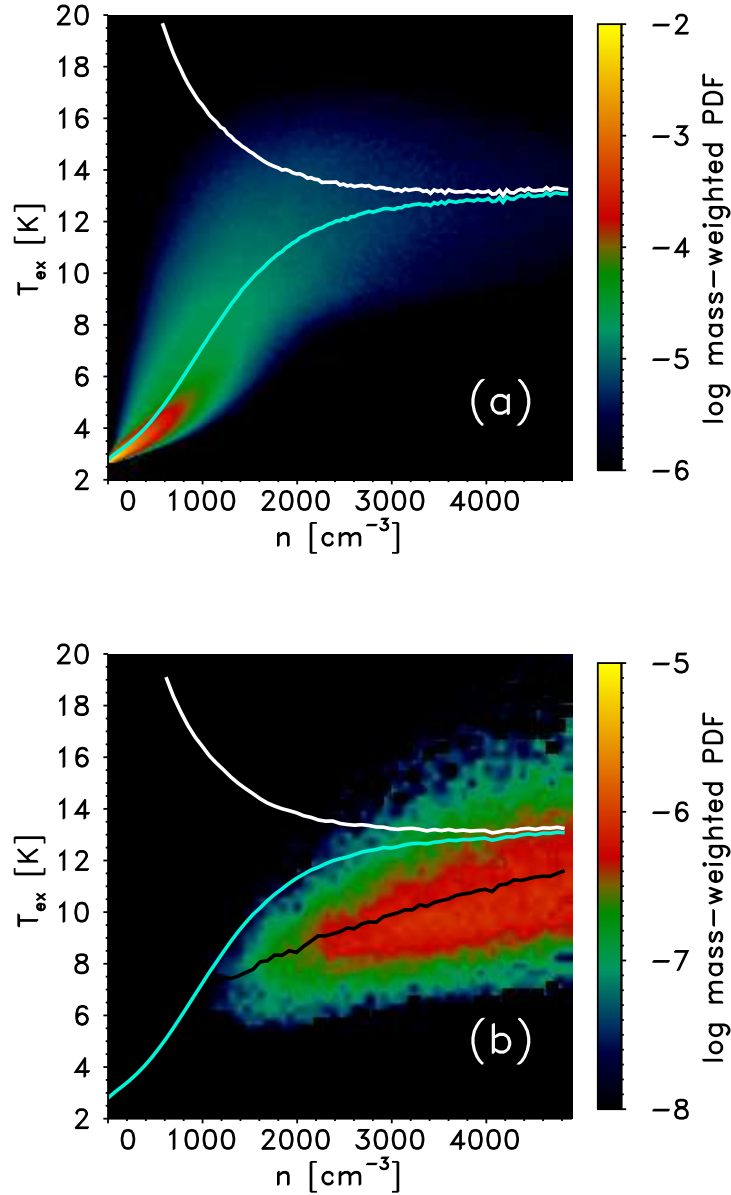


Figure 3.9: (a) Mass-weighted 2D PDF of the excitation temperature calculated considering the Boltzmann equation (Eq. 3.4) vs. number density. The cyan line indicates the average $\langle T_{\text{ex}} \rangle$ and the white line $\langle T_{\text{K}} \rangle$, in every n bin. (b) Mass-weighted 2D PDF of only the zones with $T_{\text{ex}} \approx T_{\text{K}} \pm 0.05$ K. The arrangement of lines is the same as in (a) for all but the black line, which shows the average $\langle T_{\text{ex}} \rangle_{T_{\text{K}}}$ in every n . Note that the color scales in (b) varies in comparison to (a) for a better visualization.

condition of LTE ($T_{\text{ex}} = T_{\text{K}}$) is most likely to be satisfied in regions where the gas density is above a characteristic critical density of the species of interest⁵. In the case of the CO ($J=1-0$) transition, $n_{\text{cr}} \approx 2200 \text{ cm}^{-3}$ (calculated using data from the LAMDA database, [Schöier et al., 2005](#)), and varies only weakly with T_{K} . On average, the excitation temperature is always lower than the kinetic temperature, meaning that CO is sub-thermally excited at $n \lesssim 4 \times 10^3 \text{ cm}^{-3}$, although $\langle T_{\text{ex}} \rangle$ approaches $\langle T_{\text{K}} \rangle$ within 1 K at $n \gtrsim 3 \times 10^3 \text{ cm}^{-3}$ ($T_{\text{ex}} \approx 13 \text{ K}$). For Fig. 3.9b, we select the zones where $T_{\text{K}} \approx T_{\text{ex}} \pm \sigma_{T_{\text{ex}}}$ in order to test the LTE conditions (with $\sigma_{T_{\text{ex}}} = 0.05 \text{ K}$ ⁶). The density in the cells matching the criteria varies from $n \approx 1.4 \times 10^3 \text{ cm}^{-3}$ (which is slightly smaller than n_{cr}) to $n > 5 \times 10^3 \text{ cm}^{-3}$. Most of the cells satisfying the condition have $n \gtrsim n_{\text{cr}}$. Only 0.3% of the total number of cells have $n \geq n_{\text{cr}}$, but on the other hand only 0.05% of the total data matches the criteria $T_{\text{ex}} \approx T_{\text{K}} \pm 0.05 \text{ K}$, meaning that only a sixth of the cells with $n \geq n_{\text{cr}}$ are actually in LTE. The black line shows the average of the excitation temperature as a function of density but only for the regions fulfilling the criteria. The relation between this average and the number density is subtle, it only changes by a few K.

Observationally, we cannot measure T_{ex} in the way we can in the simulations, since the values of the CO level populations and how they vary in three-dimensional space are not known. Instead, we have to rely on approximate methods for determining T_{ex} from the observed emission. One widely used approach was first proposed by [Dickman \(1978\)](#). He gives the expression

$$T_{\text{b}} = \frac{h\nu_0}{k} \left[\frac{1}{\exp(h\nu_0/kT_{\text{ex,obs}}) - 1} - \frac{1}{\exp(h\nu_0/kT_{\text{bg}}) - 1} \right] [1 - \exp(-\tau)], \quad (3.5)$$

where T_{bg} is the temperature of the background radiation, and τ is the optical depth associated with the CO ($J=1-0$) emission line. This relationship can be derived from the radiative transfer equation if we assume that the excitation temperature does not vary along the line of sight. If we also assume that the CO emission is optically thick ($\tau \rightarrow \infty$), then Eq. 3.5 can be simplified to:

$$T_{\text{ex,obs}} = \frac{5.5 \text{ [K]}}{\ln\{1 + 5.5 \text{ [K]}/(T_{\text{b}} + 0.82 \text{ [K]})\}}, \quad (3.6)$$

where $5.5 \text{ K} \equiv h\nu_0/k$, for $\nu_0 = 115.3 \text{ GHz}$ – the line center of the CO ($J=1-$

⁵The critical density is defined as the ratio of the Einstein coefficient for spontaneous emission to the coefficient for collisional de-excitation $n_{\text{cr}} \equiv A_{ul}/C_{ul}$

⁶We assume $\sigma_{T_{\text{ex}}} \pm 0.05 \text{ K}$ given the uncertainty of the observational estimates of T_{ex} reported by [Roman-Duval et al. \(2010\)](#). If we choose a different value, the number of cells fulfilling the criteria changes, although the shape of Fig. 3.9b remains the same.

0) emission. Note that this expression assesses that $T_{\text{bg}} = T_{\text{CMB}}$, i.e. that the only significant background radiation field at the frequency of interest is the CMB. The term 0.82 K is equivalent to $h\nu_0/k[\exp(h\nu_0/kT_{\text{bg}}) - 1]$.

So far, we have assumed that T_{ex} is constant along the line of sight. In reality, this is unlikely to be the case. In addition, we have not yet specified which value must be used for T_{b} in Eq. 3.6. One way to proceed at this point is to follow the approach originally used by (Dickman, 1978) and subsequently adopted by many other studies (e.g. Garden et al., 1991; Liszt and Lucas, 1998; Pineda et al., 2008; Goldsmith et al., 2008; Pineda et al., 2010). In this case, we assume that T_{ex} actually is constant along the line of sight (justified in Dickman’s case by his assumption that the cloud was in TE), and use the maximum value observed for the brightness temperature, $T_{\text{b,max}}$, at each position (x, y) . We then end up with a “column” excitation temperature

$$T_{\text{ex,obs}}^{\text{col}} = \frac{5.5 \text{ [K]}}{\ln\{1 + 5.5 \text{ [K]}/(T_{\text{b,max}} + 0.82 \text{ [K]})\}}. \quad (3.7)$$

Alternatively, we can attempt to preserve as much of the information in the observed emission as we can by computing T_{ex} for each velocity bin and each line of sight in our 3D channel map of emission. To do this, we continue to use Eq. 3.6, but now take T_{b} to be the brightness temperature of the emission in the particular velocity bin of interest. The result of this procedure is a map of T_{ex} in PPV space, which we hereafter refer to simply as $T_{\text{ex,obs}}$.

In order to visualize how this estimate of T_{ex} varies with physical conditions in the gas, we need to transform these quantities (e.g. density) from PPP space into PPV space.

Fig. 3.10 shows the mass-weighted 2D PDF of $T_{\text{ex,obs}}$ as a function of n . Comparing Figs. 3.10 and 3.9a, we see that the two PDFs are very different. A significant fraction of the mass in both plots has excitation temperatures close to T_{bg} – in the case of Fig. 3.10, 37% of the mass is at the peak of the PDF ($T_{\text{ex,obs}} \lesssim 3.5$ K), while in Fig. 3.9a, 67% of the mass is at the peak ($T_{\text{ex}} \lesssim 5$ K). The blue line indicates the average, $\langle T_{\text{ex,obs}} \rangle$ and the cyan line shows $\langle T_{\text{ex}} \rangle$ (from Eq. 3.4) in every number density bin. These two lines increase towards high n . At $n \lesssim 1500 \text{ cm}^{-3}$, $\langle T_{\text{ex}} \rangle < \langle T_{\text{ex,obs}} \rangle$. This situation reverses at higher n , $\langle T_{\text{ex}} \rangle > \langle T_{\text{ex,obs}} \rangle$ and their difference increases towards high n . At $n \approx 5000 \text{ cm}^{-3}$, $\langle T_{\text{ex}} \rangle$ is a few K higher than $\langle T_{\text{ex,obs}} \rangle$. Notice that the cyan line represents $\langle T_{\text{ex}} \rangle$ in every n bin, as shown in Fig. 3.9a, although both lines do not look exactly the same. The reason is that in Fig. 3.9a, we are using the densities in PPP space, while in Fig. 3.10 the values are in PPV space. In supersonic turbulent clouds, the random velocity variations create physically connected regions along the LoS in real space that can be

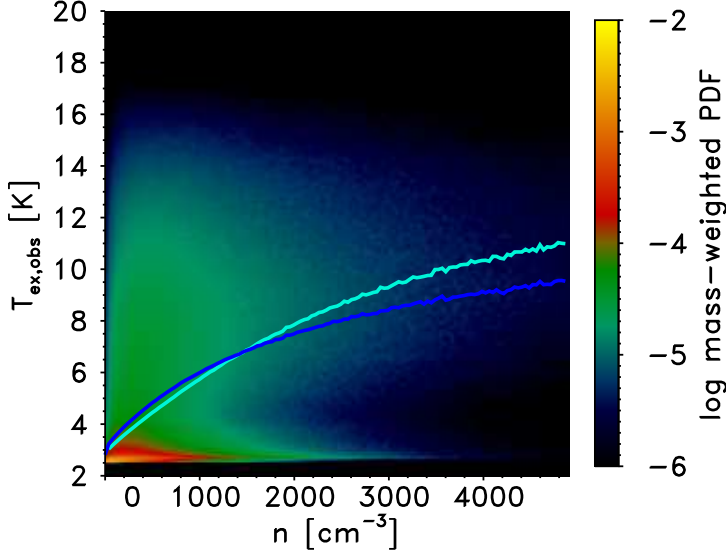


Figure 3.10: Mass-weighted 2D PDF of the “*observational*” excitation temperature $T_{\text{ex,obs}}$. We overplot the average $\langle T_{\text{ex,obs}} \rangle$ calculated in every number density bin (blue line), also the average $\langle T_{\text{ex}} \rangle$ in every n bin as in Fig. 3.9a (cyan line). Although the cyan lines in this figure and in Fig. 3.9a look different, they are equivalent. n in Fig. 3.9 is in a position-position-position (PPP) space, while here it is in position-position-velocity (PPV) space.

broken up into multiple distinct features in PPV space. Conversely, they can create coherent features in PPV space which in reality correspond to multiple, physically disconnected zones in PPP space (Adler and Roberts, 1992; Ballesteros-Paredes and Mac Low, 2002; Glover et al., 2010; Shetty et al., 2010; Beaumont and et al., 2013).

Fig. 3.12a illustrates the map of the column excitation temperature $T_{\text{ex,obs}}^{\text{col}}$ computed using the original Dickman (1978) approach (3.7). In this case, we have only a single value for each line of sight, and hence cannot explore how $T_{\text{ex,obs}}^{\text{col}}$ varies with the volume density. Instead, we show in Fig. 3.12b shows the corresponding 2D mass-weighted PDF of $T_{\text{ex,obs}}^{\text{col}}$ as a function of the column density N . 74% of the mass lies at low $T_{\text{ex,obs}}^{\text{col}}$ (2.7 K to 5 K), and the remaining mass is in sight lines distributed up to $T_{\text{ex,obs}}^{\text{col}} \approx 18$ K. The blue line represents the average $\langle T_{\text{ex,obs}}^{\text{col}} \rangle$ in every N . The white and red lines indicates the averages of the column kinetic temperatures $\langle T_{\text{K}}^{\text{co-col}} \rangle$ and $\langle T_{\text{K}}^{\text{col}} \rangle$ calculated in every N bin, respectively. $\langle T_{\text{ex,obs}}^{\text{col}} \rangle$ and $\langle T_{\text{K}}^{\text{co-col}} \rangle$ do not agree at $N \lesssim 1.5 \times 10^{22} \text{ cm}^{-2}$, although they match and cross towards

high column densities. On the other hand, $\langle T_K^{\text{col}} \rangle$ at every N exceeds the entire range of values in the $T_{\text{ex,obs}}^{\text{col}}$ PDF. $\langle T_K^{\text{col}} \rangle$ approaches the PDF only at $N \gtrsim 2 \times 10^{22} \text{ cm}^{-2}$, corresponding to $A_V \approx 10$ mag. Since $\langle T_K^{\text{co-col}} \rangle$ provides more adequate estimates of the column kinetic temperature (where CO is abundant) than $\langle T_K^{\text{col}} \rangle$, it will be hereafter be the reference column kinetic temperature.

In order to compare the estimate of the ‘‘column’’ excitation temperature, $T_{\text{ex,obs}}^{\text{col}}$, that we get from Eq. 3.7 with the real excitation temperature of the gas, we need to average the latter along each line of sight. To do this, we compute a column excitation temperature, $T_{\text{ex}}^{\text{col}}$ in the same fashion as we computed $T_K^{\text{co-col}}$ in §3.3.1, i.e. we compute a CO mass-weighted average of T_{ex} for each line of sight. Fig. 3.12c illustrates the map of $T_{\text{ex}}^{\text{col}}$. The most obvious difference between Figs. 3.12a and 3.12c is that $T_{\text{ex,obs}}^{\text{col}}$ (Figs. 3.12a) exhibits higher values than $T_{\text{ex}}^{\text{col}}$ (Fig. 3.12c). The reason is that in Eq. 3.7, only the peak of the emission along the LoS is used to calculate $T_{\text{ex,obs}}^{\text{col}}$, which is supposed to come from optically thick regions. However, the emission along the LoS is not necessarily well represented by the maximum. The PDF of τ in Fig. 3.8 shows that in the cloud, 51% of the mass has $\tau < 1$ (dotted line), but this contributes with only 19% of the total emission (solid line). Therefore, T_{ex} has variations along the LoS.

Fig. 3.12d shows the 2D mass-weighted PDF of $T_{\text{ex}}^{\text{col}}$ as a function of N . 79% of the mass lies along lines of sight with $T_{\text{ex}}^{\text{col}} \lesssim 5$ K. The rest of the mass is distributed up to $T_{\text{ex}}^{\text{col}} \approx 17$ K. At $N \gtrsim 10^{22} \text{ cm}^{-2}$, the PDF of $T_{\text{ex}}^{\text{col}}$ becomes narrower than that of $T_{\text{ex,obs}}^{\text{col}}$ (Fig. 3.12b). The cyan and blue lines show the average $\langle T_{\text{ex}}^{\text{col}} \rangle$ and $\langle T_K^{\text{co-col}} \rangle$ respectively, in every column density bin. $\langle T_{\text{ex,obs}}^{\text{col}} \rangle$ exceeds $\langle T_{\text{ex}}^{\text{col}} \rangle$ by about 2 K at $N \gtrsim 7 \times 10^{21} \text{ cm}^{-2}$. This difference naturally comes from the fact that for calculating $T_{\text{ex,obs}}^{\text{col}}$ we consider that the emission is optically thick and use only the maximum. However at $N \lesssim 6 \times 10^{21} \text{ cm}^{-2}$ the situation reverts, $\langle T_{\text{ex,obs}}^{\text{col}} \rangle < \langle T_{\text{ex}}^{\text{col}} \rangle$ by less than 1 K. Lines of sight with these column densities are perhaps optically thin and have little CO, therefore $T_{\text{ex,obs}}^{\text{col}}$ is small. In Fig. 3.12d, the white and red lines show the averages $\langle T_K^{\text{co-col}} \rangle$ and $\langle T_K^{\text{col}} \rangle$ respectively, calculated for every N bin. $\langle T_{\text{ex}}^{\text{col}} \rangle$ approaches $\langle T_K^{\text{co-col}} \rangle$ at $N \gtrsim 10^{22} \text{ cm}^{-2}$ ($T_{\text{ex}}^{\text{col}} \approx 12$ K), but remains ~ 1 K below from it. This is consistent with the results shown in Fig. 3.9, which shows that $\langle T_{\text{ex}} \rangle < \langle T_K \rangle$ at all but the highest volume densities.

In order to check for consistency of our calculations with a real observation, Fig. 3.11 shows the column excitation temperature as a function of A_V for the Perseus molecular complex from Pineda et al. (2008) (their Fig. 10). They measure the excitation temperature using the Dickman’s approxima-

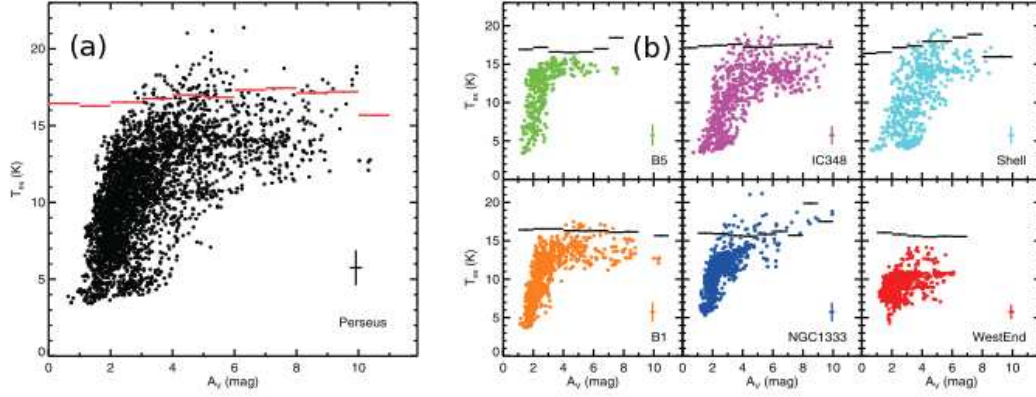


Figure 3.11: (a) Image of the column excitation temperature calculated using the Dickman (1978) formula $T_{\text{ex,obs}}^{\text{col}}$ (Eq.3.7) for the Perseus molecular complex taken from Pineda et al. (2008). (b) same as (a) but separated by regions.

tion (Eq. 3.7). The visual extinction is measured using infrared data from 2MASS. Fig. 3.11a shows $T_{\text{ex,obs}}^{\text{col}}$ for all the whole Perseus cloud. Our results in Fig. 3.12b are in very good agreement with Pineda et al. (2008). $T_{\text{ex,obs}}^{\text{col}}$ is distributed very similarly in both figures with values ranging up to ~ 17 K and up to $A_V \approx 10$ mag. Even all the individual regions⁷ in Fig. 3.11b exhibit similar distributions, with the exception of the region “WestEnd”.

In Fig. 3.12d, there is a fraction of lines of sight where $T_{\text{ex}}^{\text{col}}$ may overlap $T_{\text{K}}^{\text{co-col}}$ (Fig. 3.6b), which can apparently fulfill the LTE condition. Locally, it is more probable to find zones with $T_{\text{ex}} \approx T_{\text{K}}$ if $n \gtrsim n_{\text{cr}} = A_{\text{ul}}/C_{\text{ul}}$. However for projected quantities, a critical column density N_{cr} cannot be inferred analytically because the coefficient C_{ul} depends on the local number density, not on the column density. In consequence, we select the sight lines where $T_{\text{K}}^{\text{co-col}} \approx T_{\text{ex}}^{\text{col}} \pm \sigma_{T_{\text{ex,co}}}$ with $\sigma_{T_{\text{ex,co}}} = 0.5$ ⁸ with the aim of determining N_{cr} qualitatively. Fig. 3.14a illustrates the 3% of the total lines of sight that match the criteria. Fig. 3.14b shows the corresponding mass-weighted 2D PDF of $T_{\text{ex}}^{\text{col}}$ for the lines of sight fulfilling the criteria. In this case, the critical column density is about $N \gtrsim N_{\text{cr}} \approx 5 \times 10^{21} \text{ cm}^{-2}$ (corresponding

⁷In §4.2, we present a Perseus map as well as a brief description of the selection criteria chosen by Pineda et al. (2008)s for the regions separation.

⁸The choice of $\sigma_{T_{\text{ex,co}}} = 0.5$ corresponds to about half of the difference between $\langle T_{\text{ex}}^{\text{col}} \rangle$ and $\langle T_{\text{K}}^{\text{co-col}} \rangle$ at $N \gtrsim 1.5 \times 10^{22} \text{ cm}^{-2}$. We did not use the same $\sigma_{T_{\text{ex}}}$ as in the 3D analysis (Fig. 3.9b), because we obtained only 2 lines of sight fulfilling the criteria. We cannot have a good statistical analysis with such a small number.

to $A_V \approx 3$ mag), where $\langle T_{\text{ex}}^{\text{col}} \rangle$ is good guide to $\langle T_{\text{K}}^{\text{co-col}} \rangle$. The peak of the PDF is around $N \approx 9 \times 10^{21} \text{ cm}^{-2}$. The averages $\langle T_{\text{ex}}^{\text{col}} \rangle$ (cyan line), $\langle T_{\text{K}}^{\text{co-col}} \rangle$ (white line), and $\langle T_{\text{K}}^{\text{co-col}} \rangle$ (red line) are plotted for comparison. These results clearly suggest that even for the projected temperatures, 97% of the lines of sight do not fulfill the LTE criteria.

Finally, we notice that the line of sight average of T_{ex} depends to some extent on the method used to compute it. For instance, rather than averaging the excitation temperatures, we could instead compute an estimate $\tilde{T}_{\text{ex}}^{\text{col}}$ that uses the column densities in each level. i.e.

$$\frac{N_l}{N_u} = \frac{g_l}{g_u} \exp\left(\frac{h\nu_0}{k\tilde{T}_{\text{ex}}^{\text{col}}}\right). \quad (3.8)$$

The values of $\tilde{T}_{\text{ex}}^{\text{col}}$ calculated in this way are typically lower than $T_{\text{ex}}^{\text{col}}$ (Eq. 3.4) by approximately 1 K. This issue raises the question of which method is the most accurate for computing the projected temperature? Also, how does projection affect other quantities requiring temperature estimates? In the next section, we will use the excitation temperatures estimated in this section in order to calculate the CO column density in the level $J=0$ and the total CO column density with the aim of quantifying the differences between the estimates from Eqs. 3.4 and 3.6. We will also test how the projection of the excitation temperatures affects those CO column density estimates.

3.4 CO column density

In this section, we compare estimates of the CO column density obtained using the results of the previous section with the “true” CO column density (i.e. that output by the MHD simulation). We obtain this output value by first converting the data from a position-position-position (PPP) to a position-position-velocity (PPV) cube (see Appendix). We then sum up the individual column densities – $\mathcal{N}_{\text{CO}}(x, y, v)$ – in every velocity channel along the LoS in order to obtain the CO column density at every (x, y) position (N_{CO}).

Fig. 3.15 shows the 2D mass-weighted PDF of the CO column density N_{CO} as a function of N . As in previous plots, A_V is indicated as a reference at the top. The black line indicates the average $\langle N_{\text{CO}} \rangle$ in every N bin which closely follows the peak of the PDF. N_{CO} grows with increasing column density as expected from Fig. 3.4. Moreover, the dispersion in column density N around the average increases towards high N_{CO} , with a maximum at $N_{\text{CO}} \sim 10^{17} \text{ cm}^{-2}$ (top purple line in Fig. 3.15). For future reference in §3.4 and 3.4.1,

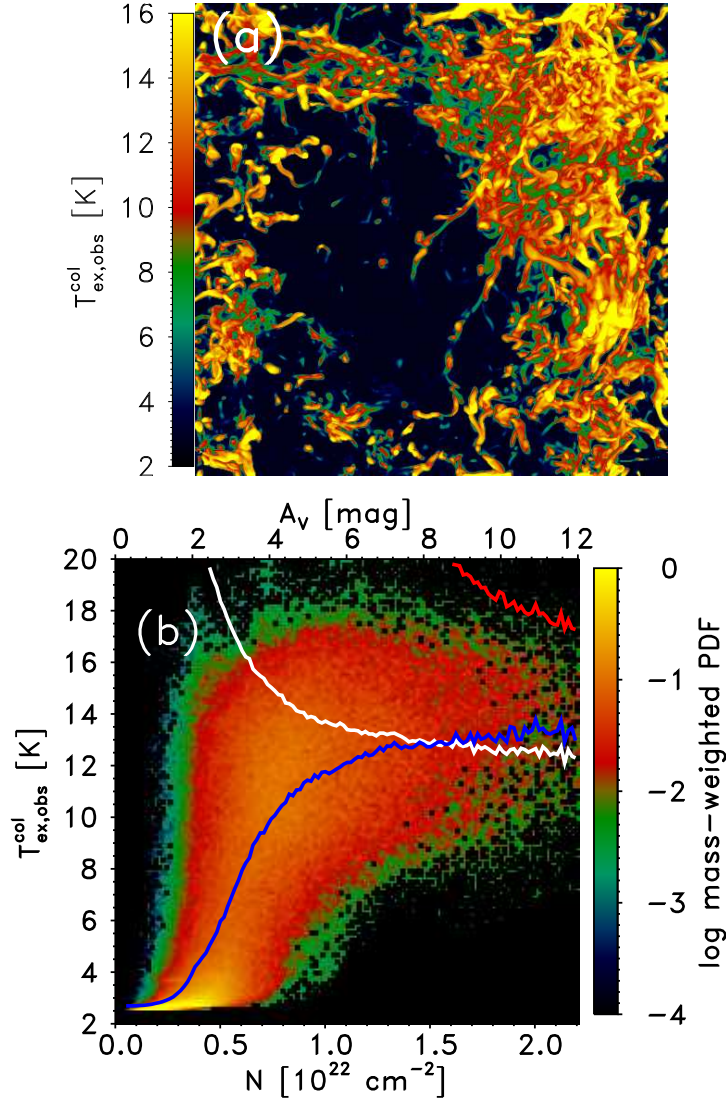


Figure 3.12: (a) Image of the column excitation temperature calculated using the Dickman (1978) formula $T_{\text{ex,obs}}^{\text{col}}$ (Eq.3.7). (b) Mass-weighted 2D PDF of $T_{\text{ex,obs}}^{\text{col}}$ vs. column density. The visual extinction A_V corresponding to N is indicated at the top of the figure for reference. The solid lines show the averages $\langle T_{\text{ex,obs}}^{\text{col}} \rangle$ (blue line), $\langle T_{\text{K}}^{\text{co-col}} \rangle$ (white line), and $\langle T_{\text{K}}^{\text{col}} \rangle$ (red line) in every N bin.

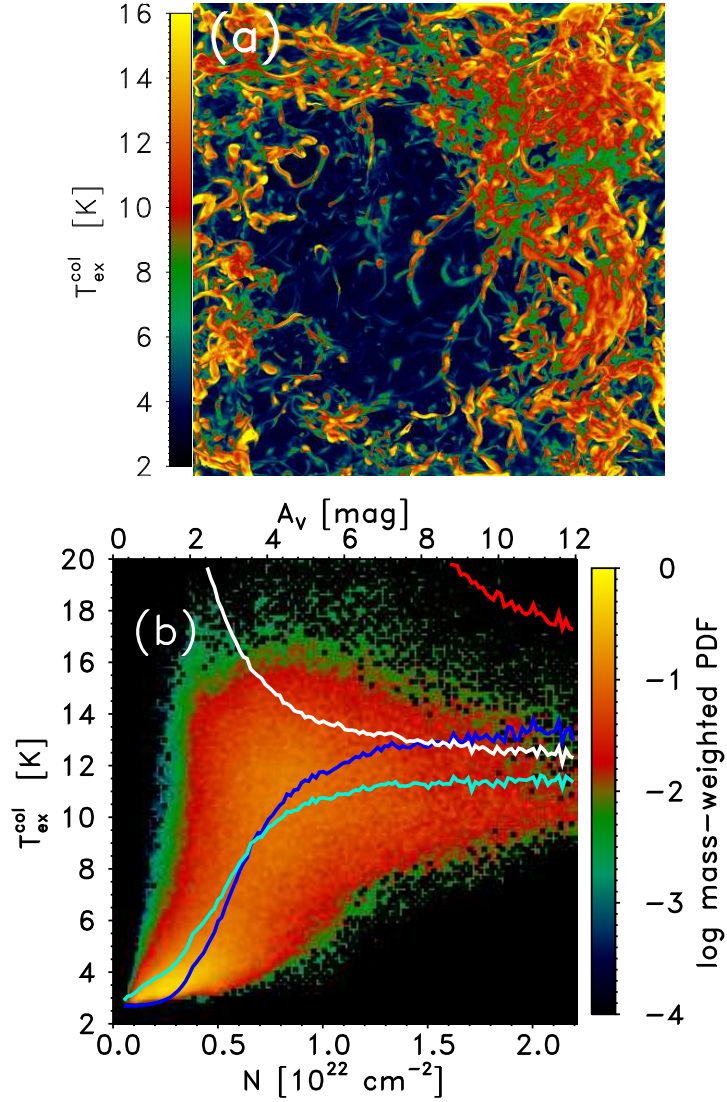


Figure 3.13: (a) Image of the column excitation temperature calculated considering the Boltzmann equation (Eq. 3.4) $T_{\text{ex}}^{\text{col}}$, which is projected as the CO mass-weighted average of T_{ex} along the LoS. (b) Mass-weighted 2D PDF of $T_{\text{ex,obs}}^{\text{col}}$ vs. column density. As in Fig. 3.12b, the visual extinction is indicated at the top of the figure. The cyan line shows the average $\langle T_{\text{ex}}^{\text{col}} \rangle$. The arrangement of lines is the same as in Fig. 3.12b.

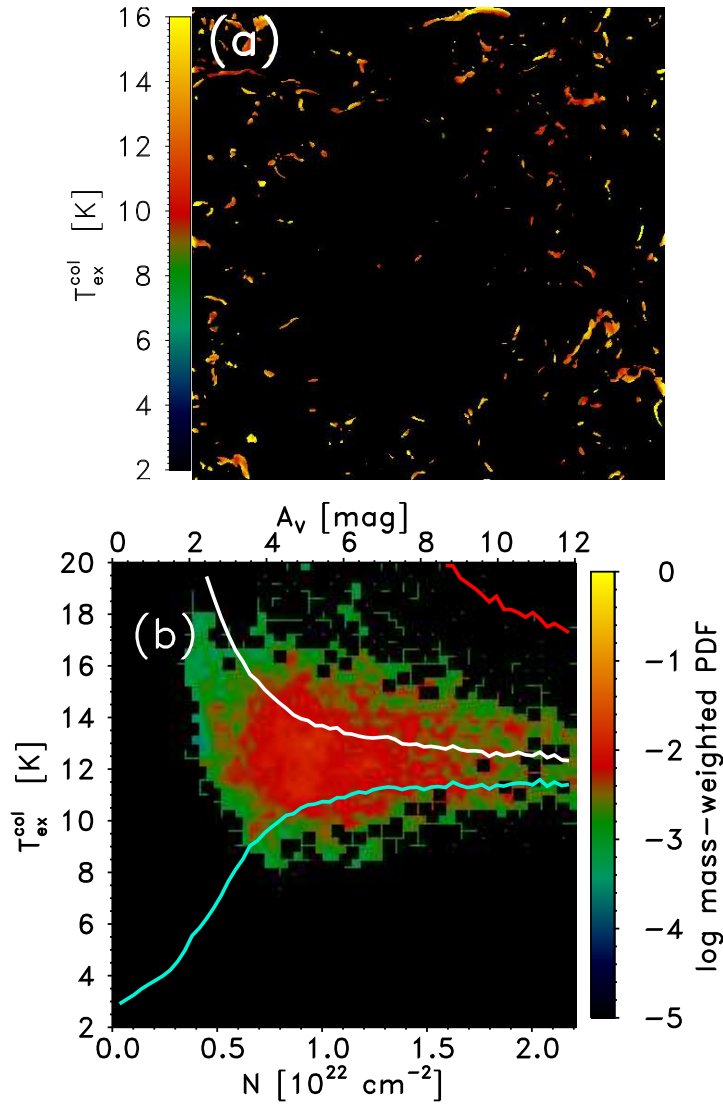


Figure 3.14: (a) Map of $T_{\text{ex}}^{\text{col}}$ (calculated from the Boltzmann equation and projected along the LoS) for the lines of sight fulfilling the condition $T_{\text{ex}}^{\text{col}} \approx T_{\text{K}}^{\text{co-col}} \pm 0.5$ K. (b) Mass-weighted 2D PDF of only the zones with $T_{\text{ex}}^{\text{col}} \approx T_{\text{K}}^{\text{co-col}} \pm 0.25$ K. A_V is at the top of the figure for reference. The cyan, white and red lines are the same as in Fig. 3.12d.

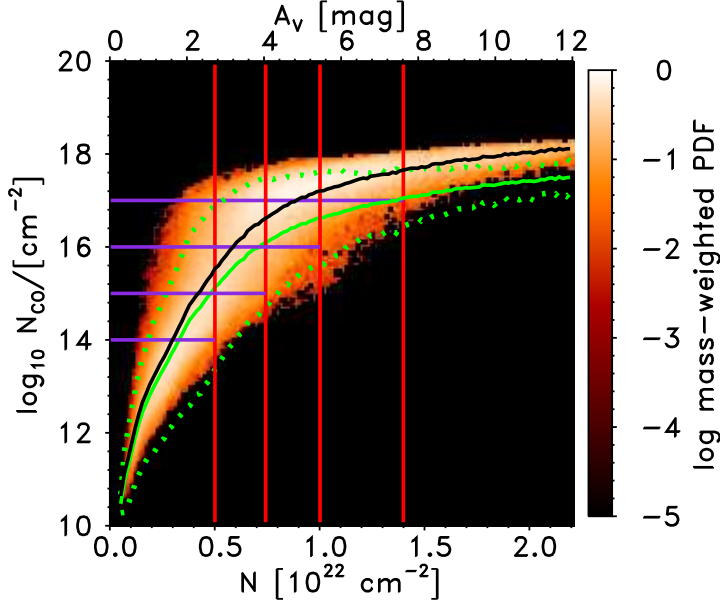


Figure 3.15: Mass-weighted 2D PDF of the total CO number density. The black line shows the average $\langle N_{\text{CO}} \rangle$ in every column density bin. The purple lines indicate the values $N_{\text{CO}} = 10^{14}, 10^{15}, 10^{16}$ and 10^{17} cm^{-2} as a reference and are drawn up to a column density where the PDF is ~ 0.01 . The red lines intersect those purple lines to indicate column densities and visual extinction values at each of these values of N_{CO} . The green solid line shows the average of CO($J=0$) column density $\langle N_{\text{CO},J=0} \rangle$ in every N bin for reference. The dotted green lines shows $\langle N_{\text{CO},J=0} \rangle \pm 2.5\sigma$, enclosing $\sim 96\%$ of the data.

the purple lines indicate constant $N_{\text{CO}} = 10^{14}, 10^{15}, 10^{16}$ and 10^{17} cm^{-2} . Those lines are drawn from $N = 0 \text{ cm}^{-2}$ up to the column density at which the PDF has dropped to 0.01 of the peak value. The red lines indicate those column densities ($N = 5 \times 10^{21}, 7.5 \times 10^{21}, 10^{22}$ and $1.4 \times 10^{22} \text{ cm}^{-2}$) and the correspondent visual extinction ($A_V \approx 2.7, 4, 5.3$ and 7.5 mag).

Additionally, Fig. 3.15 shows the average of the “true” CO($J=0$) column density $\langle N_{\text{CO},J=0} \rangle$ in every N bin (green solid line). This green line follows a similar behavior to the black line (the total $\langle N_{\text{CO}} \rangle$ vs. N). By definition, the mass of CO in the level $J=0$ has to be less than or equal to the total mass of CO in all levels. In this particular example, the mass of CO in the $J=0$ level is 24% of the total mass of CO. The largest differences between N_{CO} and $N_{\text{CO},J=0}$ increase with N . Fig. 3.15 also shows the dispersion of $N_{\text{CO},J=0}$ around the average $\langle N_{\text{CO},J=0} \rangle \pm 2.5\sigma$ (green dotted lines). These lines enclose $\sim 96\%$ of the $N_{\text{CO},J=0}$ values. These references will be useful in the next

subsection, where we will estimate the CO($J=0$) column density from the excitation temperature.

CO($J=0$) column density estimated from the excitation temperature

Line intensities of a given species can be used to infer its column densities. The calculation is not straightforward, although it can be achieved by taking into account some approximations. For an emission line, the column density of the lowest rotational level of the transition N_l can be inferred from the column excitation temperature, the optical depth of the rotational transitions $u \rightarrow l$ integrated along the LoS, and the Boltzmann equation (Eq. 3.4),

$$N_l = 93.28 \frac{g_l \nu_0^3}{g_u A_{ul}} \int \frac{\tau_v dv}{1 - \exp[-h\nu_0/kT_{\text{ex}}(v)]} \quad [\text{cm}^{-2}], \quad (3.9)$$

where A_{ul} is the Einstein coefficient for spontaneous emission. The units for the frequency of the line center ν_0 is GHz and linewidths dv are in km s^{-1} (Wilson et al., 2009).

For the transition between two rotational levels of a linear molecule $J \rightleftharpoons J+1$, the coefficient $A_{ul} = A_J$ depends on the frequency and a dipole moment $|\mu_J|^2 = \mu^2(J+1)/(2J+3)$, where μ is the permanent electric dipole moment of the molecule for the transition $J+1 \rightarrow J$. For emission, the Einstein coefficient in Eq. 3.9 can be written as

$$A_J = 1.165 \times 10^{-11} \mu^2 \nu_0^3 \frac{J+1}{2J+3} \quad \text{s}^{-1} \quad \text{For } J+1 \rightarrow J, \quad (3.10)$$

where μ is in Debye. For the CO molecule $\mu = 0.112D$, and since $g_J = 2J+1$, Eq. (3.9) can be written as

$$N_{\text{CO},l} = 6.38 \times 10^{14} [\text{cm}^{-2}] \frac{(2J+1)}{(J+1)} \int \frac{\tau_v dv}{1 - \exp[-h\nu_0/kT_{\text{ex}}(v)]}. \quad (3.11)$$

In general, along any line of sight, there will be a mixture of optically thin and optically thick zones. In our cloud model, τ may range from $\sim 10^{-6}$ to ~ 600 for every velocity channel in Eq. 3.11. Low $N_{\text{CO},J=0}$ regions are more likely to be optically thin, although the optically thick zones contribute significantly to the total mass along the LoS. In any case, optically thin regions account for 51% of the total mass of the cloud (see Fig. 3.8). Therefore, there should be significant contributions from $\tau \leq 1$ zones to the total $N_{\text{CO},J=0}$ (estimated from Eq. 3.11). On the other hand at high $N_{\text{CO},J=0}$, lines of sight

primarily have $\tau \gtrsim 10$. However, there are only few such LoS (see Fig. 3.8). This low contribution of τ at high $N_{\text{CO},J=0}$ may be compensated by the excitation temperature in Eq. 3.11. Although T_{ex} only changes by some units, the term in Eq. 3.11 $\{1 - \exp[-h\nu_0/kT_{\text{ex}}(v)]\}^{-1}$ has a significant role in shaping the $N_{\text{CO},J=0}$ distribution. The average $\langle T_{\text{ex}} \rangle$ grows with increasing density, however T_{ex} and $T_{\text{ex,obs}}$ have different distributions (see Figs. 3.9a and 3.10). It is therefore difficult to really differentiate qualitatively the role of the excitation temperature alone at a given $N_{\text{CO},J=0}$ in Eq. 3.11. Figs. 3.16a and 3.16b quantify the effects of using T_{ex} (Eq. 3.4) or $T_{\text{ex,obs}}$ (Eq. 3.6) in order to estimate $N_{\text{CO},J=0}$ (Eq. 3.11). Later, we also evaluate the effect of considering $T_{\text{ex}}(v)$ or simply a uniform excitation temperature along the lines of sight $T_{\text{ex}}^{\text{col}}$.

Fig. 3.16a shows the 2D mass-weighted PDF of the ratio of the estimated CO($J=0$) column density $N_{\text{CO},J=0}^{\text{th},3\text{D}}$ to the “true” CO($J=0$) column density $N_{\text{CO},J=0}$ as a function of the “true” $N_{\text{CO},J=0}$. $N_{\text{CO},J=0}^{\text{th},3\text{D}}$ is calculated by introducing the excitation temperature from the Boltzmann Equation T_{ex} (Eq. 3.4) into Eq. 3.11 and therefore accounts for variations in T_{ex} along each line of sight. The black line in Fig. 3.16a shows the one-to-one relation between $N_{\text{CO},J=0}^{\text{th},3\text{D}}$ and the “true” $N_{\text{CO},J=0}$. On average, the ratio $N_{\text{CO},J=0}^{\text{th},3\text{D}}/N_{\text{CO},J=0}$ is close to one. This is not surprising because both Eq. 3.11 and T_{ex} were derived from the Boltzmann equation. However, the PDF shows high dispersion around the average, with the highest deviation from the one-to-one line at the peak $N_{\text{CO},J=0} \approx 5 \times 10^{16} \text{ cm}^{-2}$ (47% of the mass is located above this value). Due to this dispersion, we prefer to focus on the average $\langle N_{\text{CO},J=0}^{\text{th},3\text{D}}/N_{\text{CO},J=0} \rangle$ in every $N_{\text{CO},J=0}$ bin (blue line) rather than the whole distribution. At $N_{\text{CO},J=0} \lesssim 10^{15} \text{ cm}^{-2}$, the average $\langle N_{\text{CO},J=0}^{\text{th},3\text{D}}/N_{\text{CO},J=0} \rangle$ is very close to one (black line). However, at $N_{\text{CO},J=0} \gtrsim 10^{15} \text{ cm}^{-2}$, $\langle N_{\text{CO},J=0}^{\text{th},3\text{D}}/N_{\text{CO},J=0} \rangle$ decreases as $N_{\text{CO},J=0}$ grows. There are two important reasons for this behavior. At these densities, the CO ($J=1-0$) emission line tends to be optically thick. Its distribution therefore does not follow the “true” CO column density distribution. Moreover, the number of regions with $\tau \gtrsim 10$ diminishes towards $N_{\text{CO},J=0} \gtrsim 10^{16} \text{ cm}^{-2}$ (see the drop of the τ PDF at $\tau \gtrsim 10$, Fig. 3.8). These cause $N_{\text{CO},J=0}^{\text{th},3\text{D}}$ to be lower than the “true” $N_{\text{CO},J=0}$. Averaged over all lines-of-sight, we find $N_{\text{CO},J=0}^{\text{th},3\text{D}} = 0.7 N_{\text{CO},J=0}$.

Fig. 3.16b shows the “observationally” derived 2D mass-weighted PDF of the ratio of CO($J=0$) column density $N_{\text{CO},J=0}^{\text{obs},3\text{D}}$ to the “true” $N_{\text{CO},J=0}$ as a function of the “true” $N_{\text{CO},J=0}$. $N_{\text{CO},J=0}^{\text{obs},3\text{D}}$ is calculated using $T_{\text{ex,obs}}$ (Eq. 3.6) in Eq. 3.11. The ratio $N_{\text{CO},J=0}^{\text{obs},3\text{D}}/N_{\text{CO},J=0}$ shows high dispersion and looks

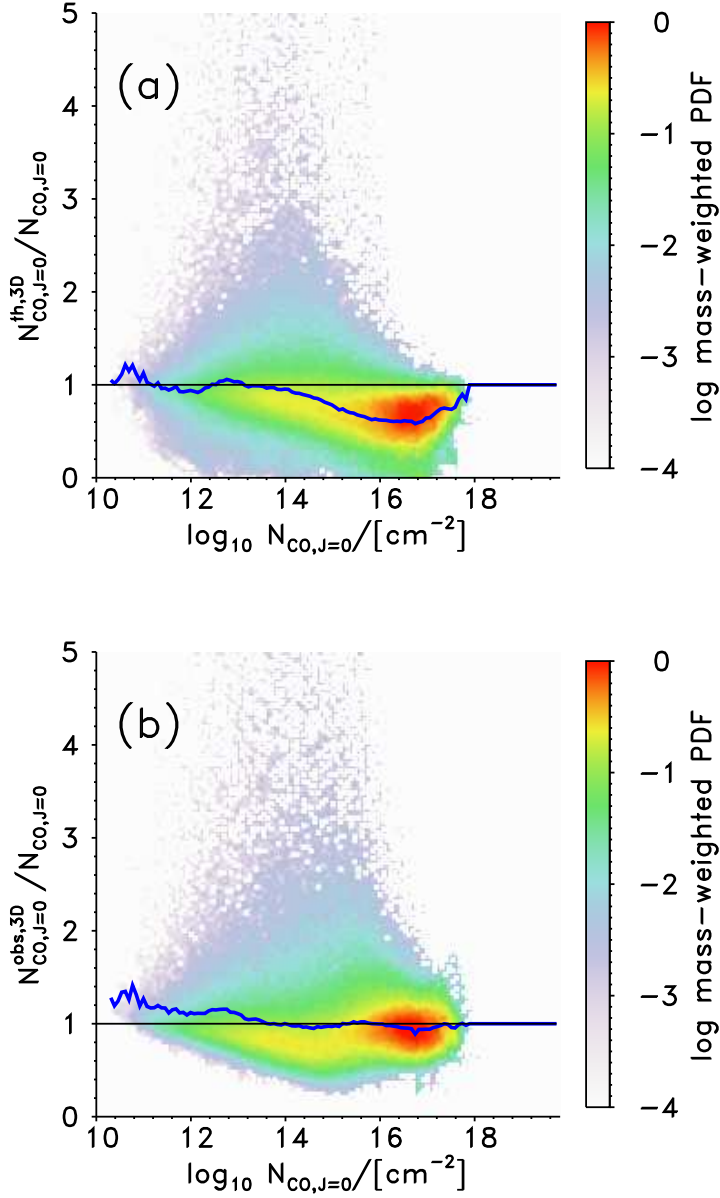


Figure 3.16: (a) Mass-weighted 2D PDF of the ratio of $N_{\text{CO},J=0}^{\text{th},3\text{D}}$ to the true $N_{\text{CO},J=0}$, as function of $N_{\text{CO},J=0}$. The blue line shows the average of this ratio in every true $N_{\text{CO},J=0}$ bin, and the black line represents $N_{\text{CO},J=0}^{\text{th},3\text{D}} = N_{\text{CO},J=0}$. In total, $N_{\text{CO},J=0}^{\text{th},3\text{D}} = 0.7 N_{\text{CO},J=0}$. The blue line is set artificially to 1 at $N_{\text{CO},J=0} > 10^{18} \text{ cm}^{-2}$ in order to avoid numerical noise. (b) Same as (a), but considering $T_{\text{ex}}^{\text{obs}}$ (Dickman, 1978). In this case, $N_{\text{CO},J=0}^{\text{obs},3\text{D}} = 0.98 N_{\text{CO},J=0}$. The arrangement of lines is the same as in (a).

very close to the one-to-one relation (black line), similar to Fig. 3.16a. Given the high dispersion in the PDF, it is again easier to analyze the behavior of the average $\langle N_{\text{CO},J=0}^{\text{obs},3\text{D}}/N_{\text{CO},J=0} \rangle$ in every $N_{\text{CO},J=0}$ bin (blue line). In Eq. 3.6, $T_{\text{ex,obs}}$ is determined assuming that the CO ($J=1-0$) emission line is optically thick. Therefore for lines of sight with $N_{\text{CO},J=0} \lesssim 10^{13} \text{ cm}^{-2}$ (which span many optically thin zones). $T_{\text{ex,obs}}$ is higher than expected (compared to T_{ex} from the Boltzmann equation). Hence, $N_{\text{CO},J=0}^{\text{obs},3\text{D}}$ overestimates the “true” $N_{\text{CO},J=0}$. At $N_{\text{CO},J=0} \gtrsim 10^{14} \text{ cm}^{-2}$, the average $\langle N_{\text{CO},J=0}^{\text{obs},3\text{D}}/N_{\text{CO},J=0} \rangle$ approaches the one-to-one line as the fraction of sight lines which are optically thick increases. In Fig. 3.16b, the average $\langle N_{\text{CO},J=0}^{\text{th},3\text{D}}/N_{\text{CO},J=0} \rangle$ increases towards high $N_{\text{CO},J=0}$, contrary to Fig. 3.16a. The reason is that zones with $\tau \gtrsim 1$ and $T_{\text{ex,obs}} \gtrsim 5 \text{ K}$ are more abundant in the observational calculation of $N_{\text{CO},J=0}^{\text{obs},3\text{D}}$ than for $N_{\text{CO},J=0}^{\text{th},3\text{D}}$. In this approach, $N_{\text{CO},J=0}^{\text{obs},3\text{D}}$ is higher than $N_{\text{CO},J=0}^{\text{th},3\text{D}}$ (Fig. 3.16a) by almost 30%. Even though the approximations of LTE, and the assumptions of the gas being isothermal and optically thick in Eq. 3.6 are not accurate, overall we find that $N_{\text{CO},J=0}^{\text{obs},3\text{D}} = 0.98 N_{\text{CO},J=0}$ when we average over all lines of sight. The reason is that most of the mass lies along lines of sight with $N_{\text{CO},J=0} \gtrsim 10^{16} \text{ cm}^{-2}$, which mostly correspond to $N \gtrsim 5 \times 10^{21} \text{ cm}^{-2}$ (see Fig. 3.15). At those column densities, a large fraction of each sight-line has $n \gtrsim 2000 \text{ cm}^{-3}$, for which $\langle T_{\text{ex}} \rangle$ is close to $\langle T_{\text{K}} \rangle$. Therefore, the Dickman approximation is very accurate for estimating $N_{\text{CO},J=0}$ at $N_{\text{CO},J=0} \gtrsim 10^{13}$ ($N \gtrsim \text{few} \times 10^{21} \text{ cm}^{-2}$ in Fig. 3.15).

In several works, the excitation temperature is considered uniform along the LoS (Garden et al., 1991; Liszt and Lucas, 1998; Pineda et al., 2008; Goldsmith et al., 2008; Pineda et al., 2010). With the aim of studying how projections change the “view” of the excitation temperature, which in turn may affect the CO($J=0$) column density calculations, we insert the column excitation temperature $T_{\text{ex}}^{\text{col}}$ in Eq. 3.11 instead of $T_{\text{ex}}(v)$. Fig. 3.17a shows the 2D mass-weighted PDF of the ratio of the estimated CO($J=0$) column density (employing $T_{\text{ex}}^{\text{col}}$ in Eq. 3.11) $N_{\text{CO},J=0}^{\text{th},2\text{D}}$ to the “true” $N_{\text{CO},J=0}$ as a function of the “true” $N_{\text{CO},J=0}$. The excitation temperature is calculated from Boltzmann equation (Eq. 3.4), and is then projected in order to obtain $T_{\text{ex}}^{\text{col}}$ (see §3.3.3 for details). In Fig. 3.17a, most of the PDF lies above the equality line. From the average of $\langle N_{\text{CO},J=0}^{\text{th},2\text{D}}/N_{\text{CO},J=0} \rangle$ in every $N_{\text{CO},J=0}$ bin (blue line), it is clear that the $\langle N_{\text{CO},J=0}^{\text{th},2\text{D}} \rangle$ is higher than $\langle N_{\text{CO},J=0} \rangle$ and that their difference increases towards low $N_{\text{CO},J=0}$. The average of the ratio is very close to one at $N_{\text{CO},J=0} \gtrsim 10^{16} \text{ cm}^{-2}$. In total, $N_{\text{CO},J=0}^{\text{th},2\text{D}}$ is 1.05 times higher than $N_{\text{CO},J=0}$. Adopting $T_{\text{ex}}^{\text{col}}$ in Eq. 3.11, produces $N_{\text{CO},J=0}^{\text{th},2\text{D}}$ which is $\sim 30\%$ higher than $N_{\text{CO},J=0}^{\text{th},3\text{D}}$ (from using T_{ex} in Eq. 3.11). The reason is that

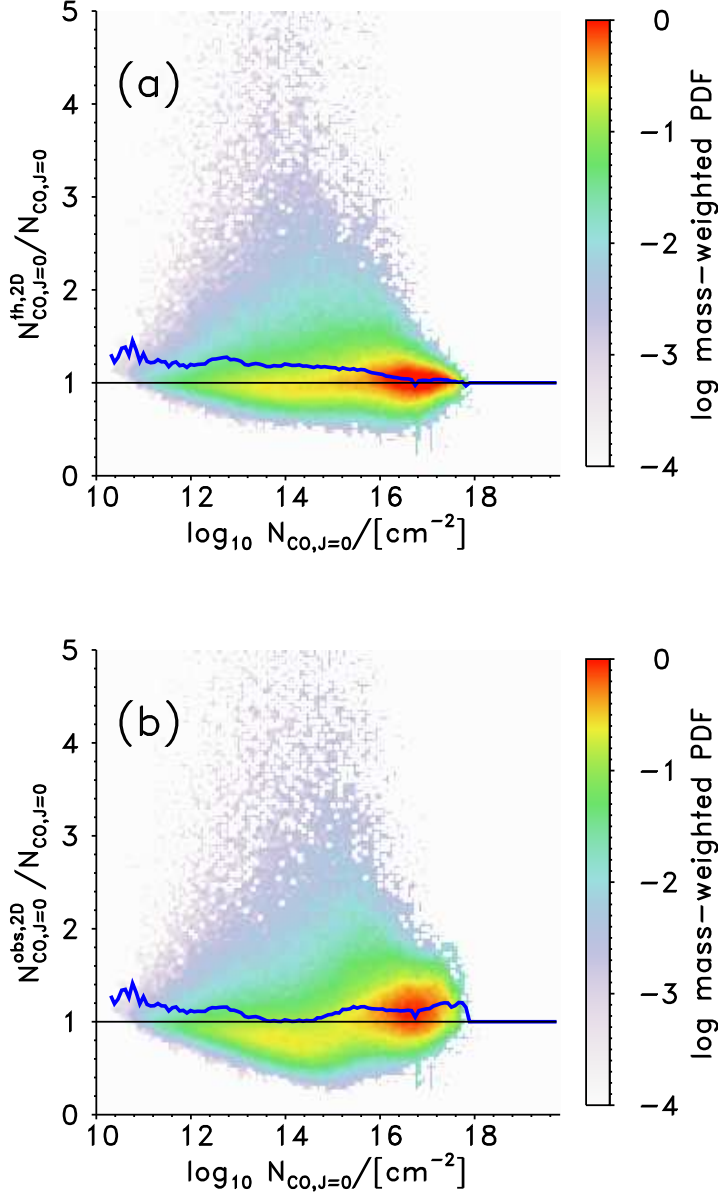


Figure 3.17: (a) Mass-weighted 2D PDF of the ratio of $N_{\text{CO},J=0}^{\text{th},2\text{D}}$ (calculated by using the uniform $T_{\text{ex}}^{\text{col}}$ (Boltzmann equation) in Eq. 3.11) – to the true $N_{\text{CO},J=0}$, as function of the true $N_{\text{CO},J=0}$. In total, $N_{\text{CO},J=0}^{\text{th},2\text{D}} = 1.05 N_{\text{CO},J=0}$. (b) Similar to (a), but for the “observational” estimated $N_{\text{CO},J=0}^{\text{obs},2\text{D}}$ considering $T_{\text{ex,obs}}^{\text{col}}$ (Dickman, 1978). In total $N_{\text{CO},J=0}^{\text{obs},2\text{D}} = 1.17 N_{\text{CO},J=0}$. The lines are arranged in the same fashion as in previous Figures.

the difference between $T_{\text{ex}}^{\text{col}}$ and T_{ex} is large. For $T_{\text{ex}}^{\text{col}}$, 77% of the mass is ≥ 5 K (Fig. 3.12d), but T_{ex} (Fig. 3.9a) on the other hand has only 33% of the mass at $T_{\text{ex}} \geq 5$ K.

The effect of projecting the observational estimate of the excitation temperature $T_{\text{ex,obs}}^{\text{col}}$ (Eq. 3.7) into the calculations of the CO($J=0$) column density $N_{\text{CO},J=0}^{\text{obs,2D}}$ (Eq. 3.11) is also quite different from the calculation of $N_{\text{CO},J=0}^{\text{obs,3D}}$. Fig. 3.17b shows the ratio of $N_{\text{CO},J=0}^{\text{obs,2D}}$ to the “true” $N_{\text{CO},J=0}$ as a function of the “true” $N_{\text{CO},J=0}$. $N_{\text{CO},J=0}^{\text{obs,2D}}$ overestimates $N_{\text{CO},J=0}$ for most of the distribution (compare to the black line as reference). In total, $N_{\text{CO},J=0}^{\text{obs,2D}} = 1.17 N_{\text{CO},J=0}$. As in the three previous plots, the blue line represents the average $\langle N_{\text{CO},J=0}^{\text{obs,2D}} / N_{\text{CO},J=0} \rangle$ as a function of $N_{\text{CO},J=0}$. For this average, there is no clear trend of the ratio with $N_{\text{CO},J=0}$. There are only small discrepancies between $N_{\text{CO},J=0}^{\text{obs,2D}}$ and $N_{\text{CO},J=0}^{\text{obs,3D}}$ which are more notable towards $N_{\text{CO},J=0} \gtrsim 10^{14} \text{ cm}^{-2}$ (Figs. 3.17b and 3.16b). For $T_{\text{ex,obs}}^{\text{col}}$, 75% of the mass is at ≥ 12 K, while $T_{\text{ex,obs}}^{\text{col}}$ has 52% of its mass above that value.

The most accurate method for estimating $N_{\text{CO},J=0}$ from Eq. 3.11 is using the excitation temperature in every spectral channel $T_{\text{ex,obs}}(v)$, for which $N_{\text{CO},J=0}^{\text{obs,3D}} \approx N_{\text{CO},J=0}$. Whether we consider T_{ex} or $T_{\text{ex}}^{\text{col}}$, the difference between $N_{\text{CO},J=0}^{\text{th,3D}}$ or $N_{\text{CO},J=0}^{\text{th,2D}}$ and the “true” $N_{\text{CO},J=0}$ is roughly 30%. On the “observational” counterpart, considering $N_{\text{CO},J=0}^{\text{obs,2D}}$ (considering $T_{\text{ex,obs}}^{\text{col}}$) overestimates the “true” $N_{\text{CO},J=0}$ by only $\sim 15\%$.

3.4.1 Total CO column density estimated from the excitation temperature

Ideally, the total column density of a species can be calculated as the summation of the individual column densities at every excitation level. For CO, the two or three lowest rotational levels are the most populated because its excitation is relatively weak (Liszt and Lucas, 1998). The energy level $J=2$ corresponds to a temperature ~ 17 K above the $J=0$ level. In our cloud model, less than 9% of the mass of CO has T_{K} above 17 K (see Fig. 5.1), and so there is a high probability that most of the CO mass lies in the three lowest populations. Indeed we know that in practice, much of the CO is subthermally excited (§3.3.3). 24% of the CO molecules are found in the $J=0$ level and 42% in $J=1$ (this level corresponds to $T \sim 5.53$ K). Most of the remaining 25% may be located at the $J=2$ level, although a small fraction (of the order of a few percent) may be found in higher excitation levels (see also Pon et al. (2012)). In this work, we focus on the $1 \rightarrow 0$ transition of the CO molecule. Therefore, to calculate the total CO column density given the

summation of different rotational levels is beyond the scope of this paper. However, we can estimate it from the CO column density in the level $J=0$ or $J=1$.

Following the derivation made by [Wilson et al. \(2009\)](#), CO can be considered as a completely rigid molecule with rotational energy:

$$E_{\text{rot}} = hB_e J(J+1), \quad (3.12)$$

where B_e is the rotational constant (for CO, $B_e = 57.66$ GHz)⁹. For a slightly elastic molecule, the rotational energy will increase by a term $hD[J(J+1)]^2$ (to first order) due to centrifugal stretching (D is the constant for centrifugal stretching). Typically, $D \approx 10^{-5}B_e$ for most molecules ([Wilson et al., 2009](#)). For CO at the levels $J \leq 2$, the correction to E_{rot} for such stretching is only $\lesssim 6 \times 10^{-5}$. Therefore, Eq. 3.12 is accurate enough for calculations based on the CO ($J=1-0$) transition.

If vibrationally excited states are not populated, the ratio of a population in a given level J to the total population is:

$$\frac{N_J}{N_{\text{total}}} = \frac{(2J+1)}{\Omega} \exp\left[-\frac{hB_e J(J+1)}{kT_{\text{ex}}}\right], \quad (3.13)$$

where Ω is the partition function ([Wilson et al., 2009](#)), which is expressed as

$$\Omega = \sum_{J=0}^{\infty} (2J+1) \exp\left[-\frac{hB_e J(J+1)}{kT_{\text{ex}}}\right]. \quad (3.14)$$

For simplicity, we assume that all the levels have the same T_{ex} ([Dickman, 1978](#)). Therefore, using Eq. 3.11 to calculate the column density of the lowest level of the transition $J+1 \rightarrow J$, the total CO column density is:

$$N_{\text{CO,total}} = \frac{6.38 \times 10^{14} [\text{cm}^{-2}]}{(J+1)} \int \frac{\tau_v \Omega \exp\left[\frac{2.78J(J+1)}{T_{\text{ex}}(v)}\right] dv}{1 - \exp\left[-h\nu_0/kT_{\text{ex}}(v)\right]}. \quad (3.15)$$

In observational studies, the information required to calculate the excitation temperature at every rotational level J is not always accessible. It is frequently assumed that kT_{ex} is large compared to the separation of energy levels ($kT_{\text{ex}} \gg hB_e$). Therefore, the summation in Eq. 3.14 is $\Omega \approx kT_{\text{ex}}/hB_e$. In this case, we can express the total column CO density as

$$N_{\text{CO,total}} \approx \frac{2.31 \times 10^{14} [\text{cm}^{-2}]/[\text{K}]}{(J+1)} \int \frac{\tau_v T_{\text{ex}}(v) \exp\left[\frac{2.78J(J+1)}{T_{\text{ex}}(v)}\right] dv}{1 - \exp\left[-h\nu_0/kT_{\text{ex}}(v)\right]}. \quad (3.16)$$

⁹<http://cccbdb.nist.gov/>

There are some caveats for applying the condition $kT_{\text{ex}} \gg hB_e$ at Eq. 3.16. For the minimum excitation temperature, $T_{\text{ex}} \approx T_{\text{bg}} = 2.7\text{K}$, kT_{ex} is very similar to hB_e , while for $T_{\text{ex}} = 12\text{K}$, $kT_{\text{ex}} \approx 4 \times hB_e$. The condition $kT_{\text{ex}} \gg hB_e$ is not fulfilled by the lowest values of the excitation temperature and the highest values barely satisfy it. In all calculations, Eq. 3.15 estimates $\sim 10\%$ more mass than Eq. 3.16 with $J=0$ in the worst case scenario. Eq. 3.15 results in higher CO column density estimates than the “true” CO column density particularly at $N_{\text{CO}} \lesssim 10^{14}\text{cm}^{-2}$, where $kT_{\text{ex}} \approx hB_e$. However, we will consider hereafter Eq. 3.16 instead of Eq. 3.15 because of the limitations usually faced in observational studies to estimate the partition function Ω (e.g. Pineda et al., 2008, Pineda et al., 2010; Roman-Duval et al., 2010).

In the two following Figures, the analysis is based on the CO column densities inferred from Eq. 3.16 by using the CO column density in the level $J=0$ and two different approaches for calculating the excitation temperature: T_{ex} (Eq. 3.4) and $T_{\text{ex,obs}}$ (Eq. 3.6). It is important to note that a major difference between Eqs. 3.16 and 3.11 – besides the coefficients of both integrals – is $T_{\text{ex}}(v)$ in the integrand of Eq. 3.16. Therefore, the physics behind Eq. 3.11 holds for Eq. 3.16 with T_{ex} playing a stronger role in determining the total CO column density. In Fig. 3.18a we plot the 2D mass-weighted PDF of the ratio of $N_{\text{CO}}^{\text{th,3D}}$ to N_{CO} as a function of N_{CO} . Most of the mass of the cloud presents a ratio $N_{\text{CO}}^{\text{th,3D}}/N_{\text{CO}}$ that lies below the one-to-one relation at every N_{CO} . The average $\langle N_{\text{CO}}^{\text{th,3D}}/N_{\text{CO}} \rangle$ (blue line) shows that at $N_{\text{CO}} \gtrsim 10^{17}\text{cm}^{-2}$, the ratio $N_{\text{CO}}^{\text{th,3D}}/N_{\text{CO}}$ has the highest deviation from the black line. This results also hold if the full partition function Ω (Eq. 3.14) is considered instead of the approximation $\Omega \approx kT_{\text{ex}}/hB_e$. The deviation is due to the low number of zones with $\tau \gtrsim 1$ at $N_{\text{CO}} \gtrsim 10^{16}\text{cm}^{-2}$. Averaged over all sight lines, $N_{\text{CO}}^{\text{th,3D}} = 0.52 N_{\text{CO}}$.

Fig. 3.18b shows the 2D mass-weighted PDF of the ratio of the estimated CO column density considering $T_{\text{ex,obs}}$ (Eq. 3.6) into Eq. 3.16 $N_{\text{CO}}^{\text{obs,3D}}$ to the “true” N_{CO} as a function of N_{CO} . The average ratio $\langle N_{\text{CO}}^{\text{obs,3D}}/N_{\text{CO}} \rangle$ in every N_{CO} bin is represented by the blue line. Similar to Fig. 3.18a, on average the ratio $N_{\text{CO}}^{\text{obs,3D}}/N_{\text{CO}}$ stays below the equality line showing that $N_{\text{CO}}^{\text{obs,3D}}$ underestimates the CO column density in every N_{CO} bin. At $N_{\text{CO}} \gtrsim 10^{15}\text{cm}^{-2}$, the average $\langle N_{\text{CO}}^{\text{obs,3D}}/N_{\text{CO}} \rangle$ approaches the black line. Given that most of the mass is located at $N_{\text{CO}} \gtrsim 10^{15}\text{cm}^{-2}$, these sight lines dominate the entire CO mass. In total, $N_{\text{CO}}^{\text{obs,3D}} = 0.93 N_{\text{CO}}$.

We now consider a uniform excitation temperature along the LoS in Eq. 3.16. Fig. 3.19a shows the 2D mass-weighted PDF of the ratio of the estimated total CO column density considering $T_{\text{ex}}^{\text{col}}$ (from Boltzmann equation and then projected along the LoS), $N_{\text{CO}}^{\text{th,2D}}$ to the total N_{CO} as function of

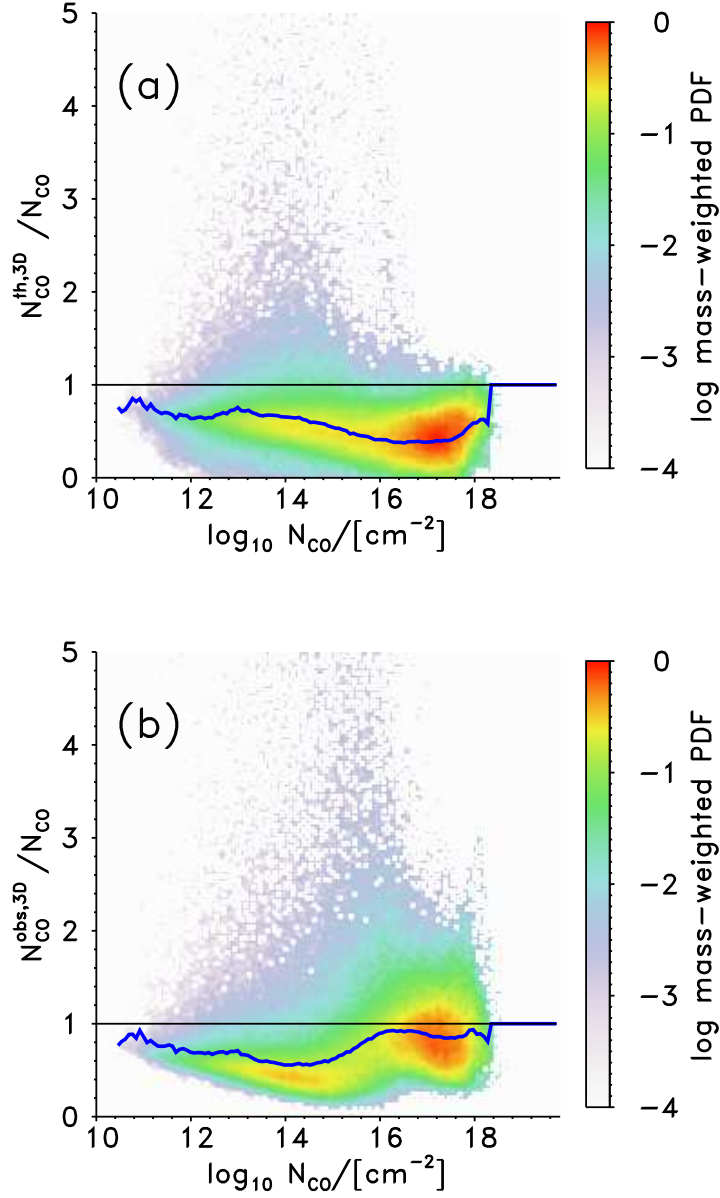


Figure 3.18: (a) Mass-weighted 2D PDF of the ratio of the estimated total CO column density using T_{ex} – Boltzmann equation, Eq. 3.4, $N_{\text{CO}}^{\text{th},3\text{D}}$ – to the true total CO column density N_{CO} , as function of the true N_{CO} . In total, $N_{\text{CO}}^{\text{th},3\text{D}} = 0.52 N_{\text{CO}}$. (b) Same as (a), but considering T_{ex} from Dickman (1978) Eq. 3.6 – $N_{\text{CO}}^{\text{obs},3\text{D}}$. In total $N_{\text{CO}}^{\text{obs},3\text{D}} = 0.93 N_{\text{CO}}$. The blue lines are set artificially to 1 at $N_{\text{CO}} > 10^{18} \text{ cm}^{-2}$ in order to avoid numerical noise. The rest of the lines are arranged in the same fashion as previous Figs.

N_{CO} . The average $\langle N_{\text{CO}}^{\text{th},2\text{D}}/N_{\text{CO}} \rangle$ in every N_{CO} bin (blue line) lies very close to the one-to-one relation. There is no clear dependence of the average ratio on CO column density. In total, $N_{\text{CO}}^{\text{th},2\text{D}}$ is 1.05 times N_{CO} . In comparison with Fig. 3.18a, $N_{\text{CO}}^{\text{th},2\text{D}}$ is ≈ 2 times $N_{\text{CO}}^{\text{th},3\text{D}}$. This is due to the distribution of $T_{\text{ex}}^{\text{col}}$ (Fig. 3.12d) which at $N \lesssim 10^{22} \text{ cm}^{-2}$ ($N_{\text{CO}} \lesssim 10^{16} \text{ cm}^{-2}$, Fig. 3.15) is very wide. 19% of the mass has $T_{\text{ex}}^{\text{col}} \geq 12 \text{ K}$, which contributes significantly to $N_{\text{CO}}^{\text{th},2\text{D}}$. On the other hand, only 10% of the mass lies at T_{ex} (see Fig. 3.9a), resulting in lower $N_{\text{CO}}^{\text{th},3\text{D}}$.

Similar to Fig. 3.19a, Fig. 3.19b shows the 2D mass-weighted PDF of the ratio of the estimated total CO column density considering $T_{\text{ex,obs}}^{\text{col}}$ (Eq. 3.7), $N_{\text{CO}}^{\text{obs},2\text{D}}$, to the total N_{CO} as function of N_{CO} . The average $\langle N_{\text{CO}}^{\text{obs},2\text{D}}/N_{\text{CO}} \rangle$ in every N_{CO} bin (blue line) exhibits the highest deviation from the one-to-one relation (black line). At $N_{\text{CO}} \lesssim 10^{15} \text{ cm}^{-2}$, the “true” N_{CO} is underestimated. At higher CO column densities, the average increases sharply, which results in $N_{\text{CO}}^{\text{obs},2\text{D}}$ overestimating N_{CO} . In total, $N_{\text{CO}}^{\text{obs},2\text{D}}$ is 1.35 times higher than N_{CO} . If we now compare Figs. 3.19b and 3.18b, the difference is again due to the projection of the excitation temperature. The distribution of $T_{\text{ex,obs}}$ is evidently different from $T_{\text{ex,obs}}^{\text{col}}$, which results in $N_{\text{CO}}^{\text{obs},3\text{D}} = 0.69 N_{\text{CO}}^{\text{obs},2\text{D}}$.

In our particular cloud model, the discrepancies between “true” and estimated (Eq. 3.16) CO column densities are $\lesssim 50\%$. In the case of considering a distribution of the excitation temperature in every velocity channel for estimating $N_{\text{CO}}^{\text{th},3\text{D}}$ (Fig. 3.18a), the true CO column density is underestimated by $\sim 48\%$. On the other hand, if $T_{\text{ex,obs}}$ (the Dickman approximation) is used in Eq. 3.16 (Fig. 3.18b), $N_{\text{CO}}^{\text{obs},3\text{D}}$ is overestimated by only $\sim 4\%$. In contrast, if a column excitation temperature is assumed to calculate $N_{\text{CO}}^{\text{th},2\text{D}}$ or $N_{\text{CO}}^{\text{obs},2\text{D}}$ (Figs. 3.19a and 3.19b, respectively) the CO column density is overestimated by values of up to 25%.

There are also differences among CO column density estimates if the Boltzmann Equation (Eq. 3.4) or the Dickman (1978) approximation is used for calculating the excitation temperature. Whether we choose the 3D excitation temperature distributions (T_{ex} , $T_{\text{ex,obs}}$), or use the projections ($T_{\text{ex}}^{\text{col}}$, $T_{\text{ex,obs}}^{\text{col}}$), the discrepancy is about 50%. In general, using the Dickman (1978) formulation produce higher estimates of the CO column density than considering Boltzmann Equation in all the cases.

Calculations of CO column densities using Eq. 3.16 provide a reasonable estimate of the true total CO column density. However, this approximation should not be taken as a proxy of the true total CO column density at $N_{\text{CO}} \lesssim 10^{15} \text{ cm}^{-2}$, where the gas is less likely to satisfy the condition $kT_{\text{ex}} \gg hB_e$. Considering Eq. 3.15 with the full partition function Ω , all the estimates of the CO column density increase by $\sim 10\%$ in comparison to Eq. 3.16.

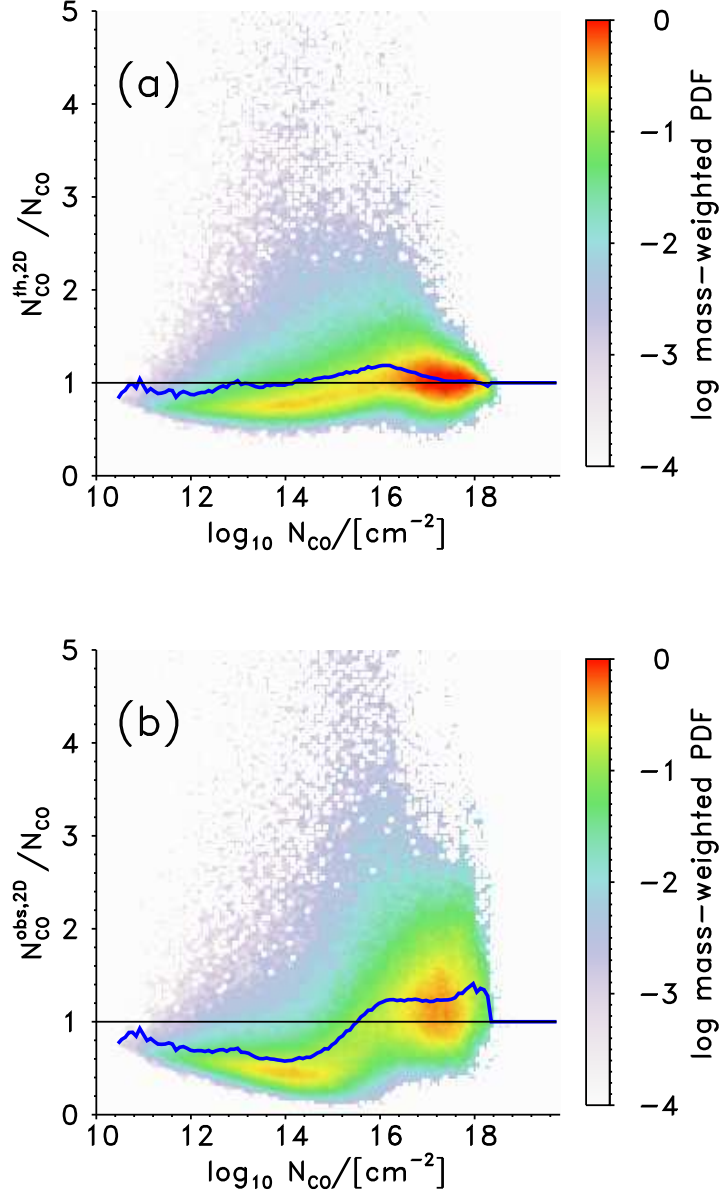


Figure 3.19: (a) Mass-weighted 2D PDF of the ratio of the estimated total CO column density using the column T_{ex} – Boltzmann equation, Eq. 3.4, projected as mass weighted average along the LoS $N_{\text{CO}}^{\text{th},2\text{D}}$ – to the true total CO column density N_{CO} , as function of the true N_{CO} . In total, $N_{\text{CO}}^{\text{th},2\text{D}} = 1.05 N_{\text{CO}}$. (b) Same as (a), but considering the column T_{ex} from Dickman (1978) Eq. 3.7 – $N_{\text{CO}}^{\text{obs},2\text{D}}$. In total $N_{\text{CO}}^{\text{obs},2\text{D}} = 1.35 N_{\text{CO}}$. The arrangement of lines is the same as previous Figs.

In particular, $N_{\text{CO}}^{\text{th},3\text{D}}$ and $N_{\text{CO}}^{\text{obs},3\text{D}}$ improves by 3%. This provides the best estimate, $N_{\text{CO}}^{\text{obs},3\text{D}} = 1.02 N_{\text{CO}}$.

3.5 Summary and conclusions

Using a high-resolution numerical model of a turbulent molecular cloud, we performed a detailed analysis of the kinetic temperature of the gas, as well as the brightness and excitation temperatures inferred from the CO ($J=1-0$) emission. We considered the standard LTE approximation of [Dickman \(1978\)](#) (Eqs. 3.6 and 3.7) in order to estimate the excitation temperature. We then compared these results with the excitation temperature calculated from Boltzmann's Equation (3.4). Finally with the aim of inferring the column density of CO in the $J=0$ level (Eq. 3.11) and the total CO column density (Eq. 3.16), we compared different methods for estimating the excitation temperature. We summarize our results as follow:

- In our cloud model, the abundance of CO increases towards high number densities, reaching the maximum $x_{\text{CO}} \approx 1.4 \times 10^{-4}$ in regions with $n \gtrsim 1000 \text{ cm}^{-3}$. As a result, we find that 95% of the CO mass is located at $n \gtrsim 400 \text{ cm}^{-3}$.
- The kinetic temperature decreases with increasing number density as $T_{\text{K}} \propto n^{-1/4}$ at $n < 10^5 \text{ cm}^{-3}$, with significant scatter around this relationship as described by [Glover and Clark \(2012b\)](#). 96% of the total mass has T_{K} ranging from 10 K to 90 K, and 95% of the mass of CO is located in regions with $T_{\text{K}} \lesssim 50 \text{ K}$.
- The column kinetic temperatures $T_{\text{K}}^{\text{col}}$ and $T_{\text{K}}^{\text{co-col}}$ decrease towards high column densities, in a similar fashion to their 3D counterpart (T_{K}). $T_{\text{K}}^{\text{col}}$ largely traces the temperature of regions along the LoS with $n \gtrsim 20 \text{ cm}^{-3}$, while $T_{\text{K}}^{\text{co-col}}$ traces only regions with $n \gtrsim 400 \text{ cm}^{-3}$. Therefore, $\langle T_{\text{K}}^{\text{col}} \rangle > \langle T_{\text{K}}^{\text{co-col}} \rangle$. For $T_{\text{K}}^{\text{co-col}}$, 93% of the gas mass lies along sight lines with $10 \text{ K} < T_{\text{K}}^{\text{co-col}} < 30 \text{ K}$, matching the standard values for molecular clouds.
- The commonly assumed relation $T_{\text{b}} \approx T_{\text{K}}$ for optically thick radiation is generally not valid in our cloud model. Emission with $T_{\text{b}} \geq 0.1 \text{ K}$ tends to come from optically thick gas. For $\tau > 1$, there is not a clear trend between T_{b} and T_{K} . On average, $\langle T_{\text{b}} \rangle \approx \text{constant}$ for $T_{\text{K}} \lesssim 16 \text{ K}$. At higher kinetic temperatures, $\langle T_{\text{b}} \rangle$ decreases towards high T_{K} . We therefore conclude that the gas is not in LTE and the radiation is not thermalized.

- The excitation temperature follows the CO abundance. T_{ex} increases with the number density, contrary to the behavior of T_{K} . On average, $\langle T_{\text{ex}} \rangle \lesssim \langle T_{\text{K}} \rangle$, indicating that the gas is mostly sub-thermally excited, although the scatter around those averages is significant. There are regions where T_{ex} and T_{K} overlap and may be in LTE. Establishing a criteria for testing the LTE condition in our simulation $T_{\text{ex}} = T_{\text{K}} \pm 0.05$, we found that only 0.05% of the cells fulfill it, which shows that the gas is mostly out of LTE. These cells are distributed along $n \gtrsim 1000 \text{ cm}^{-3}$, with a peak at $n \approx n_{\text{cr}} = 2200 \text{ cm}^{-3}$.
- The excitation temperature (T_{ex}) inferred from Boltzmanns Equation (3.4) have a different distribution than the “*observational*” estimate ($T_{\text{ex,obs}}$) calculated from the Dickman (1978) approximation (Eq. 3.6). On average at $n \lesssim 1500 \text{ cm}^{-3}$, $\langle T_{\text{ex,obs}} \rangle \gtrsim \langle T_{\text{ex}} \rangle$. Although in higher n , $\langle T_{\text{ex,obs}} \rangle < \langle T_{\text{ex}} \rangle$. Their difference increases towards high n , being $\sim 2 \text{ K}$ at $n = 5000 \text{ cm}^{-3}$.
- In some works, the excitation temperature is considered to be uniform along the LoS, and frequently calculated assuming the Dickman (1978) approximation given by Eq. 3.7. Comparing the results obtained from Eq. 3.7 ($T_{\text{ex,obs}}^{\text{col}}$) with those calculated with the Boltzmann equation (3.4, projected along the LoS: $T_{\text{ex}}^{\text{col}}$), we found that the averages $\langle T_{\text{ex,obs}}^{\text{col}} \rangle$ and $\langle T_{\text{ex}}^{\text{col}} \rangle$ increase towards high column densities. At $N \gtrsim 6 \times 10^{21} \text{ cm}^{-2}$, $\langle T_{\text{ex,obs}}^{\text{col}} \rangle$ is greater than $\langle T_{\text{ex}}^{\text{col}} \rangle$. The slope of $\langle T_{\text{ex,obs}}^{\text{col}} \rangle$ is steeper than the one for $\langle T_{\text{ex}}^{\text{col}} \rangle$, for $3 \times 10^{21} \lesssim N/[\text{cm}^{-2}] \lesssim 7 \times 10^{21}$. We conclude that Dickman (1978) formulation overestimates the excitation temperature at high column densities, because it is calculated by assuming only the peak of the emission. Although this situation changes for $N \lesssim 5 \times 10^{21} \text{ cm}^{-2}$, the emission is usually optically thin and the peak does not represent the total emission along the LoS, leading to $\langle T_{\text{ex,obs}}^{\text{col}} \rangle < \langle T_{\text{ex}}^{\text{col}} \rangle$.
- The critical column density is $N_{\text{cr}} \approx 5 \times 10^{21} \text{ cm}^{-2}$. So then $\langle T_{\text{ex}}^{\text{col}} \rangle$ is interpreted as a good guide to $\langle T_{\text{K}}^{\text{co-col}} \rangle$ for lines of sight with $N \gtrsim N_{\text{cr}}$.
- The estimates of $N_{\text{CO},J=0}$ (Eq. 3.11) and N_{CO} are different depending on the approach chosen to calculate the excitation temperature. In particular for $N_{\text{CO},J=0}$, $N_{\text{CO},J=0}^{\text{obs,3D}}$ (using $T_{\text{ex,obs}}$, from Dickman, 1978) estimates $N_{\text{CO},J=0}$ the best, which predicts 98% of the total CO mass at $J=0$. If T_{ex} (Boltzmann Eq. 3.4) is considered, $N_{\text{CO},J=0}^{\text{th,3D}}$ underestimates the “true” $N_{\text{CO},J=0}$ by 30%. This changes if the excitation temperature is assumed to be constant along the LoS in Eq. 3.11. Either $N_{\text{CO},J=0}^{\text{th,2D}}$

(using $T_{\text{ex}}^{\text{col}}$) or $N_{\text{CO},J=0}^{\text{obs},2\text{D}}$ (assuming $T_{\text{ex,obs}}^{\text{col}}$), the inferred $N_{\text{CO},J=0}$ is over-estimated by $\lesssim 15\%$.

- The uncertainties of the excitation temperature predictions affect N_{CO} (from Eq. 3.16) and $N_{\text{CO},J=0}$ (Eq. 3.11) similarly. In particular, the best results are given by $N_{\text{CO}}^{\text{obs},3\text{D}}$ (considering $T_{\text{ex,obs}}$), which estimates 93% of the true N_{CO} . $N_{\text{CO}}^{\text{obs},3\text{D}}$ is close to N_{CO} in every column density. If the full partition function Ω (Eq. 3.14) is inserted in Eq. 3.15, the estimates $N_{\text{CO}}^{\text{obs},3\text{D}}$ improves by $\sim 3\%$ in total, although with some deviation from the correspondence at $N_{\text{CO}} \lesssim 10^{16} \text{ cm}^{-2}$. If T_{ex} is assumed, $N_{\text{CO}}^{\text{th},3\text{D}}$ only predicts 52% of the total N_{CO} . On the other hand, assuming a constant excitation temperature along the LoS in Eq. 3.16, provides CO column density estimates which are $\lesssim 25\%$ higher than the “true” N_{CO} .
- Using the full PPV T_{b} spectrum for calculating $T_{\text{ex,obs}}(v)$ from Eq. 3.6 rather than assuming $T_{\text{b,max}}$ to infer $T_{\text{ex,obs}}^{\text{col}}$ (Eq. 3.7), improves the N_{CO} estimates by almost 30%.

It is noticeable that using $T_{\text{ex,obs}}$ or $T_{\text{ex,obs}}^{\text{col}}$ (Dickman, 1978) to estimate the CO($J=0$) and CO column densities produces values that are $\sim 30\%$ (using Eq. 3.11) and $\sim 40\%$ (with Eqs. 3.15 and 3.16) higher than considering the Boltzmann Equation. On the other hand, the full partition function Ω (Eq. 3.14) is considered in Eq. 3.15, the N_{CO} estimates are $\sim 10\%$ higher than their counterpart given by Eq. 3.16, regardless of the chosen excitation temperature approach.

The commonly used Eqs. 3.2, 3.3, 3.6 and 3.7 provide a misleading view of the temperatures in molecular clouds, because they assume that the radiation is thermalized and the gas in LTE. This results in differences among the excitation temperature estimates which are ~ 2 K on average. These differences affect the predictions of the CO column density in the level $J=0$ and the total CO column densities by up to $\sim 40\%$. In general, the CO ($J=1-0$) line is optically thick and the integrated emission distribution does not necessarily follow the true N_{CO} (Shetty et al., 2011a). Therefore, using the excitation temperature from this line in order to infer the true distribution of $N_{\text{CO},J=0}$, and N_{CO} , may be misleading in most molecular clouds.

Chapter 4

The H₂ mass

The molecular cloud structure is defined by the amount of H₂ that it contains. However, the lowest H₂ rotational transition at $\lambda = 28\mu\text{m}$ corresponds to a temperature $T \simeq 512$ K, which is well above the typical temperatures of molecular clouds ($T \simeq 10 - 30$ K) (Tielens, 2005; Wolfire et al., 2010; Draine, 2011). Therefore, the mass and distribution of H₂ has to be inferred from indirect methods, such as, measuring the amount of dust along the line of sight. In the ISM, the dust and gas are assumed to be well mixed (Bohlin et al., 1978). Therefore, one expects the gas mass to be proportional to the dust mass. It can be inferred by observing dust emission at infrared wavelengths (Leroy et al., 2011). Then, in order to deduce the molecular component, we assume that the gas is made up only from H₂, HI and He (the mass fraction of metals is $\sim 1\%$; Wilson et al., 2009), also assume a Galactic He abundance ($\sim 10\%$ by number, Carroll and Ostlie, 2006), and use HI observations in order to measure the amount of atomic gas along the line of sight (Bohlin et al., 1978).

Other methods implement the rotational emission lines of CO for inferring the amount of H₂, since the observed CO integrated intensity (W_{CO}) is believed to be proportional to the column density of H₂, N_{H_2} . In this sense, N_{H_2} can be easily estimated by multiplying W_{CO} by a CO-to-H₂ conversion factor X (e.g. Dickman, 1978)

$$N_{\text{H}_2} = XW_{\text{CO}}. \quad (4.1)$$

The X factor has been widely studied from observations of the CO ($J=1-0$) emission line and H₂ mass (estimated from dust) (e.g. Dickman, 1978; Pineda et al., 2008; Liszt et al., 2010; Draine, 2011; Pety et al., 2011; se also Bolatto et al., 2013 for a review). Another way of inferring this conversion factor is through the dynamics of molecular clouds. In a study based on ~ 50 molecular clouds in our Galaxy, Larson (1981) found that most of them are

gravitationally bound and in approximate virial equilibrium, and established that their velocity dispersion, size and luminosity are correlated. Later, [Solomon et al. \(1987\)](#) found a tight correlation between the CO luminosity L_{CO} and the virial mass of a cloud M_{vir} in a sample of a couple of hundred molecular clouds

$$M_{\text{vir}} \approx 39L_{\text{CO}}^{0.81} M_{\odot}, \quad (4.2)$$

where L_{CO} is expressed in units of K km s⁻¹ pc². Eq. 4.2 allows the definition of the X factor Eq. 4.1 ([Bolatto et al., 2008, 2013](#)). However, the determination of the X-factor by [Solomon et al. \(1987\)](#) assumed that there was no CO-free molecular gas, sometimes referred as “dark” molecular gas (see e.g. [Wolfire et al., 2010](#)), and that the molecular cloud consists mostly of H₂.

The X conversion factor seems to be constant for the Milky-Way, $X_{\text{MW}} \approx 2 \times 10^{20}$ cm⁻² K km s⁻¹ (e.g. [Solomon et al., 1987](#); [McKee and Ostriker, 2007](#); [Strong et al., 2007](#)). Although, there is evidence for an increase of this value with Galactocentric radius, which is related to galactic metallicity gradient ([Strong et al., 2007](#)) and can be explained from γ rays observations. γ rays are produced by the interaction between cosmic rays with the ISM, therefore, any variation in the relation between CO and H₂ may change the interpretation of their observations ([Strong et al., 2007](#)). Setting supernova remnants as the primary source of cosmic rays ([Ackermann et al., 2013](#)) in numerical models, the variations on the X factor can be explained independently together with the observations of γ rays ([Strong et al., 2004](#)).

Theorists and observers agree on a constant X factor in dense molecular gas, but this is not the case for the low density-diffuse/translucent medium ([Liszt et al., 2010](#); [Pety et al., 2011](#); [Shetty et al., 2011a,b](#)). There is also observational support for the idea that the X-factor changes depending on environmental conditions, e.g. in nearby galaxies ([Sandstrom et al., 2012](#)) and in ultraluminous infrared galaxies (ULIRGS) ([Solomon and Vanden Bout, 2005](#)).

In general, the physics behind the X factor is still not clear. Finding a relationship with environment is very important for understanding the role of the different mechanisms shaping the X-factor. It is specially useful for measurements of H₂ in external galaxies where CO observations are the only viable way of determining the amount of H₂ present. Here, we make an analysis of the CO column density N_{CO} (§4.1) and the CO ($J=1-0$) integrated emission W_{CO} (§4.2). We then study the role of N_{CO} and W_{CO} on shaping the X factor (§4.3). Finally, we estimate the mass of H₂ assuming a constant X-factor in order to compare them with the true H₂ mass. This simulation is the same used on the analysis in chapter 3. In summary, it has a resolution of

512³ cells, with typical Milky-Way cloud parameters: length size $L = 20$ pc, mean number density $n_0 = 100 \text{ cm}^{-3}$, $Z = Z_\odot$, and standard UV radiation field strength $UV=1 G_0$.

4.1 CO column density

The CO column density is sometimes considered to grow linearly with A_V (Pineda et al., 2010). Assuming that all the hydrogen is in molecular form that can be traced by the extinction, $N_{\text{H}_2}/A_V = 9.4 \times 10^{20} \text{ cm}^{-2} \text{ mag}^{-1}$ (Bohlin et al., 1978) and a constant CO-to-H₂ abundance ratio (Pineda et al., 2010), N_{CO} is

$$N_{\text{CO}} \approx 10^{17} A_V [\text{cm}^{-2}] [\text{mag}^{-1}], \quad (4.3)$$

or equivalently,

$$N_{\text{CO}} \approx 5.3 \times 10^{-5} N, \quad (4.4)$$

where N is the total column density.

Fig. 4.1 shows the mass-weighted 2D PDF of N_{CO} as a function of the column density N . The black line indicates the average of N_{CO} in every N bin. 42% of the mass lies along lines of sight with $N_{\text{CO}} \geq 10^{17} \text{ cm}^{-2}$, the value above which N_{CO} seems to increase towards high N in a linear fashion. However, the relation in Eq. 4.3 (blue line, with CO-to-H₂ abundance ratio of 1.1×10^{-4} , Pineda et al., 2010) does not predict the behavior of the PDF at any column density. The average (black line) shows that $\langle N_{\text{CO}} \rangle$ is not linear. The main reason is that our CO-to-H₂ abundance ratio is far from being constant. Rather, it changes by ~ 4 orders of magnitude (Fig. 4.3). At $N \gtrsim 10^{22} \text{ cm}^{-2}$ ($A_V \gtrsim 6 \text{ mag}$), the gas is well shielded and the CO abundance is approximately constant (CO-to-H₂ ratio $\approx 5 \times 10^{-5}$), therefore $\langle N_{\text{CO}} \rangle$ seems to increase linearly with N .

In our calculation, we are not considering freeze-out of CO. Therefore we follow an approximation for CO depletion for gas with high extinction ($A_V \geq 10 \text{ mag}$) (Pineda et al., 2010)

$$\frac{N_{\text{CO,gas+ice}}}{N_{\text{CO,gas}}} = 0.05 A_V + 0.88. \quad (4.5)$$

Fig. 4.2a shows the mass-weighted 2D PDF of $N_{\text{CO,gas+ice}}$ as a function of N . The black line depicts the average $\langle N_{\text{CO,gas+ice}} \rangle$ in every N bin. The correction on CO ices (Eq. 4.5) affects only a very small fraction of our data, although we apply it anyway in order to make consistent comparison with the study of Pineda et al. (2010) of the Taurus molecular cloud. In Fig. 4.2b

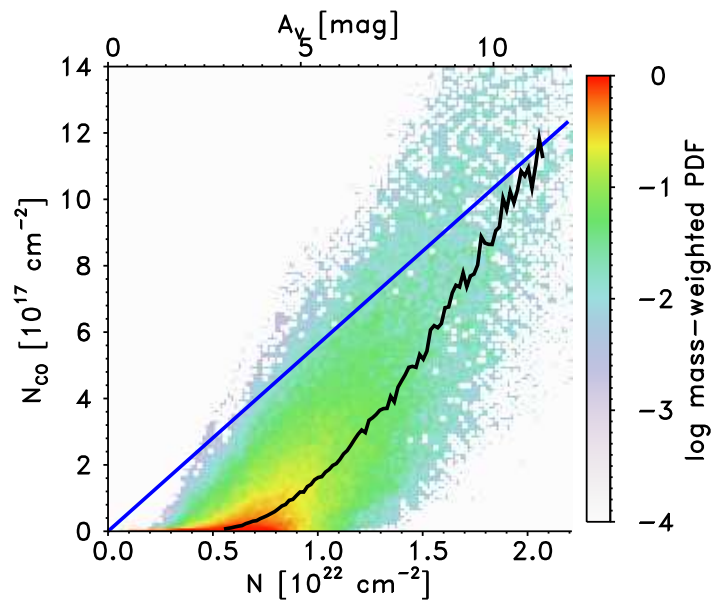


Figure 4.1: Mass-weighted 2D PDF of the CO column density N_{CO} as a function of N (bottom), and A_V as reference (top). The black line shows the average of N_{CO} as a function of N .

we show the Figure 6 of [Pineda et al. \(2010\)](#), in which they plot $N_{\text{CO,gas+ice}}$ as a function of A_V . The blue line represents Eq. 4.3 which is a good fit to their data. We obtain values of $N_{\text{CO,gas+ice}}$ that are consistent with [Pineda et al. \(2010\)](#)'s measurements. However our PDF seems quite different, which may be because we estimate the column of CO differently. To be consistent, in Fig. 4.2a, we show the average of the estimated CO column density from the CO ($J=1-0$) emission ($N_{\text{CO,gas+ice}}^{2\text{D,obs}}$, magenta line) calculated for every N bin (chapter 3) and corrected to account for CO freeze-out (Eq. 4.5). This is the method used by [Pineda et al. \(2010\)](#) and it is the most common in observational studies¹. We see that $\langle N_{\text{CO,gas+ice}}^{2\text{D,obs}} \rangle$ overestimates the true $\langle N_{\text{CO,gas+ice}} \rangle$ at all column densities, also the CO column density estimates of [Pineda et al. \(2010\)](#) (Fig. 4.2b). Our averages $\langle N_{\text{CO,gas+ice}} \rangle$ and $N_{\text{CO,gas+ice}}^{2\text{D,obs}}$ are much steeper than the blue line (Eq. 4.3).

Eq. 4.3 fits well [Pineda et al. \(2010\)](#) Figure. However to derive this equation, it was considered a constant CO-to- H_2 ratio. This is not consistent with observations of many molecular clouds, where it is known that CO and H_2 do not have the same distribution (e.g. [Langer et al., 1989](#); [Liszt et al., 2010](#); [Wolfire et al., 2010](#)). Besides, our simulations are not subject to self gravity, we therefore are not accounting for any dense cold cores with $A_V \gg 10$ mag, where CO may be frozen out. Including gravity would may be make Fig. 4.2b consistent with [Pineda et al. \(2010\)](#)'s result.

In Fig. 4.3, we plot the mass-weighted 2D PDF of the $N_{\text{H}_2\text{-to-}N_{\text{CO}}}$ ratio² as a function of N . The black line shows the average $\langle N_{\text{H}_2}/N_{\text{CO}} \rangle$ in every N bin. At $N \lesssim 7 \times 10^{21} \text{ cm}^{-2}$, the $N_{\text{H}_2\text{-to-}N_{\text{CO}}}$ ratio decreases as one looks to high N , the slope of the average is $\sim 10^{-4}$. In this regime, the molecular gas is translucent and therefore the CO molecules are easily photodissociated. For $N \gtrsim 7 \times 10^{21} \text{ cm}^{-2}$ ($A_V \gtrsim 4$ mag), the gas becomes optically thick and is well shielded, most of the carbon is locked up into CO molecules. Hence, the $N_{\text{H}_2\text{-to-}N_{\text{CO}}}$ ratio reaches an approximately constant value $\sim \langle N_{\text{H}_2}/N_{\text{CO}} \rangle \approx 1.4 \times 10^4$.

¹In this method one assumes that the gas is in LTE and the excitation temperature $T_{\text{ex,obs}}^{\text{col}}$ is uniform along the line of sight and can be calculated with Equation 3.7 from [Dickman \(1978\)](#) (e.g. [Liszt and Lucas, 1998](#); [Pineda et al., 2008](#); [Goldsmith et al., 2008](#); [Pineda et al., 2010](#)). One then uses Eq. 3.16 in order to estimate N_{CO} .

²We prefer to express the $N_{\text{H}_2\text{-to-}N_{\text{CO}}}$ ratio in this form, because it will be useful later for explaining the dependence of the X-factor on A_V .

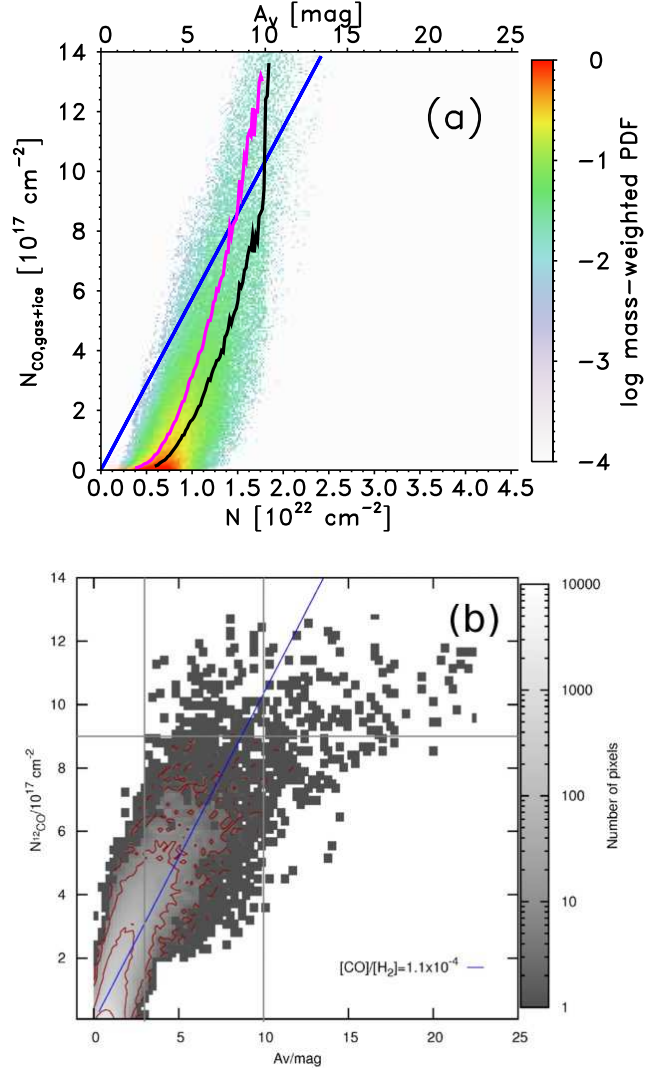


Figure 4.2: (a) Mass-weighted 2D PDF of the CO column density N_{CO} as a function of N (bottom), and A_V as reference (top). The black line shows the average of N_{CO} in every N bin. The red line shows the linear regression $\langle N_{\text{CO}} \rangle \approx 10^{-4}N - 9.5 \times 10^{17}$ made for $N \geq 10^{22} \text{ cm}^{-2}$. The blue line shows the average of $N_{\text{CO}}^{2\text{D,obs}}$ (Eq. 3.16) in every N bin (calculated considering that the excitation temperature is uniform along the line of sight, which in turn is estimated using Dickman (1978) formula $T_{\text{ex,obs}}^{\text{col}}$). (b) Figure 6 from Pineda et al. (2010): $N_{\text{CO,gas+ice}}$ derived from ^{13}CO and ^{12}CO observations in Taurus. The dark blue line represents $N_{\text{CO,gas+ice}}$ derived from A_V assuming Eq. 4.3 (Bohlin et al. 1978) and a CO-to-H₂ abundance ratio of 1.1×10^{-4} . The gray scale represents the number of pixels of a given value in the parameter space and is logarithmic in the number of pixels. The red contours are 2, 10, 100, and 1000 pixels. Each pixel has a size of $100''$ or 0.07 pc at a distance of 140 pc.

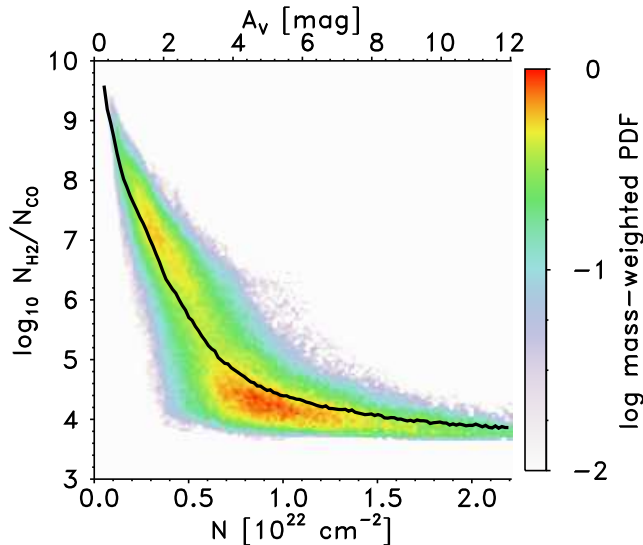


Figure 4.3: Mass-weighted 2D PDF of the N_{H_2} -to- N_{CO} ratio as a function of N (bottom), and A_V as reference (top). The black line shows the average of N_{CO} in every N bin.

4.2 CO ($J=1-0$) integrated intensity

CO ($J=1-0$) line emission is one of the most observed and useful tools for inferring molecular abundances, masses of galaxies, star formation histories, molecular masses, etc (White, 1997). Here, we focus on studying the integrated CO ($J=1-0$) along the line of sight W_{CO} as a H_2 mass estimator. It is defined (e.g. Wilson et al., 2009)

$$W_{\text{CO}} = \int T_{\text{b}}(\nu) d\nu \text{ [K km s}^{-1}\text{]}, \quad (4.6)$$

where T_{b} is the brightness temperature which is related to the CO ($J=1-0$) intensity through the Rayleigh Jeans approximation (§1.4.4). ν is the velocity along the line of sight (it is related to the frequency ν by $v = (1 - \nu/\nu_0)c$, where ν_0 is the peak of the line 115.3 GHz) and it is expressed in km s^{-1} . W_{CO} is calculated along all positions (x, y) , yielding a 2D map.

Fig. 4.4 shows the mass-weighted 2D PDF of W_{CO} as a function of N . The white line shows the average of W_{CO} for every column density bin. W_{CO} increases towards high N which is not surprising given the N_{CO} distribution seen in Fig. 4.1. In Fig. 4.4 the peak of the PDF ($W_{\text{CO}} \leq 2 \text{ K km s}^{-1}$) contains only 25% of the mass. Looking to the average, the cyan line shallows

at $N \gtrsim 8 \times 10^{21} \text{ cm}^{-2}$ in comparison with the average $\langle N_{\text{CO}} \rangle$ (Fig. 4.1, black line). This occurs because CO ($J=1-0$) is an optically thick line and the PDF of W_{CO} does not follow the PDF of N_{CO} (Shetty et al., 2011a). In Fig. 4.5 we show the mass-weighted 2D PDF of the W_{CO} -to- N_{CO} ratio as a function of N . The cyan line is the average of this ratio in every N bin. Here, it is clear that $W_{\text{CO}}/N_{\text{CO}}$ is approximately constant $\approx 10^{15} \text{ K km s}^{-1} \text{ cm}^{-2}$ at $N \lesssim 7 \times 10^{21} \text{ cm}^{-2}$ (this value is also found in observational and numerical studies, Liszt et al., 2010; Shetty et al., 2011b). At $7 \times 10^{21} \lesssim N/[\text{cm}^{-2}] \lesssim 8 \times 10^{21}$, $W_{\text{CO}}/N_{\text{CO}}$ grows sharply by approximately one order of magnitude, and at higher column densities, the average shows that this ratio grows with a shallower slope towards high N . The average $\langle W_{\text{CO}}/N_{\text{CO}} \rangle^3$ in every N bin (or equivalently, in A_V^4 bin) can be then approximated by

$$\left\langle \frac{N_{\text{CO}}}{W_{\text{CO}}} \right\rangle [\text{cm}^{-2} \text{ K}^{-1} \text{ km}^{-1} \text{ s}] \approx \begin{cases} 10^{15} & A_V < 4.25 \text{ mag} \\ 1.85 \times 10^{14} \langle A_V / [\text{mag}] \rangle^{2.15} & A_V > 4.25 \text{ mag.} \end{cases} \quad (4.7)$$

In Fig. 4.4, we also make a numerical fit to the average $\langle W_{\text{CO}} \rangle$ (white line) as a function of A_V . The cyan line shows the function found to best fit $\langle W_{\text{CO}} \rangle$

$$\langle W_{\text{CO}} \rangle \approx 12.14 \sqrt{\ln(1 + 8 \times 10^{-5} \langle A_V \rangle^{7.9})} [\text{K km s}^{-1}]. \quad (4.8)$$

The choice of the function is arbitrary, because we guess it by eye. More standard fitting techniques, like polynomial, least squares, or exponential fits were not successful. On the other hand, we choose the approach of (Pineda et al., 2008) to fit W_{CO} in the Perseus molecular cloud complex. They assumed that W_{CO} and T_b behave in the same fashion, and therefore approximate the radiative transfer equation $T_b = T_0(1 - e^{-\tau})$ (Eq. 1.55) as

$$\langle W_{\text{CO}} \rangle = W_0 [1 - e^{-k(\langle A_V \rangle - A_{V,0})}] [\text{K km s}^{-1}], \quad (4.9)$$

where W_0 is the integrated intensity at saturation, $A_{V,0}$ is the minimum extinction needed to get CO ($J=1-0$) emission, and k is the conversion factor between the amount of extinction and the optical depth. This curve is represented by the grey line in Fig. 4.4, with the fitting parameters: $W_0 = 56.7 \text{ K km s}^{-1}$, $k = 0.11 \text{ mag}^{-1}$, $A_{V,0} = 1.01 \text{ mag}$. In Fig. 4.4b, we show the W_{CO} vs. A_V plots of Pineda et al. (2008) (their Fig. 6). These authors study the

³Angle brackets indicate that the fitting is made over the averages in every column density bin.

⁴We chose A_V to make it more useful for comparisons with observations. It can be easily converted to N using the relation given in Eq. 1.4.8

Perseus complex separated in 6 components in order to avoid region-to-region variations in their analysis which are labeled as “*B5*” (green), “*IC348*” (magenta), “*Shell*” (cyan), “*B1*” (orange), “*NGC1333*” (blue) and “*WestEnd*” (red). Their selection criteria is based on the local standard of rest (LSR) velocity⁵ of different sections of the cloud (Fig. 4.6). The PDF in Fig. 4.4a is close to the W_{CO} distribution shown for all the regions in Pineda et al. (2008) (Fig. 4.4b, left). The solid lines in Fig. 4.4b (right) shows the fit Eq. 4.9 to the individual regions, with high dispersion on the data. We find that the average fitting parameters for the whole molecular cloud complex $W_0 = 42.29 \text{ K km s}^{-1}$, $k = 0.63 \text{ mag}^{-1}$, $A_{V,0} = 0.58 \text{ mag}$ (Fig. 4.4b, left) are in reasonably agreement with our data.

4.3 The X factor

We can also write the CO-to-H₂ conversion factor (Eq. 4.1) as

$$X = \left(\frac{N_{\text{CO}}}{W_{\text{CO}}} \right) \left(\frac{N_{\text{H}_2}}{N_{\text{CO}}} \right). \quad (4.10)$$

From this point of view, the X depends on 1) the H₂-to-CO column density ratio (Fig. 4.3) and 2) the ratio $N_{\text{CO}}/W_{\text{CO}}$ (Fig. 4.5). Fig. 4.7 shows the mass-weighted 2D PDF of the X-factor as a function of N . The white line shows the average of the X-factor calculated in every N bin. The N_{H_2} -to- N_{CO} ratio (Fig. 4.3) is the stronger parameter on determining the X-factor, especially at $N \lesssim 7 \times 10^{21} \text{ cm}^{-2}$ because the ratio $N_{\text{CO}}/W_{\text{CO}}$ is approximately constant in this regime. At $N \gtrsim 7 \times 10^{21} \text{ cm}^{-2}$, the ratio $N_{\text{CO}}/W_{\text{CO}}$ is close to saturation, therefore it makes the X-factor increase by less than one order of magnitude.

Our global average is $\langle X_{\text{tot}} \rangle \approx 2.1 \times 10^{20} \text{ cm}^{-2} \text{ K}^{-1} \text{ km}^{-1} \text{ s}$, which matches the canonical Milky-Way value. However, our estimate of the X-factor at $N < 10^{22} \text{ cm}^{-2}$ is $X \sim 10^{20-24} \text{ cm}^{-2} \text{ K}^{-1} \text{ km}^{-1} \text{ s}$, which is significantly higher than the one reported in observations (Liszt et al., 2010; Lee et al., 2013). In Fig. 4.7, we over-plot a fit to the average $\langle X \rangle$ shown by the dashed cyan line. We separated $\langle X \rangle$ in two segments, one at $N \lesssim 8 \times 10^{21} \text{ cm}^{-2}$ ($A_V \lesssim 4.25 \text{ mag}$), the other is at column densities above that value. The fit is

⁵This is defined as the velocity of a point at a given position in the Galactic plane which follows a circular orbit around the Galactic center with components $(\Pi, \Theta, \Gamma)_{\text{LRS}} = (0, \Theta_0, 0)$. Θ_0 is the characteristic circular velocity of the objects which depends on the Galactic radius (Mihalas and Binney, 1981)

$$\langle X \rangle [\text{cm}^{-2} \text{K}^{-1} \text{km}^{-1} \text{s}] \approx \begin{cases} 9.7 \times 10^{19} \langle A_V / [\text{mag}] \rangle^{0.37} & A_V \geq 4.25 \text{ mag} \\ 3.26 \times 10^{22} \langle A_V / [\text{mag}] \rangle^{-3.73} & A_V < 4.25 \text{ mag}. \end{cases} \quad (4.11)$$

At $A_V \geq 4.25$, the slope in the X-factor is very shallow and this segment can be approximated by the average $\langle X \rangle = 2.1 \times 10^{20} \text{ cm}^{-2} \text{ K}^{-1} \text{ km}^{-1} \text{ s}$ (red line).

[Liszt et al. \(2010\)](#) present an extensive study of diffuse and dense molecular gas in the Milky-Way. They obtain $X \approx 3 \times 10^{20} \text{ cm}^{-2} \text{ K}^{-1} \text{ km}^{-1} \text{ s}$ independent of the environmental conditions. In diffuse/translucent⁶ gas, they reported a CO abundance N_{CO}/N which is ~ 4 orders of magnitude higher than ours (see also [Shetty et al., 2011b](#)). Moreover, their measurements of the abundances of OH and HCO⁺ (important species present in some channels of CO formation) are also higher than ours by about 2-3 orders of magnitude. [Lee et al. \(2013\)](#) also measure low values of the X-factor, based in a study of the Perseus molecular cloud complex. They report values of the order $\sim 10^{19-21} \text{ cm}^{-2} \text{ K}^{-1} \text{ km}^{-1} \text{ s}$.

In order to explain a constant X-factor in these diffuse regions, it is necessary to have a N_{CO} -to- N ratio approximately 4 orders of magnitude higher than our current value. One possible explanation for this discrepancy is missing physics, i.e. physical processes that are still not included in our code. These include turbulent mixing of material (e.g. [Falgarone and Phillips, 1990](#); [Falgarone and Puget, 1995](#); [D camp and Le Bourlot, 2002](#); [Falgarone et al., 2005](#); [Glover et al., 2010](#)), C-shocks, or for example, [Shetty et al. \(2011b\)](#) explored different v_{rms} in their models, and found that the X-factor decreases when the v_{rms} increases. On the side of the chemical network, [Glover and Clark \(2012a\)](#) make a detailed analysis considering simpler and more complex chemical networks than ours. However, the CO abundance in their models changes by less than one order of magnitude.

It seems that there is still a long way to go to bring our model and observational measurements of the X-factor in diffuse/translucent gas into agreement. However, in dense gas, our average X-factor agrees very well with the canonical Milky-Way value. In the next section, we calculate the amount of molecular mass that are missed by applying a constant Milky Way X-factor to our W_{CO} map.

⁶Following [Draine \(2011\)](#), the molecular diffuse gas is defined by having $A_V \lesssim 1$ mag, while the translucent gas has $1 \lesssim A_V/\text{mag} \lesssim 5$. However in [Liszt et al. \(2010\)](#), they consider that the molecular gas is diffuse for A_V up to ~ 4 mag. We therefore define the gas as diffuse/translucent for lines of sight with $A_V \lesssim 4$ mag, see Table 1.3.

4.4 H₂ column density estimate

Fig. 4.8a illustrates N_{H_2} , projected along the z -axis of the simulation volume. In Fig. 4.8b, we show a map of the H₂ column density $N_{\text{H}_2,\text{est}}$ inferred from W_{CO} (Eq. 4.1) assuming a constant X_{MW} . Both maps show similar morphology: the gas has a filamentary structure, and there are spatial variations in the column densities which are larger in Fig. 4.8b than in Fig. 4.8a. In general, the gas appears to have a prominent over-dense region visible towards the top-right of the figure, and an under-dense region visible near the center-left of the image, which is particularly notable in Fig. 4.8b. The ratio $N_{\text{H}_2,\text{est}}/N_{\text{H}_2}$ is shown in Fig. 4.8c, where $N_{\text{H}_2,\text{est}}/N_{\text{H}_2} \approx 1$ towards the prominent over-dense zones. The biggest discrepancies between $N_{\text{H}_2,\text{est}}$ and N_{H_2} are in the less dense lines of sight. The under-dense region is mostly composed of lines of sight with $A_V \lesssim 3.5$, where CO is not shielded enough and can be easily photodissociated (e.g. van Dishoeck and Black, 1988; Visser et al., 2009; Glover and Mac Low, 2011).

In order to quantify the difference between the estimated and the true H₂ column densities, we plot the mass-weighted 2D PDF of $N_{\text{H}_2,\text{est}}$ as a function of N_{H_2} in Fig. 4.9. The yellow line indicates the correspondence $N_{\text{H}_2,\text{est}} = N_{\text{H}_2}$. Only 10% of the mass is located below $N_{\text{H}_2} \lesssim 10^{21} \text{ cm}^{-2}$, where the emission comes mostly from optically thin gas. In this regime, most of the lines of sight have $N_{\text{H}_2,\text{est}} < N_{\text{H}_2}$. For the rest of the cloud, 75% of the mass is distributed along lines of sight with $21 \lesssim \log_{10} N_{\text{H}_2}/[\text{cm}^{-2}] \lesssim 21.5$, for which the majority has $N_{\text{H}_2,\text{est}} \approx N_{\text{H}_2}$, and a significant fraction ($\sim 20\%$) is distributed along optically thin lines. Only 15% of the mass is distributed at $\log_{10} N_{\text{H}_2}/[\text{cm}^{-2}] \gtrsim 21.5$, Here the emission is optically thick and traces an important amount of the H₂ mass, hence $N_{\text{H}_2,\text{est}} \approx N_{\text{H}_2}$.

In Fig. 4.9, we show the average $\langle N_{\text{H}_2,\text{est}} \rangle$ in every N_{H_2} bin and make a linear regression over this average in the logarithmic space (red line) at $N_{\text{H}_2} < 2 \times 10^{21} \text{ cm}^{-2}$. The slope between $\langle N_{\text{H}_2,\text{est}} \rangle$ and N_{H_2} is very steep (~ 5), in linear space it can be approximated by

$$\langle N_{\text{H}_2,\text{est}} \rangle \approx \begin{cases} \langle N_{\text{H}_2} \rangle & N_{\text{H}_2} \geq 2 \times 10^{21} [\text{cm}^{-2}] \\ 4.27 \times 10^{-82} \langle N_{\text{H}_2} \rangle^{4.81} [\text{cm}^{-2}] & N_{\text{H}_2} < 2 \times 10^{21} [\text{cm}^{-2}] \end{cases} \quad (4.12)$$

Fig. 4.10 shows the fraction of H₂ gas missed by assuming a fixed X_{MW} -factor. First calculate the mass of H₂ is calculated below a given N as a function of N , then it is normalized it by the total true H₂ mass. The true H₂ mass is represented by the solid line and the estimated one by the dotted line. We find that $N_{\text{H}_2,\text{est}}$ underestimates the true H₂ mass at all column densities. In total, $N_{\text{H}_2,\text{est}}$ predicts about 85% of the H₂ mass.

In general, the fraction of H₂ mass lost by assuming a constant X_{MW}-factor can be determined considering that

$$\frac{N_{\text{H2,est}}}{N_{\text{H2}}} = \frac{X_{\text{MW}}}{X}. \quad (4.13)$$

We then use Eq. 4.11 to obtain:

$$\left\langle \frac{N_{\text{H2,est}}}{N_{\text{H2}}} \right\rangle \approx \begin{cases} 1 & A_V \geq 4.25 \text{ mag} \\ 6.14 \times 10^{-3} \langle A_V / [\text{mag}] \rangle^{3.73} & A_V < 4.25 \text{ mag} \end{cases} \quad (4.14)$$

Given that our X and X_{MW} factors are very similar at $A_V \gtrsim 4.25$, we can approximate $N_{\text{H2,est}} \approx N_{\text{H2}}$. At this regime, our calculation is in agreement with observational and theoretical evidence, in which $X \approx X_{\text{MW}}$ for dense molecular gas with approximately solar metallicity (e.g. Dickman, 1978; Pineda et al., 2008; Liszt et al., 2010; Draine, 2011; Pety et al., 2011).

4.5 Summary and Conclusions

In this chapter, we analyzed the CO column density and the CO ($J=1-0$) integrated emission along the line of sight, in order to study the physics behind the X-factor in an individual simulation considered as a fiducial model for the Milky-Way. Considering the W_{CO} map and a single fixed conversion factor for the Milky-Way $X_{\text{MW}} = 2 \times 10^{20} \text{ cm}^{-2} \text{ K}^{-1} \text{ km}^{-1} \text{ s}$, the H₂ mass was calculated. The main results are summarized as follow:

- In general, our N_{CO} ranges for values which are consistent with those obtained by Pineda et al. (2010). However, a more detailed comparison shows that both distribution have different shapes. Ours increases sharply towards high A_V , while Pineda et al. (2010)s result grows slower at high A_V .
- The ratio $N_{\text{H2}}/N_{\text{CO}}$ is not constant. It varies by ~ 4 orders of magnitude at $N \lesssim 10^{22} \text{ cm}^{-2}$. It becomes approximately constant towards higher N .
- W_{CO} increases towards high N in a similar fashion than Pineda et al. (2008) results. The ratio $N_{\text{CO}}/W_{\text{CO}}$ is roughly constant at $N \lesssim 7 \times 10^{21} \text{ cm}^{-2}$. It then increases sharply in a narrow window $7 \times 10^{21} \lesssim N / [\text{cm}^{-2}] \lesssim 8 \times 10^{21}$. At higher N , $N_{\text{CO}}/W_{\text{CO}}$ increases slowly because the CO ($J=1-0$) emission line becomes saturated.

- The X-factor exhibits a behavior represented by two “slopes” (in logarithmic space). At $N \lesssim 10^{22} \text{ cm}^{-2}$, it increases sharply by ~ 4 orders of magnitude towards lower column densities. For $N \gtrsim 10^{22} \text{ cm}^{-2}$, it is approximately constant. On average, $X_{\text{MW}} \approx \langle X_{\text{tot}} \rangle \approx 2.1 \times 10^{20} \text{ cm}^{-2} \text{ K}^{-1} \text{ km}^{-1} \text{ s}$.
- The total mass of H_2 is underestimated by $\sim 15\%$.

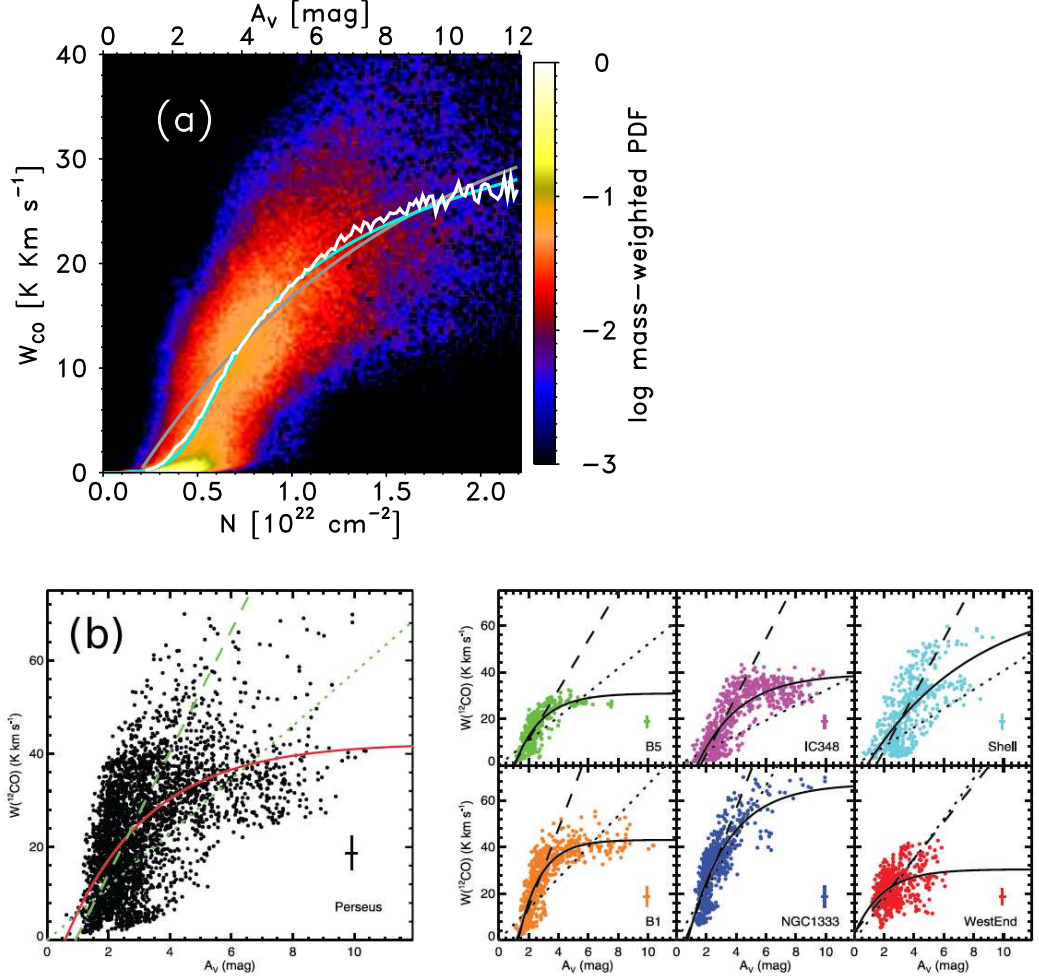


Figure 4.4: (a) Mass-weighted 2D PDF of the integrated CO ($J=1-0$) intensity W_{CO} as a function of N (bottom), and A_V as reference (top). The white line shows the average of W_{CO} in every N bin. The cyan line shows a numerical fit to the average (Eq. 4.8). The grey line shows a fit that follows the work of Pineda et al. (2008) (Eq. 4.9). (b) Figure 6 from Pineda et al. (2008): Left, Integrated intensity W_{CO} vs. A_V for the Perseus data. Right: W_{CO} vs. A_V of the individual regions (shown in Fig. 4.6) labeled as “B5” (green), “IC348” (magenta), “Shell” (cyan), “B1” (orange), “NGC1333” (blue) and “WestEnd” (red). Solid lines show the best fit of Eq. 4.9.

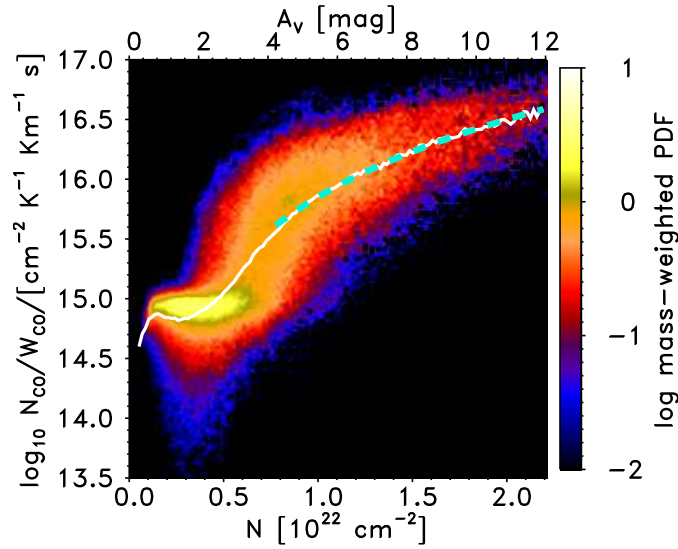


Figure 4.5: 2D mass-weighted PDF of the W_{CO} -to- N_{CO} ratio as a function of N (bottom), and A_V as reference (top). The cyan line shows the average of N_{CO} in every N bin.

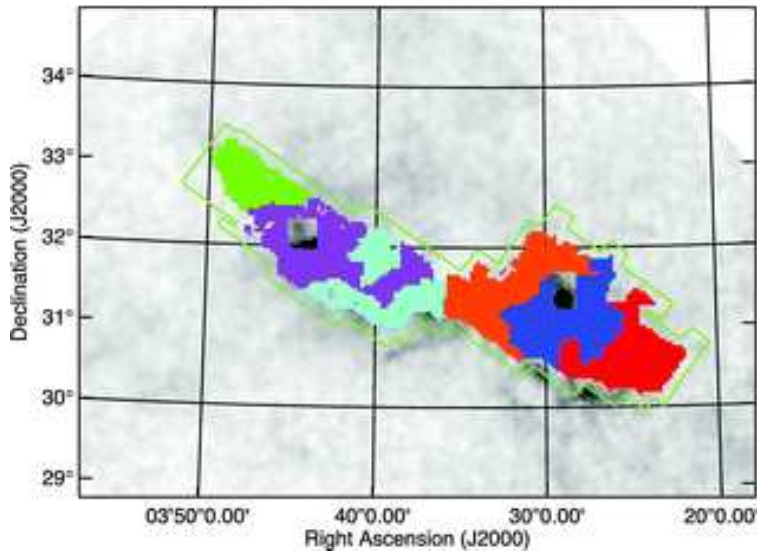


Figure 4.6: Extinction map of the Perseus molecular complex taken from [Pineda et al. \(2008\)](#) (their Fig. 3). Each of the defined regions are in a different color, “*B5*” (green), “*IC348*” (magenta), “*Shell*” (cyan), “*B1*” (orange), “*NGC1333*” (blue) and “*WestEnd*” (red).

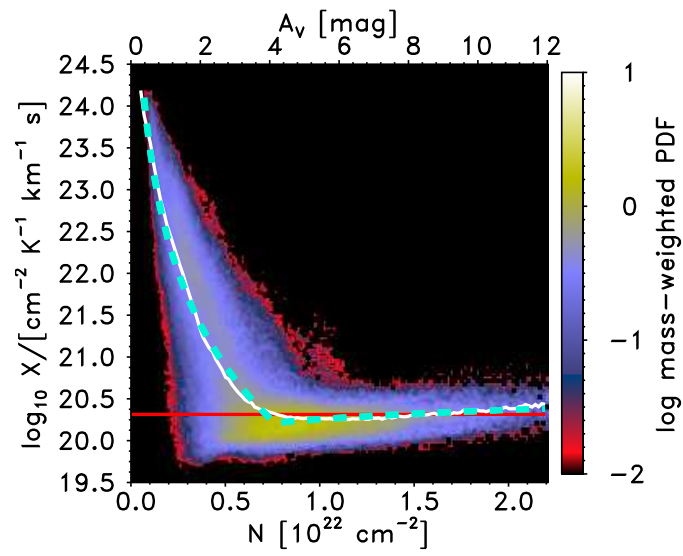


Figure 4.7: 2D mass weighted PDF of the CO-to-H₂ conversion factor X as a function of N (bottom), and A_V as reference (top). The white line shows the average of the X -factor in every N bin. The cyan dashed line shows a fit to the average.

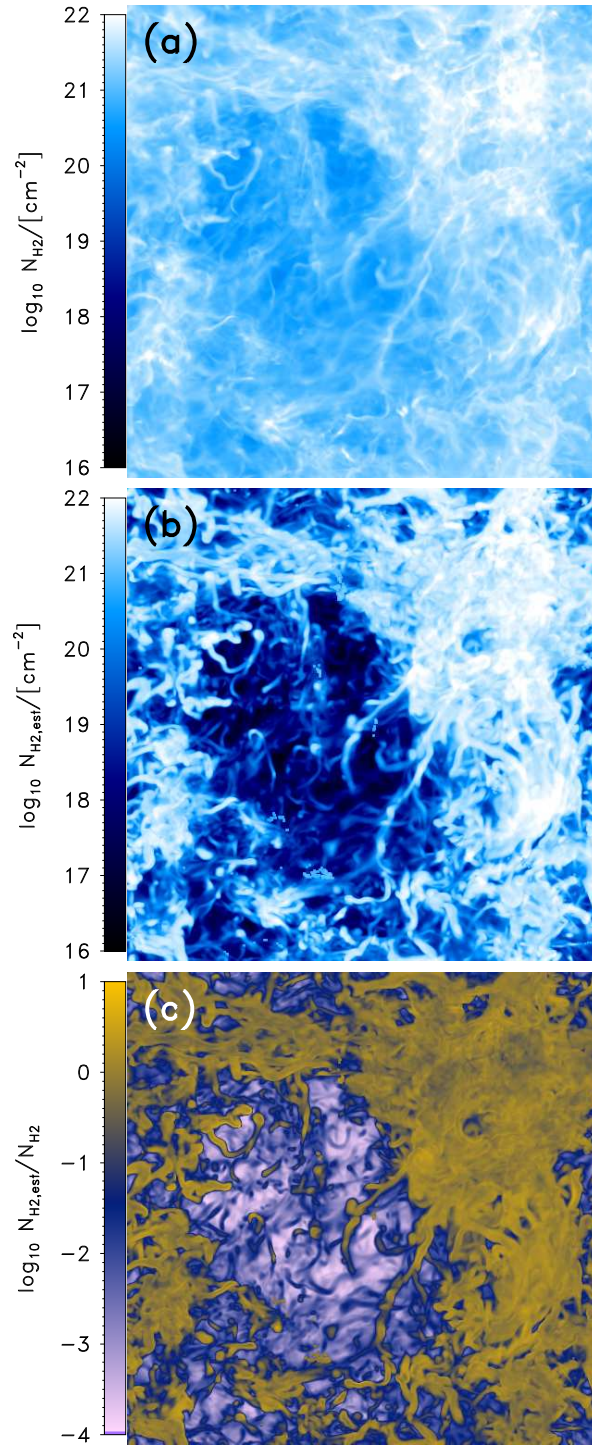


Figure 4.8: Images of: (a) the column density of H₂, N_{H_2} , viewed along a LoS parallel to the z -axis of the simulation volume. (b) As (a), but for the H₂ column density estimated from W_{CO} and considering a constant Milky-Way like $X = 2 \times 10^{20} \text{ cm}^{-2} \text{ K}^{-1} \text{ km}^{-1} \text{ s}$, $N_{\text{H}_2,\text{est}}$. (c) The $N_{\text{H}_2,\text{est}}$ -to- N_{H_2} ratio.

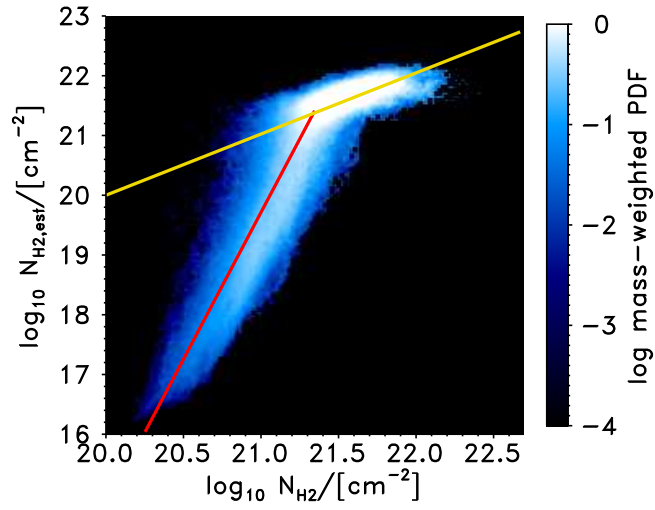


Figure 4.9: (a) Mass weighted 2D PDF of the estimated H_2 column density $N_{H_2,est}$ as a function of the true N_{H_2} . The yellow line shows the one-to-one relation. The red dashed line shows a fit of the average of $N_{H_2,est}$ in every true N_{H_2} bin, at $N_{H_2} \lesssim 2 \times 10^{21} \text{ cm}^{-2}$ where $N_{H_2,est} \approx 10^{-4} N_{H_2}$.

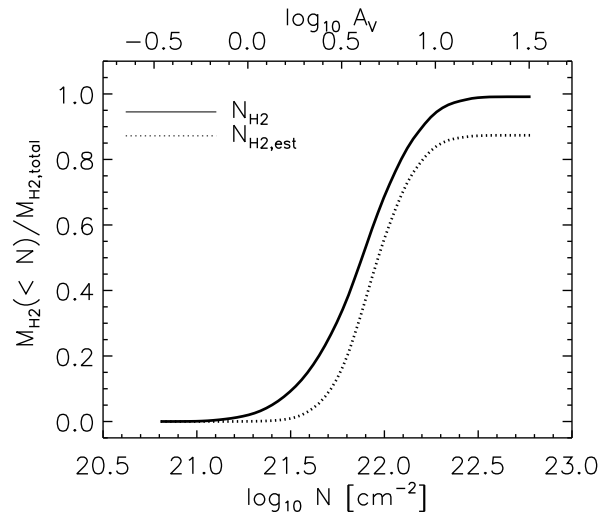


Figure 4.10: Cumulative mass of H_2 below a given column density as a function of N (A_V is plotted for reference at the top) normalized by the total true mass of H_2 . The solid line shows the true H_2 mass and the dotted line shows the H_2 mass estimated from the X-factor and W_{CO} .

Chapter 5

Statistics of the Temperatures, CO, and H₂ density distributions in simulated molecular clouds

Dense molecular clouds are the principal sites of star formation (e.g. [Reddish, 1975](#); [Shu et al., 1987](#); [Ward-Thompson et al., 2007](#)). The star formation process can be roughly explained considering the following simplification: in a gravitationally bound molecular cloud, turbulence produces the initial dense gas seeds necessary for star formation. The density distribution in the cloud is therefore not uniform, but its shape can be described by a lognormal function (§1.2.3 and §6). In places where the density is above a gravitational instability criteria (§1.2.6), the dense cores¹ may collapse to form protostellar cores, which are defined as starless cores bound by gravity. They are dense enough to accrete material from their surrounds ([Ward-Thompson et al., 2007](#)). During the accretion, a circumstellar disk forms due to angular momentum conservation ([Hartmann et al., 1998](#); [Schmeja and Klessen, 2004](#)). In addition, outflows and jets are discharged during this process, taking away part of the angular momentum from the innermost part of the disk ([Hartmann et al., 1998](#)). In this prestellar phase, the cores may break into smaller objects due to gravo-turbulent fragmentation ([Schmeja and Klessen, 2004](#); [Ward-Thompson et al., 2007](#)), in which the angular momentum is then transferred into the fragments ([Zinnecker, 2004](#)). If the radiative and dust cooling keeps the material cold, each fragment may collapse to form a rota-

¹[Ward-Thompson et al. \(2007\)](#) define a dense core as any region in molecular clouds which is relatively over-dense in comparison with its neighboring environment.

tionally supported disk, with a protostar at the center which is formed by the lowest specific angular momentum material (Draine, 2011). Depending on the initial mass, a protostar may become a star if it starts burning hydrogen at its center. In this simplified picture, we avoid the details of many different processes involved in star formation in which there are still many open questions, and in turn are seeds for different theories (e.g. Krumholz and McKee, 2005; Hennebelle and Chabrier, 2011; Padoan and Nordlund, 2011; Federrath and Klessen, 2012).

Observations are key for constraining those different model scenarios. It has been found that star formation depends on the local environment, i.e. the parent molecular cloud. Hence, some models may be relevant in different regions (Ward-Thompson et al., 2007). The effects of local density, thermal pressure, turbulence, magnetic field strength, and the presence of nearby stars, all play an important role in determining the evolution of the density fluctuations of dense molecular cloud cores (Ward-Thompson et al., 2007; Molina et al., 2012). It is therefore crucial to have an statistical analysis of simulated molecular clouds covering a wide range of environmental conditions in order to understand the physics behind the observational constraints. Conversely, this statistical analysis may help to test the approximations usually assumed in observational works.

In this chapter, we extend the analysis made in chapter 3 and chapter 4 to a large set of numerical simulations. They were performed using a fully dynamical 3D model of magnetized turbulence described in §2.1, in which we vary the mean number density (n_0), the metallicity (Z) and the incident UV radiation field strength (UV), described in table 5.1. Our aim here is to quantify the range of temperatures and densities present in the gas containing most of the CO in the clouds. Also, we want to quantify the role of CO emission on determining the H₂ and CO column densities considering commonly used observational methods.

Our choice of parameters results in average visual extinctions which cover a range from diffuse to dark molecular clouds². It is also important to mention, that the standard deviation in the extinction ranges from several tenths to several magnitudes, so most of the simulated clouds are not fully diffuse, translucent or dark. They are an ensemble of zones with number densities ranging from $10^{-3} \lesssim n/n_0 \lesssim 50$, which in turn results in lines of sight with A_V ranging from $0.1 \lesssim A_V/\langle A_V \rangle \lesssim 4$. In the particular case of the runs n30-Z01 (which has a maximum $A_V = 0.42$ mag) and n100-Z01 (in which only 4% of the gas mass has $A_V \geq 1$), they are composed almost entirely of diffuse gas.

²Our terminology here follows Draine (2011) (§1, Table 1.3)

Table 5.1: List of simulations.

	n_0 [cm ⁻³]	Z/Z_\odot	UV [G_0]	$\langle A_V \rangle$	\pm	σ_{A_V} [mag]
n300-Z01	300	0.1	1	1	\pm	0.7
n300-Z03	300	0.3	1	3	\pm	2
n300-Z06	300	0.6	1	6	\pm	4
n30	30	1.0	1	1	\pm	0.6
n100	100	1.0	1	3	\pm	2
n180	180	1.0	1	6	\pm	5
n300	300	1.0	1	10	\pm	7
n1000	1000	1.0	1	33	\pm	22
n30-Z01	30	0.1	1	0.1	\pm	0.06
n100-Z01	100	0.1	1	0.3	\pm	0.2
n1000-Z01	1000	0.1	1	3	\pm	2
UV0	300	1.0	0	10	\pm	7
UV10	300	1.0	10	10	\pm	7
UV100	300	1.0	100	10	\pm	7
UV1000	300	1.0	1000	10	\pm	7

n_0 – initial number density of hydrogen nuclei

Z/Z_\odot – metallicity

UV – ultra-violet radiation field strength expressed in the standard radiation field strength G_0 (Draine, 1978)

5.1 CO and number density distributions

Fig. 5.1a shows the cumulative gas mass normalized by the total gas mass of the cloud as a function of the number density. This plot then shows the fraction of gas mass below a given number density. All the simulations have $\sim 98\%$ of the mass at $n/n_0 \geq 0.1$, while $\sim 50\%$ of it is at $n/n_0 \geq 2$. On the other hand, the CO mass distribution does not follow that of the total gas mass. Fig. 5.1b shows the cumulative CO mass normalized by the total CO mass of the cloud as a function of n . All the simulations shows that most of the CO ($\gtrsim 95\%$) is distributed above $n \gtrsim 100 \text{ cm}^{-3}$ regardless of the mean number density, metallicity or UV radiation field strength. The density range containing most of the CO is a strong function of Z , which sets the initial carbon abundance, and control the amount of dust shielding, and the UV radiation field strength which sets the CO photodissociation rate. The curves in Fig. 5.1b becomes steeper and shift towards high n when Z decreases or the UV field strength is increased (panels b.1 and b.4). The CO distribution depends on the mean density in a weaker fashion, although in the case of the simulations n30-Z01 and n100-Z01 (orange and yellow lines in Fig. 5.1b.3), the gas is mostly diffuse and there is little CO that can survive photodissociation, given the low metallicity and mean density, which in turn causes that CO is mostly found at low densities. This also partially affects the simulation n30 which has an important diffuse component.

In order to make straightforward comparisons with observations, we might convert the volume quantities into “observables”, instead of making a full analysis of each of our simulations in the same fashion as the simulation studied in Chapters 3 and 4, because the later would be tedious and repetitive. We therefore decided to work with the averages of the individual clouds. We will use extended plots, like Figs. 5.1a and 5.1b, in some occasions. The averages and standard deviations are calculated as

$$\langle B \rangle = \sum_{i,j,k} B_{i,j,k} * weight_{i,j,k} \quad (5.1)$$

and

$$\sigma_B = \sqrt{\sum_{i,j,k} (B_{i,j,k}^2 - \langle B \rangle^2) * weight_{i,j,k}}, \quad (5.2)$$

where B is the physical quantity of our interest, and $weight_{i,j,k}$ is normalized such as

$$\frac{1}{Weight} \sum_{i,j,k} weight_{i,j,k} = 1.$$

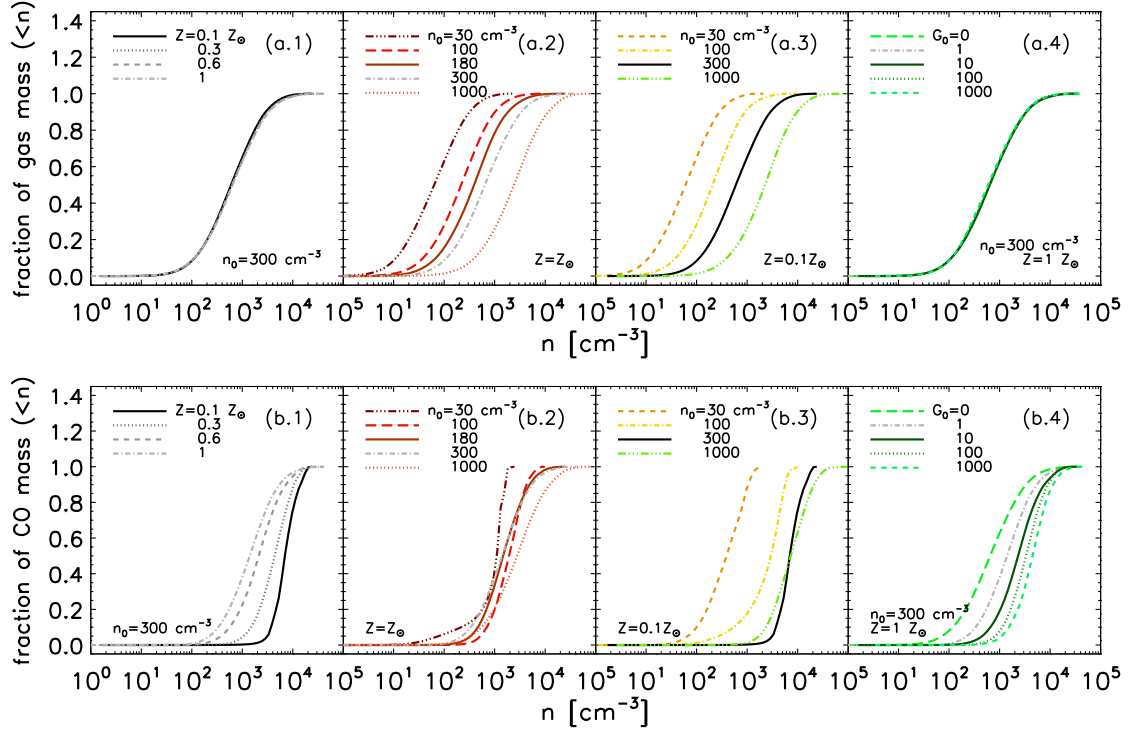


Figure 5.1: (a) Cumulative gas mass below a given number density (normalized by the total mass of the cloud) as a function of n . (b) same as (a), but for the CO mass (normalized by the total CO mass of the cloud).

Fig. 5.2 shows the mass-weighted average of the CO abundance $x_{\text{CO}} = n_{\text{CO}}/n$ (on average, $\langle n_{\text{CO}}/n \rangle \approx \langle N_{\text{CO}}/N \rangle$) as a function of the mean A_V . The arrangement of colors is the same as in the previous figure and all the simulations are labeled by their mean number density, metallicity and UV radiation field strength. x_{CO} increases sharply from $\sim 10^{-12}$ (at $A_V \approx 0.1$ mag) to few 10^{-6} (at $A_V \approx 4$ mag), where gas shielding becomes effective. It then grows slowly towards high A_V until it reaches its maximum value $x_{\text{CO}} = x_{\text{C}} = 1.41 \times 10^{-4}$. The strong influence of the extinction on the amount of CO is clear. As the extinction gets higher, the gas shielding becomes important preventing the dissociation of CO. In the case of $A_V = 10$ mag, the abundance of CO decreases by almost one order of magnitude when the UV field strength is increased to $\sim 10^3 G_0$. There are more photons permeating the cloud, therefore the probability of destroying CO molecules grows.

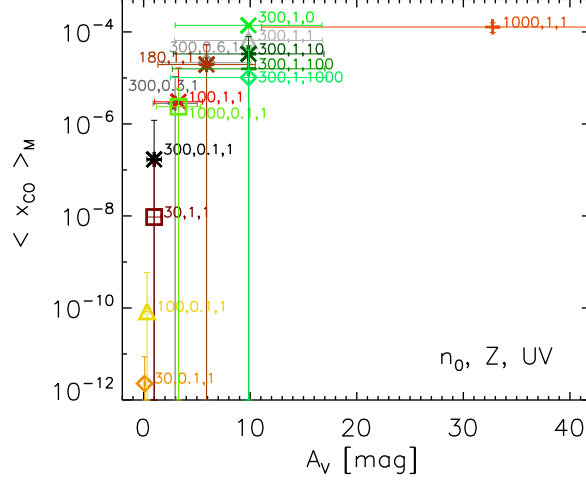


Figure 5.2: Mass-weighted average of the CO abundance $x_{\text{CO}} = n_{\text{CO}}/n$ as a function of the mean visual extinction $\langle A_V \rangle$. In all the figures, we refer to $\langle A_V \rangle$ simply as A_V . The colors are arranged in the same fashion as in the previous figure. All the simulations are labeled by their mean number density n_0/cm^{-3} , metallicity Z/Z_\odot and UV radiation field strength UV/G_0 .

5.2 Tracing the temperature of molecular clouds

In the previous section, we analyzed the range of number densities containing most of the CO in molecular clouds. Now, we study the range of temperatures in which CO is mostly distributed.

5.2.1 Kinetic temperature

Fig. 5.3 shows the mean kinetic temperature in every n bin as a function of number density. The temperature is not constant, but generally decreases towards higher densities. The rise at high density in the low metallicity runs is caused by H₂ formation heating and may be overestimated. For the simulations with $Z = Z_\odot$ and $UV=1$, the temperature scales approximately as $\langle T_K \rangle_n \propto n^{-0.45}$. The simulations with lower Z present higher $\langle T_K \rangle_n$ at $n \gtrsim 10 \text{ cm}^{-3}$, because the CO abundance falls and the dominant coolant changes from CO to C⁺. For the simulations with $Z = 0.1Z_\odot$, the temperature scales roughly as $\langle T_K \rangle_n \propto n^{-0.4}$. In the case where we consider different UV radiation field strengths, the relationship changes from the cloud with $UV=0$, in which $\langle T_K \rangle_n \propto n^{-0.23}$ (at $n \lesssim 100 \text{ cm}^{-3}$, $\langle T_K \rangle_n$ is $\sim 15 \text{ K}$ at

higher number densities), to the simulation with $UV=1000$: $\langle T_K \rangle_n \propto n^{-0.6}$. The change on the slope for the runs with $UV > 1$ is caused by the graving effectiveness of photoelectric heating from dust grains. Comparing Fig. 5.3 with Fig. 5.1b, we see that most of the CO is located at temperatures of 15-70 K, even though these regions may represent only a small fraction of the cloud volume.

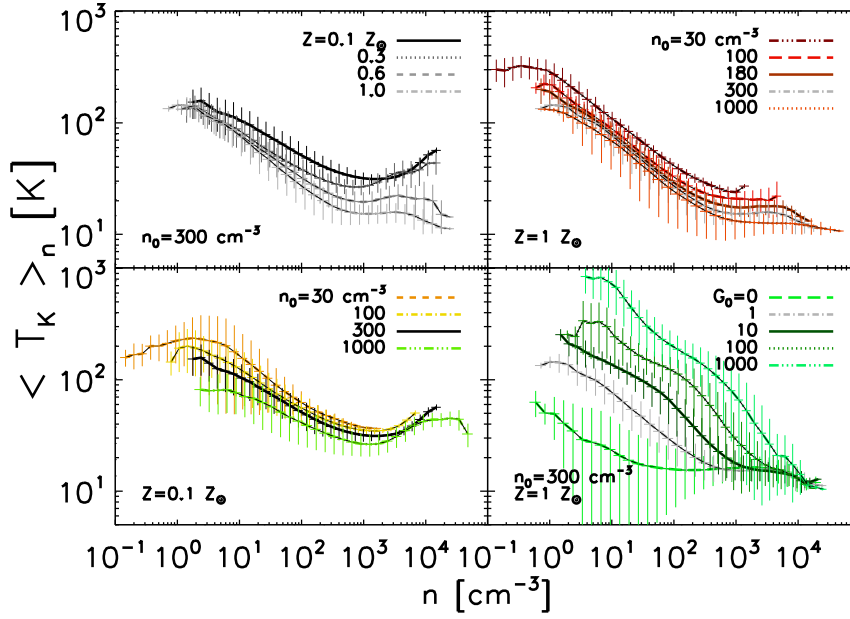


Figure 5.3: Average of the kinetic gas temperature in every number density bin $\langle T_K \rangle_n$ as a function of the number density. The error bars indicate the scatter ($\pm 1\sigma_{T_K}$) around the average. The lines and colors are arranged in the same fashion as in Fig. 5.1.

Fig. 5.4 (top) shows the mass-weighted average of the temperature $\langle T_K \rangle_M$ as a function of the mean A_V . The mean temperature decreases towards high A_V , although the scatter in $\langle T_K \rangle_M$ at $A_V = 10$ mag is very large, it is about 100 K. We anyway performed a linear regression over the logarithm of the data (black line) and find that $\langle T_K \rangle_M$ relates to $\langle A_V \rangle$ roughly as $\langle T_K \rangle_M \propto \langle A_V \rangle^{-1/5}$. On the other hand, Fig. 5.4 (bottom) shows a similar plot for the kinetic temperature but the CO mass-weighted average³. In this case, the data shows less scatter around the linear regression (black line).

³We choose the CO mass-weighted average in this case because we will compare the kinetic temperature with the temperature obtained from CO emission later.

$\langle T_K \rangle_{\text{CO}} \leq \langle T_K \rangle_M$ because CO traces only the highest density-cold gas in the cloud. $\langle T_K \rangle_{\text{CO}}$ decreases from ~ 50 K at $\langle A_V \rangle = 0.1$ mag to ~ 12 K at $\langle A_V \rangle = 33$ mag. This correspond to a relationship between temperature and visual extinction that can be approximated by $\langle T_K \rangle_{\text{CO}} \propto \langle A_V \rangle^{-1/4}$. The linear regression confirms the results, with a bit of scatter around this line that increases as A_V decreases.

5.2.2 CO ($J=1-0$) brightness temperature

At frequencies below sub-millimeter ($\nu \leq 1.5$ THz), the intensity at a given frequency ν emitted by from an astrophysical object is usually expressed in terms of the brightness temperature T_b given by the Rayleigh-Jeans approximation (§1.4.4, Wilson et al., 2009)

$$T_b = \frac{c^2}{2k\nu^2} I_\nu. \quad (5.3)$$

From the radiative transfer equation (§1.4.4) it is commonly assumed that in LTE, $T_b \approx T_K$ for optically thick gas (e.g. Wilson et al., 2009; Draine, 2011). We therefore test if the assumption of LTE is valid for our cloud models by using the CO ($J=1-0$) emission⁴. In Fig. 5.5 (top), we plot the CO mass-weighted average of the brightness temperature $\langle T_b \rangle_{\text{CO}}$ as a function of $\langle T_K \rangle_{\text{CO}}$. The scatter in this plot is large and there is not a clear trend between $\langle T_b \rangle_{\text{CO}}$ and $\langle T_K \rangle_{\text{CO}}$. The values of $\langle T_K \rangle_{\text{CO}}$ are always above 10 K, while $\langle T_b \rangle_{\text{CO}}$ is below 5 K. We therefore can say that on average the emission is not thermalized.

As we are dealing here with averages over whole clouds, in Fig. 5.5 (bottom), we plot the CO mass-weighted average of integrated intensity along the line of sight divided by $d\nu \langle W_{\text{CO}}/d\nu \rangle_{\text{CO}}$ ⁵ as a function of $\langle T_K \rangle_{\text{CO}}$. In most of the simulations $\langle W_{\text{CO}}/d\nu \rangle_{\text{CO}} > \langle T_K \rangle$. The simulation n30 is the only one which has $\langle W_{\text{CO}}/d\nu \rangle_{\text{CO}} \approx \langle T_K \rangle$. We skip the simulations n30-Z01, n100-Z01 because they have $A_V \lesssim 1$ mag which implies low CO abundance along the cloud.

The CO ($J=1-0$) transition is considered optically thick (e.g. Dickman, 1978; Liszt and Lucas, 1998; Pineda et al., 2008; Shetty et al., 2011a). Under the assumption of LTE, the peak of this emission is used to calculate the excitation temperature (Dickman, 1978), and from the excitation temperature many other quantities like optical depths, CO column densities, and mass of clouds. In Fig. 5.6, we select the maximum of the brightness temperature

⁴CO ($J=1-0$) transition is usually assumed to be thermalized (e.g. Martin et al., 1982; Walmsley and Ungerechts, 1983; Roman-Duval et al., 2010)

⁵ $W_{\text{CO}} = \int T_b(\nu) d\nu$, see §4.2

along the line of sight. We then calculate the CO mass-weighted average of these peaks $\langle T_{\text{b,max}} \rangle_{\text{CO}}$ and plot it as a function of $\langle T_{\text{K}} \rangle_{\text{CO}}$. $\langle T_{\text{b,max}} \rangle_{\text{CO}}$ grows with increasing $\langle T_{\text{K}} \rangle_{\text{CO}}$. The black line shows the one-to-one relation between the temperatures. The simulations with $n_0 \geq 180 \text{ cm}^{-3}$ and $Z \geq 0.3Z_{\odot}$ approach the black line, also the simulation n1000-Z01, showing that the peak of the emission is indeed thermalized or close to be. We also skip in this case the simulations with $A_V \lesssim 1 \text{ mag}$.

5.2.3 Excitation temperature

The excitation temperature T_{ex} of the level $u = 1$ relative to the level $l = 0$ is defined from the Boltzmann equation by (e.g. [Draine, 2011](#))

$$T_{\text{ex}} = \frac{E_{10}/k}{\ln \left(\frac{n_0/g_0}{n_1/g_1} \right)}, \quad (5.4)$$

where n_0 and n_1 are the number density of molecules in the ground and first excited level, with statistical weights g_0 and g_1 respectively, and E_{10} is the difference of energies between both levels. If the system is in LTE, then $T_{\text{ex}} = T_{\text{K}}$ (see §3.3.3).

In order to find if our cloud models fulfill the LTE condition, we show the CO mass-weighted average of the excitation temperature calculated using Eq. 5.4, $\langle T_{\text{ex}}^{\text{col}} \rangle_{\text{CO}}$ ⁶, as a function of $\langle T_{\text{K}} \rangle_{\text{CO}}$ in Fig. 5.7 (top). The black line shows the one-to-one relation between the temperatures. All the data points lie below the black line indicating that on average the simulations are sub-thermally excited. However, the simulations with $n_0 \geq 300 \text{ cm}^{-3}$ and $Z \geq 0.3Z_{\odot}$, as well as the simulation n1000-Z01, approach closely to the one-to-one relation, indicating that they are close to LTE, on average.

We also calculate the excitation temperature from an ‘‘observational’’ point of view, using the [Dickman \(1978\)](#) formula (see §3.3.3):

$$T_{\text{ex,obs}}^{\text{col}} = \frac{5.5 \text{ [K]}}{\ln \{ 1 + 5.5 \text{ [K]} / (T_{\text{b,max}} + 0.82 \text{ [K]}) \}}. \quad (5.5)$$

Fig. 5.7 (bottom) shows the CO mass-weighted average of this excitation temperature $\langle T_{\text{ex,obs}}^{\text{col}} \rangle_{\text{CO}}$ as a function of $\langle T_{\text{K}} \rangle_{\text{CO}}$. The simulations with $n_0 \geq 100 \text{ cm}^{-3}$ and $Z \geq 0.3Z_{\odot}$, and the simulation n1000-Z01, are very close to the one-to-one relation (black line). These cloud models have $\langle T_{\text{b,max}} \rangle$

⁶We consider the same convention as in §3.3.3, where we assumed the column excitation temperature when we average T_{ex} along the line of sight. Here, we are considering the average over all three spatial directions, and name this average as $\langle T_{\text{ex}}^{\text{col}} \rangle$ for consistency reasons.

which are close to be thermalized. It is therefore not surprising that their correspondent $\langle T_{\text{ex,obs}}^{\text{col}} \rangle$ approach well to the black line.

[Roman-Duval et al. \(2010\)](#) present a very complete analysis of the physical properties of 750 molecular clouds located in the Milky Way. They argue that the average excitation temperature of the clouds diminishes by about 3 K with Galactocentric radius. In this work, we are not attempting to fit the initial condition of our simulations to the environmental conditions at different Galactocentric radius. However, we can study how our estimates of the excitation temperature may change compared with different physical parameters, like mean A_V , N , or UV radiation field strength.

Fig. 5.8 (top) shows the CO mass-weighted average of $\langle T_{\text{ex}}^{\text{col}} \rangle_{\text{CO}}$ as a function of $\langle A_V \rangle$. In Fig. 5.8 (bottom), we plot the same but for $\langle T_{\text{ex,obs}}^{\text{col}} \rangle_{\text{CO}}$. There is not correlation between the visual extinction and the excitation temperature in either of both plots. In Figs. 5.9 (top and bottom), we repeat the same calculation but this time the excitation temperature is plotted as a function of the column density N . In particular, Fig. 5.9 (top) indicates that $\langle T_{\text{ex}}^{\text{col}} \rangle_{\text{CO}}$ grows with increasing N up to $N \approx 2 \times 10^{22} \text{ cm}^{-2}$, although there is large scatter from simulations n300-Z01 and n300-Z03. From the “observational” point of view (Fig. 5.9 bottom), $\langle T_{\text{ex,obs}}^{\text{col}} \rangle_{\text{CO}}$ increases towards high N with less scatter than in Fig. 5.9 (top). We do not know if there is a clear change in the average A_V or N with Galactocentric radius, although it is a possibility worthy to be explored in more detail.

On the other hand, it is known that the UV radiation field strength increases towards the Galactic center ([Rodríguez-Fernández et al., 2004](#)), as well as in nearby galaxies ([Heiner et al., 2008](#)). Hence in Figs. 5.10 (top) and 5.10 (bottom), we plot $\langle T_{\text{ex}}^{\text{col}} \rangle_{\text{CO}}$ (top) and $\langle T_{\text{ex,obs}}^{\text{col}} \rangle_{\text{CO}}$ as a function of the UV radiation field strength. For those simulations with $1 \leq \text{UV}/G_0 \leq 1000$ ($n_0 = 300 \text{ cm}^{-3}$ and $Z = Z_\odot$), $\langle T_{\text{ex}}^{\text{col}} \rangle_{\text{CO}}$ (Fig. 5.10 top) increases from ~ 13 K for $\text{UV}/G_0 = 1$ to ~ 16 K for $\text{UV}/G_0 = 1000$. In the case of Fig. 5.10 (bottom), $\langle T_{\text{ex,obs}}^{\text{col}} \rangle_{\text{CO}}$ increases from ~ 15 K for $\text{UV}/G_0 = 1$ to ~ 21 K for $\text{UV}/G_0 = 1000$. These results indicates that the subtle increment in [Roman-Duval et al. \(2010\)](#) findings may be explained by the photoelectric heating of the gas, which in turn is caused by the incident UV radiation field.

5.3 CO column density

Fig. 5.11 shows the mass-weighted average of the “true”⁷ CO column density N_{CO} as a function of the mean A_V . N_{CO} increases towards high A_V , scaling in a relationship (black line) which is approximated as

$$\langle N_{\text{CO}} \rangle = 3.63 \times 10^{14} \langle A_V \rangle^{3.77} [\text{cm}^{-2}]. \quad (5.6)$$

However, N_{CO} cannot be directly inferred from observations. It is estimated from CO ($J=1-0$) observations using the excitation temperature and the optical depth τ (for details see §3.4.1), generally using the relation

$$N_{\text{CO},\text{total}} \approx \frac{2.31 \times 10^{14} [\text{cm}^{-2}]/[\text{K}]}{(J+1)} \int \frac{\tau_v T_{\text{ex}}(v) \exp \left[\frac{2.78J(J+1)}{T_{\text{ex}}(v)} \right] dv}{1 - \exp \left[-h\nu_0/kT_{\text{ex}}(v) \right]}. \quad (5.7)$$

In some observational works (Roman-Duval et al., 2010), the excitation temperature is calculated at every velocity position along the line of sight, then integrated together with the optical depth as indicated in Eq. 5.7, while in other works, it is considered to be constant along the line of sight (e.g. Goldsmith et al., 2008; Pineda et al., 2010). In the following figures, we compare the effect of the method chosen to calculate the excitation temperature in different environments⁸.

On one hand, Fig. 5.12 (top) shows the ratio between the CO mass-weighted CO column density calculated by using $T_{\text{ex}}(v)$ from the Boltzmann Equation 5.4 into Eq. 5.7 $N_{\text{CO}}^{\text{th},3\text{D}}$ -to-the “true” N_{CO} as a function of the mean A_V . For all the simulations, the “true” N_{CO} is underestimated by more than 30%, $\langle N_{\text{CO}}^{\text{th},3\text{D}}/N_{\text{CO}} \rangle_{\text{CO}} < 0.7$. This ratio increases from ~ 0.05 at $\langle A_V \rangle = 1$ mag to ~ 0.65 at $\langle A_V \rangle = 33$ mag, although at $\langle A_V \rangle = 10$ mag the scatter is large.

On the other hand, Fig. 5.12 (bottom) indicates the same as Fig. 5.12 (top) but considering $T_{\text{ex,obs}}(v)$ calculated from the Dickman (1978) formula (Eq. 3.6) $N_{\text{CO}}^{\text{obs},3\text{D}}$. In this case, the estimates of the CO mass-weighted averages of the CO column density are higher than in the previous calculation, resulting in better estimations of the “true” $\langle N_{\text{CO}} \rangle$. The ratio $\langle N_{\text{CO}}^{\text{obs},3\text{D}}/N_{\text{CO}} \rangle_{\text{CO}}$

⁷We assume as “true” the column densities obtained directly from ZEUS-MP calculations. This convention will be used for forthcoming comparisons with the estimates of the CO and H₂ column density from CO ($J=1-0$) emission.

⁸We intentionally left the simulations n30-Z01, n100-Z01, and n30 out of this part of the analysis because of their low CO abundances, which in turn result in unrealistic estimates of the CO column density.

increases from ~ 0.6 at $\langle A_V \rangle = 1$ mag to ~ 1.15 at $\langle A_V \rangle = 33$ mag. Particularly at $\langle A_V \rangle = 10$ mag, the simulations with variable UV present large scatter, although the cloud model UV10 has the best estimation of the “true” $\langle N_{\text{CO}} \rangle$. The difference between using $T_{\text{ex}}(v)$ and $T_{\text{ex,obs}}(v)$ into Eq. 5.7 range from $\sim 40\%$ at $\langle A_V \rangle = 33$ mag to $\sim 90\%$ at $\langle A_V \rangle = 1$ mag. At $\langle A_V \rangle = 10$ mag, the difference can be as high as 80% .

We now consider that the excitation temperature in Eq. 5.7 is constant at every position along the line of sight. First, we calculate T_{ex} from the Boltzmann Equation 5.4, then make the CO mass-weighted average along the line of sight, $T_{\text{ex}}^{\text{col}}$, in order to estimate $N_{\text{CO}}^{\text{th,2D}}$. Fig. 5.13 shows the average of the ratio of $N_{\text{CO}}^{\text{th,2D}}$ to the “true” N_{CO} as a function of the mean A_V . $\langle N_{\text{CO}}^{\text{th,2D}}/N_{\text{CO}} \rangle$ does not show a clear trend with $\langle A_V \rangle$, and for most of the simulations, it is very close to 1 (which is different from Fig. 5.12 top). For all the cloud models but for n1000, UV10 and UV100, the “true” N_{CO} is overestimated.

On the other hand, Fig. 5.13 (bottom) depicts the same as Fig. 5.13 (top), but for the estimated CO column density $N_{\text{CO}}^{\text{obs,2D}}$ (Eq. 5.7) calculated from Dickman (1978) formulation ($T_{\text{ex,obs}}^{\text{col}}$, Eq. 5.5). The ratio $\langle N_{\text{CO}}^{\text{obs,2D}}/N_{\text{CO}} \rangle$ grows towards high $\langle A_V \rangle$. All the simulations but n300-Z01 overestimates the “true” N_{CO} from $\sim 20\%$ at $\langle A_V \rangle = 3$ mag to $\sim 50\%$ at $\langle A_V \rangle = 33$ mag. A comparison between $\langle N_{\text{CO}}^{\text{obs,2D}}/N_{\text{CO}} \rangle$ and its counterpart in 3D (Fig. 5.12 bottom) results in ratios which are 25-50% larger if one uses $T_{\text{ex,obs}}^{\text{col}}$ instead of $T_{\text{ex,obs}}(v)$ in Eq. 5.7.

The results in this section are consistent with the ones shown in §3.4.1. The best estimates of the CO column density are given by considering the Dickman (1978) approximation, but assuming that the excitation temperature is NOT uniformly distributed along the line of sight $T_{\text{ex,obs}}$ (Eq. 3.6).

5.4 The X_{CO} -factor and H₂ column density estimates

Historically, the CO-to-H₂ conversion factor (the X_{CO} -factor) was proposed as an statistical study of CO and H₂ column densities, covering many locations within many clouds in order to have general applicability of the results (Dickman, 1978). In chapter 4, we studied this conversion factor along many sight lines, but over only a single cloud example. In this section, we extend that analysis to all the simulations.

The mass-weighted average of X_{CO} is defined as

$$\langle X_{\text{CO}} \rangle_{\text{M}} = \frac{\langle N_{\text{H}_2} \rangle_{\text{M}}}{\langle W_{\text{CO}} \rangle_{\text{M}}}, \quad (5.8)$$

with standard deviation

$$\sigma_{X_{\text{CO}}} = \sqrt{\left(\frac{\sigma_{N_{\text{H}_2}}^2}{N_{\text{H}_2}^2} + \frac{\sigma_{W_{\text{CO}}}^2}{W_{\text{CO}}^2} - 2 \frac{\text{COV}_{N_{\text{H}_2}W_{\text{CO}}}}{N_{\text{H}_2}W_{\text{CO}}} \right) X_{\text{CO}}}, \quad (5.9)$$

where $\text{COV}_{N_{\text{H}_2}W_{\text{CO}}}$ is the covariance between N_{H_2} and W_{CO} .

Following the approach of Liszt et al. (2010), we rewrite $\langle X_{\text{CO}} \rangle_{\text{CO}}$ as

$$\langle X_{\text{CO}} \rangle_{\text{M}} = \left(\frac{\langle N_{\text{CO}} \rangle_{\text{M}}}{\langle W_{\text{CO}} \rangle_{\text{M}}} \right) \left(\frac{\langle N_{\text{CO}} \rangle_{\text{M}}}{\langle N_{\text{H}_2} \rangle_{\text{M}}} \right)^{-1}. \quad (5.10)$$

For the Milky-Way, the CO-to- H_2 conversion factor $\langle X_{\text{MW}} \rangle \approx 2 \times 10^{20}$ $\text{cm}^{-2} \text{K km s}^{-1}$ (e.g. Solomon et al., 1987; McKee and Ostriker, 2007; Strong et al., 2007). Frequently, this value is used regardless of the effects of different environmental conditions, because the terms in Eq. 5.10 are considered to cancel each other (Liszt et al., 2010; Pety et al., 2011). However in §4.3, we found that the CO-to- H_2 conversion factor may be different depending on the environmental physical conditions. Therefore in the next sections, we study how the two fractions in Eq. 5.10⁹ influence the shape of $\langle X_{\text{CO}} \rangle_{\text{M}}$ in our cloud models.

5.4.1 The N_{CO} -to- N_{H_2} ratio

Usually, the N_{CO} -to- N_{H_2} ratio is referred as ‘‘CO abundance relative to H_2 ’’ (e.g. Leung and Liszt, 1976; Dickman, 1978; Frerking et al., 1982; Burgh et al., 2007; Goldsmith et al., 2008; Liszt et al., 2010; Pineda et al., 2010; Pety et al., 2011). For avoiding confusions with the definition of CO abundance ($x_{\text{CO}} = n_{\text{CO}}/n$, §5.1), we refer to it simply as CO/ H_2 . The measurements of N_{CO} and N_{H_2} are independent, therefore we consider the average of their ratio as $\langle N_{\text{CO}} \rangle / \langle N_{\text{H}_2} \rangle$. It is important to mention that $\langle N_{\text{CO}} \rangle / \langle N_{\text{H}_2} \rangle$ is certainly different than $\langle N_{\text{CO}} / N_{\text{H}_2} \rangle$, indeed it is ~ 1 -3 higher. We choose $\text{CO}/\text{H}_2 = \langle N_{\text{CO}} \rangle / \langle N_{\text{H}_2} \rangle$, for consistency with Eq. 5.10 and with observations.

If CO/ H_2 is estimated from CO ($J=1-0$) emission (considering that N_{H_2} is calculated using the X-factor), the value is approximately constant $\sim 10^{-4}$ (e.g. Dickman, 1978; Burgh et al., 2007; Pineda et al., 2010). However in one hand, in observations it is usually necessary to assume LTE conditions

⁹The standard deviation of the two terms in Eq. 5.10 is calculated in the same fashion as in Eq. 5.9.

in order to estimate N_{CO} , which values at $A_V \lesssim 3$ mag can vary for $\pm 30\%$ (Fig. 5.13 bottom). On the other hand at $A_V \gtrsim 3$ mag, CO emission becomes optically thick (§4.2) making N_{CO} difficult to determine if observations of other CO isotopomers are not available (e.g. Pineda et al., 2008; Goodman et al., 2009a).

Fortunately, there are measurements of CO/H₂ independent of CO ($J=1-0$) emission in the diffuse/translucent molecular gas. Direct observations of the absorption lines of both species (at $\lambda \lesssim 1510\text{\AA}$ for CO, and at $912\text{\AA} \lesssim \lambda \lesssim 1110\text{\AA}$ for H₂) provide a better estimation of this ratio with values ranging from $\sim 10^{-7}$ at $A_V \approx 0.3$ mag to $\sim 10^{-5}$ at $A_V \approx 2$ mag (Burgh et al., 2007). This method was first applied for infrared sources embedded in molecular clouds towards the star clusters NGC 2024 and NGC 2264, with resulting values around $(2-3) \times 10^{-4}$ (Lacy et al., 1994).

Fig. 5.14 (top) shows mass-weighted averages $\langle N_{\text{CO}} \rangle_{\text{M}} / \langle N_{\text{H}_2} \rangle_{\text{M}}$ as a function of the mean A_V . CO/H₂ increases sharply from $\sim 10^{-10}$ at $\langle A_V \rangle \approx 0.1$ mag to $\sim 10^{-5}$ at $\langle A_V \rangle \approx 4$ mag. Our results at $\langle A_V \rangle \lesssim 1$ mag differ by approximately 3 orders of magnitude in comparison to the work of Burgh et al. (2007). We do not know exactly the reason of this discrepancy, although our guess is that our model does not allow for physical processes like turbulent mixing of material (e.g. Falgarone and Phillips, 1990; Falgarone and Puget, 1995; Décamp and Le Bourlot, 2002; Falgarone et al., 2005; Glover et al., 2010), or C-shocks that can trigger CO formation in diffuse media (Shetty et al., 2011a) (see §4.3). At $\langle A_V \rangle \gtrsim 5$ mag, CO/H₂ increases by approximately one order of magnitude towards high $\langle A_V \rangle$. CO/H₂ is approximately 10^{-4} at this regime, which is in good agreement the values measured in observations (Dickman, 1978; Lacy et al., 1994; Pineda et al., 2010).

Burgh et al. (2007) find that the column densities of CO and H₂ follows a power-law relation $N_{\text{CO}} \propto N_{\text{H}_2}^\alpha$ with $\alpha \approx 2$. Fig. 5.14 (bottom) shows $\langle N_{\text{CO}} \rangle_{\text{M}}$ as a function of $\langle N_{\text{H}_2} \rangle_{\text{M}}$. $\langle N_{\text{CO}} \rangle_{\text{M}}$ increases towards high $\langle N_{\text{H}_2} \rangle_{\text{M}}$. The black line indicates a linear regression made to the logarithm of $\langle N_{\text{CO}} \rangle_{\text{M}} \propto \langle N_{\text{H}_2} \rangle_{\text{M}}$, in which $\alpha \approx 3.2$. The slope in this figure is very steep compared to the result of Burgh et al. (2007), which is expected given our low CO/H₂ at $\langle A_V \rangle \leq 4$ mag. If we select the data with visual extinction below 4 mag, the slope is slightly shallower, with $\alpha \approx 2.8$.

5.4.2 The N_{CO} -to- W_{CO} ratio

Fig. 5.15 shows the average of the integrated CO ($J=1-0$) intensity in every A_V bin $\langle W_{\text{CO}} \rangle$, plotted as a function of the mean A_V . At $A_V \lesssim 20$ mag, $\langle W_{\text{CO}} \rangle$ changes remarkably for each of the simulations, which strongly depends on the mean physical conditions. In these regions, $\langle W_{\text{CO}} \rangle$ depends

strongly on the CO abundance more than on the H_2 density (the main collisional partner), which is lower for simulations with a significant fraction of translucent/diffuse gas (the shielding is less effective) or increasing UV radiation field strength. At $A_V \gtrsim 20$ mag, the CO ($J=1-0$) intensity becomes saturated, leading to an almost constant $\langle W_{\text{CO}} \rangle \approx 80 \text{ K km s}^{-1}$.

In global averages, $\langle W_{\text{CO}} \rangle$ presents large scatter at all mean visual extinctions. Fig. 5.16 shows the mass-weighted average of the integrated intensity $\langle W_{\text{CO}} \rangle_{\text{M}}$ as a function of the mean A_V . At $\langle A_V \rangle \lesssim 1$ mag, it varies from $\sim 0.1 \text{ K km s}^{-1}$ for simulations n30-Z01 and n100-Z01 to $\sim 4 \text{ K km s}^{-1}$ for simulation n300-Z01. At larger $\langle A_V \rangle$, it changes from $\sim 1 \text{ K km s}^{-1}$ to 80 K km s^{-1} . Although the scatter is large, we nevertheless perform a fitting in the same fashion as in §4.2. Eq. 5.11 shows the best fit implemented using an arbitrary function (dashed line in Fig. 5.16)

$$\langle W_{\text{CO}} \rangle_{\text{M}} \approx 12.14 \sqrt{\ln(1 + 8 \times 10^{-5} \langle A_V \rangle^{7.94})} [\text{K km s}^{-1}]. \quad (5.11)$$

On the other hand, Eq. 5.12 shows a fitting performed following the work of Pineda et al. (2008), for which they considered the radiative transfer equation assuming that W_{CO} and T_{b} behave in the same fashion (see §4.2). For the averages of our cloud models, the best fit is

$$\langle W_{\text{CO}} \rangle_{\text{M}} \approx 56.7 [1 - e^{-0.114(\langle A_V \rangle - 1.007)}] [\text{K km s}^{-1}]. \quad (5.12)$$

Given the large scatter in Fig. 5.16, Eqs. 5.11 and 5.12 roughly reproduce $\langle W_{\text{CO}} \rangle_{\text{M}}$ at $\langle A_V \rangle \lesssim 10$ mag. For the simulation at $\langle A_V \rangle = 33$ mag, Eq. 5.11 provides the best fit.

Fig. 5.17 shows the ratio of the mass weighted averages of N_{CO} -to- W_{CO} ratio as a function of the mean A_V . This ratio changes from $\sim 10^{12} \text{ cm}^{-2} \text{ K}^{-1} \text{ km}^{-1} \text{ s}$ at $\langle A_V \rangle \approx 0.1$ mag to $\sim 10^{16} \text{ cm}^{-2} \text{ K}^{-1} \text{ km}^{-1} \text{ s}$ at $\langle A_V \rangle = 4$ mag. Liszt et al. (2010) claim that for diffuse/translucent clouds $N_{\text{CO}}/W_{\text{CO}} = 10^{15} \text{ cm}^{-2} \text{ K}^{-1} \text{ km}^{-1}$, and this value is nearly universal. However, their W_{CO} detection limit is 0.2 K km s^{-1} . If we exclude the simulations n30-Z01, n100-Z01, and n30 in Fig. 5.17, $\langle N_{\text{CO}} \rangle_{\text{M}} / \langle W_{\text{CO}} \rangle_{\text{M}} \approx 10^{15} \text{ cm}^{-2} \text{ K}^{-1} \text{ km}^{-1}$, which matches Liszt et al. (2010) findings. Besides, Goldreich and Kwan (1974) note that when T_{K} is much greater than T_{ex} , $N_{\text{CO}}/W_{\text{CO}}$ decreases. In our case, $\langle T_{\text{K}} \rangle_{\text{CO}} \gg \langle T_{\text{ex}}^{\text{col}} \rangle_{\text{CO}}$ for the simulations n30-Z01, n100-Z01, and n30.

At higher $\langle A_V \rangle$ in Fig. 5.17, $\langle N_{\text{CO}} \rangle_{\text{M}} / \langle W_{\text{CO}} \rangle_{\text{M}}$ increases slowly towards high $\langle A_V \rangle$ by about one order of magnitude, which is because CO ($J=1-0$) emission becomes optically thick at high CO column densities. Eq. 5.13 shows a linear fit made in logarithmic space (dashed line in Fig. 5.17)

$$\frac{\langle N_{\text{CO}} \rangle}{\langle W_{\text{CO}} \rangle} [\text{cm}^{-2} \text{K}^{-1} \text{km}^{-1} \text{s}] \approx \begin{cases} 4.84 \times 10^{14} \langle A_V / [\text{mag}] \rangle^{2.36} & \langle A_V \rangle < 8 \text{ mag} \\ 2.75 \times 10^{15} \langle A_V / [\text{mag}] \rangle^{1.13} & \langle A_V \rangle \geq 8 \text{ mag}. \end{cases} \quad (5.13)$$

Liszt et al. (2010) find that $W_{\text{CO}} \propto N_{\text{CO}}$ for diffuse/translucent and dark gas. Eq. 5.13 at $\langle A_V \rangle \geq 8$ mag is very close to their relationship for dark gas.

5.4.3 The X-factor

Fig. 5.18 shows the mass weighted average of the X-factor as a function of the mean A_V . The X-factor decreases from $X \sim 10^{22} \text{ cm}^{-2} \text{K}^{-1} \text{km}^{-1} \text{s}$ at $\langle A_V \rangle \approx 0.1$ mag to $X = 3.5 \times 10^{20} \text{ cm}^{-2} \text{K}^{-1} \text{km}^{-1} \text{s}$ at $\langle A_V \rangle = 6$ mag. At $\langle A_V \rangle \geq 6$ mag, it is approximately constant $X \approx 3.5 \times 10^{20} \text{ cm}^{-2} \text{K}^{-1} \text{km}^{-1}$, although with significant scatter at $\langle A_V \rangle = 10$ mag. The X-factor behaves approximately as (dashed line in Fig. 5.18)

$$\langle X_{\text{CO}} \rangle [\text{cm}^{-2} \text{K}^{-1} \text{km}^{-1} \text{s}] \approx \begin{cases} 3.5 \times 10^{20} & \langle A_V \rangle \geq 6 \text{ mag} \\ 1.8 \times 10^{21} \langle A_V / [\text{mag}] \rangle^{-0.9} & \langle A_V \rangle < 6 \text{ mag}. \end{cases} \quad (5.14)$$

The relation at $\langle A_V \rangle \leq 6$ mag is calculated with a linear regression on logarithmic space, while the value $3.5 \times 10^{20} \text{ cm}^{-2} \text{K}^{-1} \text{km}^{-1}$ is the average of X_{CO} at $6 \leq \langle A_V \rangle / [\text{mag}] \leq 10$. The simulation n1000 is not included in the calculation. For including it, we make a linear regression for the data at $\langle A_V \rangle \geq 6$ mag (dotted line in Fig. 5.18), which gives

$$\langle X_{\text{CO}} \rangle = 1.3 \times 10^{20} \langle A_V / [\text{mag}] \rangle^{0.4} \quad \langle A_V \rangle \geq 6 \text{ mag}. \quad (5.15)$$

In this relation, $\langle X_{\text{CO}} \rangle$ grows smoothly towards high $\langle A_V \rangle$, which is expected because W_{CO} becomes optically thick with increasing $\langle A_V \rangle$.

$\langle X_{\text{CO}} \rangle$ differs from the CO-to-H₂ conversion factor shown in §4.3 (the single cloud example), especially at low visual extinction. Fig. 5.18 exhibits lower values than in Fig. 4.7. The reason is that in Fig. 4.7, the X-factor is shown for individual lines of sight. Here in Fig. 5.18, each point indicates a X-factor averaged over all the sight lines in different molecular clouds. The dispersion of the runs n30-Z01, n100-Z01, and n30, shows that the X-factor can be approximately as high as the X-factor in Fig. 4.7.

5.5 H₂ mass estimates

In this section, we calculate the map of N_{H_2} considering the map of W_{CO} and a fixed value $X_{\text{CO}} = X_{\text{MW}}$. The estimate of the total mass of H₂ for each simulation is

$$M_{\text{H}_2} = \sum_{i,j} W_{\text{CO}} X_{\text{MW}}, \quad (5.16)$$

where i and j covers all the sight lines.

Fig. 5.19 shows the cumulative mass of H₂ below a given N as a function of N (A_V is shown at the top for reference) normalized by the total “true” mass of H₂. The solid line indicates the “true” H₂ mass while the dotted line shows the estimated H₂ mass from Eq. 5.16. For all the simulations but n300 and UV0, the H₂ mass is underestimated if it is calculated using Eq. 5.16. For simulation n300, the estimated H₂ mass is equivalent to the “true” one up to $\log_{10} A_V / [\text{mag}] \approx 1.2$ ($A_V \approx 16$ mag). At higher A_V , the H₂ mass is underestimated by $\sim 20\%$. In the case of the simulation UV0, the estimated H₂ mass and the “true” H₂ mass are approximately equivalent. Indeed, the estimated H₂ mass overestimates slightly the “true” H₂ mass at all A_V . This particular cloud example is hypothetical, because we do not expect that a real cloud would not be affected by UV radiation at all. This simulation has a CO/H₂ ratio which is slightly higher than that corresponding to a typical Milky Way dark cloud.

Fig. 5.20 (top) shows the total estimated fraction of H₂ ($f_{\text{H}_2\text{mass}}$) as a function of the mean A_V . $f_{\text{H}_2\text{mass}}$ is the total estimated H₂ mass normalized by the total “true” H₂ mass. It grows as $\langle A_V \rangle$ increases. Considering only the simulations with UV=1 (with the exception of simulation n1000), the “true” H₂ mass is underestimated by $\sim 95\%$ at $\langle A_V \rangle \lesssim 1$ mag, up to $\sim 20\%$ at $\langle A_V \rangle \approx 10$ mag. For these cloud models, the fraction of H₂ mass lost $f_{\text{H}_2\text{mass}-\text{lost}}$ can be approximated by

$$f_{\text{H}_2\text{mass}-\text{lost}} = 1 - f_{\text{H}_2\text{mass}} \approx 1 - 0.092 \langle A_V \rangle / [\text{mag}], \quad (5.17)$$

for UV=1 and $\langle A_V \rangle \leq 10$ mag.

Fig. 5.20 (bottom) is the same as Fig. 5.20 (top), but $f_{\text{H}_2\text{mass}}$ is plotted as a function of UV. $f_{\text{H}_2\text{mass}}$ decreases towards high UV. The “true” H₂ mass is underestimated by $\sim 40\%$ for UV=10 to $\sim 65\%$ for UV=1000. For the simulations with varying UV, $f_{\text{H}_2\text{mass}-\text{lost}}$ can be approximated by

$$f_{\text{H}_2\text{mass}-\text{lost}} = 1 - f_{\text{H}_2\text{mass}} \approx \begin{cases} 0 & \text{UV} = 0 \text{ G}_0 \\ 0.2 + 0.17 \log_{10} UV & \text{UV} \geq 1 \text{ G}_0. \end{cases} \quad (5.18)$$

Environmental conditions are very important for estimating a trustworthy H₂ mass. Cloud models with CO/H₂ ratios $\sim 10^{-4}$ ($\langle A_V \rangle \gtrsim 6$ mag) present very different W_{CO} maps, not only due to CO photodissociation at local $A_V \lesssim 3$ mag, but also because of CO ($J=1-0$) intensity saturation at higher local A_V . If a unique X-factor is used in order to estimate the H₂ mass, these values may be underestimated from a small percentage up to $\sim 70\%$. This fraction cannot be related only to the visual extinction, but it has also to be linked to the variations in the radiation field strength.

5.6 Summary and Conclusions

In this chapter, we made an analysis of the temperature and CO density distributions and in a large set of numerical simulations. Radiative transfer calculations were performed in order to study the CO ($J=1-0$) emission line. From this, we calculated the brightness and excitation temperatures. The later was used to infer the CO column density purely from emission. Moreover, we found variations on the X-factor depending on the environmental conditions, as well as very different estimates of the H₂ masses when they are inferred from CO integrated intensity maps. The main results can be summarized as follow:

- Most of the CO is located at number densities greater than 100 cm^{-3} and T_K below 40 K, regardless of n_0 , Z and the UV radiation field strength.
- The CO abundance increases as the product $n_0 \times Z$ grows and/or the UV radiation field strength becomes weaker.
- The average kinetic temperature decreases towards high A_V . $\langle T_K \rangle_{\text{CO}}$ relates to A_V in a fashion $\langle T_K \rangle_{\text{CO}} \propto \langle A_V \rangle^{1/4}$.
- The average brightness temperature of the clouds does not exhibit a trend with the kinetic temperature, indicating that on average most of the clouds are not in LTE. Although the peak $T_{\text{b,max}}$ does.
- Most of the clouds are subthermally excited, meaning that $\langle T_{\text{ex}} \rangle_{\text{CO}}$ is a lower limit of $\langle T_K \rangle_{\text{CO}}$.
- $\langle T_{\text{ex}} \rangle_{\text{CO}}$ exhibits a correlation with N , but not with A_V . It also shows a correlation with the UV field strength, although it is very subtle.

- The best method to estimate the CO column density from CO emission is using the complete PPV T_b spectrum to calculate $T_{\text{ex,obs}}$ in Eq. 5.7. However, the accuracy still depends on n_0 , Z and UV on a second order.
- $\langle W_{\text{CO}} \rangle_{\text{M}}$ saturates for $A_V \gtrsim 6$ mag, causing an approximately constant X-factor. At lower visual extinctions, $\langle W_{\text{CO}} \rangle_{\text{M}}$ varies by 2-3 orders of magnitude, while the X-factor changes by less than 2.
- For $A_V \lesssim 10$ mag, the estimates of H_2 mass calculated from $\langle W_{\text{CO}} \rangle_{\text{M}}$ together with a single Milky Way-like X-factor improve towards high A_V . For higher visual extinctions, CO emission becomes saturated and the H_2 mass is underestimated.

In general, these results indicate that CO ($J=1-0$) emission does not trace the kinetic temperature of molecular clouds. Molecular clouds are on average not in LTE. It is necessary to consider other tracers for the temperatures and densities (like C^+ , HCO^+ , NH_3) of molecular gas in order to obtain a trustworthy picture of the physical conditions of molecular clouds.

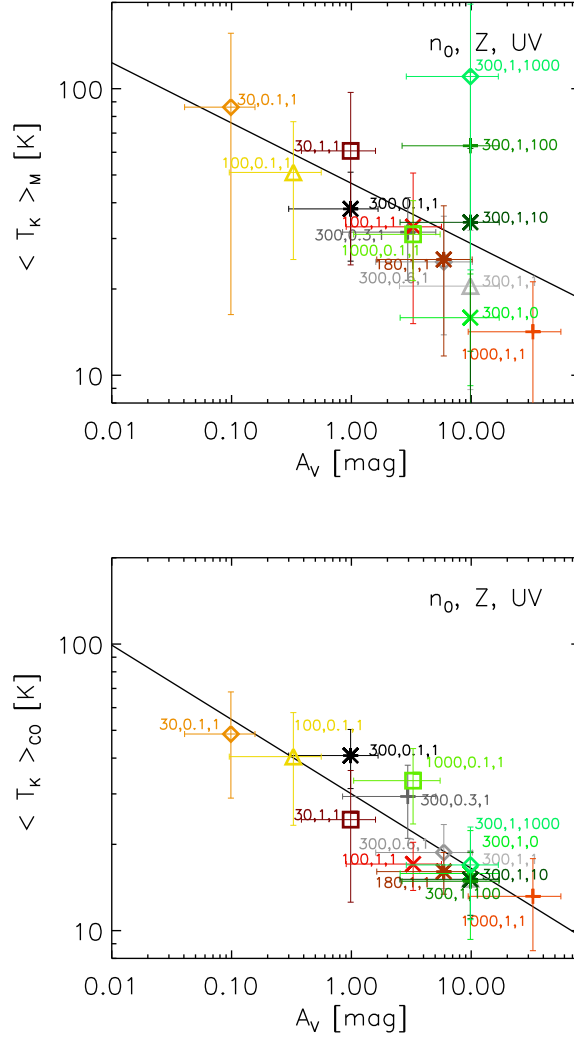


Figure 5.4: Top: mass-weighted average of the kinetic temperature $\langle T_K \rangle_M$ as a function of the mean visual extinction. The black line shows a linear regression made on the logarithm of the data, from which we obtain $\langle T_K \rangle_M \propto \langle A_V \rangle^{-1/5}$. Bottom: same as Top but CO mass-weighted average $\langle T_K \rangle_{CO}$. From the linear regression, we obtain $\langle T_K \rangle_{CO} \propto \langle A_V \rangle^{-1/4}$. The colors and labels are arranged in the same fashion as in previous figures.

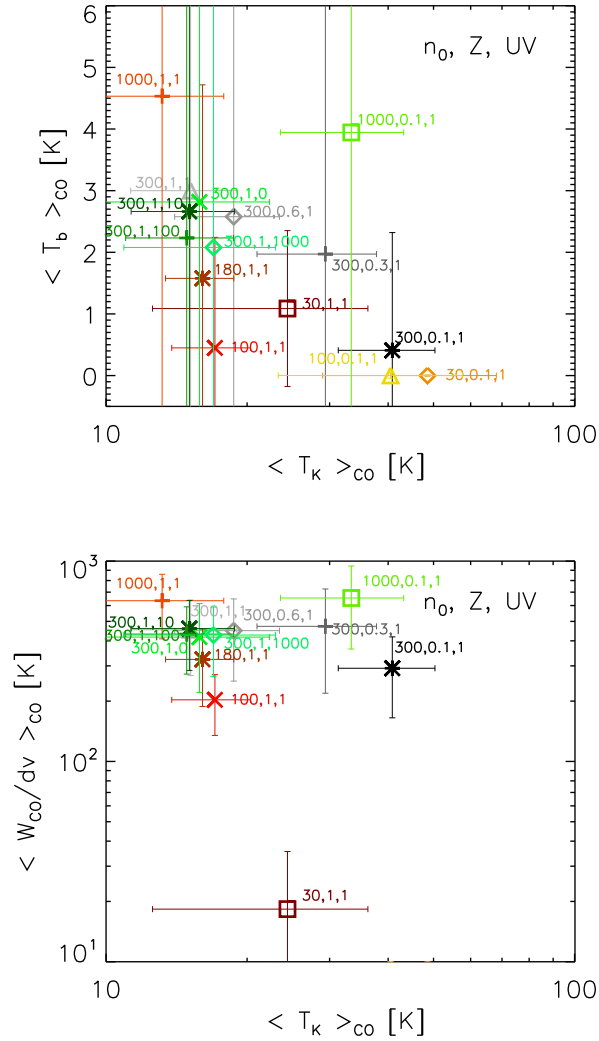


Figure 5.5: Top: CO mass-weighted average of the brightness temperature $\langle T_b \rangle$ as a function of $\langle T_K \rangle_{CO}$. Bottom: same as Top but for the integrated emission along the line of sight. The colors and labels are arranged in the same fashion as in previous figures.

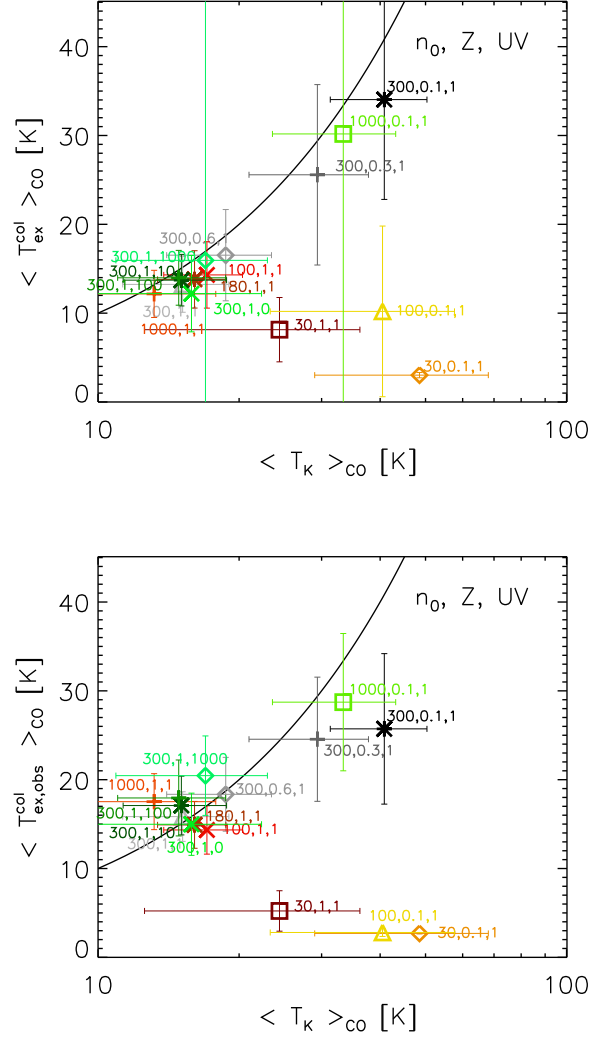


Figure 5.7: Top: CO mass-weighted average of the excitation temperature calculated using the Boltzmann Equation 5.4 $\langle T_{\text{ex}}^{\text{col}} \rangle_{\text{CO}}$ as a function of $\langle T_{\text{K}} \rangle_{\text{CO}}$. Bottom: Same as Top, but the excitation temperature is calculated considering the Dickman (1978) formula (Eq. 5.5) $\langle T_{\text{ex,obs}}^{\text{col}} \rangle_{\text{CO}}$. In both figures, the black line shows the one-to-one relation between the temperatures. The arrange of colors and labels are the same as in previous figures.

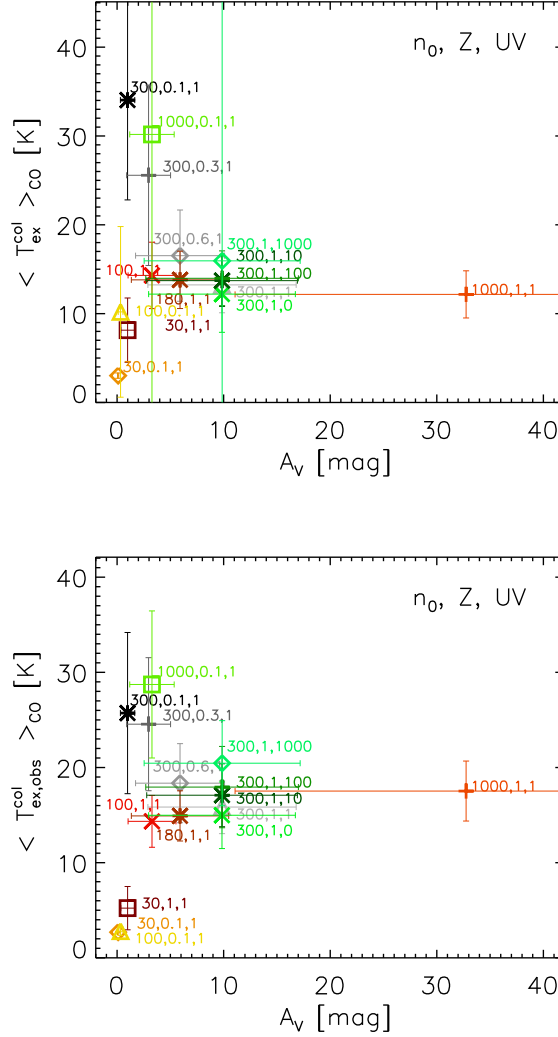


Figure 5.8: Top: CO mass-weighted average of $\langle T_{\text{ex}}^{\text{col}} \rangle_{\text{CO}}$ as a function of $\langle A_V \rangle$. Bottom: Same as Top, but the excitation temperature is calculated considering the [Dickman \(1978\)](#) formula $\langle T_{\text{ex,obs}}^{\text{col}} \rangle_{\text{CO}}$. The arrange of colors and labels are the same as in previous figures.

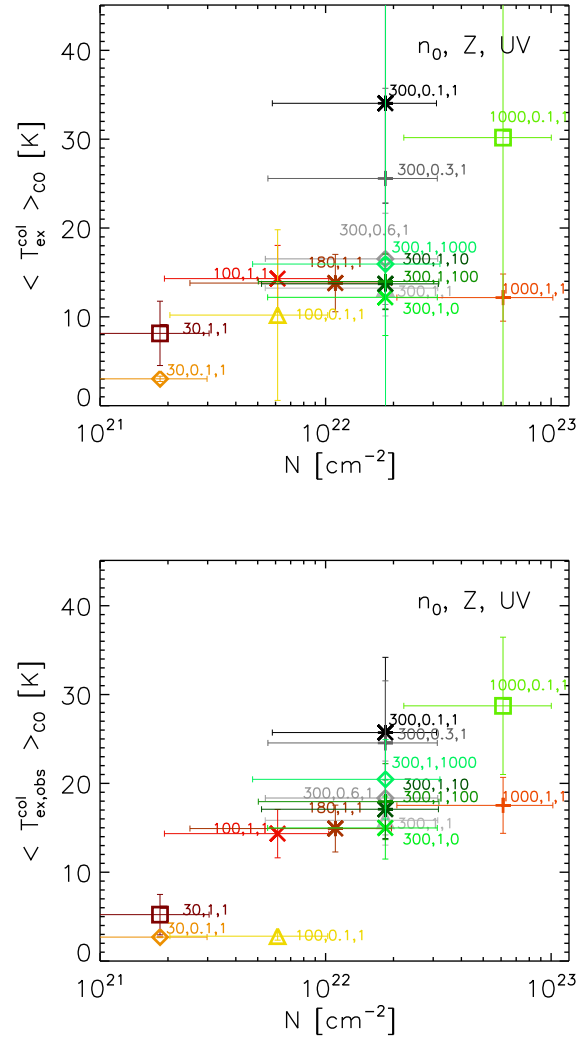


Figure 5.9: Top: CO mass-weighted average of $\langle T_{\text{ex}}^{\text{col}} \rangle_{\text{CO}}$ as a function of $\langle N \rangle$. Bottom: Same as Top, but for $\langle T_{\text{ex,obs}}^{\text{col}} \rangle_{\text{CO}}$. The arrange of colors and labels are the same as in previous figures.

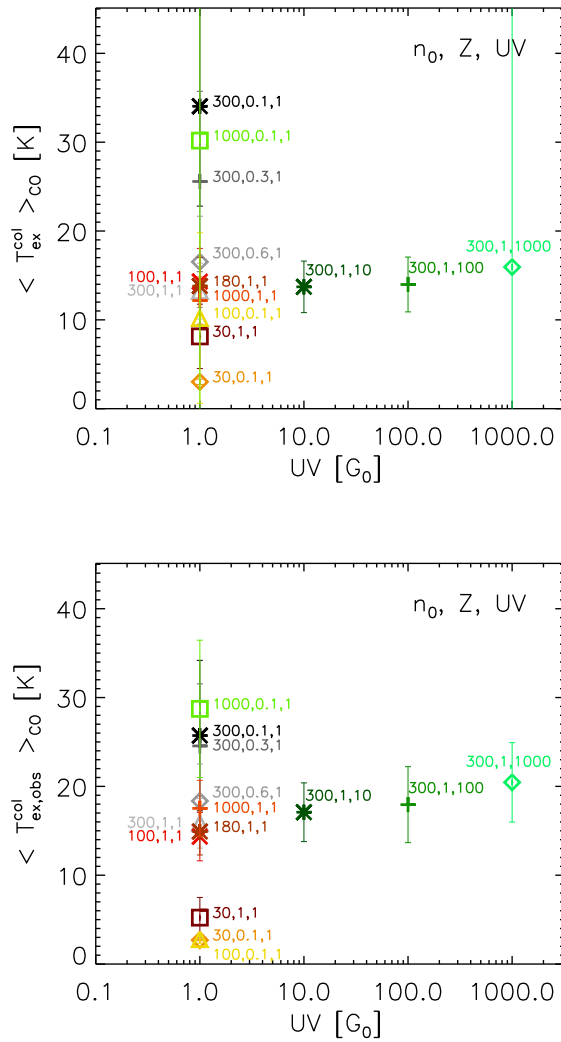


Figure 5.10: Top: CO mass-weighted average of $\langle T_{\text{ex}}^{\text{col}} \rangle_{\text{CO}}$ as a function of $\langle N \rangle$. Bottom: Same as Top, but for $\langle T_{\text{ex,obs}}^{\text{col}} \rangle_{\text{CO}}$. The arrange of colors and labels are the same as in previous figures.

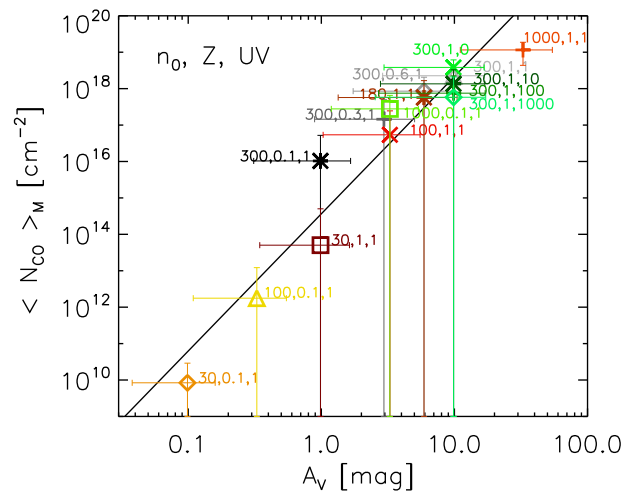


Figure 5.11: Mass-weighted average of the “true” CO column density N_{CO} as a function of the mean A_V . The arrange of colors and labels are the same as in previous figures.

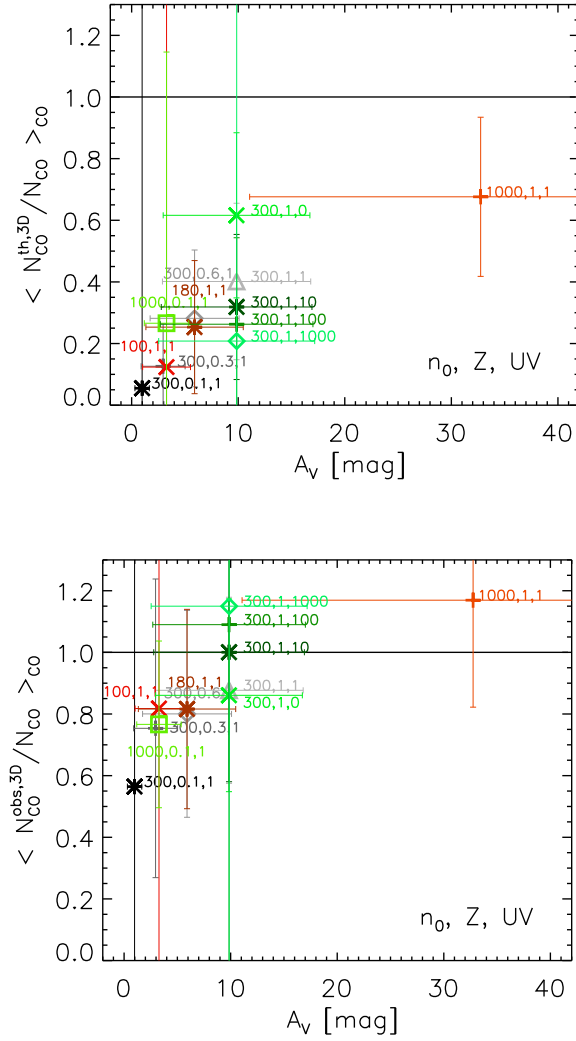


Figure 5.12: Top: CO mass-weighted average of the estimated CO column density using $T_{\text{ex}}(v)$ (Boltzmann Equation 5.4) into Eq. 5.7 as a function of $\langle A_V \rangle$. Bottom: Same as Top, but considering $T_{\text{ex,obs}}(v)$ (Dickman, 1978 formula, Eq. 3.6). The arrange of colors and labels are the same as in previous figures.

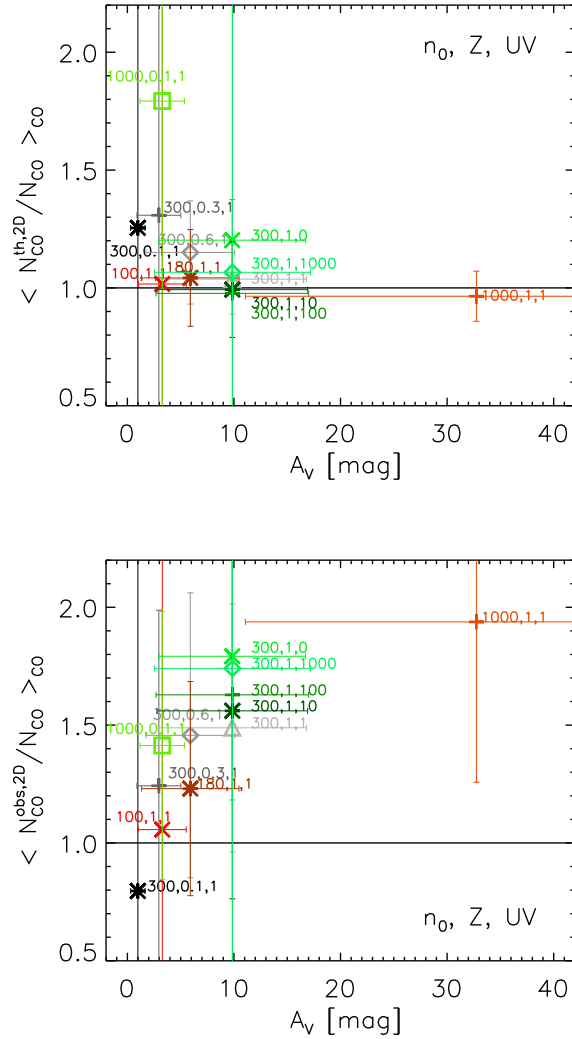


Figure 5.13: Top: CO mass-weighted average of the estimated CO column density using $T_{\text{ex}}^{\text{col}}$ (from Boltzmann Equation 5.4) into Eq. 5.7 as a function of $\langle A_V \rangle$. Bottom: Same as Top, but considering $T_{\text{ex,obs}}^{\text{col}}$ (Dickman, 1978 formula, Eq. 5.5). The arrange of colors and labels are the same as in previous figures.

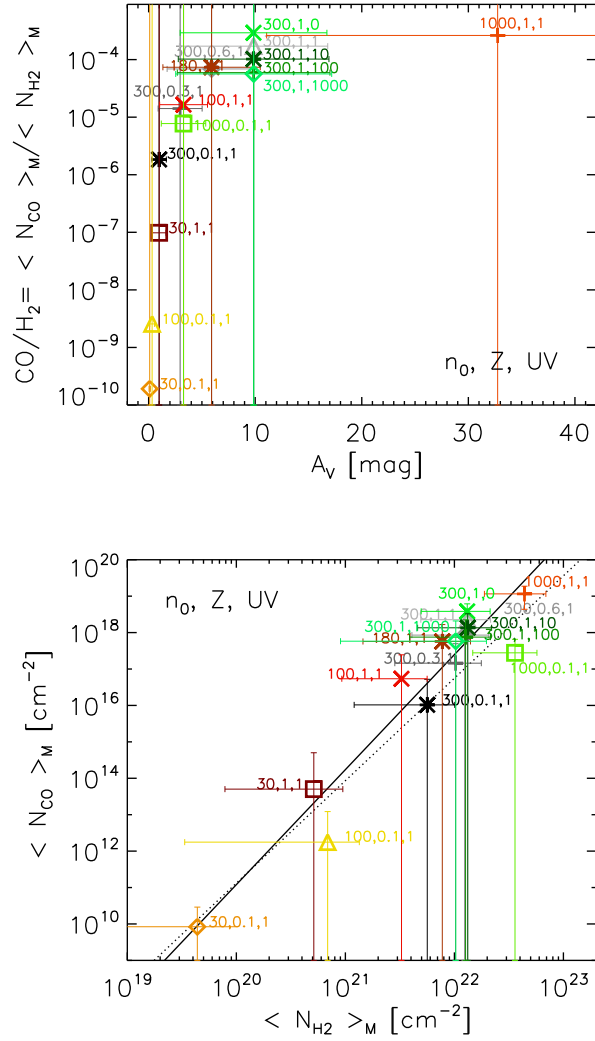


Figure 5.14: Top: ratio of the mass-weighted averages $\langle N_{\text{CO}} \rangle_M / \langle N_{\text{H}_2} \rangle_M$ as a function of the mean A_V . Bottom: mass-weighted average of N_{CO} as a function of the mass-weighted average of N_{H_2} . The black line shows the relationship $\langle N_{\text{CO}} \rangle_M \propto \langle N_{\text{H}_2} \rangle_M^{3.2}$. For $A_V \leq 4$ mag, $\langle N_{\text{CO}} \rangle_M \propto \langle N_{\text{H}_2} \rangle_M^{2.8}$ (dotted line). The colors and labels are arranged in the same fashion as previous figures.

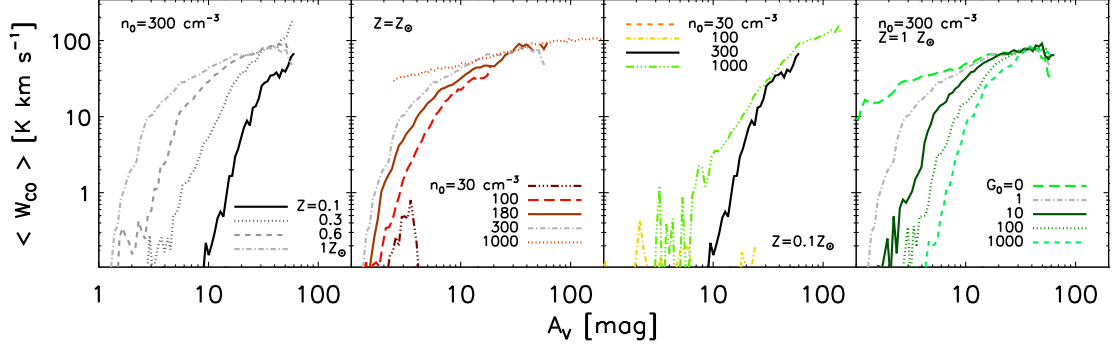


Figure 5.15: Average of the integrated intensity at every A_V bin $\langle W_{\text{CO}} \rangle$ as a function of A_V . The lines and colors are arranged in the same fashion as Fig. 5.1.

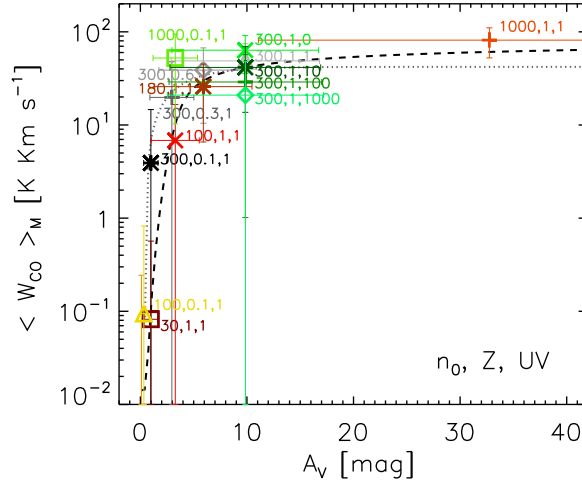


Figure 5.16: Mass-weighted average of the integrated intensity $\langle W_{\text{CO}} \rangle_M$ as a function of the mean A_V . The dashed line shows the fitting function $\langle W_{\text{CO}} \rangle_M \approx 12.14 \sqrt{\ln(1 + 8 \times 10^{-5} \langle A_V \rangle^{7.94})}$ [K km s⁻¹]. Following Pineda et al. (2008), the dotted line indicates the fitting $\langle W_{\text{CO}} \rangle_M \approx 56.7 [1 - e^{-0.114(\langle A_V \rangle - 1.007)}]$ [K km s⁻¹]. The arrange of colors and labels are the same as in previous figures.

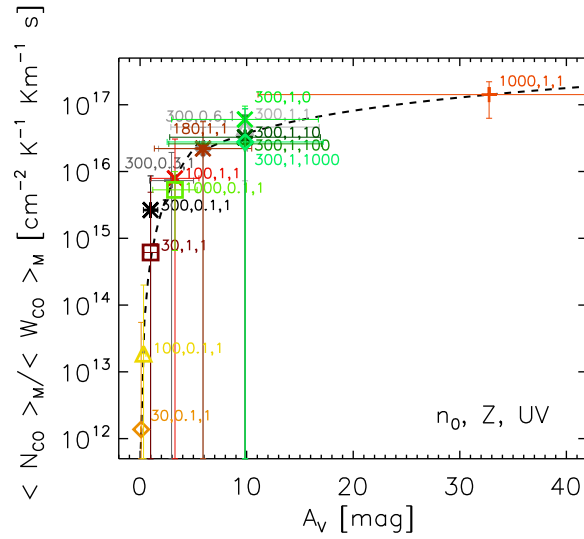


Figure 5.17: Ratio of the mass weighted averages of N_{CO} -to- W_{CO} as a function of the mean A_V . The dashed line shows the fit shown in Eq. 5.13. The arrange of colors and labels are the same as in previous figures.

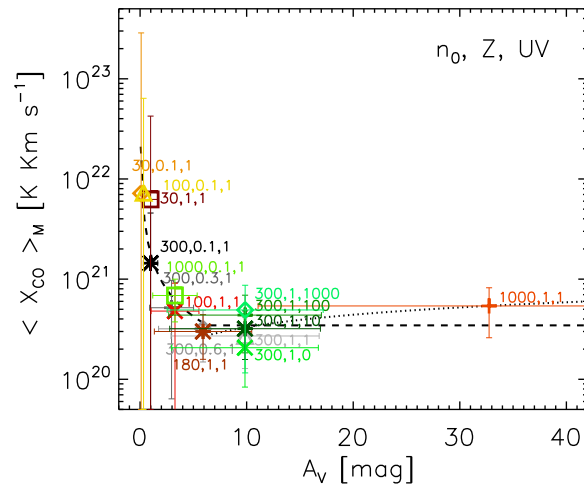


Figure 5.18: Mass weighted average of the X-factor as a function of the mean A_V . The dashed line shows the relationship given in Eq. 5.14 and the dotted line indicates the fitting made for the data at $\langle A_V \rangle \geq 6$ mag. The arrange of colors and labels are the same as in previous figures.

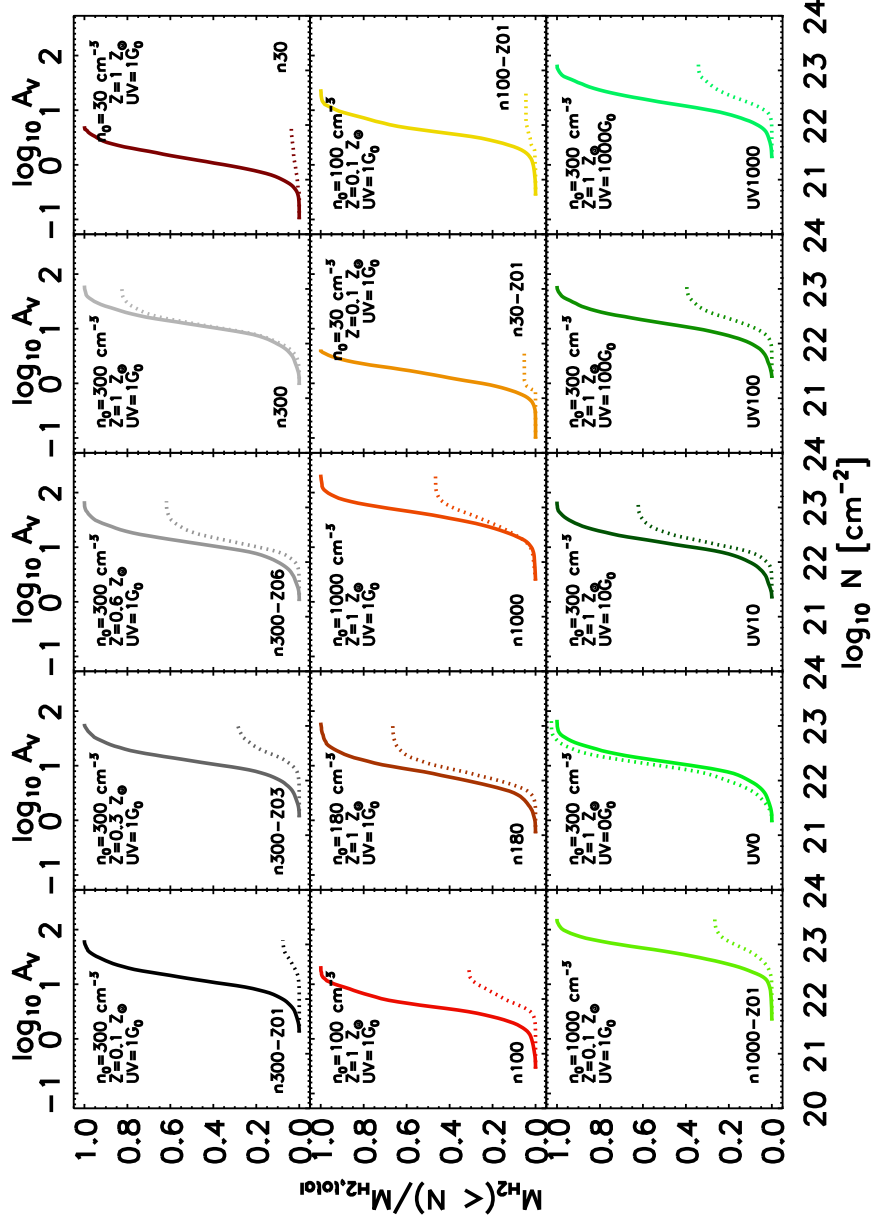


Figure 5.19: Cumulative mass of H_2 below a given column density as a function of N (A_V is plotted as reference at the top) normalized by the total “true” mass of H_2 . The solid lines shows the true H_2 mass and the dotted lines shows the H_2 mass estimated from X_{MW} and W_{CO} . The lines and colors are arranged in the same fashion as previous figures.

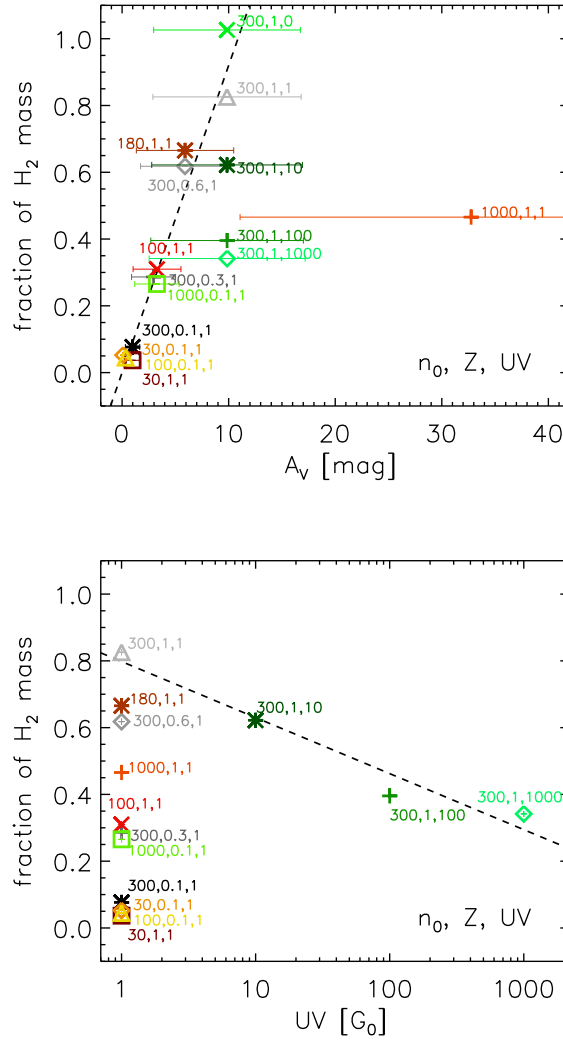


Figure 5.20: Top: Total fraction of H₂ estimated from Eq. 5.16 and normalized by the total “true” H₂ mass as a function of the mean A_V . The dashed line shows a linear regression for the data with $UV=1$, excluding the simulations n_{1000} . Bottom: same as Top, but as a function of UV . The dashed line indicates a linear regression made for the simulations with $UV \geq 1$. The lines and colors are arranged in the same fashion as previous figures.

Chapter 6

Density variance–Mach number relation

¹ Detailed knowledge about the statistical characteristics of the density structure is of pivotal importance for many fields in astronomy and astrophysics. Probability distribution functions (PDFs) of the density have been introduced as a simple and robust measure of the one-point statistics for many applications, ranging from cosmology, where the Press-Schechter formalism was primarily established ([Press and Schechter, 1974](#)), to star formation and theories of the initial mass function or the core mass function (e.g., [Fleck, 1982](#); [Zinnecker, 1984](#); [Padoan et al., 1997](#); [Klessen and Burkert, 2000](#); [Li et al., 2004](#); [Hennebelle and Chabrier, 2008, 2009](#); [Padoan and Nordlund, 2011](#)).

In the star formation context, the relation between the width of the density PDF – the density variance or standard deviation – and the root-mean-square (rms) Mach number in supersonic turbulent flow is a key ingredient for analytical models of the star formation rate ([Krumholz and McKee, 2005](#); [Padoan and Nordlund, 2011](#)), and for the stellar initial mass function or the core mass function ([Padoan and Nordlund, 2002](#); [Hennebelle and Chabrier, 2008, 2009](#)). In this framework, supersonic turbulence plays a fundamental role in determining the density and velocity statistics of the interstellar medium ([Elmegreen and Scalo, 2004](#); [McKee and Ostriker, 2007](#)) and controls stellar birth ([Mac Low and Klessen, 2004](#)). Conversely, the importance of magnetic fields in the star formation process is still inconclusive, despite decades of research ([Mouschovias and Ciolek, 1999](#); [McKee and Ostriker, 2007](#); [Crutcher et al., 2009](#); [Crutcher et al., 2010](#); [Bertram et al., 2012](#)). Hence, the question of how magnetic fields affect the density variance–Mach

¹This chapter is partially based on the published work in [Molina et al. \(2012\)](#).

number relation is still not clearly answered, despite the empirical findings of [Ostriker et al. \(2001\)](#) and the analytical ansatz provided by [Padoan and Nordlund \(2011\)](#).

For purely hydrodynamical, supersonic, isothermal, turbulent gas, the relation between the density variance and Mach number has been identified and widely studied in numerical simulations (e.g., [Padoan et al., 1997](#); [Passot and Vázquez-Semadeni, 1998](#); [Federrath et al., 2008a](#); [Federrath et al., 2008b](#); [Federrath et al., 2010](#); [Price et al., 2011](#)). This relation is commonly assumed to be linear,

$$\sigma_{\rho/\rho_0} = b\mathcal{M}, \quad (6.1)$$

where σ_{ρ/ρ_0}^2 is the density variance (to emphasise the density fluctuations about the mean ρ_0 , it makes sense to express the density in terms of the density contrast ρ/ρ_0), b is a proportionality constant of order unity as explained in more detail below, and \mathcal{M} is the rms Mach number. Usually, the density contrast is written in terms of its logarithm, $s \equiv \ln(\rho/\rho_0)$.

Several authors have noted that the PDF of the logarithm of the density contrast s – produced by supersonic turbulent flow of isothermal gas – follows approximately a lognormal distribution (e.g. [Vázquez-Semadeni, 1994](#); [Padoan et al., 1997](#); [Passot and Vázquez-Semadeni, 1998](#); [Nordlund and Padoan, 1999](#); [Klessen, 2000](#); [Ostriker et al., 2001](#); [Li et al., 2003](#); [Kritsuk et al., 2007](#); [Federrath et al., 2008b](#); [Lemaster and Stone, 2008](#); [Schmidt et al., 2009](#); [Glover et al., 2010](#); [Federrath et al., 2010](#); [Padoan and Nordlund, 2011](#); [Collins et al., 2011](#); [Price et al., 2011](#)),

$$p_s ds = \frac{1}{\sqrt{2\pi\sigma_s^2}} \exp\left[-\frac{(s-s_0)^2}{2\sigma_s^2}\right] ds, \quad (6.2)$$

where the mean s_0 is related to the density variance by $s_0 = -\sigma_s^2/2$, due to the constraint of mass conservation. Besides the empirical findings of [Vázquez-Semadeni \(1994\)](#), [Padoan et al. \(1997\)](#), and [Passot and Vázquez-Semadeni \(1998\)](#), there is no clear explanation for the shape of the PDF. From a mathematical point of view, a log-normal distribution is the result of independent random perturbations driven in a stationary system ([Pope and Ching, 1993](#)) as a consequence of the central limit theorem ([Vázquez-Semadeni, 1994](#); [Padoan et al., 1997](#); [Nordlund and Padoan, 1999](#); [Federrath et al., 2010](#)). The physical interpretation is that density fluctuations present at a given location are produced by successive passages of shocks with amplitudes independent of the local density. For a log-normal distribution, the density variance – given by Equation (6.1) – is equivalent to

$$\sigma_s^2 = \ln [1 + b^2 \mathcal{M}^2]. \quad (6.3)$$

The parameter b in Equations (6.1) and (6.3) is related to the kinetic energy injection mechanism – the forcing \mathbf{F} , which drives the turbulence. Federrath et al. (2008b) found that $b = 1$ for purely compressive (curl-free) forcing, $\nabla \times \mathbf{F} = 0$, while $b = 1/3$ for purely solenoidal (divergence-free) forcing, $\nabla \cdot \mathbf{F} = 0$. In a follow-up study, Federrath et al. (2010) showed that b increases smoothly from $1/3$ to 1 , when the fraction of energy in compressive modes, $F_{\text{comp}}/(F_{\text{sol}} + F_{\text{comp}})$ is gradually increased from 0 to 1 . For the natural mixture of modes, $F_{\text{comp}}/(F_{\text{sol}} + F_{\text{comp}}) = 1/3$, which is also the mixture of forcing modes used in all our numerical experiments here, they found $b \approx 0.4$, so we will later use that value for comparing our analytic model with numerical simulations.

When magnetic fields are included, the density variance is significantly lower than in the unmagnetised case for simulations with Mach numbers $\mathcal{M} \gtrsim 10$ (Ostriker et al., 2001; Price et al., 2011). Recently, Padoan and Nordlund (2011) provided an analytical ansatz for the hydrodynamical density contrast in supersonic, turbulent flow, which in turn follows the approach of Dyson and Williams (1980) for obtaining the density contrast for strong adiabatic shocks, but extended to the magnetic case. Their σ_s - \mathcal{M} relation was, however, not tested with numerical simulations.

The density PDF may or may not deviate from a log-normal form when other processes – like heat exchange and gravitation – are included. For example, when a non-isothermal equation of state is considered, the PDF still closely follows a log-normal distribution over a range of densities (see e.g., Glover and Mac Low, 2007b). However, depending on whether the equation of state is softer or harder than isothermal, it might acquire power-law tails either at high or low densities (Passot and Vázquez-Semadeni, 1998; Scalo et al., 1998; Wada, 2001; Li et al., 2003; McKee and Ostriker, 2007). The density PDF also deviates from log-normal when gravity is included. In this case, the PDF exhibits a power-law tail at high densities (Klessen, 2000; Federrath et al., 2008a; Kainulainen et al., 2009; Cho and Kim, 2011; Kritsuk et al., 2011). In addition, turbulent intermittency also leads to deviations from the log-normal PDF in the wings of the distribution (Federrath et al., 2010). Consequently, the accuracy of the measurement of the density variance, using Equation (6.2), may be compromised depending on the importance of the different processes involved in real molecular clouds.

Here, we show first an analytical derivation for the σ_s - \mathcal{M} relation in supersonic turbulent isothermal gas including magnetic fields. Our results are in qualitative agreement with Ostriker et al. (2001) and Price et al. (2011),

however, here we present quantitative predictions and tests. Then, we present the extension of the analytical prediction for non-isothermal gas.

6.1 Analytical derivation

Our basis for obtaining the density variance–Mach number relationship involves determining how the density contrast changes with the Mach number. The density variance σ_{ρ/ρ_0} and the density contrast are related by:

$$\sigma_{\rho/\rho_0}^2 = \frac{1}{V} \int_V \left(\frac{\rho}{\rho_0} - 1 \right)^2 dV, \quad (6.4)$$

where ρ is the local density, ρ_0 is the mean density in the volume, and V is the volume of the cloud. The density contrast is a measure of the density fluctuations in the flow, and therefore it is useful for identifying the disturbances that originate from shock fronts and compressions.

6.1.1 Density contrast in magnetohydrodynamics

Supersonic turbulence in the interstellar medium generates a complex network of shock waves (or simply shocks). When the velocity of the fluid exceeds that of sound, it leads to the formation of shocks that are one of the most important distinctive effects of the compressibility of the fluid (e.g., [Landau and Lifshitz, 1987](#)).

In order to study the density contrast in a molecular cloud, we first consider the physics of the discontinuity formed by a single shock front. We then generalize the results to the ensemble of shocks confined in a cloud. Following [Lequeux \(2005\)](#), we describe a shock by choosing two control surfaces, one on either side of the discontinuity, and parallel to each other. Let us choose the shock surfaces as the reference frame, such that the control surfaces are stationary with respect to the shock. We also define the “parallel” direction as the one parallel to the flow of gas through the shock (i.e., perpendicular to the shock front). From the well known equations of fluid dynamics, it is then possible to derive equations that express the conservation of matter, momentum, and energy flux for a magnetized inviscid, non-self gravitating, neutral fluid:

$$v_{\parallel,1}\rho_1 = v_{\parallel,2}\rho_2, \quad (6.5)$$

and

$$\rho_1 \left(v_{\parallel,1}^2 + \frac{c_{s,1}^2}{\Gamma_1} + \frac{v_{A\perp,1}^2}{2} \right) = \rho_2 \left(v_{\parallel,2}^2 + \frac{c_{s,2}^2}{\Gamma_2} + \frac{v_{A\perp,2}^2}{2} \right), \quad (6.6)$$

respectively. In these equations, the subscripts 1 and 2 indicate the pre- and post-shock conditions, respectively. The velocity of the gas into the shock is v_{\parallel} , while c_s is the adiabatic sound speed, Γ corresponds to the index of a polytrope $P_{th} = K\rho^{\Gamma}$, and $v_{A\perp}$ is the Alfvén velocity, defined here as $v_{A\perp} = B_{\perp}/(4\pi\rho)^{1/2}$, where B_{\perp} is the magnetic field perpendicular to the flow direction. The post-shock density is described by ρ_2 .

For the energy conservation equation, Eq. 1.5, we assume that the shock surfaces are sufficiently close that the term for the net gain or loss of internal energy due to radiative and chemical heating and cooling (Λ) in the shock jump conditions is approximately (Draine, 2011)

$$\int_1^2 \Lambda dx \approx 0, \quad (6.7)$$

where x denotes the “parallel” direction. Moreover, the thermal conductivity is neglected $\kappa_T \vec{\nabla} T = 0$.

The equation for the conservation of energy is then:

$$\left(\frac{v_1^2}{2} + h_1 + v_{A\perp,1}^2 \right) \rho_1 \vec{v}_1 = \left(\frac{v_2^2}{2} + h_2 + v_{A\perp,1}^2 \right) \rho_2 \vec{v}_2, \quad (6.8)$$

where h is the enthalpy. The enthalpy is

$$h = \frac{\Gamma}{\Gamma - 1} \frac{P_{th}}{\rho}. \quad (6.9)$$

Introducing Eq. 6.9 into Eq. 6.8 and considering only the module of the “parallel” component of the velocity, we rewrite Eq. 6.8 as

$$\frac{v_{\parallel,1}^2}{2}(\Gamma_1 - 1) + c_{s,1}^2 + v_{A\perp,1}^2 = \frac{v_{\parallel,2}^2}{2}(\Gamma_2 - 1) + c_{s,2}^2 + v_{A\perp,2}^2, \quad (6.10)$$

where the sound speed is

$$c_s^2 = \left(\frac{\partial P_{th}}{\partial \rho} \right) = \frac{\Gamma P_{th}}{\rho}. \quad (6.11)$$

6.1.2 The isothermal case

We now make two important approximations. As we wish to focus on the role of magnetic fields in determining the density variance first, we assume that the gas is isothermal, deferring consideration of non-isothermal effects to §6.3. Our assumption of isothermality implies that $\Gamma_1 = \Gamma_2 = 1$, and

here that $c_{s,1} = c_{s,2} = c_s$. Second, as we are considering an entire molecular cloud, we approximate it as an ensemble of shocks. We assume that we can express the average pre-shock velocity in terms of the rms velocity v_0 – hereafter, the subscript “0” indicates the volume averages – as $v_{\parallel,0}^2 = b^2 v_0^2$, where the factor b depends on the number of degrees of freedom available for the compressive modes (Federrath et al., 2008b). We also assume that the typical pre-shock magnetic and thermal pressures are just those given by volume averages over the total volume, allowing us to write them in terms of the volume-averaged density ρ_0 and the rms Alfvénic velocity $v_{A,0}$. Similarly, we assume that the typical pre-shock density is simply the volume-averaged density. Making these assumptions, and introducing the ratio of the thermal pressure to magnetic pressure

$$\beta \equiv \frac{P_{\text{th}}}{P_{\text{mag}}} = 2 \frac{c_s^2}{v_A^2}, \quad (6.12)$$

we can rewrite Equation (6.6) as

$$b^2 \mathcal{M}^2 \frac{\rho_0}{\rho_2} \left(1 - \frac{\rho_0}{\rho_2} \right) + \frac{\rho_0}{\rho_2} (1 + \beta_0^{-1}) = (1 + \beta_2^{-1}), \quad (6.13)$$

where the rms Mach number is given by $\mathcal{M} = v_0/c_s$.

In order to solve this equation for the characteristic density contrast associated with the shocked gas, ρ_2/ρ_0 , it is necessary to determine β_2 , the post-shock ratio of the thermal to magnetic pressures. The value of this will depend on the change in the magnetic field strength through the shock, which in turn depends on the orientation of the field with respect to the flow of gas through the shock. Using magnetic flux and mass conservation during compression, one can show that $B \propto \rho^\alpha$ with $0 \leq \alpha \leq 1$, depending on the field geometry and direction of compression. In the extreme case where the gas flows in a direction parallel to the field lines, the field strength will be the same on either side of the shock despite the jump in density, and the field strength then will be independent of density, i.e., $\alpha = 0$. In the other extreme case where the field is oriented at right-angles to the gas flow, the shock jump conditions for magnetic flux freezing imply that $B \propto \rho$, i.e., $\alpha = 1$. Meanwhile, compression of an isotropic field along all three spatial directions gives $B \propto \rho^{2/3}$. However, for our “average shock”, we expect behaviour that lies somewhere between $0 \lesssim \alpha \lesssim 1$. By looking at observations and existing simulations, we can get some guidance as to what this intermediate behaviour should be.

Observationally, Crutcher (1999) presented a study of the magnetic field strength in molecular clouds measured with the Zeeman effect. He fitted

the results with a power law $B \propto \rho^\alpha$ and found that $\alpha = 0.47 \pm 0.08$. [Crutcher et al. \(2003\)](#) provided additional support for this result. More recently, [Crutcher et al. \(2010\)](#) have presented a detailed compilation of Zeeman data based on a much larger number of measurements. They find that at number densities $n < 300 \text{ cm}^{-3}$, the data is consistent with a field strength that is independent of density, while at higher densities they obtain $B \propto \rho^{0.65 \pm 0.05}$.

From a theoretical point of view, [Padoan and Nordlund \(1999\)](#) noted that their B distributions closely match the observational scaling given by [Crutcher \(1999\)](#) and [Crutcher et al. \(2003\)](#), $B \propto \rho^{1/2}$, for high B in their high Alfvénic Mach number regime. [Kim et al. \(2001\)](#) also study the relationship between B and ρ , and find that $\alpha \simeq 0.4$, albeit with large scatter, especially at low densities. Additionally, [Banerjee et al. \(2009\)](#) report that the magnetic field strength appears to scale in their simulations as $B \propto \rho^{1/2}$ for number densities $10^2 \lesssim n \lesssim 10^4 \text{ cm}^{-3}$, although with significant scatter around this value. On the other hand, [Hennebelle and Pérault \(2000\)](#) found that the magnetic field does not necessarily increase with the density. Aside from these reports, if the magnetic flux is not conserved, but increases due to turbulent dynamo amplification during compression, α can become larger than the values quoted above, depending on the Reynolds numbers of the gas ([Schleicher et al., 2010](#); [Sur et al., 2010](#); [Federrath et al., 2011](#); [Schober et al., 2012b,a](#)). Thus, even if the gas is compressed only parallel to the field lines, turbulent tangling of the field can lead to $\alpha > 0$ during compression.

Given the different possible relations between the magnetic field strength and the density, we consider three cases to include in Equation (6.13): the two extreme cases, where B is independent of the density, and where $B \propto \rho$, and an intermediate case with $B \propto \rho^{1/2}$. We also note that if we were to take instead the relation $B \propto \rho^{0.65}$ suggested by the most recent observational data, then we would obtain results quite similar to the $B \propto \rho^{1/2}$ case.

First case: B independent of ρ

We start by considering one extreme, the case where B is independent of the density. In this scenario, Equation (6.13) becomes a second-order equation, independent of the magnetic field strength

$$\left(\frac{\rho_2}{\rho_0}\right)^2 - (b^2 \mathcal{M}^2 + 1) \left(\frac{\rho_2}{\rho_0}\right) + b^2 \mathcal{M}^2 = 0.$$

This equation results in a density contrast

$$\frac{\rho_2}{\rho_0} = b^2 \mathcal{M}^2. \quad (6.14)$$

Equation (6.14) matches the density contrast for the non-magnetic regime (see e.g., Padoan et al., 1997). This is not surprising, because in this case we are assuming that the gas and the magnetic field are not coupled. Therefore, amplification of the magnetic field with density is not expected under these conditions.

Second case: $B \propto \rho^{1/2}$

In the intermediate case in which $B \propto \rho^{1/2}$, we again find a second-order equation for the density contrast, but with a dependence on the magnetic field expressed in terms of β_0 . From Equation (6.13), we obtain

$$(1 + \beta_0^{-1}) \left(\frac{\rho_2}{\rho_0} \right)^2 - (b^2 \mathcal{M}^2 + 1 + \beta_0^{-1}) \left(\frac{\rho_2}{\rho_0} \right) + b^2 \mathcal{M}^2 = 0.$$

This equation has the solution:

$$\frac{\rho_2}{\rho_0} = b^2 \mathcal{M}^2 \left(\frac{\beta_0}{\beta_0 + 1} \right). \quad (6.15)$$

In other words, the effect of the magnetic field in this case is to reduce the density contrast by a factor $\beta_0/(\beta_0 + 1)$. We see from this that in the weak field limit where $\beta_0 \rightarrow \infty$, we recover the hydrodynamical result, while for strong fields we have a smaller density contrast in the MHD case than in the non-magnetic case.

Third case: $B \propto \rho$

Finally, we investigate the other extreme case, where the magnetic field strength is proportional to the density. In this case, Equation (6.13) results in a third-order equation,

$$\beta_0^{-1} \left(\frac{\rho_2}{\rho_0} \right)^3 + \left(\frac{\rho_2}{\rho_0} \right)^2 - (b^2 \mathcal{M}^2 + 1 + \beta_0^{-1}) \left(\frac{\rho_2}{\rho_0} \right) + b^2 \mathcal{M}^2 = 0.$$

The solution for the density contrast is

$$\frac{\rho_2}{\rho_0} = \frac{1}{2} \left(-1 - \beta_0 + \sqrt{(1 + \beta_0)^2 + 4b^2 \mathcal{M}^2 \beta_0} \right). \quad (6.16)$$

6.2 The isothermal σ_S - \mathcal{M} relation

In the previous section, we presented three different expressions for the density contrast. They correspond to three different assumptions regarding the relationship $B \propto \rho^\alpha$, with $\alpha = 0, 1/2$, and 1. We now determine the density variance of a fluid in which there are many shocks, for each of these three cases.

We start by noting that in a highly supersonic flow, the dominant contribution to the integral in Equation (4) will come from shocked regions, and thus we can consider this equation as a volume average over an ensemble of many shocks. We next assume that we can approximate the value of this integral with the result of integrating over a single ‘‘average’’ shock of the kind considered in the previous section. As we already know the density contrast of this representative shock, the only thing that remains to be done before we can solve Equation (4) is to determine the appropriate volume over which to integrate.

We approximate the cloud as a cubic box of side L , and consider an infinitesimal part of its volume dV that encloses one shock. Therefore, the size of dV depends on the size of the shock itself

$$dV \approx dV_{sh}. \quad (6.17)$$

To define the shock volume, we make use of an approximation introduced by [Padoan and Nordlund \(2011\)](#), where the volume of the shock is given by the area of the box face times the shock width λ , $V_{sh} = L^2\lambda$. However, in the absence of viscosity, it is not straightforward to define the shock width λ . Therefore, we follow [Padoan and Nordlund \(2011\)](#) and assume that the shock width, if the compression is driven at the box scale, is given by

$$\lambda \simeq \theta L \rho_0 / \rho_2, \quad (6.18)$$

where θ is the integral scale of the turbulence. Then, the volume of the shock V_{sh} is given by

$$V_{sh} \simeq \theta L^3 \frac{\rho_0}{\rho_2}. \quad (6.19)$$

For turbulence driven on large scales, as appears to be the case in real molecular clouds ([Ossenkopf and Mac Low, 2002](#); [Brunt et al., 2009](#)), we have $\theta \simeq 1$. Having made the assumption that the appropriate volume over which to average is the volume of our representative shock, and considering Equation 6.17, we approximate dV by

$$dV = L^3 \left(\frac{\rho_0}{\rho_2} \right)^2 d \left(\frac{\rho_2}{\rho_0} \right). \quad (6.20)$$

Finally, inserting Equation (6.17) into Equation (6.4), yields

$$\sigma_{\rho/\rho_0}^2 = \int_1^{\frac{\rho}{\rho_0}} \left(1 - \frac{\rho_0}{\rho_2} \right)^2 d \left(\frac{\rho_2}{\rho_0} \right) = \frac{\rho}{\rho_0} - \frac{\rho_0}{\rho} - 2 \ln \left(\frac{\rho}{\rho_0} \right). \quad (6.21)$$

It is important to note that in this formulation, Equation (6.21) is physically meaningless if the lower limit of the integral is set between $0 < \rho/\rho_0 < 1$. This is due to the definition adopted for the shock width (Eq. 6.36), where the shock thickness is defined only for $\rho_2/\rho_0 > 1$. For highly supersonic turbulence, which is the regime that concerns us, the assumption $\rho \gg \rho_0$ is valid. Then, the first term in Equation (6.21) dominates the variance and we get

$$\sigma_{\rho/\rho_0}^2 \approx \frac{\rho}{\rho_0}. \quad (6.22)$$

For practical reasons, we prefer to consider the variance of the logarithm of the density contrast, $s = \ln(\rho/\rho_0)$, instead of the variance of the linear density when we will compare this analytical model with numerical simulations. These variances are related by (e.g., Federrath et al., 2008b; Price et al., 2011)

$$\sigma_s^2 = \ln \left[1 + \sigma_{\rho/\rho_0}^2 \right]. \quad (6.23)$$

We now insert the three cases considered in §6.1.1 into Equation (6.23), in order to obtain the density variance–Mach number relation. The subscripts of the following results are chosen based on the value $\alpha = 0, 1/2$ and 1 of the $B \propto \rho^\alpha$ relationship.

- **B independent of ρ**

The density variance in this case is exactly the same as for the purely hydrodynamical, isothermal case,

$$\sigma_{s,0}^2 = \ln \left[1 + b^2 \mathcal{M}^2 \right]. \quad (6.24)$$

- **$B \propto \rho^{1/2}$**

In this case, the density variance is:

$$\sigma_{s,1/2}^2 = \ln \left[1 + b^2 \mathcal{M}^2 \left(\frac{\beta_0}{\beta_0 + 1} \right) \right]. \quad (6.25)$$

This relation is similar to Equation (6.24) except for a correction factor due to the effects of magnetic fields, which is a function of the plasma β_0 only.

- **$B \propto \rho$**

Finally, the density variance–Mach number relation in this case is given by

$$\sigma_{s,1}^2 = \ln \left[1 + \frac{1}{2} \left(-1 - \beta_0 + \sqrt{(1 + \beta_0)^2 + 4b^2 \mathcal{M}^2 \beta_0} \right) \right]. \quad (6.26)$$

The density variance has a strong dependence on β_0 , leaving the rms Mach number as a marginal quantity in this relation.

In the last two cases, when $\beta_0 \rightarrow 0$, the Alfvénic velocity is much higher than the sound speed, and both relations approach zero. In this scenario, the magnetic pressure is infinitely large and prevents density fluctuations from forming. The gas is “frozen” in the magnetic field. In the opposite limit, when $\beta_0 \rightarrow \infty$, Equation (6.25) and Equation (6.26) simplify to the purely hydrodynamical case, as expected. In the next section, we are going to test these cases with numerical simulations.

6.2.1 Numerical test of the analytical model

Simulations

We have performed simulations of the evolution of the turbulent, dense, inviscid, magnetised (MHD) and unmagnetised (HD), isothermal interstellar medium using the ZEUS-MP hydrodynamical code (Norman, 2000; Hayes et al., 2006), whose basic setup is explained in §2. We neglect chemical reactions in order to study the effects of magnetic fields in molecular clouds, leaving the inclusion of the effects of chemistry (Glover et al., 2010) for §6.3.3.

Each of our simulations begins with an initially uniform gas distribution, with a mean hydrogen number density of $n_0 = 1000 \text{ cm}^{-3}$ and a resolution of 256^3 cells. The initial velocity field is turbulent, with power concentrated on large scales with an initial rms velocity $v_{rms} = 5 \text{ km s}^{-1}$. We do not

perform a Helmholtz decomposition of the force field, and thus the turbulent forcing consists of a natural mixture of solenoidal and compressive modes, i.e., $F_{\text{sol}}/(F_{\text{sol}} + F_{\text{comp}}) \approx 2/3$. Note that Federrath et al. (2008b, 2010) tested the two limiting cases of purely solenoidal (divergence-free) and purely compressive (curl-free) forcing, as well as various mixtures of solenoidal and compressive modes of the turbulent forcing. They found a strong influence on the density PDF, producing a three times larger standard deviation for compressive forcing compared to solenoidal forcing. They parameterized the influence of the forcing by introducing the b -parameter in Equation (6.3). Purely solenoidal forcing is characterized by $b = 1/3$, while purely compressive forcing gives $b = 1$. For the natural mixture, they find $b \approx 0.4$. Using the present set of numerical models, we confirm that using $b = 0.4$ for the natural mixture of forcing modes used here gives the best fits with our analytically derived density variance–Mach number relation. The temperature of the gas is constant and fixed to an initial value $T_0 = 1062, 170, 42$ and 15 K, in order to sample a large set of Mach numbers $\langle \mathcal{M} \rangle \simeq 2, 5, 10$ and 17 , respectively. The crossing time is defined as $t_{\text{cross}} = L/2v_{\text{rms}} \approx 1.9$ Myrs. We present results from $t = 3T_{\text{cross}} \approx 5.7$ Myr, sampled every $0.17T_{\text{cross}}$, and evolved until $t = 4T_{\text{cross}} \approx 7.6$ Myr. This period of time is long enough to expect the turbulence to have reached a statistical steady state (Federrath et al., 2009; Federrath et al., 2010; Glover et al., 2010; Price and Federrath, 2010).

For the MHD cases, the simulations begin with a uniform magnetic field that is initially oriented parallel to the z -axis of the simulation. Four of these simulations begin with an initial magnetic field strength $B_i = 5.85 \mu\text{G}$, which is our standard magnetic field strength hereafter. We also perform three MHD runs with $B_i = 10, 20$ and $60 \mu\text{G}$, with $\mathcal{M} = 10$, to check the behavior of the results with increasing magnetic field strengths. We note that as the simulations run, dynamo amplification can lead to increased field strength, and thus we use the instantaneous magnetic field strength to compute β_0 . Nevertheless, for simplicity we use the initial value of the magnetic field strength to label runs MHD-B2, MHD-B20 and MHD-B60.

In Table 1, we list the simulations that we have performed. In our labels, we use “H” to denote a hydrodynamic run and “MHD” to denote a magnetohydrodynamic run. Our multiple runs with fixed (or zero) magnetic field strength but different sound-speeds are labelled with an “M”, followed by the (approximate) rms Mach number of the simulation. Finally, the three runs in which we examined the effect of varying the initial magnetic field strength are labelled with a “B”, followed by the initial field strength in μG . In Table 1, we also list the values of the quantities: β_0 , the rms Alfvénic Mach number $\mathcal{M}_{A,0} = v_0/v_{A,0}$ and the sonic Mach number. They are measured in every

Table 6.1: List of simulations.

	B_i	$\langle \beta_0 \rangle \pm 1\sigma$	$\langle \mathcal{M}_{A,0} \rangle \pm 1\sigma$	$\langle \sigma_s \rangle \pm 1\sigma$	$\langle \mathcal{M} \rangle \pm 1\sigma$
HD-M2	0	∞	0	0.77 ± 0.02	2.21 ± 0.02
HD-M5	0	∞	0	1.3 ± 0.1	5.4 ± 0.1
HD-M10	0	∞	0	1.7 ± 0.1	10.6 ± 0.2
HD-M17	0	∞	0	1.92 ± 0.09	17.6 ± 0.5
MHD-M2	5.85	25 ± 5	8.1 ± 0.9	0.69 ± 0.02	2.09 ± 0.02
MHD-M5	5.85	4.8 ± 0.4	8.4 ± 0.8	1.18 ± 0.04	4.98 ± 0.07
MHD-M10	5.85	1.4 ± 0.5	9 ± 3	1.47 ± 0.06	10.2 ± 0.3
MHD-M17	5.85	0.3 ± 0.1	7 ± 2	1.61 ± 0.06	16.8 ± 0.5
MHD-B2	2	11.3 ± 0.5	27 ± 2	1.58 ± 0.09	10.5 ± 0.2
MHD-B20	20	0.083 ± 0.005	1.94 ± 0.06	1.48 ± 0.01	9.9 ± 0.2
MHD-B60	60	0.030 ± 0.001	1.24 ± 0.03	1.34 ± 0.01	10.3 ± 0.1

B_i – initial magnetic field strength in μG .

β_0 – mean thermal to instantaneous magnetic pressure ratio.

$\mathcal{M}_{A,0}$ – rms Alfvénic Mach number.

σ_s – density variance.

\mathcal{M} – rms Mach number.

The brackets indicate the time average calculated over the snapshots after averaging over the spatial coordinates.

cell and then are spatially averaged over the datacube. The brackets denote the time average over the seven snapshots, and the 1σ shows the temporal standard deviation around the mean values.

6.2.2 Statistical Analysis

In this subsection, we explain the method used to measure the density variance for every snapshot in our simulations using the PDF as a robust statistical tool for this analysis (Price et al., 2011). Then, we parameterize the instantaneous β_0 in terms of \mathcal{M} , in the direction of testing numerically the σ_s - \mathcal{M} relations presented in §6.2. Finally, we present the comparison between our analytical model and the simulations.

Probability Density Function (PDF)

In Figure 6.1, we plot the volume-weighted dimensionless density PDFs for MHD and HD isothermal gas with the same Mach number for comparison. For these simulations, we find that all the PDFs have a log-normal shape

around their peak. However, the PDFs deviate from log-normality especially in the HD simulations at low densities, being more evident for $\mathcal{M} \gtrsim 5$. The error bars in this figure show the 1σ variations around the time average. We see that these variations cannot explain the tail at low densities. Therefore, this deviation is not explained by intermittency fluctuations, and deserves further study. However, the low-density tail does not significantly affect our σ_s estimates, because the variance is computed from a log-normal fit in a limited interval around the peak, giving the most reliable estimates of σ_s (see Price et al., 2011). In this sense, the trend of the time averages observed between MHD and HD simulations shows the magnetic field acting as a density cushion, preventing the gas from reaching very low densities during local expansion. As a consequence, there are larger parts of the volume with density $\rho \approx \rho_0$ in the MHD case than in the HD case.

In order to avoid contamination from intermittency, numerical artifacts, etc., in the wings of the PDFs, we perform a Gaussian fitting only in a data subset selected by s , in each simulation. This subset consists of 60% of the number of bins considered to calculate the density PDF which are distributed symmetrically around the mean, s_0 . Then, we fit the Gaussian profile given by Equation (6.2) to obtain σ_s in every snapshot of the simulations.

Density variance–rms Mach number test

In the interest of comparing the density variance–Mach number relation, given by Equation (6.25) and Equation (6.26), with the results obtained in the previous subsection, we parameterise the thermal-to-magnetic pressure ratio in terms of the rms Mach number for our sequence of simulations. In this sense, we rewrite Equation (6.12) as

$$\beta_0 = 2 \frac{\mathcal{M}_{A,0}^2}{\mathcal{M}^2}. \quad (6.27)$$

Note that this parameter is calculated considering the instantaneous magnetic field strength and not the initial value.

Next, we select the four MHD simulations with different rms Mach number, but the same initial magnetic field strength, and use a linear regression considering the logarithm of Equation (6.27): $\log_{10} \beta_0 = \log_{10} C - 2 \log_{10} \mathcal{M}$. From the fit shown in Figure 6.2, we find $C = 111 \pm 4$. In Figure 6.2, we plot β_0 as a function of the rms Mach number for the different snapshots. The triangles show β_0 for the selected simulations with $\langle \mathcal{M} \rangle \approx 2, 5, 10$ and 17, while the curve shows the linear regression.

In Figure 6.3, we combine the dimensionless standard deviation σ_s , obtained from the fit over the numerical PDFs for every snapshot, and the

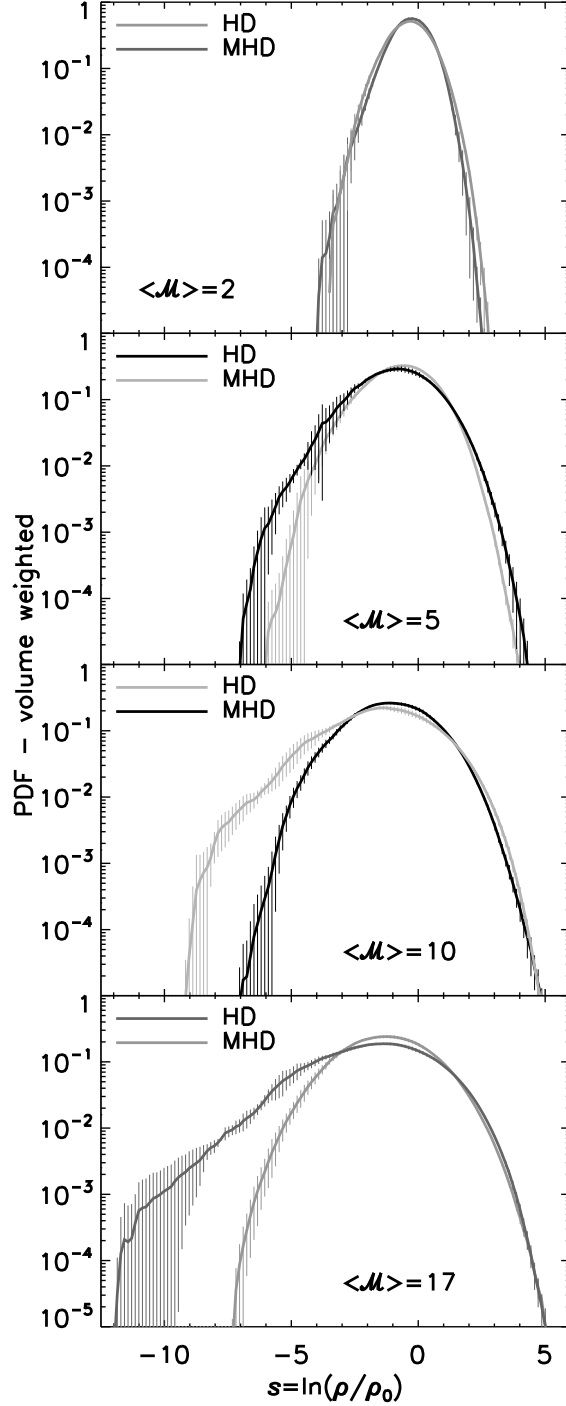


Figure 6.1: Dimensionless density PDF for magnetised and unmagnetised molecular clouds with the same initial conditions, $n_0 = 1000 \text{ cm}^{-3}$, and same turbulent rms velocity, but different sound speed. The most significant features are: 1) the density variance increases with Mach number, and 2) the density variance decreases with magnetic field strength. These simulations have a ratio between thermal pressure and magnetic pressure $\beta_0 \lesssim 10$. All simulations have a resolution of 256^3 zones.

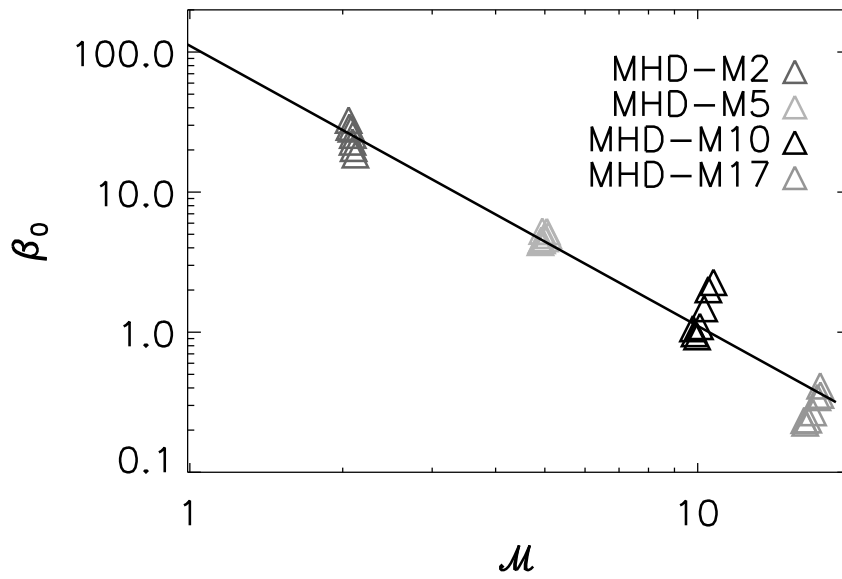


Figure 6.2: Parameterisation of $\beta_0 = P_{\text{th}}/P_{0,\text{mag}}$ with respect to the rms Mach number for the subset of simulations with roughly constant Alfvénic Mach number, $\mathcal{M}_{A,0} \approx 8$ (see Table 6.1). The curve is a linear regression of the MHD simulations with $B_i = 5.85\mu\text{G}$. The linear regression performed to the logarithm of Equation (6.27) gives $\beta_0 = (111 \pm 4)\mathcal{M}^{-2}$.

analytical prediction for the three cases of $B \propto \rho^\alpha$ – with $\alpha = 0, 1/2$, and 1 – as a function of the rms Mach number. For the triangles around a given $\langle \mathcal{M} \rangle$, the HD simulations exhibit larger σ_s compared with the MHD simulations, as was expected from Figure 6.1. For comparison, we plot the analytical prediction given by Equation (6.24), $\sigma_{\alpha,0}$. This result matches the prediction provided by Padoan et al. (1997). However, instead of using their proportionality parameter $b \approx 0.5$, we used the input value $b = 0.4$ (Federrath et al., 2010, dashed line), which is the result of the natural mixing of solenoidal and compressive modes in the turbulent forcing field. We also plot the two extreme cases for the unmagnetised gas, $\sigma_{s,HD}$, with $b = 1/3$ (lower dotted line) for purely solenoidal forcing and $b = 1$ for purely compressive forcing (upper dotted line) for comparison.

In the same Figure, we superpose Equation (6.25, light grey solid line) and Equation (6.26, dark grey solid line), both again with $b = 0.4$. We find that the best agreement with the MHD simulations is given by Equation (6.25), that is $\sigma_{s,1/2}$. The result obtained for the first case – B independent of density (Equation 6.24) – may account only for low Mach number zones. This case might be appropriate for diffuse clouds (Crutcher et al., 2010), where the mean sound speed of the cloud may be of the same order as the rms velocity. Here, at $\mathcal{M} \sim 1$, all the three cases converge to the HD result.

Our results are qualitatively in agreement with Ostriker et al. (2001) and Price et al. (2011). These authors find that the density variance in magnetised gas is significantly lower than in the HD counterparts for simulations with a Mach number $\mathcal{M} \gtrsim 10$. In addition, Cho and Lazarian (2003) study the density contrast resulting from the Alfvénic waves, slow and fast magneto-sonic waves originating in different environments. The authors concluded that the three kinds of waves can coexist in those environments. In the regime that concerns us, $\beta_0 \approx 1$ and $5 \lesssim \mathcal{M} \lesssim 10$, their density contrasts closely match ours.

To test the validity of our results for different Alfvénic Mach numbers, we also performed three simulations with an initial magnetic field strength different from the standard one, with $\mathcal{M}_{A,0} \approx 27, 1.9$, and 1.2 , at $\langle \mathcal{M} \rangle \approx 10$ (empty squares in Figure 6.3). Our model works well for $\mathcal{M}_{A,0} \gtrsim 6$, but breaks down for our test with $\mathcal{M}_{A,0} \lesssim 2$. The break occurs when the turbulence becomes trans-Alfvénic or sub-Alfvénic, i.e., when $\mathcal{M}_{A,0} \lesssim 2$. This is due to anisotropies arising in this case, i.e., the turbulence is no longer isotropic, as can be seen in Figure 6.4. This is because the back reaction of the magnetic field onto the flow is extremely strong for flows perpendicular to the magnetic field lines, if the turbulence is trans-Alfvénic or sub-Alfvénic (see e.g., Cho and Lazarian, 2003; Brunt et al., 2010; Esquivel and Lazarian, 2011). Since our analytic derivation is based on an ensemble

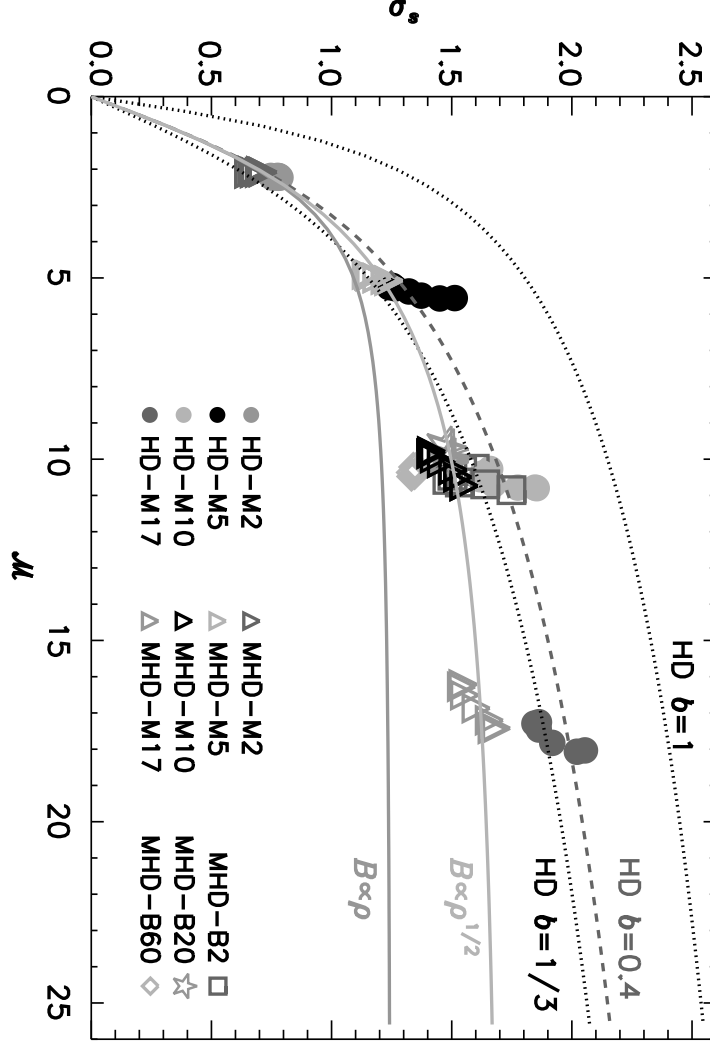


Figure 6.3: Standard deviation of the dimensionless density contrast, plotted as a function of the rms Mach number. Circles show the purely hydrodynamical simulations that follow very well the Padoan et al. (1997) prediction, $\sigma_{s,HD}^2 = \ln(1 + b^2 \mathcal{M}^2)$, with $b = 0.4$, expected for mixed-mode turbulent forcing (Federrath et al., 2010, dashed line). The dotted lines are for comparison with purely hydrodynamical model, assuming $b = 1/3$ for purely solenoidal forcing and $b = 1$ for purely compressive forcing (Federrath et al., 2008b). Triangles show the MHD simulations and the two formulas, Eqs. (6.25) and (6.26), obtained in this work: $\sigma_{s,1/2} = \{\ln[1 + b^2 \mathcal{M}^2 \beta_0 / (\beta_0 + 1)]\}^{1/2}$ (light grey solid line), and $\sigma_{s,1}$ (dark grey solid line). Those curves are plotted for $b = 0.4$, and using our parameterisation, $\beta_0 = (111 \pm 4) \mathcal{M}^{-2}$ from Fig. 6.2. Squares, stars and diamonds show the additional MHD simulations with different rms Alfvénic Mach number, $\mathcal{M}_{A,0} \approx 27$ ($B_i = 2 \mu\text{G}$), $\mathcal{M}_{A,0} \approx 1.9$ ($B_i = 20 \mu\text{G}$), and $\mathcal{M}_{A,0} \approx 1.2$ ($B_i = 60 \mu\text{G}$).

average (Eq. 6.4), assuming statistical isotropy, the anisotropies are the most likely cause for the limitation of our model to super-Alfvénic turbulence. In Figure 6.5, we show our prediction (Eq. 6.25)² for a fixed Mach number $\mathcal{M} \approx 10$ and forcing parameter $b \approx 0.4$, which fits very well the data with $\mathcal{M}_{A,0} \gtrsim 6$. These simulations show high dispersion – around the time average – in the density variance and the rms Alfvénic Mach number showing the fluctuations of the gas caused by the turbulence dominating the dynamics of the flow, in contraposition of the simulations with small Alfvénic Mach number. In the same Figure, we also plot the model curve Eq. (6.25) for the same sonic Mach number 10 and $b = 1$. Although our turbulent forcing in the simulations is by definition mixed, and thus we expect $b \approx 0.4$ (Federrath et al., 2010), we find it interesting to note that $b = 1$ – corresponding to purely compressive forcing – gives a good fit to the data with very low Alfvénic Mach number, $\mathcal{M}_{A,0} \lesssim 2$. We speculate that the density field for very high magnetic field strengths and thus very low Alfvénic Mach number starts behaving as if it was driven by purely compressive forcing. This is very different from the compression obtained with solenoidal or mixed forcing, but more similar to compressive forcing, which also directly compresses the gas (Federrath et al., 2008b). More data at $\mathcal{M}_{A,0} \lesssim 2$ would be needed to sample this region and the transition from $b = 0.4$ to 1 in detail, and we just note here that $b = 1$ seems to provide a good fit for $\mathcal{M}_{A,0} \lesssim 2$, given the data at hand.

6.3 The non-isothermal case

6.3.1 Analytical derivation

In this section, we extend the work shown in §6.1.2 in order to obtain an analytical relation between σ_s and \mathcal{M} for non-isothermal gas. Here, we relax some of the approximations applied in that section.

In the non-isothermal gas, the ratio of the thermal pressure to magnetic pressure is

$$\beta = \frac{2}{\Gamma} \frac{c_s^2}{v_A^2}. \quad (6.28)$$

The index Γ is related to the ratio of the specific heats γ by

$$Q = W \frac{(\gamma - \Gamma)}{(\gamma - 1)}, \quad (6.29)$$

²Equation (6.25) has been written in terms of the instantaneous Alfvénic Mach number (Eq. 6.27), yielding the relation for the density variance: $\sigma_s^2 = \ln[1 + 2b^2 \mathcal{M}^2 \mathcal{M}_{A,0}^2 / (2\mathcal{M}_{A,0}^2 + \mathcal{M}^2)]$.

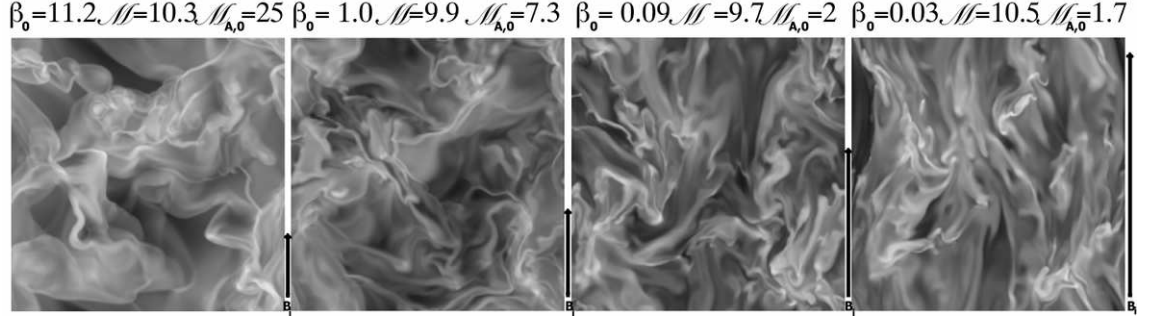


Figure 6.4: Density slices of the simulations at $t = 6$ Myr. The mean magnetic field is oriented along the vertical axis. From left to right: initial magnetic field strength $B_i = 2, 5.85, 20$ and $60 \mu\text{G}$. The turbulence remains isotropic for super-Alfvénic gas $\mathcal{M}_{A,0} \gg 1$, but when it becomes trans-Alfvénic or sub Alfvénic ($\mathcal{M}_{A,0} \lesssim 3$), the turbulence becomes highly anisotropic.

where Q is the heat exchange and W the work done by the system (Kippenhahn and Weigert, 1994; Carroll and Ostlie, 2006, www.codecogs.com³). Expressing Q and W in terms of the pre- and post-shock conditions may be tricky. In order to avoid confusions, we consider that $\Gamma_1 = \Gamma_2 = \gamma_0$ as a first approximation for simplicity (γ_0 is the volume average of γ). Later in the numerical test, we will explore the effects of considering different Γ .

In our simulations, we calculated the average of $\gamma_{\rho > \rho_0}$ only in the gas with $\rho > \rho_0$ and compared it with γ_0 . The ratio $\gamma_{\rho > \rho_0} / \gamma_0 \approx 1$ and does not depend on the Mach number. Using Eqs. 6.5 and 6.10, we can rewrite Equation (6.6) as

$$\begin{aligned}
 \frac{\rho_0}{\rho_2} (\gamma_0 b^2 \mathcal{M}^2 + 1 + \beta_0^{-1}) &= b^2 \mathcal{M}^2 \left(\frac{\gamma_0 + 1}{2} \right) \left(\frac{\rho_0}{\rho_2} \right)^2 + \frac{(\gamma_0 - 1)}{2} b^2 \mathcal{M}^2 + \\
 2 \frac{(\gamma_0 - 1)}{\gamma_0} \left(\beta_0^{-1} - \frac{\gamma_0 v_{A,2}^2}{2c_{s,1}^2} \right) &+ \frac{\gamma_0 v_{A,2}^2}{2c_{s,1}^2} + 1.
 \end{aligned} \tag{6.30}$$

In order to solve this equation for the density contrast ρ_2 / ρ_0 , it is necessary to find a relation for $v_{A,2}$ in terms of the pre-shock Alfvénic velocity $v_{A,0}$. To achieve this, we consider that the magnetic field strength and the density are related following the three cases assumed in §6.1.2.

³http://www.codecogs.com/reference/engineering/thermodynamics/idea_gases/expansion_and_compression_of_ideal_gases.php#comments

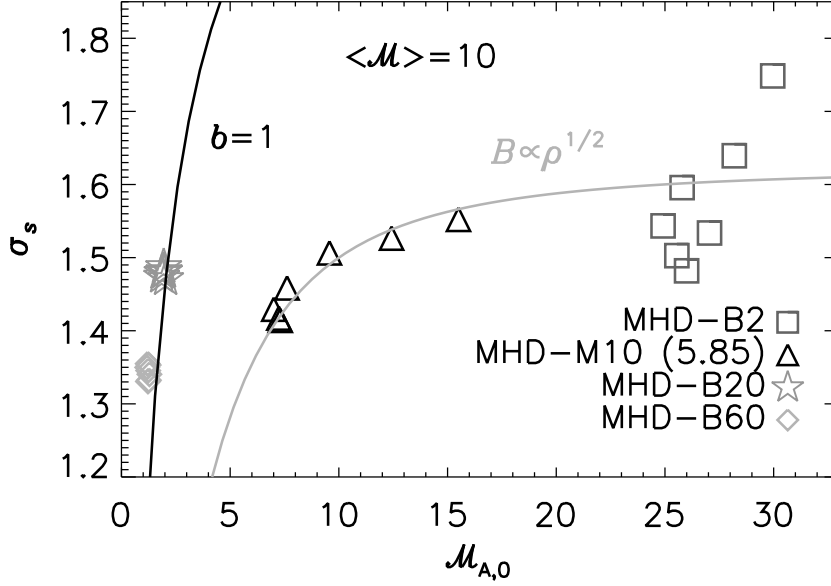


Figure 6.5: Standard deviation of the dimensionless density contrast, plotted as a function of the instantaneous rms Alfvénic Mach number at $\langle \mathcal{M} \rangle \approx 10$. The different symbols show snapshots of simulations with $\mathcal{M}_{A,0}$ time averages: $\langle \mathcal{M}_{A,0} \rangle \approx 27$ (squares), $\langle \mathcal{M}_{A,0} \rangle \approx 9$ (triangles), $\langle \mathcal{M}_{A,0} \rangle \approx 1.9$ (stars), and $\langle \mathcal{M}_{A,0} \rangle \approx 1.2$ (diamonds). When the turbulence becomes trans-Alfvénic or sub-Alfvénic, $\langle \mathcal{M}_{A,0} \rangle \lesssim 2$ (stars and diamonds), anisotropies arise in the gas, because the back reaction of the magnetic field onto the flow is extremely strong for flows perpendicular to the magnetic field lines. The grey curve shows our prediction $\sigma_{s,1/2}$ using $b \approx 0.4$ that fits very well the data. Meanwhile, the black curve shows our prediction $\sigma_{s,1/2}$ considering $b = 1$ (corresponding to purely compressive forcing). Although our turbulent forcing in the simulations is by definition mixed, and thus we expect $b \approx 0.4$ (Federrath et al., 2010), it is noteworthy to say that $b = 1$ gives a good fit to the data with very low $\langle \mathcal{M}_{A,0} \rangle \lesssim 2$.

First case: B independent of ρ

At this extreme case, Eq. 6.30 becomes a second-order equation independent of the magnetic field strength

$$\begin{aligned} & \left(\frac{\rho_2}{\rho_0}\right)^2 \left[b^2 \mathcal{M}^2 \frac{(\gamma_0 - 1)}{2} + \frac{2(\gamma_0 - 1)}{\gamma_0} \beta_0^{-1} + 1 \right] - \\ & \left(\frac{\rho_2}{\rho_0}\right) (\gamma_0 b^2 \mathcal{M}^2 + \frac{2(\gamma_0 - 1)}{\gamma_0} \beta_0^{-1} + 1) + b^2 \mathcal{M}^2 \frac{(\gamma_0 + 1)}{2} = 0. \end{aligned}$$

This equation results in

$$\frac{\rho_2}{\rho_0} = \frac{b^2 \mathcal{M}^2 (\gamma_0 + 1)}{2 \left[(\gamma_0 - 1) \left(\frac{b^2 \mathcal{M}^2}{2} + \frac{2\beta_0^{-1}}{\gamma_0} \right) + 1 \right]}. \quad (6.31)$$

In contrast with Eq. 6.14, Eq. 6.31 does depend on the magnetic field strength. We are assuming that magnetic fields and matter are not coupled. However, magnetic fields enter into play together with the non-isothermal equation of state, which is intriguing. This point needs further investigation to be understood. Eq. 6.31 reduces to $\rho_2/\rho_0 = b^2 \mathcal{M}^2$ (e.g. Padoan et al., 1997; Federrath et al., 2008b) for $\gamma_0 = 1$.

Second case: $B \propto \rho^{1/2}$

For this case, Eq. 6.30 results again in a similar second-order equation, but with a dependence on the magnetic field strength

$$\left(\frac{\rho_2}{\rho_0}\right)^2 \left[b^2 \mathcal{M}^2 \frac{(\gamma_0 - 1)}{2} + 1 + \beta_0^{-1} \right] - \left(\frac{\rho_2}{\rho_0}\right) (\gamma_0 b^2 \mathcal{M}^2 + 1 + \beta_0^{-1}) + b^2 \mathcal{M}^2 \frac{(\gamma_0 + 1)}{2} = 0.$$

The solution for this equation is

$$\frac{\rho_2}{\rho_0} = \frac{b^2 \mathcal{M}^2 (\gamma_0 + 1)}{b^2 \mathcal{M}^2 (\gamma_0 - 1) + 2(1 + \beta_0^{-1})}. \quad (6.32)$$

In this case, the density contrast changes considerably compared to the HD solution $\rho_2/\rho_0 = b^2 \mathcal{M}^2$ (Eq. 6.14), as well as compared to the magnetized-isothermal case $\rho_2/\rho_0 = b^2 \mathcal{M}^2 (1 + \beta_0^{-1})^{-1}$ (Eq. 6.15). The density contrast is reduced by $(\gamma_0 + 1)/[b^2 \mathcal{M}^2 (\gamma_0 - 1) + 2(1 + \beta_0^{-1})]$.

Third case: $B \propto \rho$

For the extreme case in which magnetic fields act proportionally to the density, Eq. 6.30 arranges into a third order equation

$$\left(\frac{\rho_2}{\rho_0}\right)^3 \frac{(2-\gamma_0)}{\gamma_0} \beta_0^{-1} + \left(\frac{\rho_2}{\rho_0}\right)^2 \left(b^2 \mathcal{M}^2 \frac{(\gamma_0-1)}{2} + \frac{2(\gamma_0-1)}{\gamma_0} \beta_0^{-1} + 1\right) - \left(\frac{\rho_2}{\rho_0}\right) (\gamma_0 b^2 \mathcal{M}^2 + 1 + \beta_0^{-1}) + b^2 \mathcal{M}^2 \frac{(\gamma_0+1)}{2} = 0,$$

which has the solution

$$\frac{\rho_2}{\rho_0} = \frac{1}{4(\gamma_0-2)} \left[(\gamma_0-1)\gamma_0\beta_0 b^2 \mathcal{M}^2 + 2\gamma_0(\beta_0+1) - \sqrt{[(\gamma_0-1)\gamma_0\beta_0 b^2 \mathcal{M}^2 + 2\gamma_0(\beta_0+1)]^2 - 8(\gamma_0+1)(\gamma_0-2)\gamma_0\beta_0 b^2 \mathcal{M}^2} \right]. \quad (6.33)$$

This density contrast changes substantially in comparison with Eq. 6.16. There is a strong influence of the plasma β_0 as in Eq. 6.16, but γ_0 seems to have preponderance as well.

6.3.2 The σ_s - \mathcal{M} relation

Here, we determine the density variance for a non-isothermal, magnetized, supersonic turbulent fluid for which there are many shocks. We present three different σ_s - \mathcal{M} relation for each of the magnetic field dependences with density. We assume Eq. 6.22 for $\rho/\rho_0 > 1$, although given that the fluid may be affected by strong heating, we have to include a contribution by the gas with $\rho < \rho_2$. Therefore, the density variance (Eq. 6.4) can be written as⁴

$$\sigma_{\rho/\rho_0}^2 = [\sigma_{\rho/\rho_0}^2]_{\rho > \rho_0} + [\sigma_{\rho/\rho_0}^2]_{\rho < \rho_0}. \quad (6.34)$$

In the absence of viscosity, we propose that the shock width in the case which $\rho < \rho_2$ is given by

$$\lambda_{\rho < \rho_0} \simeq \theta L \rho_2 / \rho_0 (\gamma_0 - 1), \quad (6.35)$$

where $\theta \simeq 1$ (Ossenkopf and Mac Low, 2002; Brunt et al., 2009). We add the term $\gamma_0 - 1$ for consistency with our previous result for highly supersonic-isothermal turbulence. The volume of the shock V_{sh} is given by

⁴We do not include $\rho \approx \rho_0$ because this corresponds to the subsonic/transonic regime.

$$V_{\text{sh}, \rho < \rho_0} \simeq L^3 \frac{\rho_2}{\rho_0} (\gamma_0 - 1). \quad (6.36)$$

This is the volume of our representative shock. The volume differential in the density variance equation 6.4 is approximately the differential of the volume of the shock (Eq. 6.17) and is given by

$$dV = L^3 (\gamma_0 - 1) d\left(\frac{\rho_2}{\rho_0}\right). \quad (6.37)$$

Inserting Eq. 6.37 into Eq. 6.4, we obtain

$$\begin{aligned} [\sigma_{\rho/\rho_0}^2]_{\rho < \rho_0} &= (\gamma_0 - 1) \int_{\frac{\rho}{\rho_0}}^1 \left(\frac{\rho_2}{\rho_1} - 1\right)^2 d\left(\frac{\rho_2}{\rho_0}\right) = \\ &(\gamma_0 - 1) \left[\frac{1}{3} - \left(\frac{\rho}{\rho_0}\right)^3 + \left(\frac{\rho}{\rho_0}\right)^2 - \frac{\rho}{\rho_0} \right]. \end{aligned} \quad (6.38)$$

where the shock thickness is defined only for $\rho_2/\rho_0 < 1$. In that case, the cubic and quadratic terms are much smaller than the linear one. Hence, Eq. 6.38 is approximately

$$[\sigma_{\rho/\rho_0}^2]_{\rho < \rho_0} \approx (\gamma_0 - 1) \left(\frac{1}{3} - \frac{\rho}{\rho_0} \right). \quad (6.39)$$

For highly supersonic turbulence, there are regions where $\rho \gg \rho_0$ as well as $\rho \ll \rho_0$ (rarefaction waves). In the limit $\rho/\rho_0 \rightarrow 0$, $[\sigma_{\rho/\rho_0}^2]_{\rho < \rho_0} = 1/3$. We are not interested in rarefaction waves by now. Besides, the width of the dimensionless density distribution σ_{ρ/ρ_0} may increase with incrementing the density contrast ρ/ρ_0 . However, the width of the density distribution $[\sigma_{\rho/\rho_0}]_{\rho < \rho_0}$ (Eq. 6.39) becomes narrower with high density contrast, we therefore change the sign of this equation. In this way, the width $[\sigma_{\rho/\rho_0}]_{\rho < \rho_0}$ increases towards high ρ/ρ_0 .

The density variance (Eq. 6.34) is then

$$\sigma_{\rho/\rho_0}^2 \approx \frac{\rho}{\rho_0} + (\gamma_0 - 1) \left(\frac{\rho}{\rho_0} - \frac{1}{3} \right). \quad (6.40)$$

The density variance is frequently expressed in terms of the logarithm of the density contrast (e.g. Padoan et al., 1997; Federrath et al., 2008b; Glover et al., 2010; Padoan and Nordlund, 2011). For our comparison with simulations, we insert Eq. 6.40 into Eq. 6.23 and get

$$\sigma_s^2 = \ln \left[\frac{(4 - \gamma_0)}{3} + \gamma_0 \left(\frac{\rho}{\rho_0} \right) \right]. \quad (6.41)$$

Now we can use our ρ/ρ_0 predictions from our three magnetic field cases into Eq. 6.41 for obtaining their correspondent density variance-Mach number analytical relations. Each of the relations are labeled in the same fashion than in §6.1.2, but adding “*th*” to differentiate them from the isothermal relations.

- **B independent of ρ**

The density variance in this case is

$$\sigma_{s,0,th}^2 = \ln \left[\frac{(4 - \gamma_0)}{3} + \frac{b^2 \mathcal{M}^2 \gamma_0 (\gamma_0 + 1)}{2 \left[(\gamma_0 - 1) \left(\frac{b^2 \mathcal{M}^2}{2} + \frac{2\beta_0^{-1}}{\gamma_0} \right) + 1 \right]} \right]. \quad (6.42)$$

- **$B \propto \rho^{1/2}$**

In this case, the density variance–Mach number relation is:

$$\sigma_{s,1/2,th}^2 = \ln \left[\frac{(4 - \gamma_0)}{3} + \frac{b^2 \mathcal{M}^2 \gamma_0 (\gamma_0 + 1)}{b^2 \mathcal{M}^2 (\gamma_0 - 1) + 2(1 + \beta_0^{-1})} \right]. \quad (6.43)$$

In the isothermal limit $\gamma_0 = 1$, Eq. 6.43 simplifies into the density contrast for the magnetized-isothermal case (Eq. 6.25), which in turn recovers the HD solution (Eq. 6.24) for weak magnetic fields, i.e. $\beta_0 \rightarrow \infty$.

- **$B \propto \rho$**

Finally, the density variance results

$$\sigma_{s,1,th}^2 = \ln \left\{ \frac{(4-\gamma_0)}{3} + \frac{\gamma_0}{4(\gamma_0-2)} [(\gamma_0 - 1)\gamma_0\beta_0 b^2 \mathcal{M}^2 + 2\gamma_0(\beta_0 + 1) - \sqrt{[(\gamma_0 - 1)\gamma_0\beta_0 b^2 \mathcal{M}^2 + 2\gamma_0(\beta_0 + 1)]^2 - 8(\gamma_0 + 1)(\gamma_0 - 2)\gamma_0\beta_0 b^2 \mathcal{M}^2}] \right\}. \quad (6.44)$$

In the isothermal limit $\gamma_0 = 1$, Eq. 6.44 becomes equivalent to Eq. 6.26, which in turn simplifies to Eq. 6.24 in the HD limit $\beta_0 \rightarrow \infty$.

All the density variance predictions has a strong dependence on γ_0 , as well as on β_0 (Eqs. 6.43 and 6.44), leaving the rms Mach number as a marginal quantity in this relation. In the next section we test Eqs. 6.42, 6.43, and 6.44 with numerical simulations.

6.3.3 Numerical test

Simulations

For this test, we include the same the simulations used in §5, which are explained in detail in §2.1. Additionally, we include other simulations with higher UV radiation field strengths, in order to study the effect of photoelectric heating from dust grains on the density variance–Mach number relation. Because these extra simulations have on average higher kinetic temperatures, \mathcal{M} is typically lower than the simulations in §5. In total, there are 25 simulations. The details are listed in Table 6.2.

For most of our simulations, we report results for only 3 snapshots of the simulation corresponding to an evolutionary time from $t \approx 5$ Myrs to $t \approx 5.7$ Myrs ($3T_{cross}$), for which we expect the simulations to have reached an statistically stationary state. For four of our simulations, we follow the evolutionary time up to ~ 30 Myrs. Although we know that this is an unrealistic lifetime for a molecular cloud (they live for times $\lesssim 10^7$ Myrs, e.g. Ballesteros-Paredes et al., 1999; Mac Low and Klessen, 2004), we wanted to check if the different dynamical parameters were stable with increasing simulation time. In total, the quantities seems to be stable, presenting only small relative variations.

In Table 6.2, we list γ_0 , β_0 , \mathcal{M}_{d} , σ_s , and \mathcal{M} at $t \approx 5.7$ Myrs.

Probability Density Function (PDF)

Fig. 6.6 shows the volume-weighted PDF of the natural logarithm of the dimensionless density $s = \ln(\rho/\rho_0)$. The simulations are grouped by similar characteristics for comparison which are specified at the top corners of the figures. The varying parameters are specified at the bottom together with the rms Mach-number. All the PDFs exhibit a log-normal shape (Eq. 6.2). The width σ_s becomes narrower as the simulations present smaller \mathcal{M} , which in turn corresponds to stronger UV radiation field strength and/or smaller product $n_0 \times Z$. Although the difference between simulations seems very subtle, it is more evident for comparisons between the subset at the top of the figure and the one at the bottom. Table 6.2 shows that σ_s changes only by some tenths, while \mathcal{M} varies by a factor of a few.

As in §6.1.2, the tail at low densities cannot be easily explained. Although, there are three plausible reasons for this behavior: 1) intermittency fluctuations (Federrath et al., 2008b), 2) the fixed pattern in which turbulence is driven (Konstandin et al., 2012b), and/or 3) the use of a computationally fixed grid. Given that two of these reasons are not physical, we measure σ_s after limiting the PDF to an interval around the peak which contain 60% of

Table 6.2: List of simulations.

	n_0 [cm ⁻³]	Z/Z_\odot	UV [G_0]	γ_0	β_0	\mathcal{M}_A	σ_s	\mathcal{M}
n300-Z01	300	0.1	1	1.61	7.22	4.3	1.357	7.2
n300-Z03	300	0.3	1	1.54	9.13	4.1	1.39	9
n300-Z06	300	0.6	1	1.49	3.3	4	1.410	10.7
n30	30	1.0	1	1.63	0.58	1.9	1.358	5.1
n100	100	1.0	1	1.55	1.02	2.49	1.392	8
n180	180	1.0	1	1.51	2.03	3.3	1.398	10.2
n300	300	1.0	1	1.47	2.42	3.9	1.424	12.4
n1000	1000	1.0	1	1.43	11.1	8.7	1.542	16.6
n30-Z01	30	0.1	1	1.67	1.60	1.6	1.312	4.3
n100-Z01	100	0.1	1	1.65	2.62	2.5	1.355	5.6
n1000-Z01	1000	0.1	1	1.51	15.77	8.8	1.495	10.5
UV0	300	1.0	0	1.46	1.65	3.9	1.422	16.6
UV10	300	1.0	10	1.47	5.87	4.1	1.396	9.7
UV100	300	1.0	100	1.51	25.59	4.3	1.332	7.2
UV1000	300	1.0	1000	1.60	20.16	4.5	1.284	5
n30-UV1000	30	1.0	1000	1.67	9.99	1.7	1.012	1.5
n60-UV1000	60	1.0	1000	1.67	40.37	2.2	1.1	2
n100-UV1000	100	1.0	1000	1.66	11.9	2.8	1.167	2.6
n180-UV100	180	1.0	100	1.57	15.17	3.9	1.278	5.4
n300Z01-UV10	300	1.0	10	1.62	13.72	4.4	1.325	5.5
n300Z01-UV100	300	1.0	100	1.66	39.37	5.2	1.21	3.9
n300Z01-UV1000	300	1.0	1000	1.67	69.44	5.2	1.145	3.1
n300Z03-UV10	300	1.0	10	1.55	7.52	4.3	1.369	6.9
n300Z03-UV100	300	1.0	1000	1.60	20.31	4.6	1.298	5
n300Z03-UV1000	300	1.0	1000	1.66	48.33	5.3	1.181	3.4

n_0 – initial number density of hydrogen nuclei

Z/Z_\odot – metallicity

UV – ultra-violet radiation field strength expressed in the standard radiation field strength G_0 (Draine, 1978)

All these quantities are calculated at $t \approx 5.7$ Myrs

γ_0 – average ratio of the specific heats

β_0 – average ratio of the thermal-to-magnetic pressure

\mathcal{M}_A – rms Alfvénic Mach number

\mathcal{M} – rms Mach number

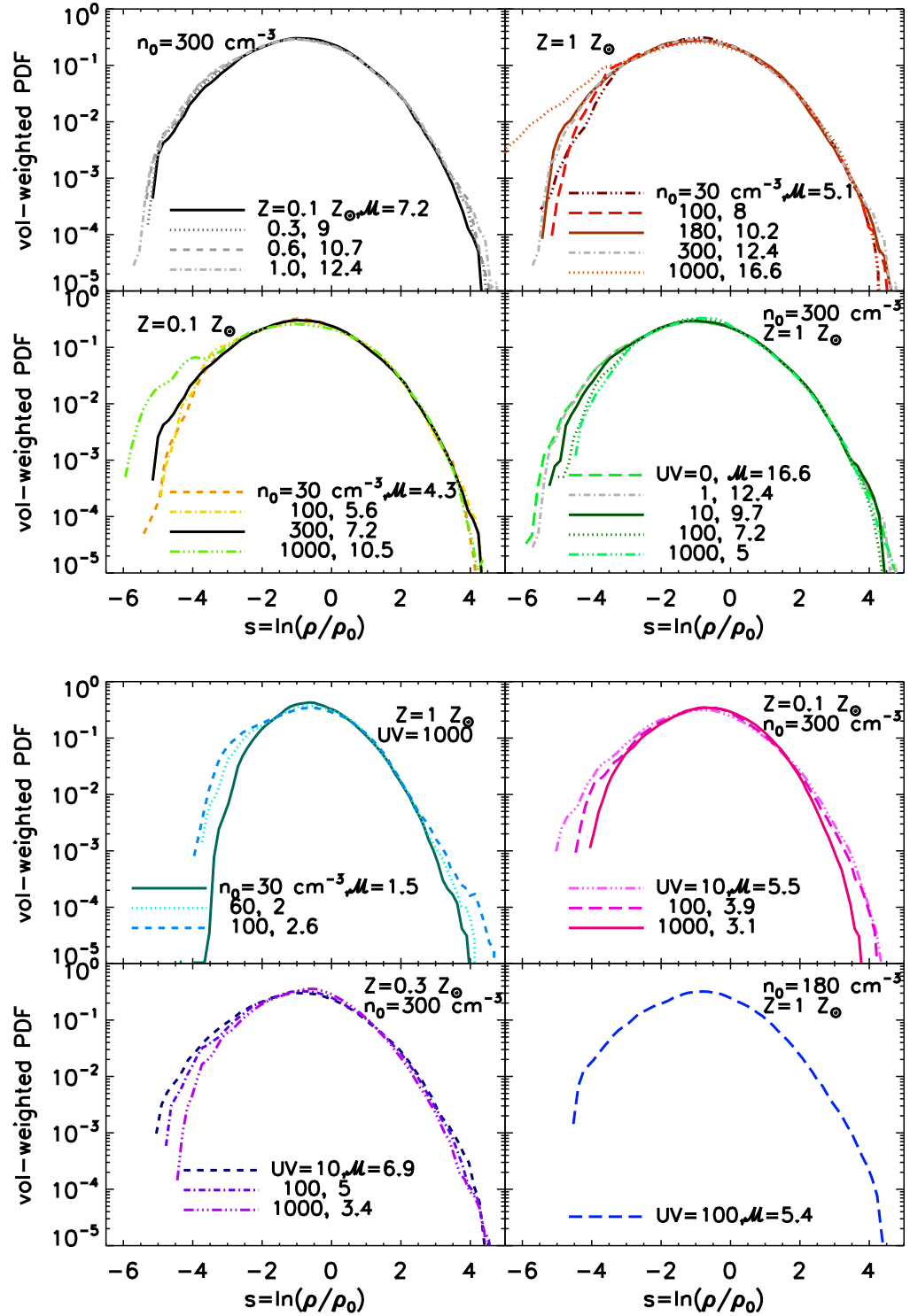


Figure 6.6: Dimensionless density PDF for magnetised non-isothermal molecular clouds. Labels in the panels indicate n_0 , Z , UV radiation field strength and rms Mach number \mathcal{M} for each simulation. The most significant features are: 1) the density variance increases with \mathcal{M} , and 2) the density variance decreases as the product $n_0 \times Z$ decreases and the UV radiation field strength becomes stronger.

the data and is not affected by high fluctuations between one snapshot and the next. Then, we perform a Gaussian fit to this interval.

σ_s - \mathcal{M} test

In order to compare our σ_s - \mathcal{M} predictions (Eqs. 6.42, 6.43, and 6.44) with numerical simulations, we first parametrize γ_0 and β_0 in terms of the rms Mach number. γ depends on the composition of the gas. For gas with a number density of helium $n_{\text{He}} = 0.1n$, and a molecular abundance of H_2 $x_{\text{H}_2} = 2n_{\text{H}_2}/n$ and an electron abundance $x_e = n_e/n$, γ is (Glover and Mac Low, 2007a)

$$\gamma = \frac{5.5 + 5x_e - 1.5x_{\text{H}_2}}{3.3 + 3x_e - 0.5x_{\text{H}_2}}, \quad (6.45)$$

where it is assumed that the rotational degrees of freedom of H_2 are populated, but the vibrational ones are unpopulated (Glover and Mac Low, 2007a).

Fig. 6.7 shows the average γ_0 as a function of \mathcal{M} . γ_0 decreases from ~ 1.66 at $\mathcal{M} \approx 1$ to ~ 1.43 at $\mathcal{M} \approx 17$. The decreases of γ_0 for simulations with higher $n_0 \times Z$ product and low UV field indicates that the hydrogen in the cloud tends to be locked in H_2 molecules.

We use three snapshots of the simulations at ≈ 5.7 Myrs to make a linear regression of these data, which results in

$$\gamma_0 = 1.705(\pm 7 \times 10^{-3}) - 0.0175(\pm 9 \times 10^{-4})\mathcal{M}. \quad (6.46)$$

For β_0 , we rewrite Eq. 6.27 as

$$\beta_0 \approx \frac{2}{\gamma_0} \frac{\mathcal{M}_{A,0}^2}{\mathcal{M}^2}. \quad (6.47)$$

Note that this parameter is calculated considering the instantaneous magnetic field strength and not the initial value.

Fig. 6.8 shows β_0 as a function of \mathcal{M} . The points with arrows indicates different simulation times from $t \approx 5$ Myrs to $t \approx 30$ Myrs. The variation in β_0 does not present any time correlation. For all the runs, β_0 presents large scatter. However applying a regression based on Eq. 6.47 in logarithmic space ($\beta_0 = 207(\pm 2)\mathcal{M}^{-2}$, dashed line), we find two important facts: 1) simulations with the same n_0 locate along a parametrization of the kind $\beta_0 = a\mathcal{M}^{-2}$ with a depending on n_0 . 2) Simulations with decreasing Z and/or increasing UV radiation field strength, lie along of the parametrization curves for their correspondent n_0 (parallel to the dashed line) towards small \mathcal{M} .

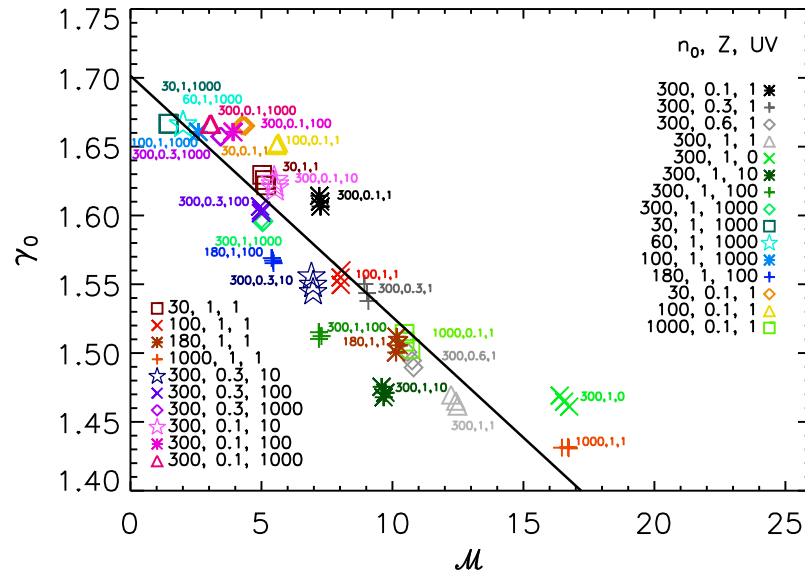


Figure 6.7: Parameterisation of γ_0 as a function of the rms Mach number. The curve is a linear regression gives $\gamma_0 = 1.705(\pm 7 \times 10^{-3}) - 0.0175(\pm 9 \times 10^{-4})\mathcal{M}$. All the simulations are labeled with their n_0 , Z , and UV . Colors are arranged in the same fashion as in the previous figures.

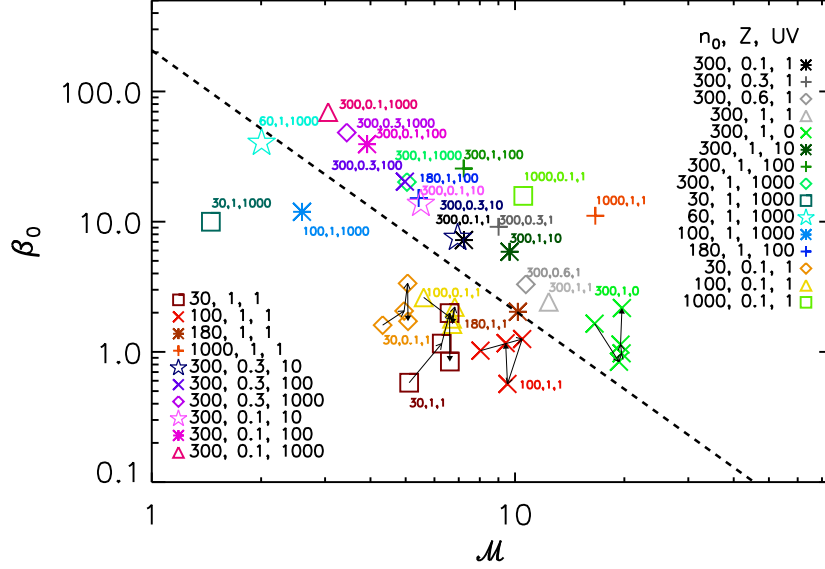


Figure 6.8: Parameterization of $\beta_0 = P_{\text{th}}/P_{0,\text{mag}}$ with respect to the rms Mach number. The curve is a linear regression on the logarithmic space (Eq. 6.47) $\beta_0 = (207 \pm 2)\mathcal{M}^{-2}$. Labels and colors in the simulations are arranged in the same fashion than in the previous figure.

The Alfvénic Mach number $\mathcal{M}_A = v_0/v_A$ (table 6.2) grows with increasing n_0 . Given that all our simulations have constant $v_0 \approx 5 \text{ km s}^{-1}$, it means that v_A decreases towards high n_0 . Remembering that the initial magnetic field strength $B_i = 5.86\mu\text{G}$ is the same for all the runs, and

$$v_A = \frac{B}{\sqrt{4\pi\rho}}, \quad (6.48)$$

it implies that the instantaneous magnetic field strength B may depend on the density $B \propto \rho^\alpha$ with $0 \leq \alpha < 1/2$. With the aim of keeping the number of free parameters as smallest as possible, we use only one parametrization with $\beta_0 = 207(\pm 2)\mathcal{M}^{-2}$, performed for the snapshots at $t \approx 5 \text{ Myrs}$.

Fig. 6.9 shows the standard deviation of the logarithmic density contrast σ_s as a function of the rms Mach number. σ_s is obtained from the Gaussian fit performed to each of the PDFs (Fig. 6.6). For each simulation, we average σ_s over three snapshots at $t \approx 5 \text{ Myrs}$. σ_s increases towards high \mathcal{M} but in a smoother fashion than for the isothermal MHD simulations shown in Fig. 6.3. The black dotted line shows the $\sigma_{s,1/2}\text{-}\mathcal{M}$ relation for the isothermal case which fits best the isothermal-MHD simulations. The colored solid lines

show our predictions for the non-isothermal-MHD gas, $\sigma_{s,0,th}$ (blue line), $\sigma_{s,1/2,th}$ (red line), and $\sigma_{s,1,th}$ (yellow line).

The three σ_s - \mathcal{M} relations predict almost the same σ_2 at $\mathcal{M} \lesssim 10$, and they seem to fit well the data. At higher \mathcal{M} , $\sigma_{s,0,th}$ and $\sigma_{s,1/2,th}$ shows better agreement with the simulations. The dashed line shows the typical $\sigma_s = \ln(1 + b^2 \mathcal{M}^2)^{1/2}$ for the HD isothermal case (e.g. Padoan et al., 1997; Federrath et al., 2008b; Molina et al., 2012). From our findings on the β_0 - \mathcal{M} relation, $\sigma_{s,0,th}$ (Eq. 6.42) and $\sigma_{s,1/2,th}$ (Eq. 6.43) work the best for our simulations. Comparing the dashed and dotted line, magnetic fields alone stop σ_s from growing at high \mathcal{M} because they work as a cushion of the gas (§6.2.1). On the other hand, when a non-isothermal equation of state is included (colored solid lines), σ_s changes by very little (~ 0.5) across all our \mathcal{M} sample.

At $\mathcal{M} \lesssim 3$, the photoelectric heating of dust grains by the UV radiation field is very strong. Together with turbulence, there are higher density contrast shocks than in the isothermal-MHD or isothermal-HD counterpart. \mathcal{M} increases as the product $n_0 \times Z$ grows and the UV radiation field strength gets weaker. At $\mathcal{M} \gtrsim 3$, σ_s only increases by few tenths, even as \mathcal{M} grows by ~ 10 . Shocks heat the gas and generally it cools down through radiative cooling. However, as \mathcal{M} increases, so does A_V , therefore part of the radiation gets trap into the high density zones and may prevent the gas of cooling itself down, and from reaching higher density contrasts. Fig. 5.3 shows that the temperature generally decreases towards high n . All the simulations, except the ones with $Z < 0.6Z_\odot$, have T_K approximately constant $\sim 10 - 15$ K at $n \gtrsim qn_0$, with q increasing as n_0 , or with increasing UV radiation field strength. This issue is not totally clear and needs further study.

We now want to see how our σ_s - \mathcal{M} relations works for $B = 0$ ($\beta_0 \rightarrow \infty$). In absence of magnetic fields, $\sigma_{s,0,th} = \sigma_{s,1/2,th}$, but $\sigma_{s,1,th}$ diverges⁵. Fig. 6.10 is the same as Fig. 6.9, but the solid red line shows $\sigma_{s,1/2,th}$ with $\beta_0 \rightarrow \infty$. $\sigma_{s,0,th}$ and $\sigma_{s,1/2,th}$ (with $\beta_0 \rightarrow \infty$) increases by less than 0.1 at $\mathcal{M} = 26$ in comparison with Fig. 6.9. This difference decreases towards lower \mathcal{M} , meaning that the role of magnetic fields is minor in comparison to the temperature variations across the cloud.

We assume $\Gamma = \gamma_0$, although in Fig. 6.11 study the effect of considering a different γ_0 . Fig. 6.11 is the same as Fig. 6.9, but assuming that Γ is a fraction of the ratio of the specific heats, $\Gamma = f * \gamma_0$ with $f = 0.8$ (dotted lines), 1 (solid lines), 1.5 (dashed lines), and 2 (dash-dotted lines). The lines indicates $\sigma_{s,0,th}$ (blue) and $\sigma_{s,1/2,th}$ (red). At $\mathcal{M} \lesssim 5$, both σ_s s matches each other for all Γ . In

⁵In the limit $\gamma_0 = 1$, $\sigma_{s,1,th}$ (Eq. 6.44) reduces to the isothermal-MHD case (Eq. 6.26), which in turn simplifies to the HD case Eq. 6.24 for $\beta_0 \rightarrow \infty$.

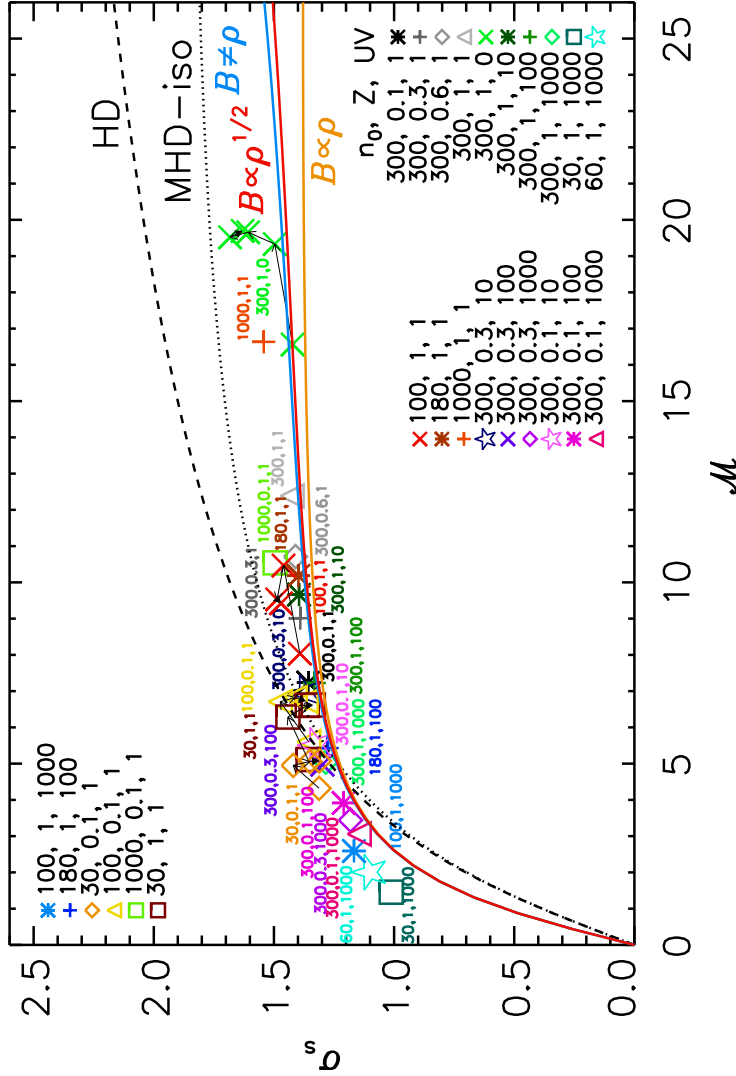


Figure 6.9: Standard deviation of the dimensionless density contrast, plotted as a function of the rms Mach number. Dashed black line shows Padoan et al. (1997) prediction, $\sigma_{s,HD}^2 = \ln(1 + b^2 \mathcal{M}^2)$, with $b = 0.4$, expected for mixed-mode turbulent forcing (Federrath et al., 2010). The dotted line shows our magnetized-isothermal prediction $\sigma_{s,1/2}^2 = \ln(1 + b^2 \mathcal{M}^2 (1 + \beta_0^{-1})^{-1})$, with $b = 0.4$. Solid colored lines show the σ_s - \mathcal{M} relations obtained in this work Eq. (6.42) $\sigma_{s,0,th}$ (blue line), Eq. (6.43) $\sigma_{s,1/2,th}$ (red line), and Eq. (6.44) $\sigma_{s,1}$ (yellow line). Those curves are plotted for $b = 0.4$, and using our parameterizations, $\beta_0 = (207 \pm 2) \mathcal{M}^{-2}$ from Fig. 6.8, and $\gamma_0 = 1.702(\pm 7 \times 10^{-3}) - (1.0175 \pm 9 \times 10^{-4}) \mathcal{M}$ from Fig. 6.7. Labels in the simulations are arranged in the same fashion as previous figures.

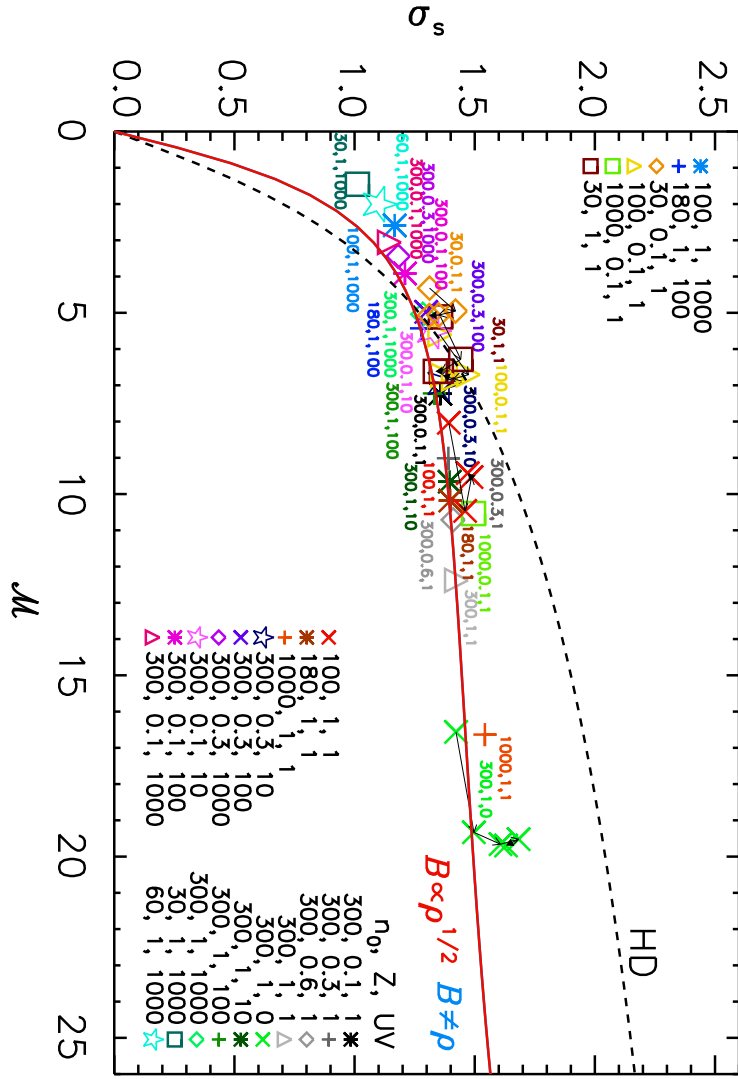


Figure 6.10: Same as Fig. 6.9, but only showing our prediction $\sigma_{s,1/2,th}$ in the limit $\beta_0 \rightarrow \infty$ (red line). The dashed shows the HD limit Eq. 6.24. Both curves are plotted considering $b = 0.4$.

The case of the softer $\Gamma = 0.8\gamma_0$, $\sigma_{s,0,th}$ and $\sigma_{s,1/2,th}$ approach the isothermal-MHD and HD relations (dotted and dashed black lines respectively). For higher Γ ($=[1, 1.5, \text{ and } 2]\gamma_0$), the $\sigma_{s,s}$ grow. At $\lesssim 5 \mathcal{M} \lesssim 9$, both $\sigma_{s,s}$ (with different Γ) are approximately the same. At $\mathcal{M} \gtrsim 5$, $\sigma_{s,s}$ with $\Gamma = (1.5, \text{ and } 2)\gamma_0$ are flat and lower than σ_s with $\Gamma = \gamma_0$. In the case of softer $\Gamma = 0.8\gamma_0$, both $\sigma_{s,s}$ increase, although it is more remarkable for $\sigma_{s,0,th}$ than for $\sigma_{s,1/2,th}$. It is noteworthy to say that $\Gamma > 1$ for all \mathcal{M} shown in this plot. It can be as high as ~ 3.4 if $f = 2$.

Finally, we compare for possible variations of b , for which $b = 1/3$ accounts for purely solenoidal forcing (divergence-free) and $b = 1$ for purely compressive forcing (curl-free) (Federrath et al., 2008b). Fig. 6.12 is the same as Fig. 6.9, but it shows only the $\sigma_{s,1/2,th}$ - \mathcal{M} relation with $b = 1/3$ (long-dashed black line), $b = 0.4$ (solid red line), and $b = 1$ (dash-dotted black line). For comparison, grey lines shows the $\sigma_{s,HD}$ for the purely HD case (the line styles are arranged in the same fashion for the different b s). At $\mathcal{M} \lesssim 3$, $\sigma_{s,1/2,th}$ as well as $\sigma_{s,HD}$ grow as b increases. At a given b , $\sigma_{s,1/2,th}$ is higher than $\sigma_{s,HD}$. At $\mathcal{M} \gtrsim 5$, $\sigma_{s,1/2,th}$ becomes flat with very small differences (~ 0.1) from $b = 1/3$ to $b = 1$. On the contrary, $\sigma_{s,HD}$ increases towards high \mathcal{M} and high b . The effect of radiative trapping at high \mathcal{M} prevents high compressions in the gas, almost independently of the mixture of the forcing modes driving the turbulence.

Considering an equation of state different than isothermal have an astonishing effect on the σ_s - \mathcal{M} relation. The density variance measured from non-isothermal MHD simulations cannot be explained by the simple canonical relation for purely hydrodynamical isothermal gas as is usually assumed. It also cannot be accounted by our approximation for the isothermal-MHD gas.

The predictions $\sigma_{s,0,th}$ and $\sigma_{s,1/2,th}$ fits very well the the simulations. Although at $\mathcal{M} \lesssim 3$, $\sigma_{s,0,th}$ and $\sigma_{s,1/2,th}$ are lower than the one measured from the simulations. It may be for three different reasons: 1) Γ may not simply scale with γ_0 . 2) Given the strong heating at these Mach numbers, b may be higher than 0.4 for this simulations, which implies that there are more compressions than expected from our input. 3) The previous point may not be physical. At these Mach number the gas is transonic. Therefore, sonic waves (which does not produce compressions) start to dominate over supersonic waves, and the compressive modes ($\nabla \cdot \mathbf{F} = 0$) should be turned off in the Navier-Stokes equation (1.2) for these particular simulations (Konstandin et al., 2012b).

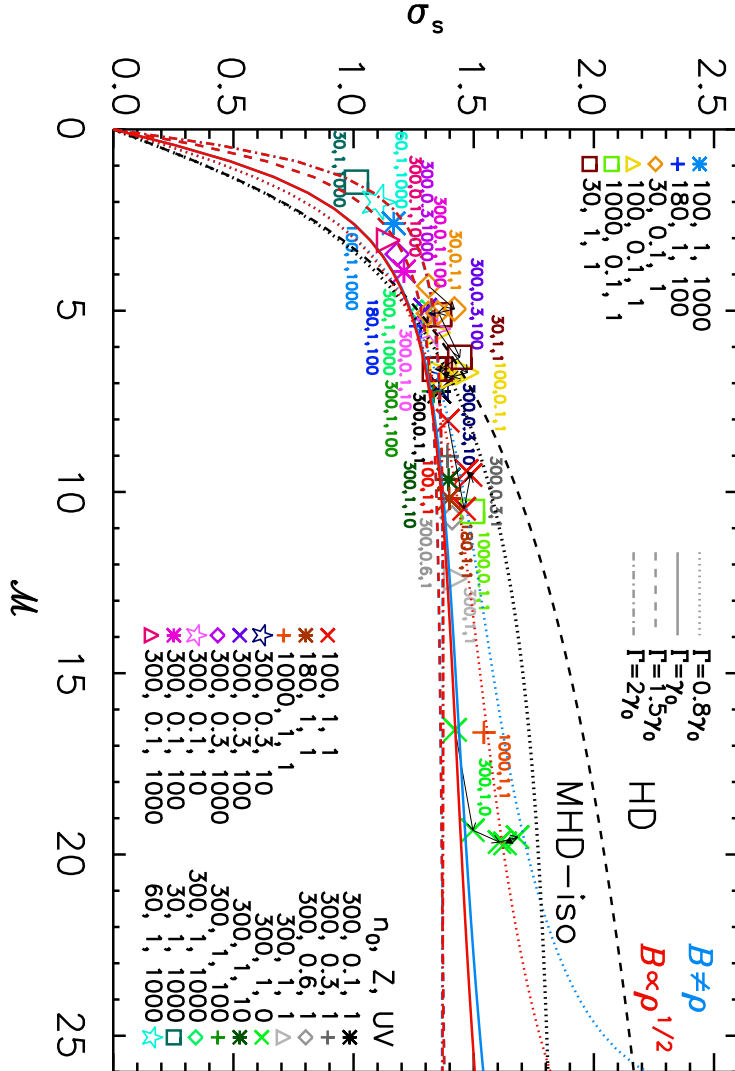


Figure 6.11: Same as Fig. 6.9, but only showing our prediction $\sigma_{s,1/2,th} = \{\ln[1 + b^2 \mathcal{M}^2 \beta_0 / (\beta_0 + 1)]\}^{1/2}$ (red line) with $b = 4$. The black long dashed shows $\sigma_{s,1/2,th}$ with $b = 1/3$ and the black dash-dotted line indicates the same function with $b = 1$. The grey lines shows the Padoan et al. (1997) prediction, $\sigma_{s,HD}^2 = \ln(1 + b^2 \mathcal{M}^2)$, with $b = 0.4$, expected for mixed-mode turbulent forcing (Federrath et al., 2010) (solid grey line), with $b = 1/3$ (long dashed grey line) and with $b = 1$ (dash-dotted grey line).

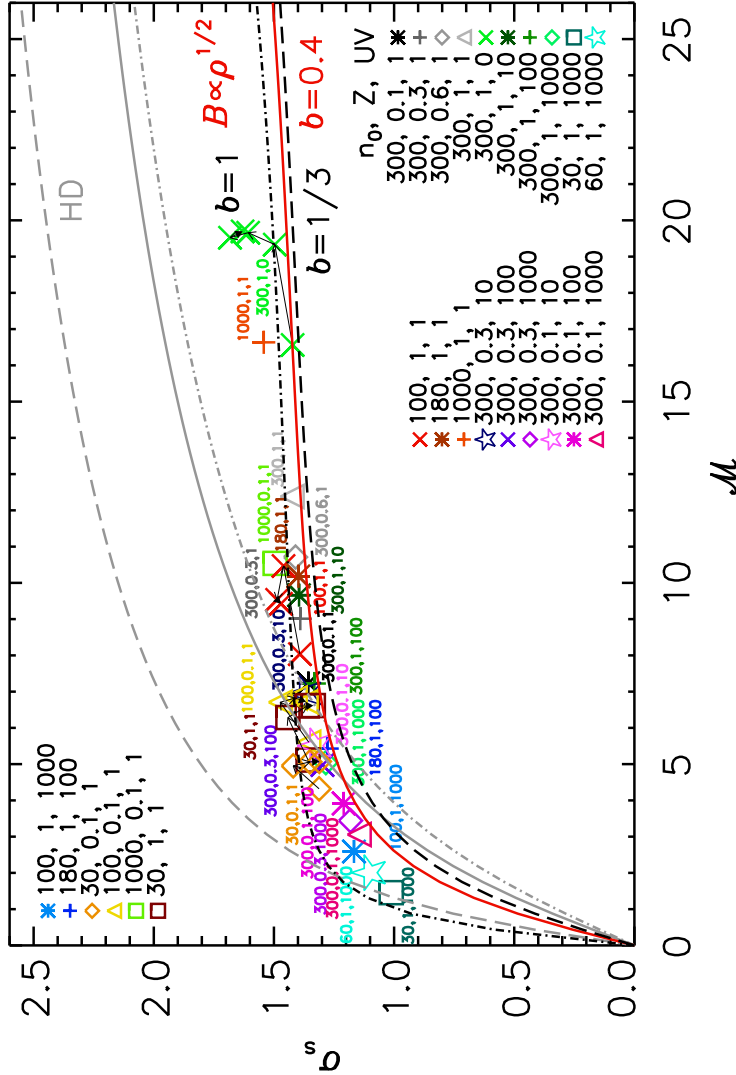


Figure 6.12: Same as Fig. 6.9, but only showing our prediction $\sigma_{s,1/2,th} = \{\ln[1 + b^2 M^2 \beta_0 / (\beta_0 + 1)]\}^{1/2}$ (red line) with $b = 4$. The black long dashed shows $\sigma_{s,1/2,th}$ with $b = 1/3$ and the black dash-dotted line indicates the same function with $b = 1$. The grey lines shows the Padoan et al. (1997) prediction, $\sigma_{s,HD}^2 = \ln(1 + b^2 M^2)$, with $b = 0.4$, expected for mixed-mode turbulent forcing (Federrath et al., 2010) (solid grey line), with $b = 1/3$ (long dashed grey line) and with $b = 1$ (dash-dotted grey line).

6.4 Summary and Conclusions

We presented analytical predictions for the density variance–Mach number relation in magnetized supersonic turbulent gas, considering a isothermal and a non-isothermal equation of state. In this formulation, we considered three different cases for the relation between the magnetic field strength and density. The first case assumes that B is independent of ρ , the second assumes that $B \propto \rho^{1/2}$, while the third is given by $B \propto \rho$. The three resulting σ_s – \mathcal{M} relations were tested against numerical simulations. From this analysis we conclude that:

- For the isothermal gas:
 - If B is independent of the density, we recover the hydrodynamical prediction of [Padoan et al. \(1997\)](#). In this case, the gas and the magnetic field are not coupled. Therefore, an amplification of the magnetic field with the shock is not expected. In this regime, all our predictions converge to the purely hydrodynamical $\sigma_{s,0}$ – \mathcal{M} relation.
 - For the second case, $B \propto \rho^{1/2}$, we found a one-to-one relation between \mathcal{M} , β_0 and the density variance. This $\sigma_{s,1/2}$ – \mathcal{M} relation (Eq. 6.25) matches very well our numerical test considering $b = 0.4$, which is the input for the natural mixture of compressive-to-solenoidal modes in the turbulent forcing field. This result is in agreement with the ones presented by [Ostriker et al. \(2001\)](#) and [Price et al. \(2011\)](#), where they found lower σ_s than in the unmagnetized case for $\mathcal{M} \gtrsim 10$. Moreover, [Cho and Lazarian \(2003\)](#) presented a density contrast that closely matches our result for $\beta_0 \approx 1$ and $5 \lesssim \mathcal{M} \lesssim 10$.
 - For the last case, $B \propto \rho$, the $\sigma_{s,1}$ – \mathcal{M} relation (Eq. 6.26) predicts a lower density variance than measured in our numerical simulations for $\mathcal{M} \geq 5$, because our isothermal simulations are closer to $B \propto \rho^{1/2}$.
 - The $\sigma_{s,1/2}$ – \mathcal{M} relation obtained for $B \propto \rho^{1/2}$ works very well for intermediate to high Alfvénic Mach number, $\mathcal{M}_{A,0} \gtrsim 6$, but breaks down for $\mathcal{M}_{A,0} \lesssim 2$ at $\langle \mathcal{M} \rangle \approx 10$. This probably occurs because in the presence of strong magnetic fields, the turbulence is no longer isotropic. This is because the back reaction of the magnetic field onto the flow is very strong for flows perpendicular to the magnetic field lines.

- Magnetic fields act as a density cushion in turbulent gas, preventing the gas from reaching very low densities as well as very high densities when the gas is isothermal.
- For the non-isothermal gas:
 - Our $\sigma_{s,th}-\mathcal{M}$ relations derived for the three possible relationships of the magnetic field strength with density show good agreement with the simulations. The results are marginally better for $\sigma_{s,0,th}$ (Eq. 6.42) and $\sigma_{s,1/2,th}$ (Eq. 6.43).
 - Particularly, If B is independent of the density, the $\sigma_{s,0,th}-\mathcal{M}$ relation (Eq. 6.42) has a magnetic field term. The reason is not well understood, although we know that this term comes from the energy transport equation. The magnetic terms in the momentum equation vanishes. This point has to be investigated in more detail. In the isothermal limit $\gamma = 1$, the magnetic term vanishes together with the non-isothermal terms and the prediction of Padoan et al. (1997) is recovered.
 - For $B \propto \rho^{1/2}$, $\sigma_{s,1/2,th}$ (Eq. 6.43) is very close to $\sigma_{s,0,th}$. In the limit $\beta_0 \rightarrow \infty$, $\sigma_{s,1/2,th} = \sigma_{s,0,th}$, which also fits very well the simulated data. This result indicates that when a non-isothermal equation is considered, magnetic fields tends to be unimportant.
 - In the case $B \propto \rho$, $\sigma_{s,1,th}$ (Eq. 6.44) differs from the other two cases only towards high \mathcal{M} .
 - The distribution of β_0 as a function of \mathcal{M} shows that magnetic fields and density have a relationship $B \propto \rho^\alpha$, with $0 \leq \alpha < 1/2$. This result explains the differences between our isothermal and non-isothermal $\sigma_s-\mathcal{M}$ relation. When the equation of state is non-isothermal, magnetic fields are diminished. This point needs a more profound study.
 - Although the current analytical derivation fits very well the data, it needs further refinement. The intention is to discern if the behavior at $\mathcal{M} \approx 1$ is caused by a stronger Γ , or if it is unphysical. Moreover, it will also help us to understand the behavior of $\sigma_{s,0,th}-\mathcal{M}$.

Chapter 7

Conclusion and outlook

In this thesis, we analyzed the physical conditions of a large set of molecular clouds. The exploration of a wide range of physical parameters, allowed us to make a rigorous study of the temperature, CO density and ($J=1-0$) emission, as well as the number density distributions. The results are summarized in two parts. The first involves the analysis based on the temperatures and CO distribution. The second corresponds to the density variance study.

7.1 Analysis on the temperatures and CO distributions

- The majority of the CO is distributed towards high density ($n \gtrsim 100 \text{ cm}^{-3}$), cold regions ($T_K \lesssim 40 \text{ K}$) where it is well shielded by dust and H_2 . Its abundance is very small at lower number densities. This condition applies regardless of the mean number density, metallicity or incident UV radiation field strength.
- Molecular clouds are not in LTE. Therefore, CO is a biased tracer of the kinetic temperature of the clouds because its radiation is not thermalized. It is generally subthermally excited $T_{\text{ex}} \lesssim T_K$. Only at high A_V , $\langle T_{\text{ex}} \rangle$ approaches $\langle T_K \rangle$, on average.
- The estimates of N_{CO} from CO ($J=1-0$) emission are closer to the “true” N_{CO} , if the approximation of [Dickman \(1978\)](#) (Eq. 3.6) is applied considering the full PPV T_b spectrum.
- The X-factor varies by $\sim 2-4$ orders of magnitude towards $A_V \lesssim 6 \text{ mag}$. At higher A_V , it is approximately constant. On average, our X-factor is approximates the canonical X-factor for the Milky Way.

- The H_2 mass estimated from CO ($J=1-0$) emission maps is generally underestimated if a constant, Milky-Way X-factor is assumed. For $A_V \lesssim 10$ mag, the amount of CO is very low compared to H_2 , its emission therefore does not represent the density of H_2 . At $A_V \gtrsim 10$ on the other hand, the CO ($J=1-0$) emission is optically thick and its integrated intensity is saturated. In this case the H_2 is underestimated as well.

With the aim of approaching better to observational conditions, one of the next steps will be to introduce “beaming” effects in the measurements of “observable” quantities. The other important point is to extend this analysis to simulations which includes self-gravity. The idea is to study how self-gravity may change the conditions of the gas, particularly regions where most of the CO exists.

7.2 Density variance–Mach number relation

- When the gas is isothermal, magnetic fields act as a density cushion in turbulent gas, preventing the gas from reaching very low densities as well as very high densities. In this case scenario, our analytical $\sigma_{s,1/2}$ – \mathcal{M} relation explains very well the simulated data, because for this simulations $B \propto \rho^{1/2}$.
- If a non-isothermal equation of state is included, magnetic fields tend to be unimportant. B depends on ρ in a weaker fashion: $B \propto \rho^\alpha$, with $0 \leq \alpha < 1/2$. The $\sigma_{s,th}$ – \mathcal{M} relations for $\alpha = 0$ and $\alpha = 1/2$ are very similar and fits very well our simulations.

The results for the non-isothermal gas need to be explored in more extend. Although our analytical derivations fits very well the data, there are still many open questions. It is very important to understand the role of magnetic fields and the equation of state in molecular clouds. Moreover, it is necessary to include self-gravity in this analysis. Because the σ_s – \mathcal{M} relation is one of the basic ingredients of theories for star formation and Initial stellar/core mass functions.

Appendix

Comparing position-position-position (PPP) and position-position-velocity data cubes

Our radiative transfer model produces a spectral position-position-wavelength ($\text{PP}\lambda \rightarrow x, y, \lambda$) cube of the emission line of interest. The cube indicates the intensity for a given wavelength at each (x, y) position (Shetty et al., 2011a). In sub-mm or radio astronomy, the observational spectra are often expressed in terms of velocity instead of wavelength or frequency. For this practical reason, we transform the wavelength in the $\text{PP}\lambda$ cube into the corresponding LoS velocity (v_z) through Doppler shift calculations $v_z = (1 - \lambda_0/\lambda)c$, where λ_0 is the wavelength of the line center. The intensity spectrum results then into a position-position-velocity (PPV) cube.

On the other hand, all the physical quantities produced by ZEUS-MP are in a position-position-position (PPP) cubic base. We then transform the PPV or PPP cubes into a common frame for comparing both datasets. For convenience, we convert the PPP into PPV cubes, because the PPV cubes do not contain information about the location of the cells along the LoS. In addition among the PPP cubes, we have information of the three components of the velocity at every position (x, y, z) . Therefore, transforming the positions along the LoS z into v_z is a much simpler procedure than the other way around.

We choose a broad range in wavelengths sufficient enough that all LoS velocities in the simulation are detected, so that all emission from the model is “observed”. The PPP cube is arranged by increasing v_z considering a Δv_z that accounts for all the channels in the PPV cube. We also include “Doppler catching” method in order to prevent Doppler jumps (see Shetty et al., 2011b, and RADMC-3D user manual¹). All the channels are equally spaced in velocity, and so it is very likely to have more than one cell in some channels and none for others. As a result, the shape of the PDF of a given physical quantity may be different if it is calculated from a PPP or a PPV cube. For example, in Fig. 1a we show the number density PDF derived from the PPP cube (solid line) which is clearly wider than the PDF from the PPV cube (dashed line). In the case of densities in the PPV cube, the cells with v_z within the same velocity channel are added, the high density and low density tails of the PDF derived from the PPV cube are therefore overpopulated in comparison with the number density PDF of the PPP cube. The number density PDF of the PPV cube looks “distorted” in comparison with the PPP

¹<http://www.ita.uni-heidelberg.de/~dullemond/software/radmc-3d/>

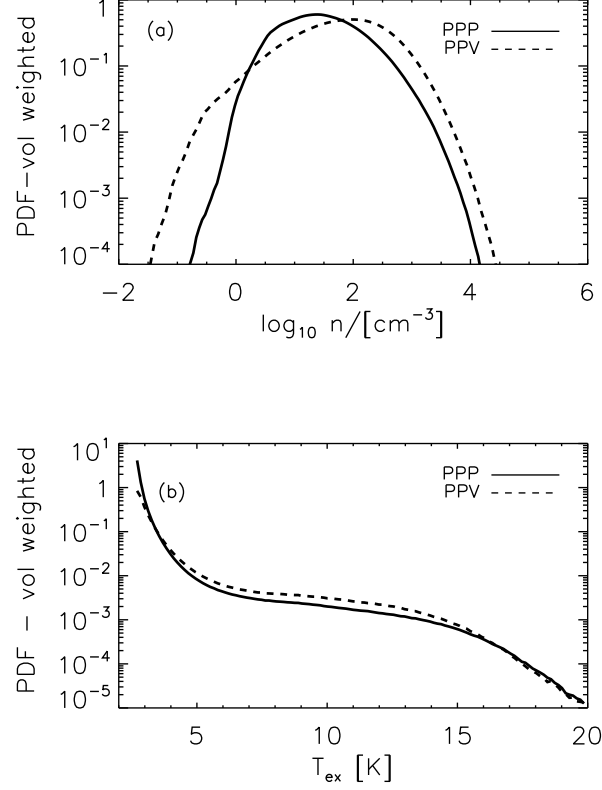


Figure 1: (a) Volume-weighted PDF of the number density. The solid line shows the PDF using the position-position-position (PPP) dataset, while the dashed line indicates the PDF using the position-position-velocity (PPV) data. (b) same as (a) but for the excitation temperature T_{ex} .

counterpart.

In the case of temperatures, we choose to compute the mass-weighted average of the temperature of the cells with v_z within the same channel. In Fig. 1b, we show the volume-weighted PDF of the excitation temperature (Eq. 3.4) from the PPP (solid line) and PPV (dashed line) cubes. We see that both PDFs have almost the same shape with very small differences and the range of T_{ex} covered by both curves is the same. In the case of the kinetic temperature, there are also some differences, but the temperature range is almost the same for both distributions. Therefore in the case of temperatures, the PPP and PPV cubes have distributions which are basically equivalent.

Bibliography

Ackermann, M., Ajello, M., Allafort, A., Baldini, L., Ballet, J., Barbiellini, G., Baring, M. G., Bastieri, D., Bechtol, K., Bellazzini, R., Blandford, R. D., Bloom, E. D., Bonamente, E., Borgland, A. W., Bottacini, E., Brandt, T. J., Bregeon, J., Brigida, M., Bruel, P., Buehler, R., Busetto, G., Buson, S., Caliandro, G. A., Cameron, R. A., Caraveo, P. A., Casandjian, J. M., Cecchi, C., Çelik, Ö., Charles, E., Chaty, S., Chaves, R. C. G., Chekhtman, A., Cheung, C. C., Chiang, J., Chiaro, G., Cillis, A. N., Ciprini, S., Claus, R., Cohen-Tanugi, J., Cominsky, L. R., Conrad, J., Corbel, S., Cutini, S., D'Ammando, F., de Angelis, A., de Palma, F., Dermer, C. D., do Couto e Silva, E., Drell, P. S., Drlica-Wagner, A., Falletti, L., Favuzzi, C., Ferrara, E. C., Franckowiak, A., Fukazawa, Y., Funk, S., Fusco, P., Gargano, F., Germani, S., Giglietto, N., Giommi, P., Giordano, F., Giroletti, M., Glanzman, T., Godfrey, G., Grenier, I. A., Grondin, M.-H., Grove, J. E., Guiriec, S., Hadasch, D., Hanabata, Y., Harding, A. K., Hayashida, M., Hayashi, K., Hays, E., Hewitt, J. W., Hill, A. B., Hughes, R. E., Jackson, M. S., Jogler, T., Jóhannesson, G., Johnson, A. S., Kamae, T., Kataoka, J., Katsuta, J., Knödlseider, J., Kuss, M., Lande, J., Larsson, S., Latronico, L., Lemoine-Goumard, M., Longo, F., Loparco, F., Lovellette, M. N., Lubrano, P., Madejski, G. M., Massaro, F., Mayer, M., Mazziotta, M. N., McEnery, J. E., Mehault, J., Michelson, P. F., Mignani, R. P., Mitthumsiri, W., Mizuno, T., Moiseev, A. A., Monzani, M. E., Morselli, A., Moskalenko, I. V., Murgia, S., Nakamori, T., Nemmen, R., Nuss, E., Ohno, M., Ohsugi, T., Omodei, N., Orienti, M., Orlando, E., Ormes, J. F., Paneque, D., Perkins, J. S., Pesce-Rollins, M., Piron, F., Pivato, G., Rainò, S., Rando, R., Razzano, M., Razzaque, S., Reimer, A., Reimer, O., Ritz, S., Romoli, C., Sánchez-Conde, M., Schulz, A., Sgrò, C., Simeon, P. E., Siskind, E. J., Smith, D. A., Spandre, G., Spinelli, P., Stecker, F. W., Strong, A. W., Suson, D. J., Tajima, H., Takahashi, H., Takahashi, T., Tanaka, T., Thayer, J. G., Thayer, J. B., Thompson, D. J., Thorsett, S. E., Tibaldo, L., Tibolla, O., Tinivella, M., Troja, E., Uchiyama, Y., Usher, T. L., Vandenbroucke, J., Vasileiou, V., Vianello, G.,

- Vitale, V., Waite, A. P., Werner, M., Winer, B. L., Wood, K. S., Wood, M., Yamazaki, R., Yang, Z., and Zimmer, S.: 2013, *Science* **339**, 807
- Adler, D. S. and Roberts, Jr., W. W.: 1992, *ApJ* **384**, 95
- Avillez, M. A., Ballesteros-Paredes, J., and Mac Low, M.-M.: 2000, in *American Astronomical Society Meeting Abstracts #196*, Vol. 32 of *Bulletin of the American Astronomical Society*, p. 711
- Ballesteros-Paredes, J., Hartmann, L., and Vázquez-Semadeni, E.: 1999, *ApJ* **527**, 285
- Ballesteros-Paredes, J. and Mac Low, M.-M.: 2002, *ApJ* **570**, 734
- Banerjee, R., Vázquez-Semadeni, E., Hennebelle, P., and Klessen, R. S.: 2009, *MNRAS* **398**, 1082
- Beaumont, C. and et al.: 2013, *in preparation*
- Bertram, E., Federrath, C., Banerjee, R., and Klessen, R. S.: 2012, *MNRAS* **420**, 3163
- Bohlin, R. C., Savage, B. D., and Drake, J. F.: 1978, *ApJ* **224**, 132
- Bolatto, A. D., Leroy, A. K., Rosolowsky, E., Walter, F., and Blitz, L.: 2008, *ApJ* **686**, 948
- Bolatto, A. D., Wolfire, M., and Leroy, A. K.: 2013, *To appear in ARAA, Annual Reviews of Astronomy and Astrophysics, ARAA issue 51 (ArXiv e-prints:1301.3498)*
- Brunt, C. M.: 2003, *ApJ* **583**, 280
- Brunt, C. M., Federrath, C., and Price, D. J.: 2010, *MNRAS* **403**, 1507
- Brunt, C. M., Heyer, M. H., and Mac Low, M.-M.: 2009, *A&A* **504**, 883
- Burgh, E. B., France, K., and McCandliss, S. R.: 2007, *ApJ* **658**, 446
- Carroll, B. W. and Ostlie, D. A.: 2006, *An introduction to modern astrophysics and cosmology*
- Cho, J. and Lazarian, A.: 2003, *MNRAS* **345**, 325
- Cho, W. and Kim, J.: 2011, *MNRAS* **410**, L8
- Collins, D. C., Padoan, P., Norman, M. L., and Xu, H.: 2011, *ApJ* **731**, 59

- Crutcher, R., Heiles, C., and Troland, T.: 2003, in E. Falgarone & T. Passot (ed.), *Turbulence and Magnetic Fields in Astrophysics*, Vol. 614 of *Lecture Notes in Physics*, Berlin Springer Verlag, pp 155–181
- Crutcher, R. M.: 1999, *ApJ* **520**, 706
- Crutcher, R. M., Hakobian, N., and Troland, T. H.: 2009, *ApJ* **692**, 844
- Crutcher, R. M., Wandelt, B., Heiles, C., Falgarone, E., and Troland, T. H.: 2010, *ApJ* **725**, 466
- Décamp, N. and Le Bourlot, J.: 2002, *A&A* **389**, 1055
- Dickman, R. L.: 1978, *ApJS* **37**, 407
- Doty, S. D., Tidman, R., Shirley, Y., and Jackson, A.: 2010, *MNRAS* **406**, 1190
- Draine, B. T.: 1978, *ApJS* **36**, 595
- Draine, B. T.: 2011, *Physics of the Interstellar and Intergalactic Medium*
- Draine, B. T. and Bertoldi, F.: 1996, *ApJ* **468**, 269
- Dullemond, C. P.: 2012, *RADMC-3D: A multi-purpose radiative transfer tool*, Astrophysics Source Code Library
- Dyson, J. E. and Williams, D. A.: 1980, *Physics of the interstellar medium*, New York, Halsted Press, 1980. 204 p.
- Elmegreen, B. G.: 1993, *ApJL* **419**, L29
- Elmegreen, B. G. and Scalo, J.: 2004, *ARA&A* **42**, 211
- Esquivel, A. and Lazarian, A.: 2011, *ApJ* **740**, 117
- Falgarone, E., Hily-Blant, P., Pety, J., and Pineau Des Forêts, G.: 2005, in E. M. de Gouveia dal Pino, G. Lugones, and A. Lazarian (eds.), *Magnetic Fields in the Universe: From Laboratory and Stars to Primordial Structures.*, Vol. 784 of *American Institute of Physics Conference Series*, pp 299–307
- Falgarone, E. and Phillips, T. G.: 1990, *ApJ* **359**, 344
- Falgarone, E. and Puget, J.-L.: 1995, *A&A* **293**, 840

- Federrath, C., Glover, S. C. O., Klessen, R. S., and Schmidt, W.: 2008a, *Physica Scripta Volume T* **132(1)**, 014025
- Federrath, C. and Klessen, R. S.: 2012, *ApJ* **761**, 156
- Federrath, C., Klessen, R. S., and Schmidt, W.: 2008b, *ApJL* **688**, L79
- Federrath, C., Klessen, R. S., and Schmidt, W.: 2009, *ApJ* **692**, 364
- Federrath, C., Roman-Duval, J., Klessen, R. S., Schmidt, W., and Mac Low, M.-M.: 2010, *A&A* **512**, A81+
- Federrath, C., Sur, S., Schleicher, D. R. G., Banerjee, R., and Klessen, R. S.: 2011, *ApJ* **731**, 62
- Fleck, Jr., R. C.: 1982, *MNRAS* **201**, 551
- Frerking, M. A., Langer, W. D., and Wilson, R. W.: 1982, *ApJ* **262**, 590
- Garden, R. P., Hayashi, M., Hasegawa, T., Gatley, I., and Kaifu, N.: 1991, *ApJ* **374**, 540
- Glover, S. C. O. and Clark, P. C.: 2012a, *MNRAS* **421**, 116
- Glover, S. C. O. and Clark, P. C.: 2012b, *MNRAS* **421**, 9
- Glover, S. C. O., Federrath, C., Mac Low, M.-M., and Klessen, R. S.: 2010, *MNRAS* **404**, 2
- Glover, S. C. O. and Mac Low, M.-M.: 2007a, *ApJS* **169**, 239
- Glover, S. C. O. and Mac Low, M.-M.: 2007b, *ApJ* **659**, 1317
- Glover, S. C. O. and Mac Low, M.-M.: 2011, *MNRAS* **412**, 337
- Goldreich, P. and Kwan, J.: 1974, *ApJ* **189**, 441
- Goldsmith, P. F.: 1988, in R. L. Dickman, R. L. Snell, and J. S. Young (eds.), *Molecular Clouds, Milky-Way and External Galaxies*, Vol. 315 of *Lecture Notes in Physics*, Berlin Springer Verlag, p. 1
- Goldsmith, P. F.: 2001, *ApJ* **557**, 736
- Goldsmith, P. F., Heyer, M., Narayanan, G., Snell, R., Li, D., and Brunt, C.: 2008, *ApJ* **680**, 428
- Goldsmith, P. F. and Langer, W. D.: 1978, *ApJ* **222**, 881

- Goodman, A. A., Pineda, J. E., and Schnee, S. L.: 2009a, *ApJ* **692**, 91
- Goodman, A. A., Rosolowsky, E. W., Borkin, M. A., Foster, J. B., Halle, M., Kauffmann, J., and Pineda, J. E.: 2009b, *Nature* **457**, 63
- Habing, H. J.: 1968, *Bull. Astron. Inst. Neth.* **19**, 421
- Hartmann, L., Calvet, N., Gullbring, E., and D'Alessio, P.: 1998, *ApJ* **495**, 385
- Hayes, J. C., Norman, M. L., Fiedler, R. A., Bordner, J. O., Li, P. S., Clark, S. E., ud-Doula, A., and Mac Low, M.-M.: 2006, *ApJS* **165**, 188
- Heiles, C. and Troland, T. H.: 2005, *ApJ* **624**, 773
- Heiner, J. S., Allen, R. J., Emonts, B. H. C., and van der Kruit, P. C.: 2008, *ApJ* **673**, 798
- Hennebelle, P. and Chabrier, G.: 2008, *ApJ* **684**, 395
- Hennebelle, P. and Chabrier, G.: 2009, *ApJ* **702**, 1428
- Hennebelle, P. and Chabrier, G.: 2011, *ApJL* **743**, L29
- Hennebelle, P. and Pérault, M.: 2000, *A&A* **359**, 1124
- Joseph, D. d.: 2006, *Proc. Nat. Acad. Sci. USA* **103(39)**, 14272
- Kainulainen, J., Beuther, H., Henning, T., and Plume, R.: 2009, *A&A* **508**, L35
- Kainulainen, J. and Tan, J. C.: 2013, *A&A* **549**, A53
- Kim, J., Balsara, D., and Mac Low, M.-M.: 2001, *Journal of Korean Astronomical Society* **34**, 333
- Kippenhahn, R. and Weigert, A.: 1994, *Stellar Structure and Evolution*
- Klessen, R. S.: 2000, *ApJ* **535**, 869
- Klessen, R. S.: 2001, *ApJ* **556**, 837
- Klessen, R. S. and Burkert, A.: 2000, *ApJS* **128**, 287
- Konstandin, L., Federrath, C., Klessen, R. S., and Schmidt, W.: 2012a, *Journal of Fluid Mechanics* **692**, 183

- Konstandin, L., Girichidis, P., Federrath, C., and Klessen, R. S.: 2012b, *ApJ* **761**, 149
- Kritsuk, A. G., Norman, M. L., Padoan, P., and Wagner, R.: 2007, *ApJ* **665**, 416
- Kritsuk, A. G., Norman, M. L., and Wagner, R.: 2011, *ApJL* **727**, L20
- Krumholz, M. R. and McKee, C. F.: 2005, *ApJ* **630**, 250
- Lacy, J. H., Knacke, R., Geballe, T. R., and Tokunaga, A. T.: 1994, *ApJL* **428**, L69
- Lai, S.-P., Velusamy, T., Langer, W. D., and Kuiper, T. B. H.: 2003, *AJ* **126**, 311
- Landau, L. D. and Lifshitz, E. M.: 1987, *Fluid mechanics*
- Langer, W. D., Wilson, R. W., Goldsmith, P. F., and Beichman, C. A.: 1989, *ApJ* **337**, 355
- Larson, R. B.: 1981, *MNRAS* **194**, 809
- Lee, M., Stanimirović, S., Wolfire, M. G., Shetty, R., Glover, S. C. O., Molina, F. Z., and Klessen, R. S.: 2013, *submitted to ApJ*
- Lemaster, M. N. and Stone, J. M.: 2008, *ApJL* **682**, L97
- Lequeux, J.: 2005, *The interstellar medium, Translation from the French language edition of: Le Milieu Interstellaire by James Lequeux, EDP Sciences, 2003 Edited by J. Lequeux. Astronomy and astrophysics library, Berlin: Springer, 2005*
- Leroy, A. K., Bolatto, A., Gordon, K., Sandstrom, K., Gratier, P., Rosolowsky, E., Engelbracht, C. W., Mizuno, N., Corbelli, E., Fukui, Y., and Kawamura, A.: 2011, *ApJ* **737**, 12
- Leung, C.-M. and Liszt, H. S.: 1976, *ApJ* **208**, 732
- Li, P. S., Norman, M. L., Mac Low, M.-M., and Heitsch, F.: 2004, *ApJ* **605**, 800
- Li, Y., Klessen, R. S., and Mac Low, M.-M.: 2003, *ApJ* **592**, 975
- Liszt, H. S. and Lucas, R.: 1998, *A&A* **339**, 561

- Liszt, H. S., Pety, J., and Lucas, R.: 2010, *A&A* **518**, A45
- Mac Low, M.-M.: 1999, *ApJ* **524**, 169
- Mac Low, M.-M. and Klessen, R. S.: 2004, *Reviews of Modern Physics* **76**, 125
- Mac Low, M.-M., Klessen, R. S., Burkert, A., and Smith, M. D.: 1998, *Physical Review Letters* **80**, 2754
- Martin, R. N., Ruf, K., and Ho, P. T. P.: 1982, *Nature* **296**, 632
- Matzner, C. D.: 2002, *ApJ* **566**, 302
- McKee, C. F. and Ostriker, E. C.: 2007, *ARA&A* **45**, 565
- Mihalas, D. and Binney, J.: 1981, *Galactic astronomy: Structure and kinematics /2nd edition/*
- Molina, F., Glover, S., and Federrath, C.: 2011, in M. Röllig, R. Simon, V. Ossenkopf, and J. Stutzki (eds.), *EAS Publications Series*, Vol. 52 of *EAS Publications Series*, pp 289–290
- Molina, F. Z., Glover, S. C. O., Federrath, C., and Klessen, R. S.: 2012, *MNRAS* **423**, 2680
- Mouschovias, T. C. and Ciolek, G. E.: 1999, in C. J. Lada & N. D. Kylafis (ed.), *NATO ASIC Proc. 540: The Origin of Stars and Planetary Systems*, p. 305
- Nelson, R. P. and Langer, W. D.: 1997, *ApJ* **482**, 796
- Nelson, R. P. and Langer, W. D.: 1999, *ApJ* **524**, 923
- Nordlund, Å. K. and Padoan, P.: 1999, in J. Franco & A. Carraminana (ed.), *Interstellar Turbulence*, p. 218
- Norman, M. L.: 2000, in S. J. Arthur, N. S. Brickhouse, & J. Franco (ed.), *Revista Mexicana de Astronomia y Astrofisica Conference Series*, Vol. 9 of *Revista Mexicana de Astronomia y Astrofisica*, vol. 27, pp 66–71
- Ossenkopf, V. and Mac Low, M.-M.: 2002, *A&A* **390**, 307
- Ostriker, E. C., Stone, J. M., and Gammie, C. F.: 2001, *ApJ* **546**, 980
- Padoan, P. and Nordlund, Å.: 1999, *ApJ* **526**, 279

- Padoan, P. and Nordlund, Å.: 2002, *ApJ* **576**, 870
- Padoan, P. and Nordlund, Å.: 2011, *ApJ* **730**, 40
- Padoan, P., Nordlund, A., and Jones, B. J. T.: 1997, *MNRAS* **288**, 145
- Passot, T. and Vázquez-Semadeni, E.: 1998, *Phys. Rev. E.* **58**, 4501
- Pety, J., Liszt, H. S., and Lucas, R.: 2011, in M. Röllig, R. Simon, V. Ossenkopf, and J. Stutzki (eds.), *EAS Publications Series*, Vol. 52 of *EAS Publications Series*, pp 151–155
- Pineda, J. E., Caselli, P., and Goodman, A. A.: 2008, *ApJ* **679**, 481
- Pineda, J. L., Goldsmith, P. F., Chapman, N., Snell, R. L., Li, D., Cambrésy, L., and Brunt, C.: 2010, *ApJ* **721**, 686
- Pon, A., Johnstone, D., and Kaufman, M. J.: 2012, *ApJ* **748**, 25
- Pope, S. B.: 2011, *Turbulent Flows.*, Cambridge University Press
- Pope, S. B. and Ching, E. S. C.: 1993, *Phys. Fluids A.* **5(7)**, 1529
- Press, W. H. and Schechter, P.: 1974, *ApJ* **187**, 425
- Price, D. J. and Federrath, C.: 2010, *MNRAS* **406**, 1659
- Price, D. J., Federrath, C., and Brunt, C. M.: 2011, *ApJL* **727**, L21
- Rachford, B. L., Snow, T. P., Tumlinson, J., Shull, J. M., Blair, W. P., Ferlet, R., Friedman, S. D., Gry, C., Jenkins, E. B., Morton, D. C., Savage, B. D., Sonnentrucker, P., Vidal-Madjar, A., Welty, D. E., and York, D. G.: 2002, *ApJ* **577**, 221
- Rathborne, J. M., Jackson, J. M., Chambers, E. T., Stojimirovic, I., Simon, R., Shipman, R., and Frieswijk, W.: 2010, *ApJ* **715**, 310
- Reddish, V. C.: 1975, *MNRAS* **170**, 261
- Ridge, N. A., Di Francesco, J., Kirk, H., Li, D., Goodman, A. A., Alves, J. F., Arce, H. G., Borkin, M. A., Caselli, P., Foster, J. B., Heyer, M. H., Johnstone, D., Kosslyn, D. A., Lombardi, M., Pineda, J. E., Schnee, S. L., and Tafalla, M.: 2006, *AJ* **131**, 2921
- Rodríguez-Fernández, N. J., Martín-Pintado, J., Fuente, A., and Wilson, T. L.: 2004, *A&A* **427**, 217

- Roman-Duval, J., Jackson, J. M., Heyer, M., Rathborne, J., and Simon, R.: 2010, *ApJ* **723**, 492
- Rybicki, G. B. and Lightman, A. P.: 1979, *Radiative processes in astrophysics*
- Sandstrom, K. M., Leroy, A. K., Walter, F., Bolatto, A. D., Croxall, K. V., Draine, B. T., Wilson, C. D., Wolfire, M., Calzetti, D., Kennicutt, R. C., Aniano, G., Donovan Meyer, J., Usero, A., Bigiel, F., Brinks, E., de Blok, W. J. G., Crocker, A., Dale, D., Engelbracht, C. W., Galametz, M., Groves, B., Hunt, L. K., Koda, J., Kreckel, K., Linz, H., Meidt, S., Pellegrini, E., Rix, H.-W., Roussel, H., Schinnerer, E., Schrubba, A., Schuster, K.-F., Skibba, R., van der Laan, T., Appleton, P., Armus, L., Brandl, B., Gordon, K., Hinz, J., Krause, O., Montiel, E., Sauvage, M., Schmiedeke, A., Smith, J. D. T., and Vigroux, L.: 2012, *ArXiv e-prints*
- Scalo, J. and Elmegreen, B. G.: 2004, *ARA&A* **42**, 275
- Scalo, J., Vazquez-Semadeni, E., Chappell, D., and Passot, T.: 1998, *ApJ* **504**, 835
- Schleicher, D. R. G., Banerjee, R., Sur, S., Arshakian, T. G., Klessen, R. S., Beck, R., and Spaans, M.: 2010, *A&A* **522**, A115
- Schmeja, S. and Klessen, R. S.: 2004, *A&A* **419**, 405
- Schmidt, W., Federrath, C., Hupp, M., Kern, S., and Niemeyer, J. C.: 2009, *A&A* **494**, 127
- Schober, J., Schleicher, D., Bovino, S., and Klessen, R. S.: 2012a, *Phys. Rev. E* **86(6)**, 066412
- Schober, J., Schleicher, D., Federrath, C., Klessen, R., and Banerjee, R.: 2012b, *Phys. Rev. E* **85(2)**, 026303
- Schöier, F. L., van der Tak, F. F. S., van Dishoeck, E. F., and Black, J. H.: 2005, *A&A* **432**, 369
- Sembach, K. R., Howk, J. C., Ryans, R. S. I., and Keenan, F. P.: 2000, *ApJ* **528**, 310
- Shetty, R., Collins, D. C., Kauffmann, J., Goodman, A. A., Rosolowsky, E. W., and Norman, M. L.: 2010, *ApJ* **712**, 1049
- Shetty, R., Glover, S. C., Dullemond, C. P., and Klessen, R. S.: 2011a, *MNRAS* **412**, 1686

- Shetty, R., Glover, S. C., Dullemond, C. P., Ostriker, E. C., Harris, A. I., and Klessen, R. S.: 2011b, *MNRAS* **415**, 3253
- Shetty, R., Kauffmann, J., Schnee, S., Goodman, A. A., and Ercolano, B.: 2009, *ApJ* **696**, 2234
- Shu, F. H., Adams, F. C., and Lizano, S.: 1987, *ARA&A* **25**, 23
- Sobolev, V. V.: 1957, *SvA* **1**, 678
- Solomon, P. M., Rivolo, A. R., Barrett, J., and Yahil, A.: 1987, *ApJ* **319**, 730
- Solomon, P. M. and Vanden Bout, P. A.: 2005, *ARA&A* **43**, 677
- Strong, A. W., Moskalenko, I. V., and Ptuskin, V. S.: 2007, *Annual Review of Nuclear and Particle Science* **57**, 285
- Strong, A. W., Moskalenko, I. V., Reimer, O., Digel, S., and Diehl, R.: 2004, *A&A* **422**, L47
- Sur, S., Schleicher, D. R. G., Banerjee, R., Federrath, C., and Klessen, R. S.: 2010, *ApJL* **721**, L134
- Tielens, A. G. G. M.: 2005, *The Physics and Chemistry of the Interstellar Medium*
- van der Tak, F. F. S., Black, J. H., Schöier, F. L., Jansen, D. J., and van Dishoeck, E. F.: 2007, *A&A* **468**, 627
- van Dishoeck, E. and Black, J. H.: 1986, *ApJ* **307**, 332
- van Dishoeck, E. F. and Black, J. H.: 1988, *ApJ* **334**, 771
- Vázquez-Semadeni, E.: 1994, *ApJ* **423**, 681
- Visser, R., van Dishoeck, E. F., and Black, J. H.: 2009, *A&A* **503**, 323
- von Weizsäcker, C. F.: 1951, *ApJ* **114**, 165
- Wada, K.: 2001, *ApJL* **559**, L41
- Walmsley, C. M. and Ungerechts, H.: 1983, *A&A* **122**, 164
- Ward-Thompson, D., André, P., Crutcher, R., Johnstone, D., Onishi, T., and Wilson, C.: 2007, *Protostars and Planets V* pp 33–46

- White, G. J.: 1997, in W. B. Latter, S. J. E. Radford, P. R. Jewell, J. G. Mangum, and J. Bally (eds.), *IAU Symposium*, Vol. 170 of *IAU Symposium*, pp 101–109
- Wienen, M., Wyrowski, F., Schuller, F., Menten, K. M., Walmsley, C. M., Bronfman, L., and Motte, F.: 2012, *A&A* **544**, A146
- Wilson, T. L., Rohlfs, K., and Hüttemeister, S.: 2009, *Tools of Radio Astronomy*, Springer-Verlag
- Wolfire, M. G., Hollenbach, D., and McKee, C. F.: 2010, *ApJ* **716**, 1191
- Yang, B., Stancil, P. C., Balakrishnan, N., and Forrey, R. C.: 2010, *ApJ* **718**, 1062
- Zinnecker, H.: 1984, *MNRAS* **210**, 43
- Zinnecker, H.: 2004, in G. Garcia-Segura, G. Tenorio-Tagle, J. Franco, and H. W. Yorke (eds.), *Revista Mexicana de Astronomia y Astrofisica Conference Series*, Vol. 22 of *Revista Mexicana de Astronomia y Astrofisica Conference Series*, pp 77–80

Acknowledgments

First and foremost I want to express my gratitude to my supervisors Prof. Dr. Ralf S. Klessen and Priv.-Doz. Dr. Simon C. O. Glover for their great support and help during all these years. This thesis would not have been possible without the assistance and comments from my collaborators Dr. Rahul Shetty and Dr. Christoph Federrath. I would like to also extend my gratitude to Priv.-Dz. Dr. Henrik Beuther for the very useful discussions and advice which helped to improve considerably this thesis, as well as for refereeing it. Moreover, I want to extend the acknowledgements to the evaluation committee Prof. Dr. Eva Grebel and Prof. Dr. Markus Oberthaler. Furthermore, I thank Prof. Dr. Cornelis Dullemond and Dr. Frank Bigiel for their assistance and useful discussions.

During the course of my PhD, I counted on the help and support of many individual who in one way or another contributed in the completion of my studies. For their advice and friendship, I would like to thank Paola Pinilla, Gustavo Dopcke, Paulina Troncoso, Michael Morales, Milica Micic, Lukas Konstandin, Jennifer Schober, Joanna Drazkowska, Philipp Girichidis (Dr. Zementidis), Christian Baczynski, Laszlo Szücs, Esteban Morales, Juan Camilo Ibañez (Pesadilla) and Mei Sasaki. I would also like to extend my gratitude to all the colleagues at ITA, specially Paul Clark, Daniel Seifried, Robi Banerjee, Rowen Smith, Diane Cormier, Volker Gaibler, Dimitrios Gouliermis, Svitlana Zhukovska, Erik Bertram, Clio Bertelli, Roxana Chira, Tilman Hartwig and Camilo Peñaloza. I also want to acknowledge the secretaries Ana Zacheus and Sylvia Matyssek for helping me to sort with all kind of bureaucracy.

I owe my deepest gratitude and love to my parents, Matilde and Germán for supporting and understanding me in all my life decisions. Thanks for their unconditional love, I have achieve all my goals. I would also like to express my love and acknowledgment to my brother German Alberto and nephew Diego, for always be in touch and support me on every step. I would like to especially express my gratitude and love to Héctor, who is my cornerstone, my support during all this years, for his patience and love. My friends Takae

Kato and Inga Bacher, as well as the Soka Gakkai International.

Finally, I would like to acknowledge the International Max Planck Research School for Astronomy and Cosmic Physics at the University of Heidelberg (IMPRS-HD), specially to Priv.-Dz. Dr. Christian Fendt and the Heidelberg Graduate School of Fundamental Physics (HGSFP). Also the European Southern Observatory for hosting me during several visits. I acknowledge subsidies from the Baden-Württemberg-Stiftung for contract research via grant P-LS-SPII/18, the Deutsche Forschungsgemeinschaft via SFB project 881 “The Milky Way System” (subprojects B1, B2, B3, and B5), and the German Bundesministerium für Bildung und Forschung for funding via the ASTRONET project STAR FORMAT (grant 05A09VHA). The simulations were performed using the *Ranger* cluster at the Texas Advanced Computing Center, using time allocated as part of Teragrid project TG-MCA99S024.

Dankeschön!